



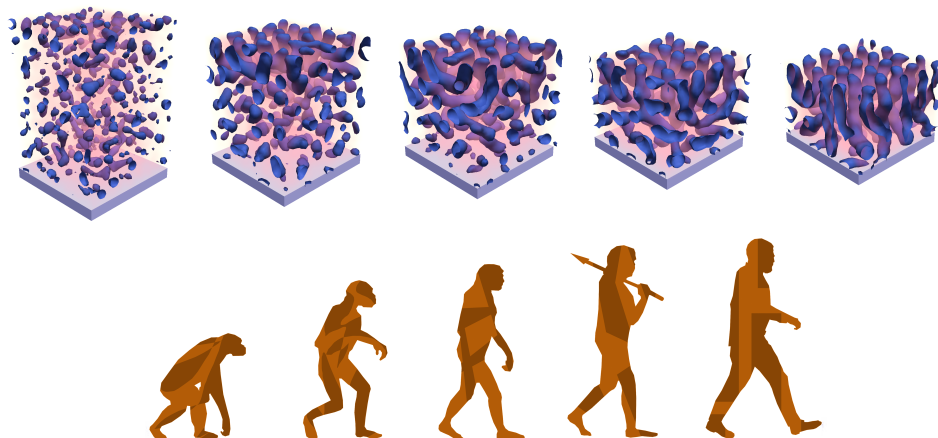
# Annual Report 2015



Physik-Department

Lehrstuhl für Funktionelle Materialien  
mit dem  
Fachgebiet Physik Weicher Materie

Technische Universität München



Prof. Dr. Winfried Petry  
Chair of Functional Materials  
Physik-Department

Deputy chairman for Prof. Dr. Winfried Petry:  
Prof. Dr. Peter Müller-Buschbaum

Prof. Dr. Christine M. Papadakis  
Soft Matter Physics Group

Physik-Department  
Technische Universität München  
James-Franck-Straße 1  
85748 Garching

Secretaries: Marion Waletzki  
Susanna Fink

Tel.: +49(0)89 289 12452

Fax: +49(0)89 289 12473

Email: [peter.mueller-buschbaum@ph.tum.de](mailto:peter.mueller-buschbaum@ph.tum.de)

[papadakis@tum.de](mailto:papadakis@tum.de)

[marion.waletzki@ph.tum.de](mailto:marion.waletzki@ph.tum.de)

[susanna.fink@ph.tum.de](mailto:susanna.fink@ph.tum.de)

<http://www.functmat.ph.tum.de>

<http://www.softmatter.ph.tum.de>

Editor: Dr. Anatoly V. Berezkin

### **Cover-page picture:**

Upper row: evolution of a block-copolymer film structure during a solvent vapor annealing as simulated with dissipative particle dynamics. Bottom row: human evolution.

### **Copyright:**

Inquiries about copyright and reproduction, etc. should be addressed to the authors.

## 1 Preface

It is a great pleasure to present the annual report for the year 2015 in the name of the staff of the Chair of Functional Materials and the Soft Matter Physics Group. It provides an overview of our teaching, research, and development activities. Our research activities are focused on functional materials and cover a broad range from soft matter physics to developments of methods and instrumentation. We examine the fundamental physics of material properties using mainly scattering methods (neutron, x-ray and light scattering). The general goal of our research is to explain the functional characteristics of soft condensed matter from the knowledge of the molecular dynamics and nanostructure.

In 2015, the chair activities covered the specific areas of water-based polymer systems, thin polymer films, polymer films for application in photovoltaics, polymer-hybrid systems and new materials. The activities in the fields of polymer films for application in photovoltaics and polymer-hybrid systems are successfully increasing. With *"TUM.solar"*, the keylab in the network of in the Bavarian Collaborative Research Project *"Solar Technologies go Hybrid"* (SolTec) headed by Prof. Müller-Buschbaum was running in the fourth year of funding. Research on *"Improved power conversion efficiency of P3HT:PCBM organic solar cells by strong spin-orbit-coupling-induced delayed fluorescence"* and on *"The crystallization of PEDOT:PSS polymeric electrodes probed in-situ during printing"* were featured on front covers of the high impact journals *Advanced Energy Materials* and *Advanced Materials*, respectively. Investigations on perovskite solar cells complemented these activities. Moreover, stimuli-responsive polymer systems as well as polymers for medical applications were again in the focus of the research.

The in-house experiments available in the laboratories of the chair were supplemented by the lively activities at numerous large scale facilities, comprising synchrotron radiation and neutron scattering experiments, also at the FRM II. In particular, the in-house x-ray scattering experiments were operated with full time schedule. Glovebox environment for improved sample preparation of devices relying on air sensitive materials such as conjugated polymers was established. With the addition of instruments to measure the external quantum efficiencies and the development of a novel slot die coater for printing of polymer films, new experimental options were added to our facilities. The sample environment for in-situ investigations of solvent vapor annealing was substantially improved, allowing higher flexibility. Moreover, together with our guest, Prof. Alfons Schulte, the high-pressure sample environments were again put into operation.

In 2015, the Chair of Functional Materials comprised 9 fellows, 44 PhD students, 39 master students, 14 bachelor students, 4 student assistants and 8 administrative and technical staff members. One external habilitation and 3 PhD theses were accomplished; moreover, 15 master theses as well as 14 bachelor theses were finished. As all the years before, we had the pleasure to host several guests from abroad, which stimulated a lively and inspiring scientific atmosphere.

In general, all members of the chair were very active at conferences and workshops, participating with both, talks and posters. Natalya Vishnevetskaya won a poster prize at the 15th Conference of the International Association of Colloid and Interface Scientists. Moreover, important conferences were organized by members of the chair: Prof. Winfried Petry organized the *"35th Symposium on Dynamical Properties of Solids"* (DyProSo) in Freising. Prof. Müller-Buschbaum was member of the international advisory board of the *"European Polymer Conference"* EPF2015 held in Dresden in June, member of the scientific program

committee of the “*International conference on grazing incidence small angle scattering*” (GISAS2015) in Nice and member in the scientific program committee of the “*International conference on small angle scattering*” (SAS2015) in Berlin. Prof. Christine M. Papadakis co-organized the Greek-German Workshop 2015 “*Structural investigation and molecular dynamics of nanostructured polymeric materials*” held in Athens in September in the framework of the partnership with The National Technical University of Athens, as well as the 2nd Workshop “*Fluorescence Correlation Spectroscopy in Polymer Science*” held in September in Aachen. Again, two Edgar-Lüscher seminars were organized, this year on the subjects “*Laser- und Quantenphysik*” and “*Grossprojekte in der Physik*”. The 5th Colloquium of the Munich School of Engineering “*Innovations for Energy Systems, Mobility, Buildings and Materials*” took place in Garching. The chair participated in the biannual meeting with the colleagues from the Munich research reactor MLZ in Grainau. Everybody enjoyed the extensive discussions in combination with a fascinating landscape a lot!

Regarding teaching activities of the chair, we offered general physics lectures for the TUM elite engineers in the Munich School of Engineering (MSE) (Müller-Buschbaum) and advanced physics for teachers for vocational schools (Papadakis). Specialized lectures comprised “*Polymer physics*” and “*Nanostructured soft materials*”. Prof. Papadakis acted again as a deputy women’s representative of the Physics Department. Moreover, Prof. Müller-Buschbaum is heading the activities in the “*Network Renewable Energies (NRG)*” in the MSE.

As a service to the community, Prof. Papadakis acted as one of the Editors-in-Chief of “*Colloid and Polymer Science*” and Prof. Müller-Buschbaum served as Associate Editor at “*ACS Applied Materials & Interfaces*”.

This annual report comprises a selection of the different research topics and projects carried out in the individual groups of the chair. It highlights the dedicated and successful research activities and collaborations with other groups and large scale facilities. We wish all chair members a fruitful continuation and a very successful year 2016.

Peter Müller-Buschbaum and Christine M. Papadakis

February 2016

## Contents

<b>1</b>	<b>Preface</b>	<b>3</b>
<b>2</b>	<b>Water based polymer systems</b>	<b>9</b>
2.1	pH-responsive, self-assembling hydrogels from a PMMA- <i>b</i> -(PDEA- <i>co</i> -PMAA)- <i>b</i> -PMMA telechelic polyampholyte . . . . .	10
2.2	Chain conformation in thin films of cyclic PNIPAM . . . . .	12
2.3	Hydration behavior of thermo-responsive polymers in aqueous solution . . . . .	14
2.4	PNIPAM dynamics in water-methanol mixtures studied by neutron spin echo spectroscopy . . . . .	16
2.5	A thermoresponsive amphiphilic diblock copolymer based on poly(methoxydiethylene glycol acrylate) (PMDEGA) . . . . .	18
2.6	Polystyrene- <i>block</i> -poly(methoxy diethylene glycol acrylate)- <i>block</i> -polystyrene triblock copolymers in aqueous solution – a SANS study of the temperature-induced switching behavior . . . . .	20
2.7	Quantifying the interactions in the aggregation of thermoresponsive polymers – the effect of cononsolvency . . . . .	22
2.8	Self-assembly of thermoresponsive micelles leading to monodisperse aggregates	24
2.9	Aggregation behavior of doubly thermo-responsive poly(sulfobetaine- <i>b</i> -( <i>N</i> -isopropylmethacrylamide) diblock copolymers . . . . .	26
2.10	HPMA-based micelles as drug carriers: influence of chain architecture and molar mass . . . . .	28
2.11	Macromolecular HPMA-based drug delivery system - behavior in protein environment . . . . .	30
2.12	Weakly amphiphilic triblock copolymers from poly(2-oxazoline) as carriers of a strongly hydrophobic cancer drug . . . . .	32
2.13	Development of internally self-assembled lipid-based systems for vaccine delivery	34
<b>3</b>	<b>Thin polymer films</b>	<b>37</b>
3.1	Simulations of solvent vapor annealing of cylinder-forming block copolymer thin films . . . . .	38
3.2	In-situ investigation of morphological changes in block copolymer thin films during solvent vapor annealing using vapor mixtures . . . . .	40
3.3	Towards an equilibrium structure in lamellar diblock copolymer thin films using solvent vapor annealing – an in-situ time-resolved GISAXS study . . . . .	42
3.4	In-situ GISAXS microfluidics investigation of the sorption, diffusion and swelling processes of thin hydrophilic polymer films . . . . .	44
3.5	Lithium-salt-containing PS- <i>b</i> -PEO block copolymer films . . . . .	46
3.6	Structure of the PLMA- <i>b</i> -PMAA diblock copolymer electrolyte . . . . .	48
3.7	Structure of thermoresponsive polystyrene- <i>b</i> -poly( <i>N</i> -isopropylacrylamide) / cobalt oxide nanocomposite thin films . . . . .	50
3.8	Optical and morphological investigation of photoactive, low band gap polymer films . . . . .	52
3.9	Full thermoelectric characterization of highly conducting PEDOT:PSS thin films .	54
3.10	Artificial nanostructuring of thin polymer films . . . . .	56
<b>4</b>	<b>Polymer films for applications in photovoltaics</b>	<b>59</b>
4.1	Light-induced degradation in the active layer of high-efficiency organic solar cells	60

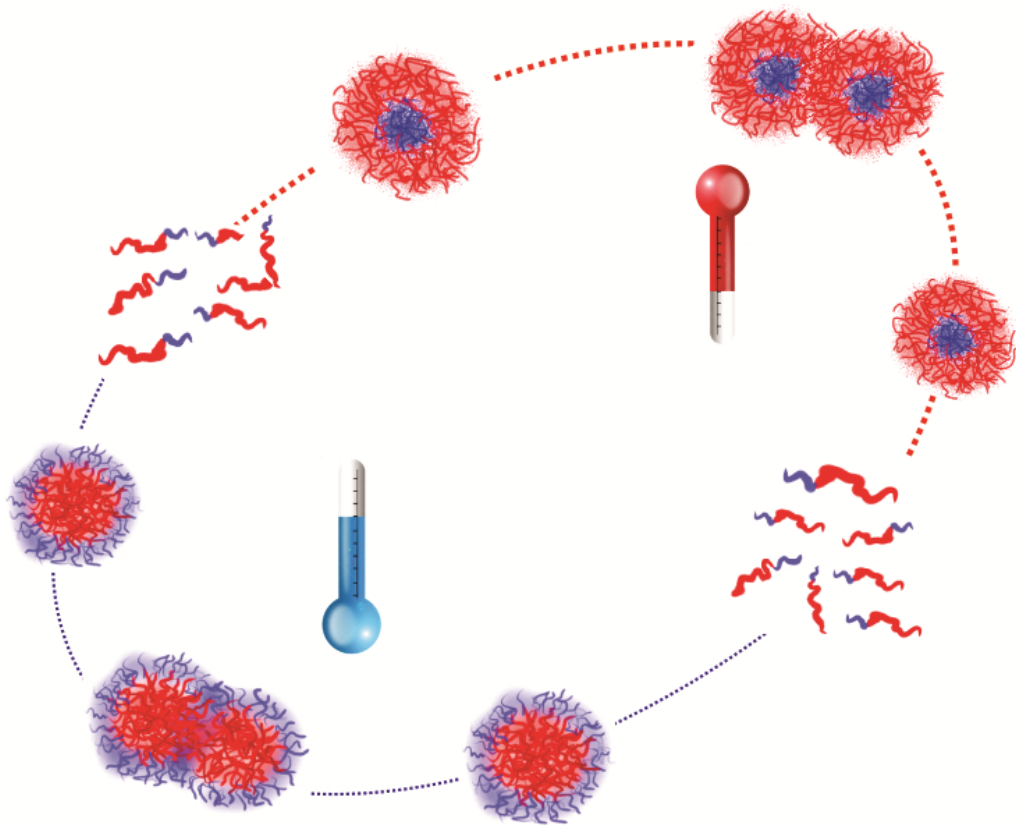
4.2	In operando morphology investigation of inverted P3HT:PCBM solar cells by GISAXS . . . . .	62
4.3	Printing high efficiency solar cells . . . . .	64
4.4	Light absorption and inner morphology of the active layer: Influence of blend ratio of bulk heterojunction organic solar cells . . . . .	66
4.5	Characterization of thiophene-selenophene-tellurophene copolymer thin films for OPV applications . . . . .	68
4.6	Degradation in printed polymer:fullerene thin films as active layers for organic photovoltaic devices . . . . .	70
4.7	Effect of solvent additives on the morphology and stability of polymer-fullerene blend thin films for organic photovoltaics . . . . .	72
4.8	In-situ tracking of crystalline evolution in P3HT:PCBM organic solar cells . . . . .	74
4.9	Following the morphology formation in situ in printed active layers for organic solar cells . . . . .	76
4.10	Effect of a medium boiling point selective solvent additive on P3HT:PCBM based solar cells . . . . .	78
<b>5</b>	<b>Polymer-hybrid systems</b>	<b>81</b>
5.1	Aqueous processed hybrid solar cells with laser-ablated titania nanoparticles . . . . .	82
5.2	Superstructuring titania films via nanoimprinting for photovoltaic applications . . . . .	84
5.3	Superstructuring of mesoporous titania thin films via wet-imprinting . . . . .	86
5.4	Nanostructured zinc oxide films for application in hybrid photovoltaics . . . . .	88
5.5	Hybrid based thermoelectrics . . . . .	90
5.6	Investigating the energy-level alignment at hybrid interfaces between ZnO and p-doped organic semiconductors . . . . .	92
5.7	Porous titania-based electrodes for high capacity lithium-ion batteries . . . . .	94
5.8	Nanostructured hybrid block copolymer electrolytes as a membrane for lithium-ion batteries . . . . .	96
5.9	Morphology of nanocomposite copolymer electrolytes for Li <sup>+</sup> /polymer batteries . . . . .	98
5.10	Self-assembled hybrid materials for lithium-ion batteries . . . . .	100
5.11	In situ DC-sputter deposition of Al on PS templates . . . . .	102
5.12	Structure and properties of metal oxide-block copolymer nanocomposites . . . . .	104
5.13	Printed diblock copolymer films with embedded magnetic nanoparticles . . . . .	106
5.14	Parallel lamella via self-assembly of PSd- <i>b</i> -PBMA with embedded maghemite nanoparticles . . . . .	108
5.15	Spray deposition of titania films with incorporated crystalline nanoparticles . . . . .	110
5.16	Dynamics of nanocomposites composed of HEUR polymer and magnetite iron oxide nanoparticles . . . . .	112
5.17	Unraveling the mechanisms of 2-step perovskite synthesis for highly efficient hybrid photovoltaics . . . . .	114
<b>6</b>	<b>New materials</b>	<b>117</b>
6.1	Metal decoration of nanoparticles attached to a substrate . . . . .	118
6.2	Mesostructured ZnO scattering layer . . . . .	120
6.3	Two dimensional organometal halide perovskite nanosheets in light emitting application . . . . .	122
6.4	The morphology and formation chemistry of solution-processed MAPbI <sub>3</sub> films . . . . .	124
6.5	Increasing achievable states of order in Heusler systems by quenched-in vacancies . . . . .	126
6.6	Magnesium battery electrolytes: Mg(BH <sub>4</sub> ) <sub>2</sub> in tetrahydrofuran studied by quasielastic neutron scattering . . . . .	128

---

6.7	Strain induced martensitic transformation in austempered ductile iron (ADI) . . .	130
6.8	Synthesis and morphological characterization in PDMS-polythiophene segmented polyureas . . . . .	132
6.9	Crystallization and mesophase formation of bottle brush copolymers with poly(propylene oxide)- <i>b</i> -poly(ethylene oxide) side chains . . . . .	134
6.10	Quasielastic neutron scattering on $\alpha$ -Mg(BH <sub>4</sub> ) <sub>2</sub> . . . . .	136
6.11	A quantum dot array to template gold nanostructure growth . . . . .	138
<b>7</b>	<b>Teaching and outreach</b>	<b>141</b>
7.1	Lectures, seminars and lab courses . . . . .	141
7.2	Conferences and public outreach . . . . .	142
7.3	Service to the community . . . . .	148
<b>8</b>	<b>Publications, talks and funding</b>	<b>149</b>
8.1	Publications . . . . .	149
8.2	Talks . . . . .	156
8.3	Posters . . . . .	165
8.4	Invited Talks at LS Funktionelle Materialien . . . . .	171
8.5	Funding . . . . .	173
<b>9</b>	<b>The chair</b>	<b>175</b>
9.1	Staff . . . . .	175
9.2	Graduations . . . . .	178
9.3	Guests . . . . .	180



## 2 Water based polymer systems



## 2.1 pH-responsive, self-assembling hydrogels from a PMMA-*b*-(PDEA-*co*-PMAA)-*b*-PMMA telechelic polyampholyte

M. A. Dyakonova, G. Gotzamanis<sup>1</sup>, B.-J. Niebuur, N. Vishnevetskaya, K. N. Raftopoulos, S. Gkempoura<sup>1</sup>, Z. Di<sup>2</sup>, C. Tsitsilianis<sup>1</sup>, C. M. Papadakis

<sup>1</sup> University of Patras, Department of Chemical Engineering, Greece

<sup>2</sup> JCNS at FRM II, Garching, Germany

Telechelic polymers composed of a linear hydrophilic and pH responsive chain which is end-capped by short hydrophobic groups have attracted special attention because of their well-defined and controllable macromolecular architecture which results in tunable rheological properties [1]. Their properties are mainly determined by the charge conditions, controlled by the pH value and the solvent nature. Identification of the corresponding changes in the structure may help to understand the mechanisms, responsible for a peculiar rheological behavior.

We have investigated the influence of the pH value on the structure of hydrogels and solutions formed by the triblock terpolymer poly(methyl methacrylate-*b*-2-(diethylamino)ethyl methacrylate-*co*-methacrylic acid)-*b*-methyl methacrylate) PMMA<sub>86</sub>-*b*-P(DEA<sub>190</sub>-*co*-MAA<sub>96</sub>)-*b*-MAA<sub>86</sub> by rheology and small-angle neutron scattering (SANS). The PMMA end blocks are hydrophobic and form dense micellar cores. The middle block P(DEA<sub>190</sub>-*co*-MAA<sub>96</sub>) is ampholytic, and its degree of ionization depends strongly on pH: PDEA is protonated at low pH, resulting in a positive net charge of the middle block, whereas PMAA is deprotonated at high pH, resulting in a negative net charge [2]. Repulsive electrostatic interactions between equally charged sequences lead to strong stretching of the middle block, which, already at low concentration is able to stretch and bridge neighboring micelles, leading to a formation of a gel network, when the degree of ionization is sufficiently high.

In Fig. 2.1a, the low shear viscosity of 30 mg/ml solutions of PMMA<sub>86</sub>-P(DEA<sub>190</sub>-*co*-MAA<sub>96</sub>)-PMMA<sub>86</sub> is presented as a function of pH. At pH 4, the solution exhibits maximum viscosity (of the order of several 10<sup>4</sup> Pas), manifesting the formation of a strong free-standing hydrogel. Reaching the region 5.4 < pH < 6.6, the viscosity drops by four orders of magnitude, revealing a gel-to-sol transition. This abrupt transition is attributed to the strong attractive electrostatic interactions among the oppositely charged DEA and MAA units on the middle polyampholyte block, which induce the collapse of the middle block. The interactions are presumably intramolecular since they should lead to a shrinkage of the potentially bridging chains, preventing the formation of a 3D network. This sharp transition upon a very small pH variation determines the high responsivity of the system. This rich rheological behaviour with a gel-to-sol transition in the physiological pH may be of interest as injectable hydrogels for biomedical applications.

The SANS curves of PMMA<sub>86</sub>-*b*-P(DEA<sub>190</sub>-*co*-MAA<sub>96</sub>)-*b*-PMMA<sub>86</sub> at 30 mg/ml in D<sub>2</sub>O at different pD values are presented in Fig. 2.1b. At low pD values (3-6), the curves exhibit a pronounced peak maximum, which is associated with the electrostatic repulsion between the micelles, and a rather broad shoulder, ascribed to the internal structure of the micelles. Increasing pD, the peak gets broader and finally vanishes at pD 7.4. The model fitting indicates that hydrogels at low pD values (3.0, 4.0 and 6.0) consist of charged fuzzy spheres, interacting with each other via the screened Coulomb potential. The spheres are formed by the hydrophobic PMMA blocks, whereas the ionized P(DEA-*co*-MAA) middle blocks spread out from the sphere surface. At low pH, the PDEA units are strongly protonated. Being stretched, they carry the

non-ionized PMAA units and prevent their collapse with the PMMA cores. The sphere radius grows with increasing pD, which is related to a decrease of the fraction of ionized DEA units, which enhances the hydrophobicity of the middle block and following collapse with the core. In addition, at pH 6.0, some of the PMAA units are deprotonated and electrostatically interact with the remaining protonated PDEA segments, which leads to their mutual neutralization, promoting the shrinkage of the middle block and its partial merging with the PMMA cores. Due to the same reason, the charge on the spheres diminishes. As a result, with increasing pD the reduced repulsion along the polyampholyte chains at the interface makes them less stretched and lowers the extent of cross-linking in the network.

At pD 7.4, *i.e.* close to the isoelectric point, the SANS curve features no more peak, *i.e.* there is no evidence of correlation between the particles, which explains the gel-to-sol transition and the significant viscosity drop, observed in rheological studies. The particle radius is found to be larger than the one at the lower pD values, which is ascribed to the steadily increasing hydrophobicity of the middle blocks, in this case due to the mutual neutralization of charged DEA and MAA segments close to the isoelectric point of polymer.

Reaching pD 11.0, the aggregates become smaller, since now the MAA sequences are ionized and, hence stretched, leaving solely PMMA in the core. The low fraction of ionized PMAA sequences does not allow the polyampholytic block to stretch enough in order to bridge different micelles, preventing the formation of a 3D network.

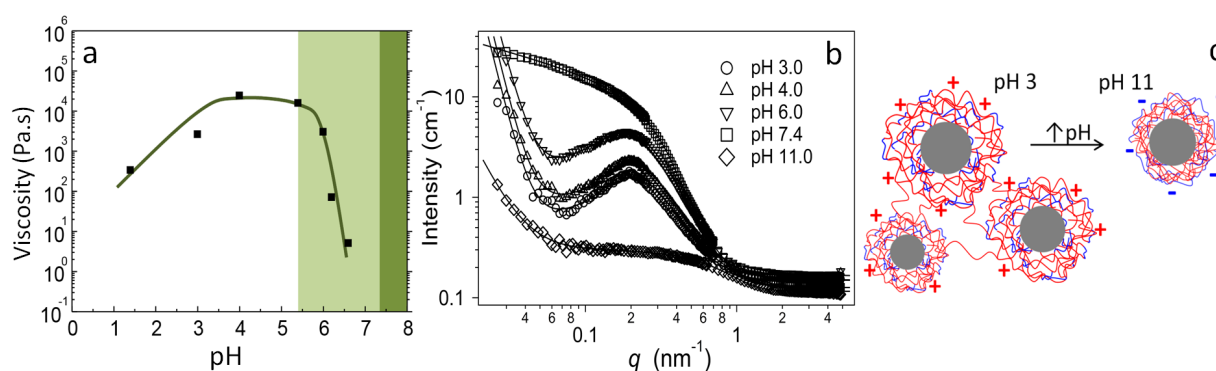


Figure 2.1:

(a) pH dependence of the low shear viscosity of 30 mg/ml MAA<sub>86</sub>-(DEA<sub>190</sub>-co-MAA<sub>96</sub>)-MAA<sub>86</sub> polymer solutions in H<sub>2</sub>O. The lighter green area marks the region of the electrostatic attractions between the oppositely charged units of polyampholyte, whereas the dark green area denotes the precipitation regime of the polymer. The line is a guide to the eye. (b) SANS curves of PMMA<sub>86</sub>-*b*-P(DEA<sub>190</sub>-co-MAA<sub>96</sub>)-*b*-PMMA<sub>86</sub> at 26°C and at the pD values indicated in the graphs. The solid lines are the model fits. (c) Schematic representation of the self-assembled structures at pH 3.0 and 11.0.

A highly correlated network is found at low pD values, which disintegrates upon the decrease in ionization degree of the middle polyampholytic block achieved at higher pD.

This project was supported by DAAD and IKY in the framework of the IKYDA program.

[1] C. Tsitsilianis, T. Aubry, I. Iliopoulos, S. Norvez, *Macromolecules* **43**, 7779 (2010)

[2] C. Tsitsilianis, G. Gotzamanis, Z. Iatridi, *Eur. Polym. J.* **47**, 497 (2011)

## 2.2 Chain conformation in thin films of cyclic PNIPAM

D. Magerl, M. Philipp, E. Metwalli, P. Gutfreund<sup>1</sup>, X.-P. Qiu<sup>2</sup>, F. M. Winnik<sup>2</sup>, P. Müller-Buschbaum

<sup>1</sup> ILL, Grenoble, France

<sup>2</sup> Université de Montréal, Canada

The chain conformation of flexible polymers near surfaces is a fundamental problem in polymer physics. Thin films are an ideal system to study the chain conformation in the confinement close to interfaces, as thin to ultrathin films consist in large parts of the interface. Studies on linear polymers in thin films have shown that the chain segments in the vicinity of an interface are oriented more parallel to the surface and are consequently flattened along the surface normal [1,2].

The behavior of ring polymers in solutions and in melts significantly differs from that of linear polymers. For example, ring polymers adopt much more compact conformations than their linear counterparts. Thus, the question occurs whether and to what extent ring polymers are also influenced by the confinement of thin films.

Experimental access to the radius of gyration ( $R_g$ ) and thus the conformation of single chains in an ensemble can be achieved by small angle scattering. For a good comparison between the unperturbed chains and the chains within the thin films,  $R_g$  has to be determined in both cases. The unperturbed chains were measured by small angle X-ray scattering on a dilute cyclic PNIPAM solution at a wavelength of  $\lambda = 0.1542$  nm. About 50 microliter sample was filled in a quartz cuvette and measured at various temperatures.

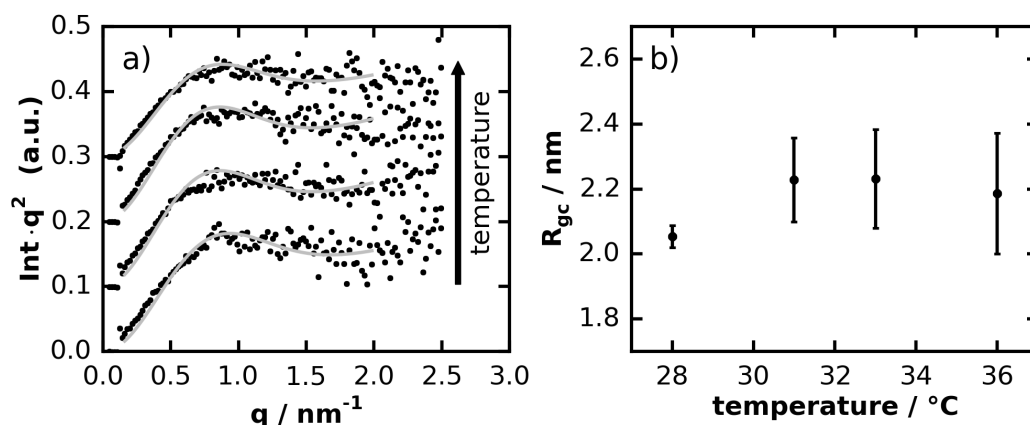


Figure 2.2:

a) Kratky plot of the azimuthally averaged SAXS data. Black dots are data; gray lines correspond to the fits described in the text. Curves are shifted vertically for clarity. b) Radii of gyration obtained from the fits in a) for the different temperatures [5].

Fig. 2.2a shows the azimuthally averaged SAXS data at different temperatures in the Kratky representation, fitted by a form factor. The curves are fitted with a model using a Padé approximant [3]. The resulting radii of gyration of the cyclic chain ( $R_{gc}$ ) are shown in Fig. 2.2b. The values at 31  $^{\circ}\text{C}$ , 33  $^{\circ}\text{C}$  and 36  $^{\circ}\text{C}$  are very close together at 2.2 nm. This region also includes the theta temperature where the net influence of the solvent on the chain cancels and the chains behave like in a melt. Thus, 2.2 nm marks the unperturbed radius of gyration.

While in the SAXS experiment on dilute solutions the distance between the chains was high enough to measure individual chains, this is not the case in a thin film. Therefore, contrast between the individual chains was achieved in grazing incidence small angle neutron scattering (GISANS) by deuteration of half of the cyclic PNIPAM chains. The GISANS investigations

were conducted at the high-flux SANS instrument D22 at the Institut Laue-Langevin (ILL) in Grenoble, France, with a neutron beam at a wavelength of 6 Å. Investigated were 3 films with thicknesses of 3.3 nm, 9.8 nm and 117 nm.

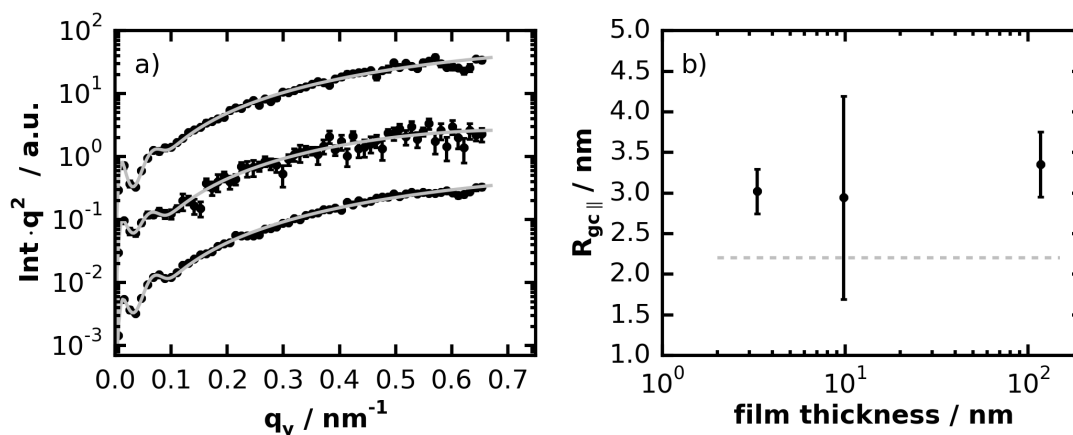


Figure 2.3:

a) Kratky plot of the line cuts of the 2D GISANS data. Black dots are data; gray lines correspond to the fits described in the text. Curves are shifted vertically for clarity. Film thicknesses (bottom to top): 3.3 nm, 9.8 nm, and 117 nm. b)  $R_{gc||}$  versus film thickness. The undisturbed  $R_{gc}$  is indicated by the gray, dashed line at 2.2 nm [5].

Analysis of the GISANS data was performed analogously to the SAXS data analysis. The data together with the fits are shown in Fig. 2.3a in the Kratky representation. An additional term in the fitting was needed to account for a feature below  $0.1 \text{ nm}^{-1}$  originating from the silicon substrate. The resulting  $R_{gc}$  parallel to the surface ( $R_{gc||}$ ) are shown in Fig. 2.3b. The  $R_{gc||}$  in all three films has a value of  $3.0 \pm 0.5 \text{ nm}$  independent of film thickness, within error bars. There are two reasons why this finding is especially interesting. First, the determined  $R_{gc||}$  lies above the unperturbed  $R_{gc}$  determined by SAXS, even for the thickest film. And second, contrary to earlier publications on homopolymers the  $R_{gc||}$  is not decreasing with thickness but stays constant within the margin of error.

In the 3.3 nm film the  $R_g$  perpendicular to the surface can be set to an upper limit of 1.6 nm from the film thickness. Together with the measured  $R_{gc||}$  this leads to an aspect ratio of about 2:1. Therefore, it is clear that the chains are stretched along the surface and squeezed perpendicular to it. Remarkably, the same increased  $R_{gc||}$  is seen in the two other films, although no such confinement is expected especially in the 117 nm film. Thus, we surmise that for all film thicknesses the same orientation effect of the cyclic PNIPAM rings parallel to the substrate is induced. Van-der-Waals forces may facilitate the preferential selection of the stretched conformation as they are known to form long-range interactions between polymer chains and substrates in planar film geometry [4,5].

- [1] K. Shuto, Y. Oishi, T. Kajiyama, C. C. Han, *Macromolecules* **26**, 6589-6594 (1993).
- [2] J. Kraus, P. Müller-Buschbaum, T. Kuhlmann, D. W. Schubert, M. Stamm, *Europhys. Lett.* **49**, 210-216 (2000).
- [3] A. M. Rubio, G. Alvarez, J. J. Freire, *Polymer* **49**, 628-634 (2008).
- [4] C. H. Wang, S. Mukherjee, A. K. M. Maidul Islam, Y. W. Yang, M. Mukherjee, *Macromolecules* **44**, 5750-5757 (2011).
- [5] D. Magerl, M. Philipp, E. Metwalli, P. Gutfreund, X.-P. Qiu, F. M. Winnik, P. Müller-Buschbaum, *ACS Macro Lett.* **4**, 1362-1365 (2015).

### 2.3 Hydration behavior of thermo-responsive polymers in aqueous solution

M. Philipp, K. Kyriakos, W. Lohstroh<sup>1</sup>, W. Petry<sup>1</sup>, A. Schulte<sup>2</sup>, C. M. Papadakis, P. Müller-Buschbaum

<sup>1</sup> MLZ, Garching, Germany

<sup>2</sup> University of Central Florida, Orlando, US

In engineering, bioengineering and medicine exists a huge demand for tailor-made polymeric materials that possess the ability to undergo massive changes in their volume, their elasticity or related properties when exposed to small stimuli [1, 2]. In order to design novel stimuli-responsive materials with the desired switching behavior, a multitude of complex architectures of responsive hydrogels, brushes, thin films, colloids and micellar systems have been synthesized. The switching mechanism is generally provoked by a sharp demixing phase transition, which is often of the lower critical solution temperature type for aqueous systems. In case of hydrogels the phase separation is commonly denoted as a volume phase transition, which hints at the fact that the volume expansion coefficient can be considered as the macroscopic order parameter susceptibility [3, 4]. On the molecular scale, important variations in hydrophobic interactions and hydrogen bond interactions seem to be at the origin of the phase separation and provoke a coil-to-globule transition in case of individual polymer chains [1, 2]. As a consequence, important changes in structure and in molecular diffusion occur [5, 6].

One prerequisite for major progress and future innovation in this growing field of smart synthetic polymeric materials is a more fundamental understanding of the molecular driving mechanisms of the phase separation. Another crucial point is the elucidation of the impact of the molecular processes on those properties, which are strongly coupled to the macroscopic order parameter. In order to contribute to these issues, we studied the hydration behavior at the demixing phase transition of a novel thermo-responsive polymer in aqueous solution. The study of responsive polymer solutions – as compared to the above-mentioned technologically more valuable materials like hydrogels, or thin films - enables us to concentrate on the basics of the demixing phase transition by avoiding its interference with mechanical constraints exerted on the macromolecules by covalent network knots or by interfacial interactions.

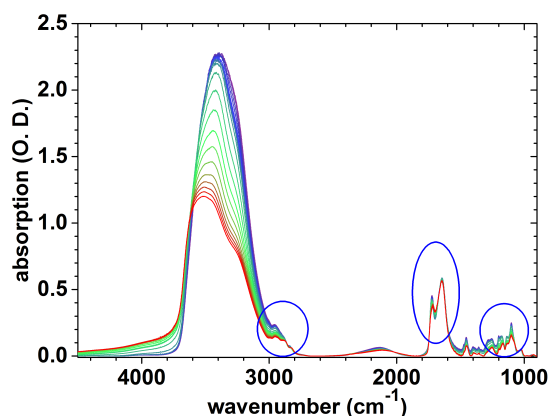


Figure 2.4:

a) Investigation of water-polymer interactions during phase separation by studying the vibration behavior of the polymer and water molecules upon heating (from blue to red lines) using Fourier transform infrared spectroscopy. The ellipses indicate those bands, which correspond to vibrations of the polymer chains.

Changes in intermolecular interactions and in molecular transport are at the origin of the phase separation [1-5]. We focused on the intermolecular interactions and the diffusion dynamics of

the hydration water and the almost freely diffusing water across the demixing transition of different concentrated aqueous solutions of thermo-responsive polymers with the aim to access the molecular order parameter [5]. The demixing temperature lies between 313 and 320 Kelvin. As shown in Fig. 2.4, the changes in intermolecular interactions between the polymer and water were studied by Fourier transform infrared spectroscopy upon heating the aqueous polymer solutions across the demixing phase transition. Fig. 2.5 provides first insights into the diffusion behavior of the water molecules across the phase separation. These incoherent neutron scattering experiments were performed at the cold neutron time-of-flight spectrometer TOF-TOF at the MLZ in Garching. As the linewidths decreases with temperature in the inset of Fig. 2.5, it qualitatively shows that, and how, part of the hydration water is released during phase separation. The spectra are fitted using two Lorentzian contributions for two populations of hydration water.

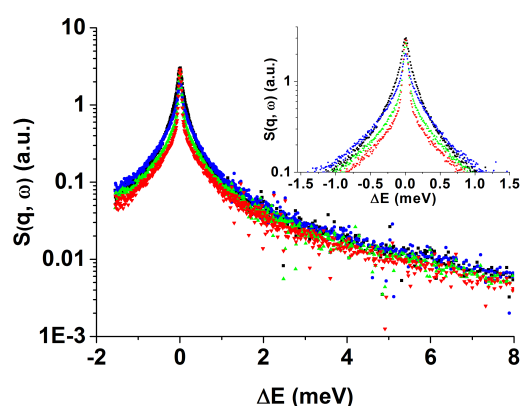


Figure 2.5:

a) Investigation of the local diffusion behavior of the different water populations upon heating (from black squares, blue dots, green triangles to red triangles) using quasi-elastic neutron scattering. Inset: zoom on the center of the spectra.

To conclude, incoherent neutron scattering experiments, combined with Fourier transform infrared spectroscopic investigations, provide first novel insights into the molecular-mechanistic understanding of the hydration behavior and thereby into demixing phase transitions of a novel type of thermo-responsive polymer in aqueous solution.

- [1] M. A. Cohen Stuart et al., *Nature Materials* **9**, 101-113 (2010)
- [2] I. Tokarev et al., *Soft Matter* **5**, 511 (2009)
- [3] M. Philipp, R. Aleksandrova, U. Müller, M. Ostermeyer, R. Sanctuary, P. Müller-Buschbaum, J. K. Krüger, *Soft Matter* **10**, 7297-7305 (2014)
- [4] M. Philipp, K. Kyriakos, L. Silvi, W. Lohstroh, W. Petry, J. K. Krüger, C. M. Papadakis, P. Müller-Buschbaum, *J. Phys. Chem. B* **118**, 4253-4260 (2014)
- [5] M. Philipp, V. Körstgens, D. Magerl, C. Heller, Y. Yao, W. Wang, G. Santoro, S. V. Roth, P. Müller-Buschbaum, *Langmuir* **31**, 9619-9627 (2015)
- [6] K. Kyriakos, M. Philipp, J. Adelsberger, S. Jaksch, A. V. Berezkin, D. M. Lugo, W. Richtering, I. Grillo, A. Miasnikova, A. Laschewsky, P. Müller-Buschbaum, C. M. Papadakis, *Macromolecules* **47**, 6867-6879 (2014)

## 2.4 PNIPAM dynamics in water-methanol mixtures studied by neutron spin echo spectroscopy

K. Kyriakos, K.N. Raftopoulos, O. Holderer<sup>1</sup>, O. Ivanova<sup>1</sup>, M. Ohl<sup>2</sup>, P. Müller-Buschbaum, C.M. Papadakis

<sup>1</sup> JCNS at MLZ, Garching, Germany

<sup>2</sup> JCNS at Oak Ridge, Tennessee, USA

Poly(N-isopropylacrylamide) (PNIPAM) in aqueous solution collapses and precipitates above a certain temperature termed as the *cloud point*. Interestingly, the cloud point in mixtures of water and methanol is lower than that in pure water. This phenomenon is termed *cononsolvency* [1]. Three mechanisms have been proposed for the molecular origin of cononsolvency. (i) Tanaka et al. suggest that water and methanol attach to the chain in a collective manner, i.e. solvent molecules attach to the chain preferentially close to positions already occupied by molecules of the same species. Thus, the two solvents form sequences along the macromolecular chain, whereas some chain segments remain without any solvent molecule attached and for this reason are prone to collapse [2]. (ii) Zhang and Wu propose that the two co-solvents form complexes, i.e. water prefers to interact with the methanol and thus withdraws it from the polymer chain [3]. (iii) Mukherji et al. propose that the alcohol interacts strongly with the chain and thus forms bridges between chain segments, which initiate the collapse [4].

In semidilute polymer systems under good solvent conditions, two types of dynamics have been observed, depending on the momentum transfer ( $q$ ) range: For small length scales (large  $q$ ), Zimm dynamics is expected. It scales as  $\Gamma \propto q^3$ , where  $\Gamma$  is the relaxation rate. For length scales the chains entangle with each other, and they form a transient network with mesh size  $\xi_c$ , which corresponds to the entanglement length. For length scales larger than  $\xi_c$ , the dynamics is of the Rouse type, i.e. scales with  $q$  as  $\Gamma \propto q^2$ . At theta conditions, self-entanglements occur, and have a characteristic scale  $\xi_{ci} < \xi_c$ . Between  $\xi_c$  and  $\xi_{ci}$ , a region with dynamic scaling as  $\Gamma \propto q^1$  exists [6]. Just below the cloud point, the solutions are in theta condition, and the quality of the solvent may be controlled not only by the temperature, but also by the cosolvent.

In order to contribute to the understanding of the origin of cononsolvency, we investigate these dynamics and their dependence on the polymer concentration and the composition of the solvent mixture by neutron spin echo (NSE) spectroscopy. The experiments were carried out using the JCNS Neutron Spectrometer at FRM II. A  $q$  range of  $0.03 - 0.21 \text{ \AA}^{-1}$  and a time range of  $10^{-1} - 10^2 \text{ s}$  were covered. We chose a low and a high concentration of PNIPAM (10 and 25 wt%), and three methanol fractions (0, 10 and 15 v/v%). Experiments were performed 2 and 5 K below the respective cloud points. Fig. 2.6 shows representative intermediate scattering functions for various  $q$  values.

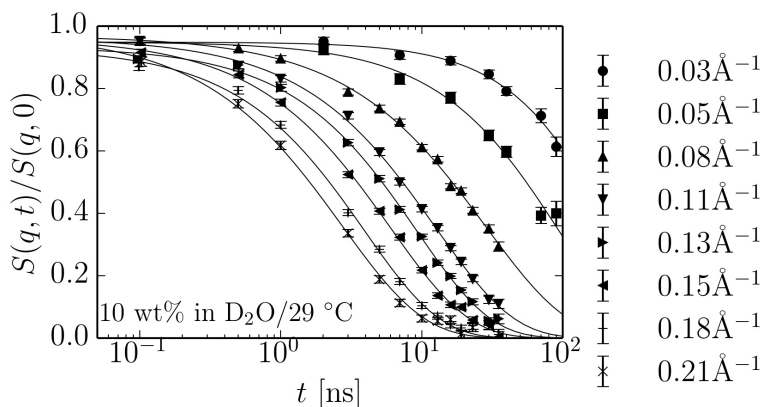


Figure 2.6:  
Normalized intermediate scattering functions of the 10 wt% PNIPAM solution in  $D_2O$  at  $29 \text{ }^\circ\text{C}$  at different momentum transfers. The lines are fits of stretched exponentials.

The curves are described well by a stretched exponential function:

$$\frac{S(q, t)}{S(q, 0)} = A \cdot \exp [-(\Gamma t)^\beta]$$

where  $\beta$  is the stretching exponent. The resulting relaxation rates  $\Gamma$  are plotted against  $q$  in Fig. 2.7.

It is observed that, as expected, the lower the concentration, the faster is the relaxation (higher  $\Gamma$ ). With increasing methanol content, the dynamics slows down considerably. To some extent, this is related to the increase of the viscosity of the solvent mixture, but the deceleration is stronger than one would expect if this was the sole mechanism. Hence, the deceleration is also related to the solvent-polymer interaction. The temperature, close to the cloud point, does not have a significant effect on the dynamics.

With respect to the scaling of the relaxation rate  $\Gamma$  with  $q$ , we observe that the slope in the log-log plot changes at  $\sim 0.07 \text{ \AA}^{-1}$ . Below this value, the  $q$  resolution of the measurement does not allow for the determination of a scaling exponent, but the few points on each curve indicate compatibility with a scaling exponent of  $\sim 2$ , which is predicted for collective Rouse dynamics. At  $q > 0.07 \text{ \AA}^{-1}$ , the scaling exponent increases, but a power law fit gives values in the range 2.2 – 2.5, instead of 3 which would be expected by the Zimm model. This observation indicates that the dynamics is more complex than predicted by the Zimm model. No intermediate region with  $\Gamma \propto q^1$  can be detected.

The stretching exponent  $\beta$ , as calculated by the fitting of stretched exponential function, is consistently around 0.8, a value higher than that expected by Zimm (2/3) or Rouse (1/2) dynamics [5].

This work has pointed out that attachment of methanol to the polymer chains slows down their dynamics and may be related to the thermoresponsive behavior.

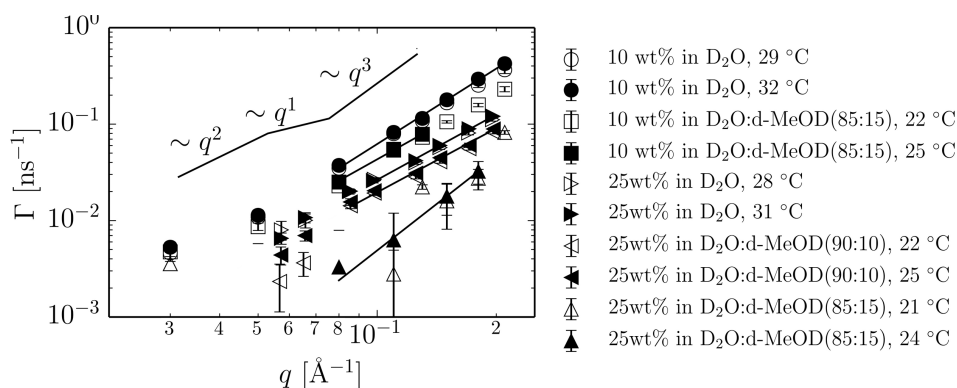


Figure 2.7:

Relaxation rates  $\Gamma$ , obtained by fitting of a stretched exponential, as a function of momentum transfer  $q$  in a double logarithmic representation. The lines are fits of power laws.

**Acknowledgement:** K.N.R. was supported by the TUM University Foundation Fellowship.

- [1] K. Kyriakos, M. Philipp, J. Adelsberger, S. Jaksch, A.V. Berezkin, D.M. Lugo, W. Richtering, I. Grillo, A. Miasnikova, A. Laschewsky, P. Müller-Buschbaum, C.M. Papadakis, *Macromolecules* **47**, 6867-6879 (2014).
- [2] F. Tanaka, T. Koga, H. Kojima, F.M. Winnik, *Macromolecules* **42**, 1321-1330 (2009).
- [3] G. Zhang, C. Wu, *J. Am. Chem. Soc.* **123**, 1376-1380 (2001).
- [4] D. Mukherji, C.M. Marques, K. Kremer, *Nat. Commun.* **5**, 4882 (2014)
- [5] B. Ewen, D. Richter, *Adv. Polym. Sci.* Vol. 134, 1-129 Springer-Verlag, Berlin, 1997.

## 2.5 A thermoresponsive amphiphilic diblock copolymer based on poly(methoxydiethylene glycol acrylate) (PMDEGA)

D. Aravopoulou<sup>1</sup>, K. Kyriakos, A. Miasnikova<sup>2</sup>, A. Laschewsky<sup>2</sup>, A. Kyritsis<sup>1</sup>, C.M. Papadakis

<sup>1</sup> Physics Department, National Technical University of Athens, Greece

<sup>2</sup> Institut für Chemie, Universität Potsdam

Thermoresponsive polymers in aqueous solution respond reversibly to small temperature stimuli by strong changes in their solubility and chain conformation, i.e. they show lower critical solution temperature (LCST) behavior. Therefore, they have received increased attention as smart materials, e.g. for biomedical applications. A significant amount of studies have focused on the self-assembled polymeric nanostructures formed by diblock or triblock copolymers, featuring thermoresponsive and hydrophobic blocks. In aqueous solution, self-assembly leads to a great variety of morphologies [1].

We report here on the temperature-dependent structures formed by a diblock copolymer polystyrene-*b*-poly(methoxy diethylene glycol acrylate) (PS<sub>11</sub>-*b*-PMDEGA<sub>331</sub>) in aqueous solution which we studied using small-angle X-ray scattering (SAXS). It features a recently synthesized new type of polymers, PMDEGA, which contain thermoresponsive oligoethylene glycol side chains. In dilute solution, the cloud point (CP) of the homopolymer PMDEGA is in the physiologically particularly interesting range of 35–42 °C for degrees of polymerization  $N > 100$ , as measured previously using turbidimetry [2]. Since the PS block is very short, the diblock copolymer is directly soluble in water. It is expected to form spherical core-shell micelles with a PS core and a PMDEGA shell.

SAXS measurements were carried out using a Ganesha 300XL SAXS-WAXS instrument which was operated at a wavelength of 1.54 Å and sample-to-detector distances of 406.2 mm and 1056.2 mm. Measurement times were 60 min and 120 min. The polymer was dissolved in water at a concentration of 25 wt%. It was mounted in a quartz capillary. The background from the empty capillary was subtracted. Using calorimetry, the CP was found at 41.3 °C.

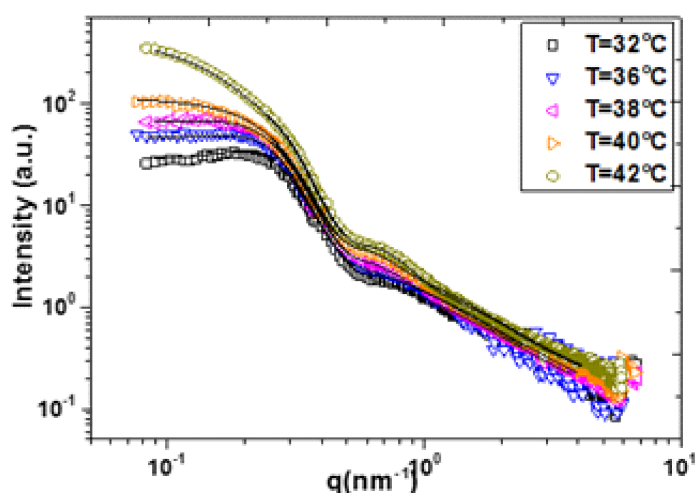


Figure 2.8:  
Representative SAXS curves in dependence on temperature. From bottom to top: 32 °C, 36 °C, 38 °C, 40 °C, 42 °C. The lines are model fits, see text.

Fig. 2.8 presents the SAXS curves below and above the CP of PS<sub>11</sub>-*b*-PMDEGA<sub>331</sub> at 25 wt%. At 32 °C, a maximum is observed at  $q \sim 0.02 \text{ nm}^{-1}$  ( $q$  is the momentum transfer) which we attribute to the correlation between the positions of the micelles. Moreover, at  $\sim 0.05 - 0.2 \text{ nm}^{-1}$ , a shoulder is present, and above, a smooth decay. With increasing temperature, the correlation peak becomes weaker and, at the same time, the forward scattering below  $0.01 \text{ nm}^{-1}$  increases,

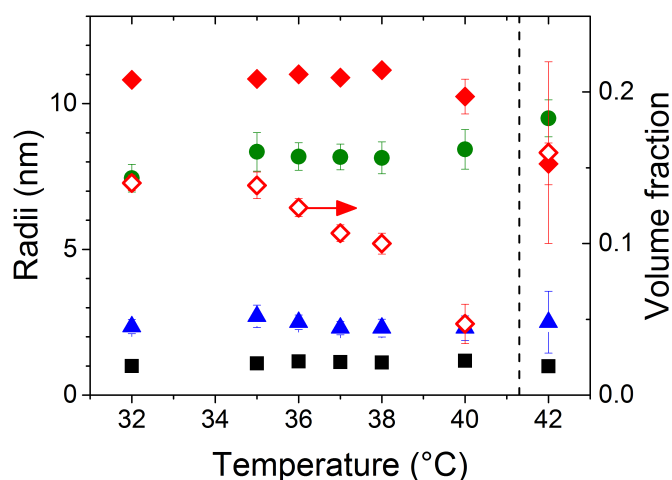


Figure 2.9: Structural parameters resulting from model fitting. Left axis: correlation length (black squares), core radius (blue triangles), micellar radius (green circles), hard-sphere radius (red closed diamonds). Right axis: volume fraction (red open diamonds).

implying the formation of larger aggregates. At 42 °C, i.e. above the CP, the maximum is not discernible any longer, but overlaps with a smooth decay.

The curves were analyzed by model fitting. Below the CP, a form factor of spherical core-shell micelles with a polydisperse core was used together with an Ornstein-Zernike term to account for concentration fluctuations within the swollen micellar shell. Above the CP, the Guinier form factor was used in addition to model the forward scattering from large aggregates.

The core radius is  $\sim 2.5$  nm in the entire temperature range, as one can see in Fig. 2.9. Above the CP, the micellar radius is  $\sim 8.3$  nm up to the CP and  $9.5 \pm 0.6$  nm above, i.e. at a higher value than below. The correlation length describing the correlation length between the PMDEGA chains, is of the order of 1.0 nm up to the CP and stays rather constant above. The hard-sphere radius,  $r_{HS}$ , is  $\sim 11$  nm below the CP. Above the CP,  $r_{HS}$  is found at a lower value, namely  $7.9 \pm 0.3$  nm, i.e. the distance between the micelles has decreased compared to the swollen state below the CP, as expected. The volume fraction,  $\eta_{HS}$ , decreases from  $0.14 \pm 0.01$  at 32.0 °C to  $0.05 \pm 0.01$  at 40.0 °C. At 42.0 °C,  $\eta_{HS}$  increases again to  $0.17 \pm 0.06$ , i.e. the correlation between the micelles is reinstalled. Aggregates having a radius of gyration of 26 nm are observed at 42 °C. At temperatures above 42 °C, precipitation prevents further investigations by SAXS. The temperature of  $41 \pm 1$  °C, where structural changes are found with SAXS coincides with the CP measured using calorimetry (41.3 °C).

Comparison with the results from a previously studied PS<sub>11</sub>-*b*-PMDEGA<sub>505</sub> [3] reveals that the micellar radius of this diblock copolymer having a longer PMDEGA block is larger, as expected. All other features, especially the counterintuitive absence of a change of the micellar radius at the CP, are observed in both diblock copolymers.

The project was funded by DFG and by DAAD in the framework of the program "Hochschulpartnerschaften mit Griechenland".

- [1] A. Laschewsky, P. Müller-Buschbaum, C.M. Papadakis, *Progr. Colloid Polym. Sci.* **140**, 15 (2013)
- [2] A. Miasnikova, A. Laschewsky, *J. Polym. Sci. A: Polym. Chem.* **50**, 3133 (2012)
- [3] K. Kyriakos, D. Aravopoulou, L. Augsbach, J. Sapper, S. Ottinger, C. Psylla, A. Aghebat Rafat, C.A. Benitez-Montoya, A. Miasnikova, Z. Di, A. Laschewsky, P. Müller-Buschbaum, A. Kyritsis, C.M. Papadakis, *Colloid Polym. Sci.* **292**, 1757 (2014)

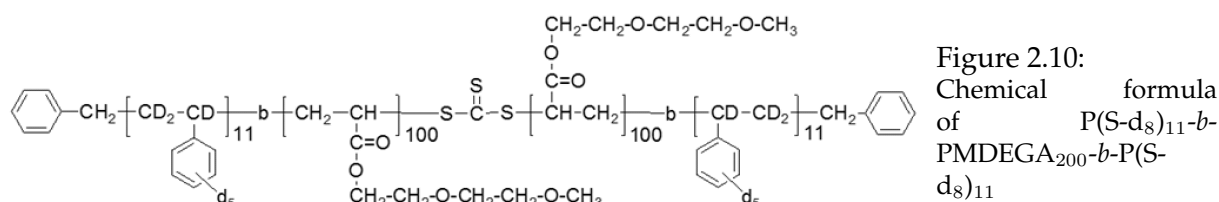
## 2.6 Polystyrene-*block*-poly(methoxy diethylene glycol acrylate)-*block*-polystyrene triblock copolymers in aqueous solution – a SANS study of the temperature-induced switching behavior

J. Adelsberger, A.M. Bivigou-Koumba<sup>1</sup>, A. Miasnikova<sup>1</sup>, P. Busch<sup>2</sup>, A. Laschewsky<sup>1</sup>, P. Müller-Buschbaum, C.M. Papadakis

<sup>1</sup> Universität Potsdam, Institut für Chemie

<sup>2</sup> Jülich Centre for Neutron Science JCNS, Forschungszentrum Jülich GmbH, Garching

Amphiphilic triblock copolymers with hydrophobic end blocks and a thermoresponsive middle block may form flower-like core-shell micelles in aqueous solution with a thermoresponsive shell. We investigate a micellar solution of a triblock copolymer which has a novel thermoresponsive polymer, namely poly(methoxy diethylene glycol acrylate) (PMDEGA), as a middle block and polystyrene (PS) end blocks. P(S-d<sub>8</sub>)<sub>11</sub>-*b*-PMDEGA<sub>200</sub>-*b*-P(S-d<sub>8</sub>)<sub>11</sub> (Fig. 2.10) is studied around the cloud point (CP) using small-angle neutron scattering (SANS) [1]. Using fully deuterated P(S-d<sub>8</sub>) blocks and D<sub>2</sub>O as solvent, excellent scattering contrast between the PMDEGA shell with respect to the PS core and to the solvent is achieved.



P(S-d<sub>8</sub>)<sub>11</sub>-*b*-PMDEGA<sub>200</sub>-*b*-P(S-d<sub>8</sub>)<sub>11</sub> was dissolved in D<sub>2</sub>O at a concentration of 300 mg ml<sup>-1</sup>. SANS measurements were carried out at the instrument KWS-2 of JCNS at FRM II, Garching, using a neutron wavelength of 7 Å and sample-detector distances of 2 m and 8 m. The sample cell was mounted in a thermostated oven. Measuring times were 5-10 min. The curves were azimuthally averaged, the background was subtracted, and the data were brought to absolute scale.

The SANS curves are shown in Fig. 2.11a,b. At temperatures up to 26.0 °C, a maximum is observed at  $q = 0.024 \text{ \AA}^{-1}$  ( $q$  is the momentum transfer) which we assign to the first maximum of the structure factor. A shoulder at  $q \sim 0.09 \text{ \AA}^{-1}$  reflects the form factor of the micelles. Above 26.0 °C, the maximum becomes less pronounced and moves to lower  $q$  values, and the scattering at  $q < 0.02 \text{ \AA}^{-1}$  increases up to 38.0 °C. Above, it decreases again, and above 42.0 °C, distinct forward scattering appears below  $0.01 \text{ \AA}^{-1}$ ). Thus, the structural changes are complex and occur on many length scales. In particular, in the range between 37.5 °C and 40.0 °C, changes are observed, especially on large length scales.

Good fits are obtained using a model comprising the form factor of spherical core-shell micelles, a Percus-Yevick structure factor to describe the correlation between the micelles, and the Guinier form factor to model aggregates formed by the micelles above the CP. The resulting parameters are compiled in Fig. 2.11c-f. Best fits were obtained when the core radius was fixed at 31 Å (Fig. 2.11c), which is consistent with the contour length of the P(S-d<sub>8</sub>)<sub>11</sub> block of  $\sim 28 \text{ \AA}$ . The micellar radius increases upon heating towards the CP (Fig. 2.11c), and decreases slightly above 36.5 °C. The absence of a discontinuity at the CP and the shallow decrease above is in line with our previous results on a similar triblock copolymer [2]. The volume fraction of D<sub>2</sub>O in the shell (Fig. 2.11d) decreases between 15.0 °C and 36.5 °C. Thus, already below the CP, the content of D<sub>2</sub>O in the shell decreases. It stays at low values up to 42 °C, and then increases again up to 50.0 °C. Possibly, at high temperatures, water diffuses into the aggregates.

The hard-sphere radius,  $r_{HS}$ , which is equivalent to half the center-to-center distance between micelles (Fig. 2.11c) decreases steeply at the CP within 3.5 K. The volume fraction of correlated

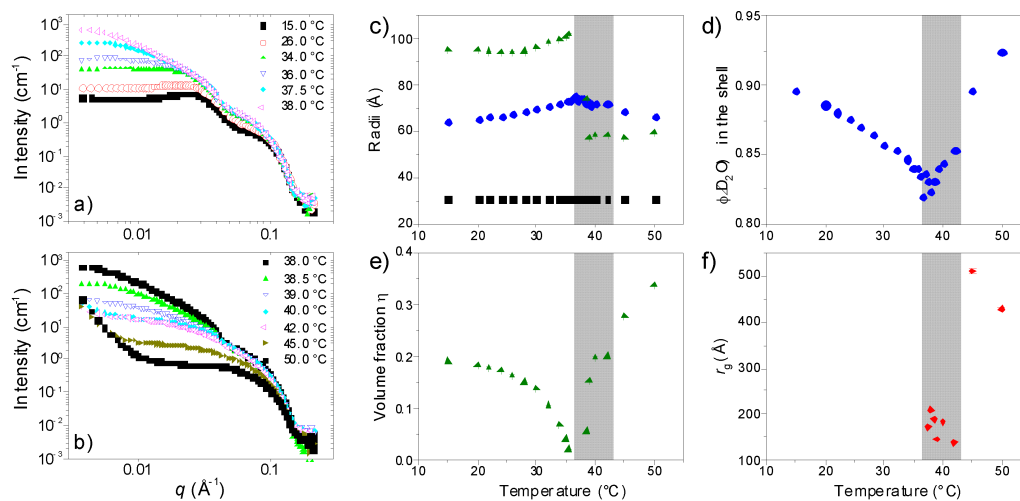


Figure 2.11:

Representative SANS curves at low (a) and at high temperatures (b). The temperatures are given in the graphs. (c-f) Results from the fits. (c) Radii: black squares:  $r_c$ , blue circles:  $r_m$ , green triangles:  $r_{HS}$ . (d) Volume fraction of  $D_2O$  in the micellar shell. (e) Volume fraction of the correlated micelles from the respective structure factor. (f) Radius of gyration of the aggregates. The grey areas indicate the transition region (36.5-43.0 °C).

micelles,  $\eta$ , decreases strongly as the CP is approached from below (Fig. 2.11e). At temperatures between 36.0 °C and 38.0 °C, the structure factor is very weak (Fig. 2.11a,b), and  $\eta$  is close to zero, thus lower than the value expected from the polymer concentration. Presumably, only few micelles participate in aggregate formation. Above 38.5 °C,  $\eta$  increases steeply. At these temperatures, small aggregates are observed as well (Fig. 2.11f).

To summarize, the transition region of this triblock copolymer ranges from 36.5 °C to 43.0 °C and is thus rather broad, in contrast to the sharp transition observed in turbidimetry. Apparently, aggregates having radii of only 170 Å result already in turbid solutions. The overall behavior is similar to the one of the recently investigated concentrated solution of a P(S-d<sub>8</sub>)<sub>11</sub>-b-PMDEGA<sub>505</sub> diblock copolymer in D<sub>2</sub>O [3]. However, the micellar radius changes slightly at the CP, which is not the case in the diblock copolymer. Moreover, for the triblock copolymer solution, the spatial correlation between the micelles just above the CP is more pronounced than for the diblock copolymer solution. Thus, as expected, bridging of the micelles in the triblock copolymer has an influence on their correlation. Interestingly, the aggregates formed right above the CP are larger in the diblock copolymer than in the triblock copolymer solution.

The project was funded by DFG within the priority program SPP1259 "Intelligente Hydrogele" (grants Pa771/4, Mu1487/8, La611/7).

[1] J. Adelsberger, C.M. Papadakis et al., *Colloid Polym. Sci.* **293**, 1515 (2015)

[2] A. Miasnikova, G. De Paoli, C.M. Papadakis et al., *Langmuir* **28**, 4479 (2012)

[3] K. Kyriakos, C.M. Papadakis et al., *Colloid Polym. Sci.* **292**, 1757 (2014)

## 2.7 Quantifying the interactions in the aggregation of thermoresponsive polymers – the effect of cononsolvency

K. Kyriakos, M. Philipp, C.-H. Lin, M. Dyakonova, N. Vishnevetskaya, I. Grillo<sup>1</sup>, A. Zaccone<sup>2</sup>, A. Miasnikova<sup>3</sup>, A. Laschewsky<sup>3</sup>, P. Müller-Buschbaum, C.M. Papadakis

<sup>1</sup> Institut Laue-Langevin, Grenoble, France

<sup>2</sup> Theorie weicher Materie, Physik-Department, Technische Universität München

<sup>3</sup> Institut für Chemie, Universität Potsdam

Colloidal dispersions of soft matter particles in aqueous media are ubiquitous, *e.g.* in paints or as drug delivery systems. For many applications, a detailed control of the aggregation behavior in solution is of fundamental importance. A special kind of colloidal dispersions showing a rich responsive behavior is formed by self-assembly of lower critical solution (LCST) type thermoresponsive polymers in aqueous solutions. Above the cloud point,  $T_{cp}$ , these polymers collapse and form mesoglobules in the colloidal size range. The pathway from molecularly dissolved polymers to mesoglobules is, however, under debate. Poly(N-isopropyl acrylamide) (PNIPAM) is a widely studied thermoresponsive polymer with an LCST of  $\sim 27 - 32$  °C. The addition of small volume fractions of a cosolvent, *e.g.* a short-chain alcohol, to aqueous solutions of PNIPAM homopolymers results in a considerable decrease of  $T_{cp}$ , in spite of these alcohols being good solvents for PNIPAM. The arrangement of water and the cosolvent along the PNIPAM chain in sequences, the change of the water structure by the kosmotropic alcohol and bridging of the PNIPAM chains by the alcohol have been put forward as possible mechanisms.

In the present work, we focus on the influence of two cosolvents—methanol and ethanol—on the colloidal growth process of aqueous PNIPAM-based micellar solution [1]. We probe the aggregation of thermoresponsive micelles of P(S-d<sub>8</sub>)-*b*-PNIPAM (P(S-d<sub>8</sub>) stands for fully deuterated polystyrene) in the presence of the cosolvents during a rapid increase of temperature (temperature jump) through  $T_{cp}$  using time-resolved small-angle neutron scattering (TR-SANS). A P(S-d<sub>8</sub>)<sub>11</sub>-*b*-PNIPAM<sub>431</sub> diblock copolymer was dissolved at 30 mg ml<sup>-1</sup> in pure D<sub>2</sub>O or in mixtures of D<sub>2</sub>O:*d*-MeOD or D<sub>2</sub>O:*d*-EtOD (fully deuterated ethanol), each with 5 mole-% of the alcohol. TR-SANS measurements were performed at D22, ILL in Grenoble, France. Temperature jumps were realized using a modified Biologic SFM-300 stopped-flow instrument. The solutions were equilibrated at  $T_{cp} - 3$  K and were transferred remotely into the sample cell which had been preheated to  $T_{cp} + 2$  K. The measuring times were between 0.2 s and 15 s, and the entire measurement lasted 1500 s. The neutron wavelength was  $\lambda = 0.8$  nm and the sample-to-detector distances (SDDs) 4.0 and 14.4 m. The data were brought to absolute units and were azimuthally averaged.

SANS curves of P(S-d<sub>8</sub>)<sub>11</sub>-*b*-PNIPAM<sub>431</sub> in D<sub>2</sub>O:*d*-MeOD are shown as an example in Fig. 2.12a. Three different regimes are distinguished: (I) below  $T_{cp}$ , core-shell micelles with swollen shells is observed (see below); (II) as soon as  $T_{cp}$  is crossed, their shells collapse, the micelles become hydrophobic and form aggregates which grow with time; and finally (III), the aggregate size exceeds the instrumental resolution. Fig. 2.12b compiles representative structural parameters for P(S-d<sub>8</sub>)<sub>11</sub>-*b*-PNIPAM<sub>431</sub> in D<sub>2</sub>O:*d*-MeOD.

The growth rate of the aggregates above  $T_{cp}$  is related to their interaction potential. To quantify this relationship, the aggregate radii,  $r_{agg}(t)$ , from regime II are normalized by their initial values,  $r_{agg}^{cp}$  (see above) and replotted in Fig. 2.12c versus the reduced time ( $t_{cp}$  denotes the time when  $T_{cp}$  is crossed). A linear dependence is observed in all three cases with the slope increasing with the molar volume of the cosolvent. To derive the interaction potential between the colloidal aggregates consisting of self-assembled, collapsed micelles, we adapt the reversible association model proposed for suspensions of thermoresponsive nanoparticles [2]. In this model,

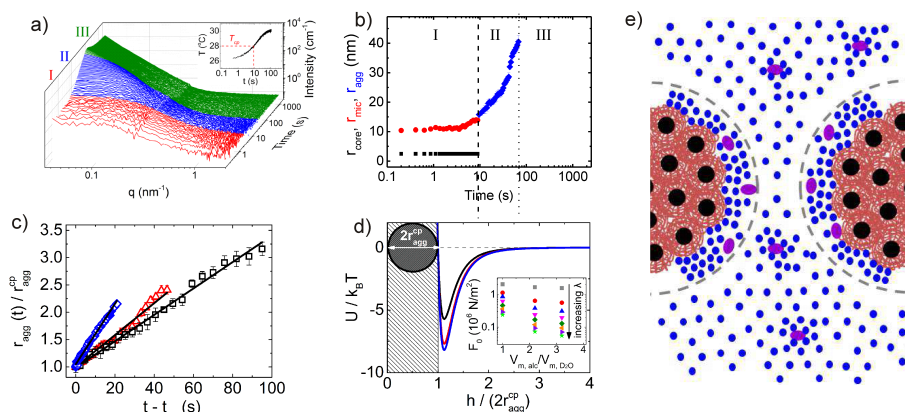


Figure 2.12:

(a) SANS curves of  $P(S-d_8)_{11}-b-PNIPAM_{431}$  in  $D_2O:d\text{-MeOD}$  during a temperature jump from  $25\text{ }^\circ\text{C}$  to  $30\text{ }^\circ\text{C}$ . Regimes I-III are indicated. The inset shows the temperature profile. (b) Corresponding structural parameters as a function of time after injection. Black squares: radii of the micellar cores,  $r_{core}$ ; red circles: micellar radii,  $r_{mic}$ ; blue diamonds: radii of gyration of the aggregates,  $r_{agg}$ . The dashed and dotted lines mark the transition times between regimes I and II,  $t_{cp}$ , and between regimes II and III, respectively. (c) Normalized aggregate radii as a function of the reduced time. Solution in  $D_2O$  (black squares), in  $D_2O:d\text{-MeOD}$  (red triangles) and in  $D_2O:d\text{-EtOD}$  (blue diamonds). The solid lines are linear fits. (d) Total interaction potentials for the aggregation of collapsed micelles in pure  $D_2O$  (black line, uppermost curve), in  $D_2O:d\text{-MeOD}$  (red line, middle curve) and in  $D_2O:d\text{-EtOD}$  (blue line, lowermost curve). (e) Schematic drawing of the proposed model describing the final state in  $D_2O:d\text{-MeOD}$ . The collapsed core-shell micelles are depicted in black and brown,  $D_2O$  molecules as small blue spheres and  $d\text{-MeOD}$  as pink ellipses.

collapsed hydrophobic nanoparticles associate at a rate  $k_+$  and dissociate at a rate  $k_-$ . The association is diffusion-limited.  $r_{agg}(t)$  is proportional to an effective rate  $K_{eff}$  which is a function of  $k_+$ ,  $k_-$  and the initial number of aggregates. From the slopes in Fig. 2.12c, the  $K_{eff}$  values are determined.

Using these  $K_{eff}$  values, the interaction potential between two colloidal aggregates can be calculated and the depth of the potential  $V$  can be determined (Fig. 2.12d). At this, a truncated Lennard-Jones potential is assumed. The well depth depends on the solvent mixture; hence, the observed change of the aggregation kinetics is indeed due to the influence of the cosolvent on the interaction potential. The potential can be assumed to comprise an attractive and a repulsive part. The repulsion at short distances (up to a few nm) is attributed to layers of structured water hydrating the surface of the colloidal aggregates. We propose that alcohol molecules are present in this layer of hydration water near the aggregate surface and disrupt its structure (Fig. 2.12e). Consequently, both the strength and the range of the resulting repulsive interaction potential are affected by the cosolvent, leading to an acceleration of the aggregate growth.

To summarize, we relate the aggregation kinetics of self-assembled thermoresponsive polymeric nanoparticles (core-shell micelles), occurring on the mesoscopic length scale, to the interaction potential and propose that the increasing hydrophobicity of the aggregates upon addition of the cosolvents is mainly due to the disruption of residual hydrophilic patches at the aggregate surface.

The project was funded by DFG within the priority program SPP1259 "Intelligente Hydrogele" (Pa771/4, Mu1487/8, La611/7).

[1] K. Kyriakos, C.M. Papadakis et al., *Macromol. Rapid Commun.* (2016), ASAP.

[2] A. Zaccone, J. Crassous, M. Ballauff, *J. Chem. Phys.* **138**, 104908 (2013)

## 2.8 Self-assembly of thermoresponsive micelles leading to monodisperse aggregates

A. V. Berezkin, K. Kyriakos, I. Grillo<sup>1</sup>, A. Miasnikova<sup>2</sup>, A. Laschewsky<sup>2,3</sup>, P. Müller-Buschbaum, C. M. Papadakis

<sup>1</sup> Institut Laue-Langevin, Large Scale Structures Group, Grenoble, France

<sup>2</sup> Universität Potsdam, Institut für Chemie, Potsdam-Golm, Germany

<sup>3</sup> Fraunhofer Institut für Angewandte Polymerforschung, Potsdam-Golm, Germany

Structures from thermo-responsive polymers with a well-defined size are in demand for scientific and bio-medical applications. One of the efficient routes toward such structures is a hierarchical self-assembly which usually has complex multi-stage kinetics. We investigate the self-assembly of micelles formed by thermo-responsive polystyrene-*b*-poly(*N*-isopropylacrylamide) (PS<sub>14</sub>-*b*-PNIPAM<sub>310</sub>) into large aggregates to understand the aggregation mechanism, and how the size and polydispersity of the aggregates can be controlled. The formation of micelles of PS<sub>14</sub>-*b*-PNIPAM<sub>310</sub> in water-based systems is driven by a hydrophobic attraction between the PS blocks, forming the core of the micelle. Further aggregation of the micelles into large aggregates is controlled by a weak attraction of the corona-forming thermo-responsive PNIPAM blocks. In the experiment, the aggregation is triggered by the addition of a co-solvent (methanol) to the aqueous micellar solution [1]. The temperature is chosen above the cloud point of the final mixture. A theory, supported by Monte Carlo calculations, was proposed to explain an unusually slow aggregation in the late stage.

Time-resolved small-angle neutron scattering (TR-SANS) at the high-flux SANS instrument D22 at ILL (Grenoble, France) was used to observe the evolution of the sizes and shapes of aggregates at a concentration of 20 g/l solution of PS<sub>14</sub>-*b*-PNIPAM<sub>310</sub> in 90:10, 85:15 and 80:20 (v/v) mixtures of D<sub>3</sub>O and deuterated methanol (CD<sub>3</sub>OD). Aggregation is initiated by heating the solutions up to temperatures  $T = 29^\circ\text{C}$ ,  $27^\circ\text{C}$  and  $23^\circ\text{C}$  respectively, i.e. 3 K above the cloud point.

These experiments show that micelles are formed before the addition of co-solvent. Upon addition of CD<sub>3</sub>OD, the micelles start to aggregate, and the size of the aggregates rapidly grows, as seen in Fig. 2.13. Two stages of the aggregation are distinguished: a fast initial growth of small aggregates during the first 10 s, which change shape from elongated to spherical during this time and slow “logarithmic” growth of the aggregate radius at times  $t > 10$  s.

To explain the latter behavior, we assume that the coalescence of large spherical aggregates is hindered by an energy barrier,  $\Delta U$ , which is proportional to their radius, i.e.  $\Delta U = u(R/R_0)$ . Here,  $u$  is the potential energy of a weak long-range repulsion between two micelles, normalized by  $k_B T$ . We suppose that this repulsion appears between two micelles, even if the polymer is slightly solvophobic and their short-range interactions are strongly attractive. The molecular origin of this repulsion is unclear yet. The weak repulsion does not affect the aggregation of small micelles, but an extensive contact area of larger aggregates means a stronger repulsion, and as soon as the energy of repulsion exceeds  $k_B T$ , it becomes a rate-limiting factor of aggregation. The rate of aggregation of aggregates with radii  $R_i$  and  $R_j$  equals to

$$\frac{dn_{ij}}{dt} \propto -k_{\log} \frac{(R_i + R_j)^2}{V} \exp(-\Delta U) n_i n_j. \quad (2.1)$$

$n_{ij}$  is the number of aggregation events,  $k_{\log}$  is an aggregation rate constant,  $R_i + R_j$  the distance between particles upon collision,  $V$  the total volume of the solution, and  $n_i$  and  $n_j$  are

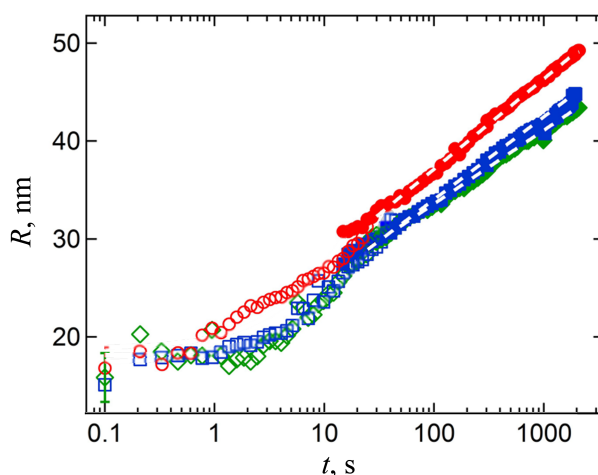


Figure 2.13:

Aggregate radius as a function of time for  $D_2O:CD_3OD$  ratios of 90:10 (green diamonds), 85:15 (blue squares), and 80:20 (red circles), all v/v. The lines show the theoretical dependencies (eq. 2.2).

the time-dependent numbers of aggregates. The exponential term expresses the probability of aggregation upon collision.

The numerical solution of eq. 2.1 with a Monte Carlo technique demonstrates that the aggregate size distribution tends to become monodisperse, because the smaller aggregates grow faster than the larger ones. For the monodisperse case,  $R_i = R_j$ , and eq. 2.1 can be simplified and solved analytically, giving the experimentally observed logarithmic trend

$$\left(\frac{c_0}{c}\right)^{1/3} = \frac{R}{R_0} = u^{-1} \ln \left( \exp[u] + \frac{u}{3} \frac{t}{\tau_{\log}} \right), \quad (2.2)$$

where  $c$  and  $c_0$  are the concentrations of the aggregates at time  $t$  and the initial concentration of micelles, respectively,  $R$  and  $R_0$  are the average radii of the aggregate and the micelle, and  $\tau_{\log}$  is the characteristic time of logarithmic aggregation,  $\tau_{\log} = (k_{\log} R_0^2 c_0)^{-1}$ . The first equality in eq. 2.2 follows from the mass conservation law for homogeneous spherical aggregates of constant density.

As seen in Fig. 2.13, the theoretical prediction given in eq. 2.2 agrees well with the experimental data for  $t > 10$  s. The aggregation behaviour is affected by the content of  $CD_3OD$ . Addition of higher amounts of methanol reduces the characteristic time  $\tau_{\log}$ , as well as the energy barrier  $u$ , which results in larger aggregates.

Thus, the combination of TR-SANS measurements with theoretical and computational approaches helps to understand complex aggregation kinetics in self-assembled, stimuli-responsive copolymer solutions, and demonstrates the route towards monodisperse functional particles, which have a high potential in biomedical applications.

This work was funded by Deutsche Forschungsgemeinschaft (Pa771/4).

- [1] K. Kyriakos, M. Philipp, J. Adelsberger, S. Jaksch, A. V. Berezkin, D. M. Lugo, W. Richtering, I. Grillo, A. Miasnikova, A. Laschewsky, P. Müller-Buschbaum, C. M. Papadakis, *Macromolecules* **47**, 6867 (2014).

## 2.9 Aggregation behavior of doubly thermo-responsive poly(sulfobetaine-*b*-(*N*-isopropylmethacrylamide) diblock copolymers

N. Vishnevetskaya, V. Hildebrand<sup>1</sup>, M. Philipp, A. Laschewsky<sup>1,2</sup>, I. Grillo<sup>3</sup>, P. Müller-Buschbaum, C. M. Papadakis

<sup>1</sup> Institute of Chemistry, University of Potsdam, Germany

<sup>2</sup> Fraunhofer Institut für Angewandte Polymerforschung, Potsdam-Golm

<sup>3</sup> Institute Laue-Langevin, Grenoble, France

Thermoresponsive polymers are a class of “smart” materials that have attracted much scientific interest. These polymers may have a lower critical solution temperature (LCST) or an upper critical solution temperature (UCST), depending on whether the miscibility gap is found at high or low temperatures, respectively. Diblock copolymers consisting of a non-ionic poly(*N*-isopropylmethacrylamide) (PNIPMAM) or poly(*N*-isopropylacrylamide) (PNIPAM) block and a zwitterionic poly(sulfobetaine) (PSPP block) (Fig. 2.14a) feature both a LCST and an UCST in aqueous solution [1]. PSPP is a permanently zwitterionic polymer, and its UCST can be tuned by adding small amounts of electrolyte [2]. This special feature of PSPP will affect the phase transition temperatures of the diblock copolymers, as it is shown in Fig. 2.14b.

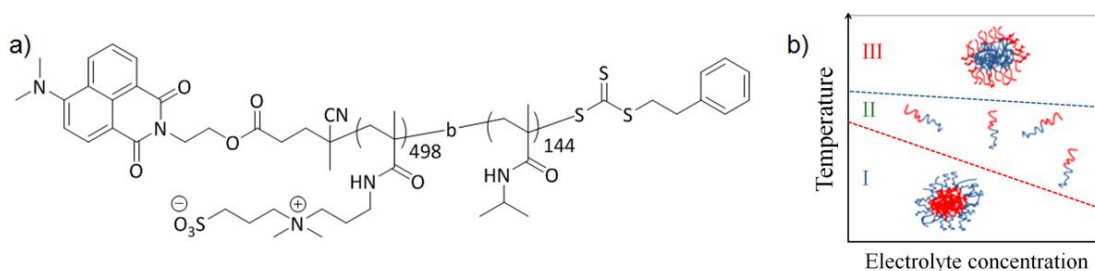


Figure 2.14:

(a) Chemical structure of P(SPP-*b*-NIPMAM). (b) Expected structures (three possible phases in water): (I) micelles with a PNIPMAM/PNIPAM shell and a PSPP core at low temperatures, (II) unimers in the intermediate temperature range and (III) reverse micelles at high temperatures, with changes in UCST transitions caused by the addition of an electrolyte.

Using turbidimetry, we have identified two phase transition temperatures for both 5 wt.-% solutions of the P(SPP-*b*-NIPMAM) and the P(SPP-*b*-NIPAM) in D<sub>2</sub>O, which are presumably due to the aggregation of the PSPP (UCST) and PNIPMAM/PNIPAM (LCST). Both values are more than 10 K lower for P(SPP-*b*-NIPAM) than in the case of P(SPP-*b*-NIPMAM). In an 0.004 M solution of NaBr in D<sub>2</sub>O, an increase of the UCST value is observed, while the LCST is not sensitive to the presence of salt in the solution, which illustrates the salting-in effect that leads to the behavior sketched in Fig. 2.14b.

The aggregation behavior, which is responsive to two stimuli (temperature and electrolyte concentration), together with variation of the architecture of the non-ionic block, is studied by dynamic light scattering (DLS) and temperature-resolved small-angle neutron scattering (SANS).

The DLS measurements show results in a good agreement with the results of transmittance measurements: in regime (I), a turbid solution with very large aggregates (> 700 nm), in regime (II), the solution is clear with small particles (10 nm); in regime (III), the solution is “semi-turbid” with big aggregates (100 nm).

SANS experiments were performed to study the aggregation behavior of 5 wt.-% solutions of the P(SPP-*b*-NIPMAM) and the P(SPP-*b*-NIPAM) (164 500 and 149 500 g/mol) at 0 and 0.004 M NaBr in D<sub>2</sub>O. The solutions were heated from 15 °C to 60 °C in steps of 7 – 10 °C, the

equilibration time was 15 min and the measurement time 50-60 min. SANS experiments were performed at the instrument D11 at the Institut Laue-Langevin (ILL) in Grenoble, France.

The temperature-resolved SANS curves of the diblock copolymers in aqueous solution are shown in Fig. 2.15a,b. For both diblock copolymers and in all regimes, the scattering curves are best described by polydisperse spheres, together with a hard-sphere structure factor, an Ornstein-Zernike (OZ) and a Porod term, describing the inner polymer structure and large aggregates at low and high  $q$ -values respectively. The scattering length density of PSPP and PNIPAM/PNIPAM are alike, which does not allow to distinguish between the micellar core and shell. Only in regime III of P(SPP-*b*-NIPAM), core-shell micelles are evident, presumably due to more hydrophobic core from PNIPAM. We conclude that both diblock copolymers form spherical particle in all regimes with increased sizes in regimes I and III, indicating aggregation. The particles' aggregation depend both on the temperature, on the chemical structure and the molar mass of either block. The salt-induced structural changes are evident only below the UCST, where the presence of the electrolyte promotes aggregation, which is assigned to the ionic-strength sensitive properties of the zwitterionic block (Fig. 2.15c,b).

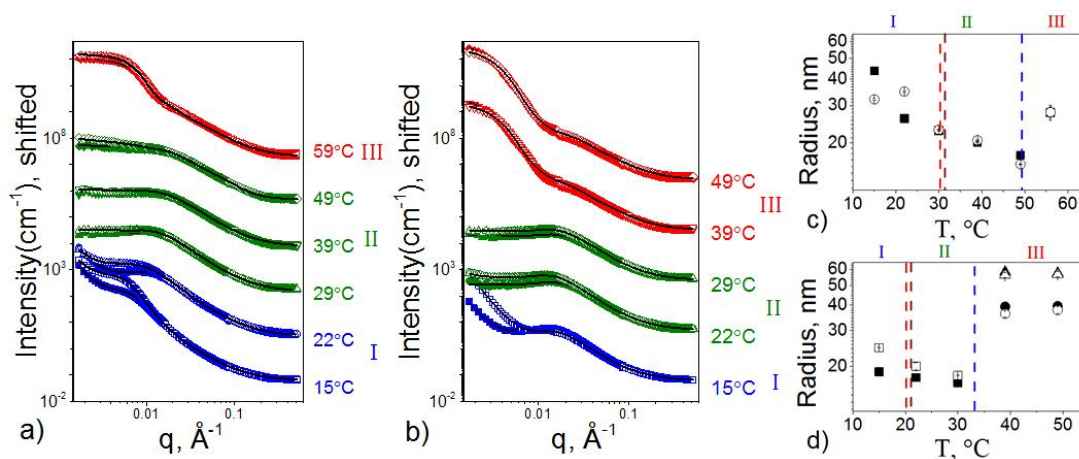


Figure 2.15:

Temperature-resolved SANS curves from 5 wt.-% solutions of P(SPP-*b*-NIPAM) (a) and P(SPP-*b*-NIPAM) (b) in salt-free D<sub>2</sub>O (closed symbols) and in 0.004 M NaBr (open symbols) in D<sub>2</sub>O, in log-log representation, the corresponding radii (c) and (d), respectively, with and without salt (NaBr) (c).

The work is funded by the DFG (Pa771/14-1).

- [1] M. Mertoglu, S. Garnier, A. Laschewsky, K. Skrabania, J. Storsberg, *Polymer* **46**, 7726 (2005)
- [2] P. Köberle, A. Laschewsky, T.D. Lomax, *Makromol. Chem., Rapid Commun.* **12**, 427 (1991)

## 2.10 HPMA-based micelles as drug carriers: influence of chain architecture and molar mass

B.J. Niebuur, X. Zhang, N. Vishnevetskaya, P. Chytil<sup>1</sup>, S.K. Filippov<sup>1</sup>, C.M. Papadakis

<sup>1</sup> Institute of Macromolecular Chemistry, Prague, Czech Republic

Nowadays, a common way to treat cancer is to apply cytotoxic chemotherapy. With this therapy, an anti-cancer agent aims to destroy tumors by attacking fast-dividing cells in particular. The medicine is inserted in the bloodstream to be distributed in the body. With this method of treatment, the tumor is damaged, but healthy cells are harmed as well. The main goal of site-specific treatment is to reduce side effects by site-specific delivery of anti-cancer agents. A promising way to achieve site-specific delivery of anticancer agents is to use the enhanced permeation and retention (EPR) effect of self-assembled nanoparticles from N-(2-hydroxypropyl) methacrylamide (HPMA) containing hydrophobic cholesterol moieties and the drug doxorubicin (Dox) [1,2]. The present project focuses on the investigation of the particle structure and tuning of their properties. A low critical micelle concentration (CMC) and particle sizes in the range of 1-100 nm are of importance.

The aim of the present study is to investigate the influence of the molar mass of the HPMA backbone with randomly distributed cholesterol moieties. Using fluorescence correlation spectroscopy (FCS) and small-angle neutron scattering (SANS), the CMC as well as the size and structure of the nanoparticles are determined.

For these experiments, three samples containing HPMA polymers with varying molar masses were investigated; 14 000 g mol<sup>-1</sup>, 27 300 g mol<sup>-1</sup> and 40 300 g mol<sup>-1</sup>. The cholesterol content for these samples was approximately 2 mole%, and no doxorubicin was attached. FCS experiments were performed on a ConfoCor 2 from Carl Zeiss Jena GmbH, the laser wavelength was 448 nm. For the SANS measurements, the instrument KWS-1 at the MLZ in Garching was used. At a wavelength of 4.5 Å, measurements were performed at the sample-detector distance of 0.99 m, 3.63 m and 19.63 m for 5, 15 and 30 min. respectively.

For FCS measurements, the samples were dissolved in phosphate-buffered saline (PBS) in a wide concentration range. By determining the diffusion coefficient of the nanoparticles, unimers and micelles could be identified. In this way, the CMC of the polymers as well as the hydrodynamic radius,  $R_H$ , of the micelles in the solutions could be determined. Fig. 2.16 gives the obtained values for the CMC as well as the hydrodynamic radius of the investigated polymers. The experiments show that the CMC decreases with increasing polymer molar mass. This property allows tuning of the system to reduce the amount of polymer needed for treatment. The results for the hydrodynamic radius of the micelles are also advantageous. Neither the polymer molar mass nor the mass fraction of the hydrophobic block have an influence on the hydrodynamic radius of micelles. This means that the system is robust against changes in the polymer molar mass, allowing the system to be tuned to minimize the CMC. The nanoparticles have sizes in the range of 4.5 nm and are thus suitable for site-specific drug delivery.

SANS measurements for determination of the precise size and structure of the micelles were performed using D<sub>2</sub>O as the solvent, providing excellent contrast between polymer and solvent. Fig. 2.17 shows the scattering curves. They can be fitted using a model including cylinders with a polydisperse radius, describing the shape of the micelles, an Ornstein-Zernike term for the concentration fluctuations inside the micelles and a term for fractal aggregates,

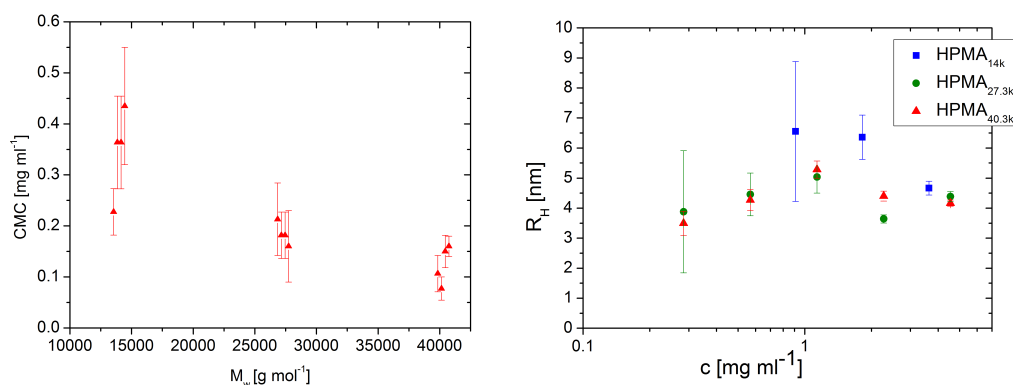


Figure 2.16: CMC and  $R_H$  of the investigated statistical polymers, determined with FCS.

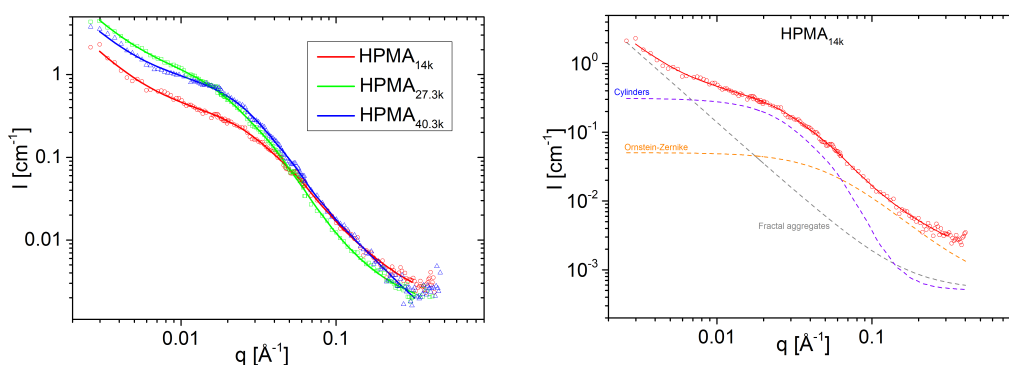


Figure 2.17: Scattering curves of the investigated sample obtained with SANS.

describing the aggregates formed by micelles. For the sample with the lowest polymer molar mass, the scattering curve including the individual form factors is also given in Fig. 2.17. Thus, the micelles have a cylindrical structure. The core is expected to consist of stacked cholesterol molecules, the core is surrounded by HPMA chains.

The cylindrical radius ranges for the three samples between 2 and 3 nm and the length of the cylinders is determined to be around 20 nm. The sizes of the micelles determined with SANS are comparable to the values found for the hydrodynamic radius, determined with FCS. The formation of aggregates, observed with SANS measurements, is not observed with FCS measurements. Additional FCS measurements showed that the use of D<sub>2</sub>O as the solvent is probably responsible for this deviation.

With the described experiments, it is shown that nanoparticles formed by HPMA polymers are of suitable sizes for drug-delivery purposes. The CMC can be decreased by using polymers with a high molar mass without altering the shape or size of the nanoparticles. This project is supported by DAAD within the framework of the program "Projektbezogener Personenaustausch mit Tschechien".

- [1] S. K. Filippov, P. Chytil, P. V. Konarev, M. Dyakonova, C. M. Papadakis, A. Zhigunov, J. Plestil, P. Stepanek, T. Etrych, K. Ulbrich and D. I. Svergun, *Biomacromolecules* **13**, 2594 (2012)
- [2] S. K. Filippov, J. M. Franklin, P. V. Konarev, P. Chytil, T. Etrych, A. Bogomolova, M. Dyakonova, C. M. Papadakis, A. Radulescu, K. Ulbrich, P. Stepanek, and D. I. Svergun, *Biomacromolecules* **14**, 4061 (2013)

## 2.11 Macromolecular HPMA-based drug delivery system - behavior in protein environment

X. Zhang, B.-J. Niebuur, P. Chytil<sup>1</sup>, T. Etrych<sup>1</sup>, S. K. Filippov<sup>1</sup>, A. Kikhney<sup>2</sup>, F. Wieland<sup>2</sup>, D. I. Svergun<sup>2</sup>, C. M. Papadakis

<sup>1</sup> Institute of Macromolecular Chemistry, Prague, Czech Republic

<sup>2</sup> The European Molecular Biology Laboratory, Hamburg, Germany

In dilute aqueous solution, polymer drug carriers based on N-(2-hydroxypropyl)methacrylamide (HPMA) copolymers (Fig. 2.18) with hydrophobic cholesterol moieties and the anti-cancer drug Doxorubicin (Dox) have been found to form micelle-like elongated core-shell nanoparticles (NPs) [1]. However, there is a lack of knowledge on the behavior of these drug carriers in real human blood environment. Human blood contains more than 1000 different proteins and lipids, which are expected to interact with the drug delivery carriers and make the investigation extremely complicated. We study the copolymers in an aqueous solution of human serum albumin (HSA), the most abundant protein in human blood.

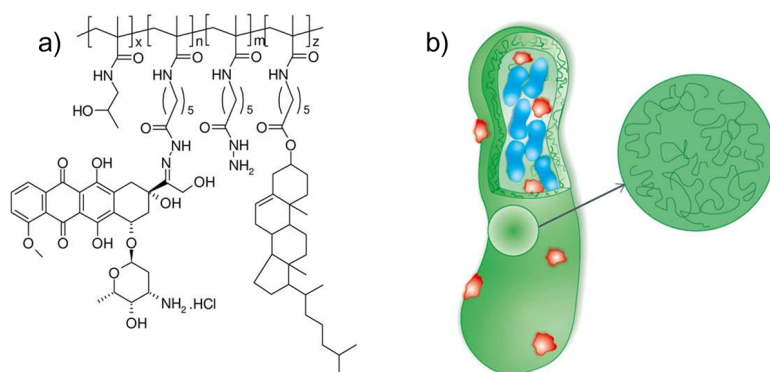


Figure 2.18:

a) Schematic of the HPMA copolymer-drug conjugate bearing cholesterol moiety. b) Structure of the self-assembled NPs. green: HPMA, blue: cholesterol, red: Dox [1].

We use fluorescence life-time correlation spectroscopy (FLCS) to determine the critical micelle concentration (CMC) as well as the NP size. Compared with fluorescence correlation spectroscopy (FCS), a separate autocorrelation function is calculated for each fluorescent component, as determined by its fluorescence life-time. This way, the background and spectrum overlap from different components in blood can be eliminated, resulting in corrected autocorrelation functions. HPMA copolymers bearing cholesterol moieties, Dox and labeled with a fluorescent dye AF633 were measured in phosphate buffered saline (PBS) with and without HSA being present.

FLCS measurements show the CMC to lie between 0.32 mg/ml and 0.64 mg/ml (Fig. 2.19a). Above the CMC, NPs with a hydrodynamic radius ( $R_h$ ) of ca. 45 nm are observed. In the presence of only 0.0035 mg/ml HSA,  $R_h$  decreases dramatically to ca. 30 nm (Fig. 2.19b). At higher HSA concentrations,  $R_h$  stays constant. No clear dependence of  $R_h$  on copolymer concentration and HSA concentration is evident.

More detailed structural information regarding the interaction between the NPs and HSA is revealed by small-angle X-ray scattering (SAXS) on the NPs in dependence on polymer and HSA concentration. All samples were dissolved in PBS, then mixed with an aqueous solution of HSA, resulting in HSA concentrations of 0.35 mg/ml, 3.5 mg/ml and 35 mg/ml. Polymer solutions without HSA are measured as control. All samples were measured at 37 °C at the beamline P12, DESY, Hamburg. The wavelength of X-ray was 0.123 nm. The sample-detector distance (SDD) was 3 m, and the exposure time for each curve was 45 ms. The scattering patterns were azimuthally integrated.

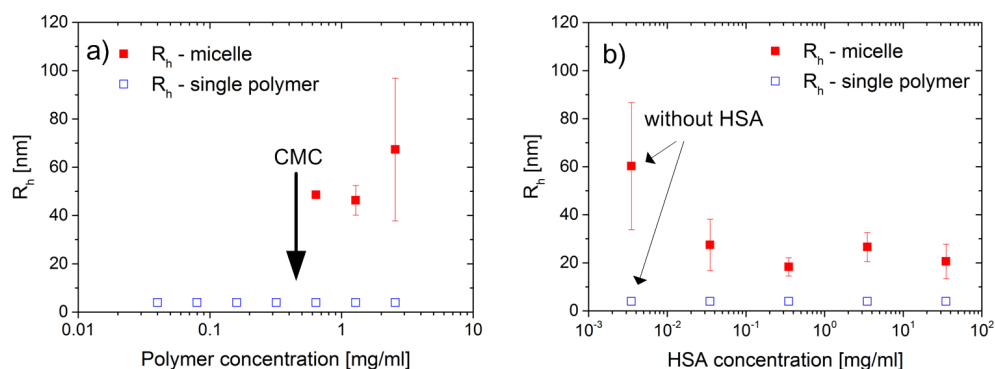


Figure 2.19: (a) CMC determination by FLCS and (b) hydrodynamic radii of the NPs at a polymer concentration of 2.56 mg/ml in dependence on HSA concentration.

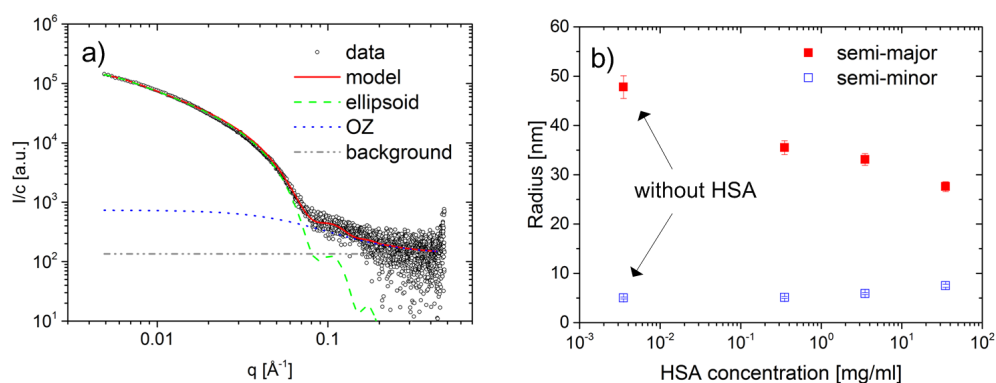


Figure 2.20: (a) SAXS curve and fit of the HPMA NPs at 2 mg/ml. (b) Radii of the NPs at a polymer concentration of 2 mg/ml with varying HSA concentration.

The SAXS curves were modeled by a form factor of ellipsoidal particles, together with an Ornstein-Zernike structure factor describing correlations between HPMA chains surrounding the NPs (Fig. 2.20a). By measuring a concentration series of the copolymers, the CMC is found to be at 0.5 mg/ml, which is in agreement with the result from FLCS (Fig. 2.19a). Above, the semi-major axis of the modeled ellipsoids increases with concentration, whereas the semi-minor axis does not change. Upon addition of HSA, it is observed that the semi-major axis of the NPs decreases dramatically, together with a slight increase in the semi-minor axis (Fig. 2.20b). We suspect that HSA binds to cholesterol moieties which are removed from the NPs.

To summarize, we investigate HPMA-based copolymers for drug delivery in a protein environment by SAXS and FLCS. Both methods confirm a decrease in micelle size in the presence of HSA, which is caused presumably by the binding of HSA to cholesterol moieties.

The project is funded by DFG (Pa771/17-1) and the Czech Science Foundation.

- [1] S. K. Filippov, P. Chytil, P. V. Konarev, M. Dyakonova, C. M. Papadakis, A. Zhigunov, J. Plestil, P. Stepanek, T. Etrych, K. Ulbrich, and D. I. Svergun, *Biomacromolecules* **13**, 2594 (2012)

## 2.12 Weakly amphiphilic triblock copolymers from poly(2-oxazoline) as carriers of a strongly hydrophobic cancer drug

S. Jaksch, A. Schulz<sup>1</sup>, Z. Di<sup>2</sup>, R. Luxenhofer<sup>3</sup>, R. Jordan<sup>1</sup>, C.M. Papadakis

<sup>1</sup> Department Chemie, Technische Universität Dresden

<sup>2</sup> Jülich Centre for Neutron Science JCNS, Forschungszentrum Jülich GmbH, Garching

<sup>3</sup> Functional Polymer Materials, University Würzburg

Drug formulation is one of the most crucial issues in pharmaceutical technology, especially for poorly water-soluble drugs. For instance, paclitaxel (PTX), a potent cytostatic drug, clinically used for the treatment of a number of tumors, has an extremely low water solubility. For its delivery, several approaches such as nano- and microparticles, liposomes and polymeric micelles have been studied with the aim of achieving a high loading capacity and solubility. However, currently used clinical formulations only allow less than 1 wt% of active drug, and the carriers may cause considerable side effects. Doubly amphiphilic poly(2-oxazoline)s (POx) were found to be efficient as a drug delivery system for the hydrophobic PTX with an unprecedented high loading capacity of almost 50 wt%, excellent shelf stability of more than half a year, low toxicity and limited complement activation.

Interestingly, although PTX is very hydrophobic, the best solubilization results were achieved with micelles formed by amphiphilic P(MeOx-*b*-*n*BuOx-*b*-MeOx) triblock copolymers comprising a weakly hydrophobic core of 2-*n*-butyl-2-oxazoline (BuOx) and hydrophilic poly(2-methyl-2-oxazoline) (MeOx) end blocks [1]. In the present study, small-angle neutron scattering (SANS) was used to characterize aqueous solutions of P(MeOx-*b*-*n*BuOx-*b*-MeOx) with different PTX loadings [2].

Solutions of the triblock copolymers were prepared by dissolving P[MeOx<sub>33</sub>-*b*-*n*BuOx<sub>26</sub>-*b*-MeOx<sub>45</sub>] in D<sub>2</sub>O at 10 mg mL<sup>-1</sup>. Drug-loaded sample solutions were prepared via the thin film hydration method described in ref. 1. SANS experiments were performed at the KWS-1 instrument at FRM II in Garching. A neutron wavelength  $\lambda = 6.9 \text{ \AA}$  and sample-detector distances (SDD) of 1.72-19.72 m were used. Exposure times were 5-30 min. The samples were mounted in flat Hellma quartz-glass cuvettes with a light path of 2 mm. The experiments were conducted at 37 °C.

SANS curves of solutions of P[MeOx<sub>33</sub>-*b*-*n*BuOx<sub>26</sub>-*b*-MeOx<sub>45</sub>] in D<sub>2</sub>O with PTX concentrations  $c_{PTX} = 0.2 - 4.8 \text{ mg mL}^{-1}$  are shown in Fig. 2.21. They reveal significant changes of the curve shape upon loading with PTX. For the unloaded solutions and for  $c_{PTX} = 0.2 \text{ mg mL}^{-1}$ , a plateau at low  $q$  values ( $q$  is the momentum transfer), a shallow maximum at  $q = 0.015 \text{ \AA}^{-1}$  and a smooth decay at higher  $q$  values is observed. At  $c_{PTX} = 0.9 \text{ mg mL}^{-1}$ , the maximum becomes more pronounced and moves to higher  $q$  values. At higher concentrations (1.9-4.8 mg mL<sup>-1</sup>), the maximum becomes even more pronounced, changes shape and moves to lower  $q$  values with increasing  $c_{PTX}$ . This maximum indicates the correlation between the micelles. Moreover, a secondary maximum arises at  $q = 0.1 \text{ \AA}^{-1}$ .

For model fitting of the curves at low PTX concentration (0 and 0.2 mg mL<sup>-1</sup>), the micelles were described by a form factor for homogeneous spheres and their correlation with a Percus-Yevick structure factor. Excellent fits were obtained over the full  $q$  range for both solutions. The parameters resulting from fitting are compiled in Fig. 2.21b,c. The micellar radius is  $R_{mic} = 45.6 \pm 0.1 \text{ \AA}$  for the pure triblock copolymer and  $49.9 \pm 0.1 \text{ \AA}$  at  $c_{PTX} = 0.2 \text{ mg mL}^{-1}$  (Fig. 2.21b). At higher PTX concentrations, the secondary maximum cannot be captured by the form factor of a homogeneous sphere any longer. Therefore, a formfactor for raspberry-like particles was successfully used to describe the data for  $c_{PTX} = 0.9 - 4.8 \text{ mg mL}^{-1}$ . The raspberry particles are homogeneous spheres with small spherical particles—which we attribute to PTX domains—immersed at a certain depth from the particle surface. The radii of the raspberry micelles,  $R_{mic}$ ,

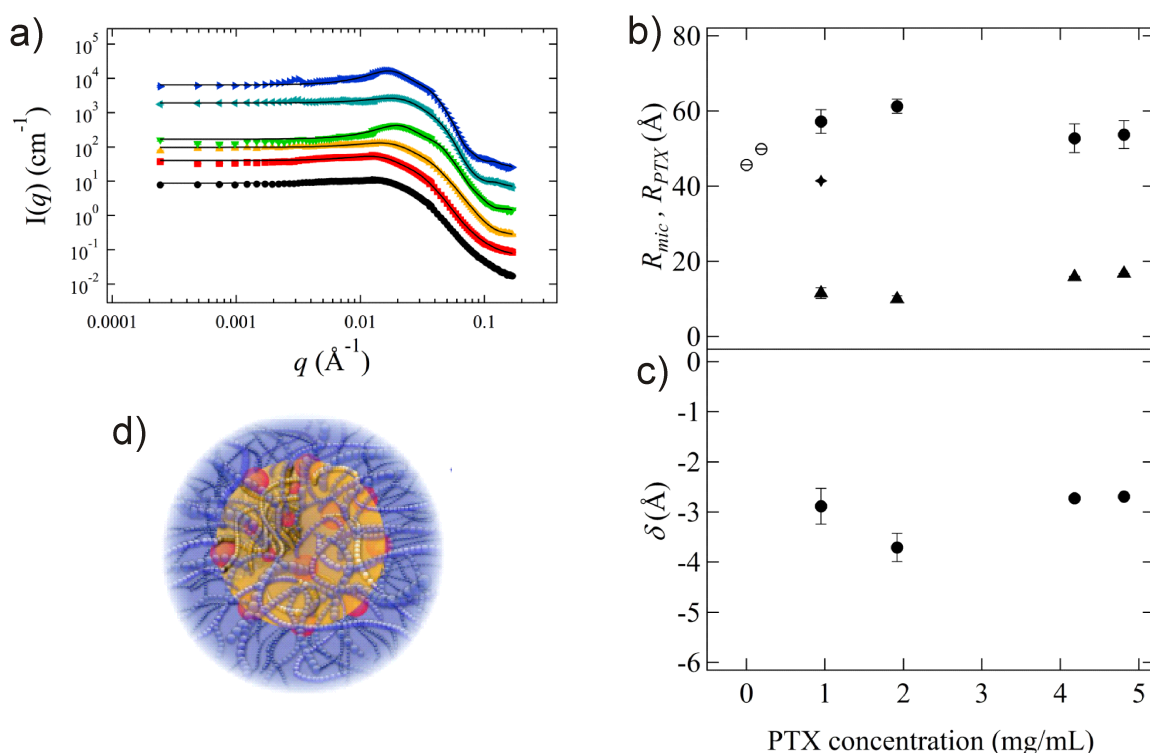


Figure 2.21:

(a) SANS curves for  $c_{PTX} = 0, 0.2, 0.9, 1.9, 4.2$  and  $4.8$  mg mL<sup>-1</sup> (from below). The curves were shifted vertically by factors of 4, 16, 256, 1024 and 4096, respectively. The full lines are model fits. (b) Resulting radii of the spherical micelles (○) and of the raspberry particles (●) and of the embedded PTX domains (filled triangles). (c) Immersion depth of the PTX domains. (d) Graphical representation of a PTX loaded micelle.

are in the range  $53 - 61$  Å, independent of  $c_{PTX}$  (Fig. 2.21b). The radius of the embedded PTX domains increases with  $c_{PTX}$  from  $R_{PTX} = 11.5 \pm 1.4$  Å at  $0.9$  mg mL<sup>-1</sup> to  $16.8 \pm 0.1$  Å for  $4.8$  mg mL<sup>-1</sup> (Fig. 2.21b). Thus, the domains seem to consist of an increasing number of PTX molecules, as their concentration is increased. The average immersion depth of the PTX domains, lies between  $-2.7$  and  $-3.7$  Å (Fig. 2.21c). The correlation between the micelles is found to be very weak.

Since the PMeOx shell of the micelles is presumably loosely packed, and the scattering contrast between the solvent-swollen shell and the solvent is weak, we assume that PTX, at high loading, is located rather in the inner part of the shell close to the micellar P $n$ BuOx core. Possibly, PTX is located at the diffuse core-shell interface (Fig. 2.21d). The formation of the raspberry-like micelles may explain its high loading capacity: Not only is PTX immersed in the core, but it also decorates the core/shell interface. The incorporation of PTX beyond the confinements of the hydrophobic core may be one of the reasons for the tremendous loading capacity of the described POx based polymer when compared to other POx amphiphiles and conventional excipients, respectively.

The project was funded by DFG (Pa771/6-2, Jo287/4-3) and National Cancer Institute Alliance for Nanotechnology in Cancer (U01 CA116591).

- [1] A. Schulz, S. Jaksch, R. Schubel, E. Wegener, Z. Di, Y. Han, A. Meister, J. Kressler, A. V. Kabanov, R. Luxenhofer, C. M. Papadakis, R. Jordan, *ACS Nano* **8**, 2686 (2014)
- [2] S. Jaksch, A. Schulz, Z. Di, R. Luxenhofer, R. Jordan, C.M. Papadakis, *Macromol. Chem. Phys.*, in press.

## 2.13 Development of internally self-assembled lipid-based systems for vaccine delivery

L. P. Rodrigues<sup>1</sup>, K. Kyriakos, C. M. Papadakis, G. Winter<sup>1</sup>, M. Hubert<sup>1</sup>

<sup>1</sup> Ludwig-Maximilians-Universität München, Department of Pharmacy, Pharmaceutical Technology and Biopharmacy

New vaccine candidates are typically based on highly purified antigenic epitopes derived from pathogens (subunit vaccines). In spite of their enhanced tolerability compared to whole pathogen vaccines, these formulations show insufficient immunogenicity [1]. Several strategies have been studied to improve the magnitude and type of the elicited immune response. In this context, the co-administration of immunostimulatory compounds and an antigen loaded into particulate systems has revealed promising perspectives [2].

The present work proposes the development of self-assembled lipid-based particles with non-lamellar internal structure and adjuvant properties for vaccine delivery. Non-lamellar topologies are known to show fusogenicity, which contributes to the delivery of antigens to the cytosol of antigen-presenting cells (APCs), stimulating cytotoxic T lymphocyte (CTL) immune responses. Here, formulations containing phytantriol (Phy) and mannide monooleate (MaMo) are investigated. Phytantriol is a well-characterized lipid able to form non-lamellar phases in fully hydrated systems. Mannide monooleate is an emulsifier applied in several adjuvant systems and is known to elicit Th1 and Th2 responses in emulsion form. Through the combination of immunogenicity and improved antigen delivery in one system, we aim to promote potent and specific immunoprotective reactions.

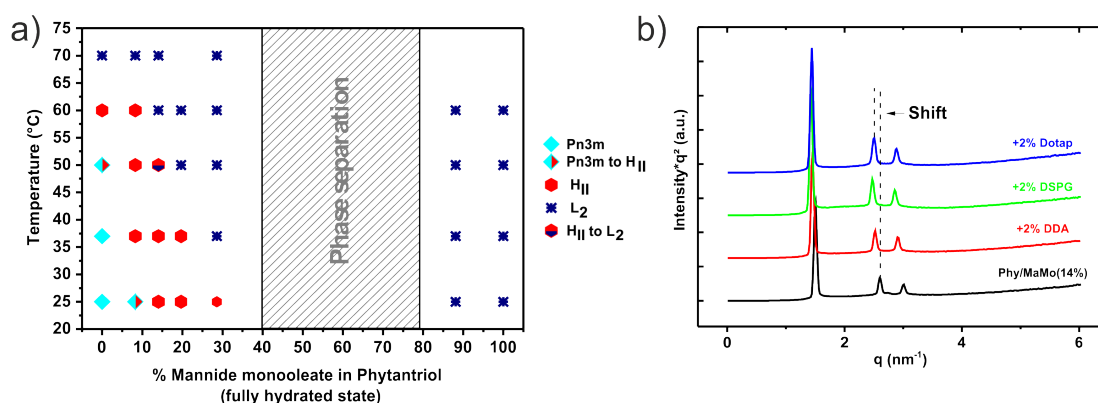


Figure 2.22:

(a) Phase diagram obtained by SAXS analyses for fully hydrated bulk phases of Phy/MaMo systems. Pn3m (cubic double diamond), HII (inverse hexagonal), L2 (inverse micellar). (b) SAXS curves of charged Phy/MaMo (14 wt%) phases in the fully hydrated state.

In order to prepare bulk phases, appropriate amounts of Phy and MaMo were thoroughly homogenized at 60 °C, and highly purified water (60 °C) was added to obtain fully hydrated samples [final lipid concentration of 50 wt%]. Considering the relevance of the overall surface charge in the interactions with cells, charged systems were also produced through the incorporation of different charged phospholipids in the Phy/MaMo (14 wt%) formulation. More specifically, DDA (dimethyldioctadecyl-ammonium bromide), Dotap (1,2-dioleoyl-3-trimethylammonium-propane chloride), or DSPG [1,2-dioctadecanoyl-sn-glycero-3-phospho-(1'-rac-glycerol) (sodium salt)] were added at 2 wt% of the total lipid. Particles were produced through the dispersion of the bulk samples in an aqueous solution of Poloxamer 407 (5 wt% of the total lipid) using sonication. The final lipid concentration in the particulate systems was approximately 10 wt%.

In order to fully understand the impact of MaMo addition to Phy systems, SAXS analyses were performed using a Ganesha 300XL SAXS-WAXS instrument. The instrument was operated with a wavelength of 1.54 Å and a sample-to-detector distance of 406.2 mm. Measurement times were 30 and 120 min for bulk samples and particles, respectively. The structures of the bulk phases and associated phase transitions were identified (Fig. 2.22a). In pure Phy systems, a phase transition from cubic double-diamond (Pn3m) to inverse hexagonal phase (HII) occurs at approximately 50 °C. Increasing concentrations of MaMo reduces the transition temperature to values below 25 °C. This indicates that the addition of MaMo to Phy phases facilitates the formation of inverse hexagonal structures. Similarly, the phase transition temperature from HII to micellar (L2) also progressively decreases with higher MaMo ratios. More specifically, in bulk samples of pure phytantriol, the HII topology changes to L2 between 60 and 70 °C. In systems containing 28% MaMo, the micellar phase is already present at 37 °C.

Among all Phy/MaMo ratios evaluated, Phy/MaMo (14 wt%) maintains the hexagonal structure for the largest temperature range including room and body temperatures. For this reason, this bulk phase was used as a base for further formulation development. DDA, Dotap, and DSPG were included in the formulation to provide surface charge, which is relevant considering the performance of carriers in biological environment. Polarization micrographs of bulk phases containing the different phospholipids showed that all samples were birefringent, suggesting that the HII structure was maintained. This hypothesis was confirmed by SAXS (Fig. 2.22b). The SAXS analyses also revealed an increase of the lattice parameter. This effect is especially pronounced for Dotap and DSPG, possibly due to their larger headgroups, which promote higher inter-headgroup repulsion, resulting in an enlargement of the unit cell.

Preliminary experiments concerning the preparation of nanoparticles with these formulations have been performed as well. Bulk phases could be successfully dispersed in aqueous solutions of Poloxamer 407 with sonication, yielding stable particles with diameters of ca. 200 nm. SAXS measurements indicate that the internal organization of the original bulk was retained in the particle nanostructure even after the inclusion of different model proteins, such as lysozyme and ovalbumin (Fig. 2.23).

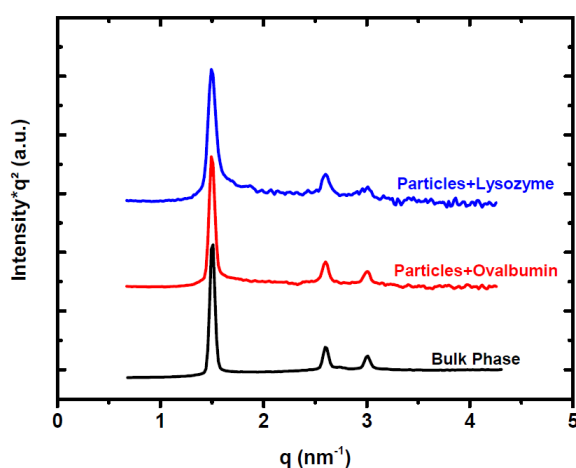


Figure 2.23: SAXS curves of Phy/MaMo (14 wt%) based particles, loaded with 1 wt% (of total lipid) protein, as indicated in the graph.

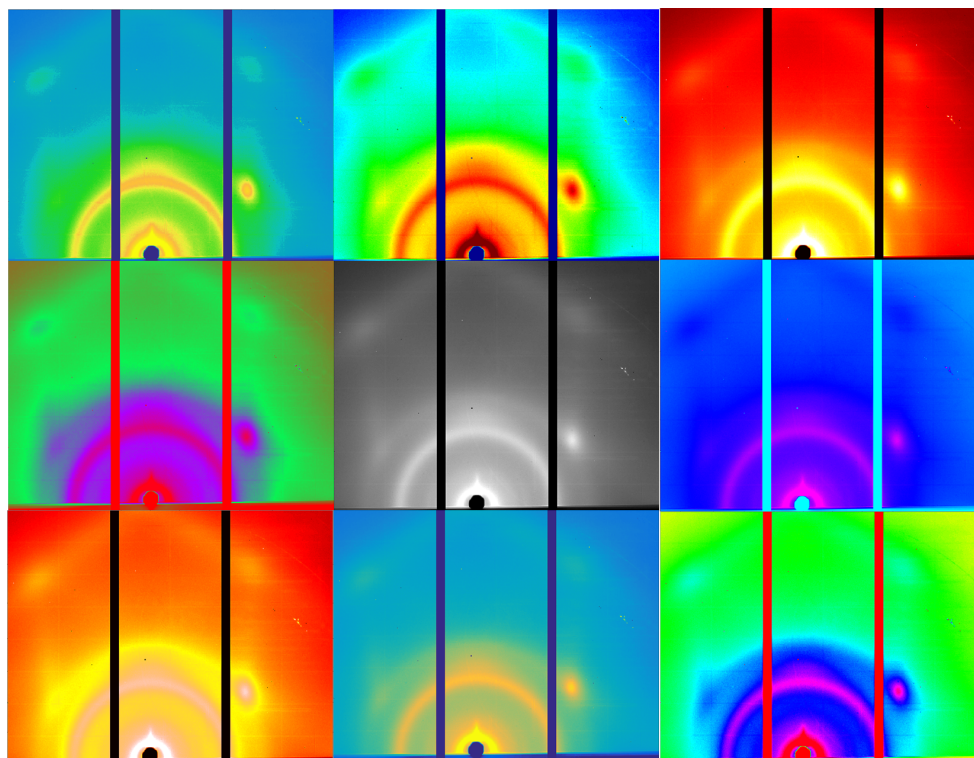
In summary, this work reports the promising combination of Phy and MaMo to prepare robust and stable internally self-assembled systems for future applications in the vaccination field. The capacity of MaMo to modulate Phy mesophase and phase transition temperature can be used in future applications to control loading efficiencies and release profiles of the loaded antigen.

[1] M. F. Bachmann, G. T. Jennings, *Nature Reviews Immunology* **10**, 787 (2010)

[2] S. Rizwan, *J. Control. Release* **165**, 16 (2013)



### 3 Thin polymer films



### 3.1 Simulations of solvent vapor annealing of cylinder-forming block copolymer thin films

A. V. Berezkin, I. I. Potemkin<sup>1</sup>, C. M. Papadakis

<sup>1</sup> Lomonosov Moscow State University, Physics Department, Russia

Ordered block copolymer films are promising as functional templates for block copolymer lithography, molecular biology, colloid science etc. For many of these applications, the domains in the film need to have both, long-range order and a properly controlled orientation. These aims can be reached using solvent vapor annealing (SVA). In this method, the copolymer film, being exposed to the vapor of a solvent, swells up to certain controlled degree, and then dries at a controlled rate. Relaxation of defects in domain structure is attained due to the increased molecular mobility in the film upon SVA. However, the final morphology and the domain orientation are strongly affected by the polymer-solvent interactions. To investigate the general mechanism of SVA, we simulated drying of thin films of asymmetric cylinder-forming A-block-B copolymers [1].

The simulations were performed using dissipative particle dynamics (DPD) [2], a coarse-grained molecular simulation technique, which reproduces the Flory-Huggins theory. The Flory-Huggins parameter ( $\chi_{ij}$ ) for two molecular moieties or components is related to the repulsion parameter  $a_{ij}$  of DPD particles  $i$  and  $j$  via the equation  $\chi_{ij} = 0.306(a_{ij} - 25)/(1 + 3.9N^{-0.51})$  where  $N$  is the number of statistical segments (particles) in the polymer molecule.

The simulation proceeded in a rectangular periodic box of size  $l_x \times l_y \times l_z = 50 \times 50 \times 70$ , containing initially three components: copolymers of length  $N = 20$  with block lengths  $N_A = 5$  and  $N_B = 15$ , solvent (S-particles) and gas (G-particles). At the bottom of the box, the homogeneous copolymer/solvent mixture with an initial volume fraction of solvent,  $\phi_{S0}$ , is located, while the space above the film is filled with a mixture of S and G particles at the ratio 1:3. The bottom and upper sides of the box are impenetrable for all particles and non-selective to A and B blocks.

During the molecular dynamics simulation, all molecules were able to diffuse, but the solvent particles being found at a distance larger or equal to a height  $\delta$  above the film surface (i.e. in the gas phase) were irreversibly transformed into gas particles to simulate solvent vapor dilution by the solvent-free gas flow. As the result, the film dried due to gradual removal of solvent.

The final film thickness,  $h_0$ , was varied in a range from 5 to 30 particle sizes ( $r_c$ ). A simulated thermal annealing predicted lying cylinders within this range of thicknesses, except at  $h_0 = 5$ , when hexagonally packed spherical domains appear. Oppositely, simulations of SVA revealed a wide range of conditions, where SVA stabilizes perpendicular and well-ordered cylinders even in thick films ( $h_0 = 30$ ).

Firstly, the order-to-disorder transition must be induced upon swelling of the film. This condition ensures the independence of the structure formation during drying on the history, i.e. the preparation conditions, and it can be attained when the initial solvent concentration is in the range  $0.2 \leq \phi_{S0} \leq 0.5$ . Secondly, the weak segregation regime has to be achievable during the evaporation process. This condition provides more "pathways" for structural transformations which are not accompanied by a strong penalty in the interfacial energy. The third condition for the vertical orientation of the cylindrical domains is a weak selectivity of the solvent to the long blocks. This is probably necessary to compensate entropy-driven adsorption of short blocks at the film surfaces, revealed by recent systematic theoretical studies of confined block copolymer

films. The region of polymer-solvent repulsion parameters resulting in ordered perpendicular cylinders is shown in Fig. 3.1.

We investigated the mechanism of domain ordering. In the swollen state, a higher swelling of the long blocks results in the formation of the spherical micelles (rather than cylindrical). Upon solvent evaporation, the film stays disordered up to a certain point. When the degree of swelling drops below  $h(t)/h_0 = 1.25$ , hexagonal ordering of spherical domains starts near the free interface. Then, the spheres are transformed into perpendicular, hexagonally packed cylinders.

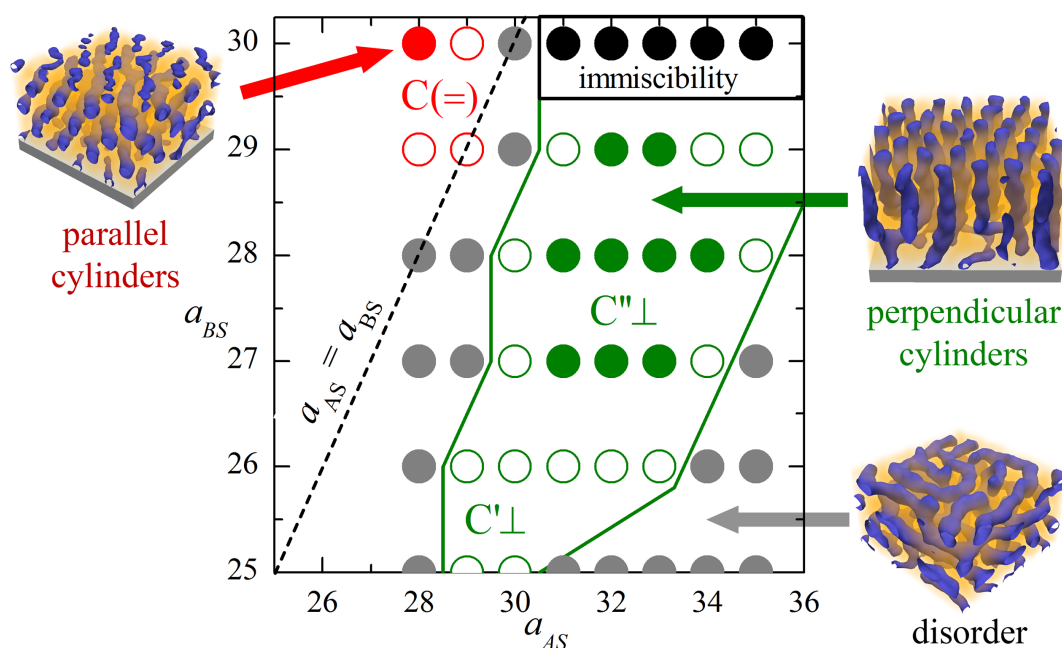


Figure 3.1:

Effect of polymer-solvent interactions on the domain ordering. Black dashes show the non-selective solvent conditions ( $a_{AS} = a_{BS}$ ). Red, green and gray circles denote the parallel, perpendicular and worm-like cylinders in the dried film, respectively, as shown in the simulation snapshots.

Equivalent dry films have considerably different final structures after SVA and thermal annealing. We suppose that the vertical orientation of nanodomains during SVA is governed by the diffusion-driven solvent flow through the system of nanodomains having different viscosities and permeabilities in a selective solvent, as well as by the interfacial flows of components along interdomain interfaces, triggered by the gradient of surface tension (so called Gibbs-Marangoni effect). This investigation demonstrates the potential of molecular simulation techniques for an in-depth understanding of non-equilibrium phenomena at the macromolecular space-scales.

The financial support from the DFG (Pa771/10-2) and from the Russian Ministry of Education and Science (14.613.21.0027 RFMEFI61314X0027) is gratefully acknowledged. The simulations were performed on the supercomputer "Chebyshev" at Moscow State University.

[1] A. V. Berezkin, C. M. Papadakis, I. I. Potemkin, *Macromolecules* **49**, 415-424 (2016)

[2] R. D. Groot, P. B. Warren, *J. Chem. Phys.* **107**, 4423 (1997)

### 3.2 In-situ investigation of morphological changes in block copolymer thin films during solvent vapor annealing using vapor mixtures

F. Jung, A.V. Berezkin, D.-M. Smilgies<sup>1</sup>, D. Posselt<sup>2</sup>, C.M. Papadakis

<sup>1</sup> Cornell University, Ithaca, NY, USA

<sup>2</sup> Roskilde University, IMFUFA, Denmark

Block copolymers have attracted a lot of interest due to the ability to self-assemble into microdomains with lengthscales of 10-100 nm. This so-called bottom-up approach offers a wide range of interesting applications, e.g. as templates in nanolithography.

The equilibrium morphology depends on the volume fraction of the minority block,  $f$ , the degree of polymerization,  $N$ , and the Flory-Huggins parameter,  $\chi$ . The resulting theoretical phase diagram has been predicted using self-consistent field theory. In thin films, confinement and surface energy also play a role. Solvent vapor annealing (SVA) has attracted a lot of interest due to its ability to increase the mobility of the polymer blocks and overcome kinetically trapped states, which leads to a higher degree of order and a larger grain size. So far, SVA has been carried out using only one solvent; however, mixing the vapors of two selective solvents offers additional possibilities. The mixed vapor will swell the domains differently, depending on the vapor composition and selectivity of the solvents, thus altering the effective volume fraction,  $f_{eff}$ . Changing the composition of the vapor enables one to move sideways in the phase diagram. Thus, order-order transitions may be induced. This opens up access to a wide range of structures from the same block copolymer.

In this work, we investigate the thin film morphology of polystyrene-*b*-polydimethyl siloxane (PS-*b*-PDMS) with a number average molar mass  $M_n = 39.5$  kg/mol and a volume fraction of the PDMS block of  $f = 0.32$ , which is expected to form cylinders in the bulk. Films were prepared by spin coating of silicon wafers. SVA was performed using toluene, which is selective for PS, and *n*-heptane, which is selective for PDMS. The vapor was created by bubbling nitrogen gas at a certain flow rate through two liquid solvent bubblers and by exposing the sample to a continuous flow of the saturated vapor mixture. In-situ grazing-incidence small-angle X-ray scattering (GISAXS) experiments were performed at beamline D1, CHESS at Cornell University (wavelength  $\lambda = 0.1155$  nm, incident angle  $\alpha_i = 0.14^\circ$ , sample-detector distance 1845 mm). Typical measuring times were 1 s every 30 s. Fig. 3.2 shows the film thickness and 2D GISAXS images at representative times during swelling of a sample having an initial film thickness  $d_0 = 180$  nm. The as-prepared film displays two Debye-Scherrer rings, indicating low orientational order, though a large fraction of the cylinders are vertical (Fig. 3.2b/c, 1). The film was swelled in toluene for 50 min. During swelling, the two rings merged (Fig. 3.2c, 2). The cylinders are relatively unoriented with slight preferences to purely vertical or purely parallel cylinders, indicated by the intensity variations along the ring. With increasing film thickness, a structure appears which we attribute to lying cylinders on a hexagonal lattice (Fig. 3.2c, 3-5, b, 4). The appearance of two peaks in the diffuse scattering region might be due to a coexistence of hexagonal lattices which are rotated by  $30^\circ$  with respect to each other. Simulations of this kind of mixed structure confirm this assumption. The effective volume fraction at a degree of swelling of 2.1 in toluene is estimated to be in the range of 0.25 – 0.3, considering that toluene is not purely selective for PS but also swells the PDMS block [1]. After swelling in toluene, *n*-heptane was introduced into the mixture, and the ratio of the two solvents was varied in steps of 5 min, while keeping the total flow constant (Fig. 3.2a). The film thickness decreases rapidly, which may be explained by the high selectivity of *n*-heptane towards the minority block. We observe that the response of the film to the changed vapor condition is delayed by 5-10 min, which is the timescale of equilibration of the vapor composition. With increasing fraction of *n*-heptane in the vapor mixture, the lying cylinders start to disorder again as can be seen by the reappearance

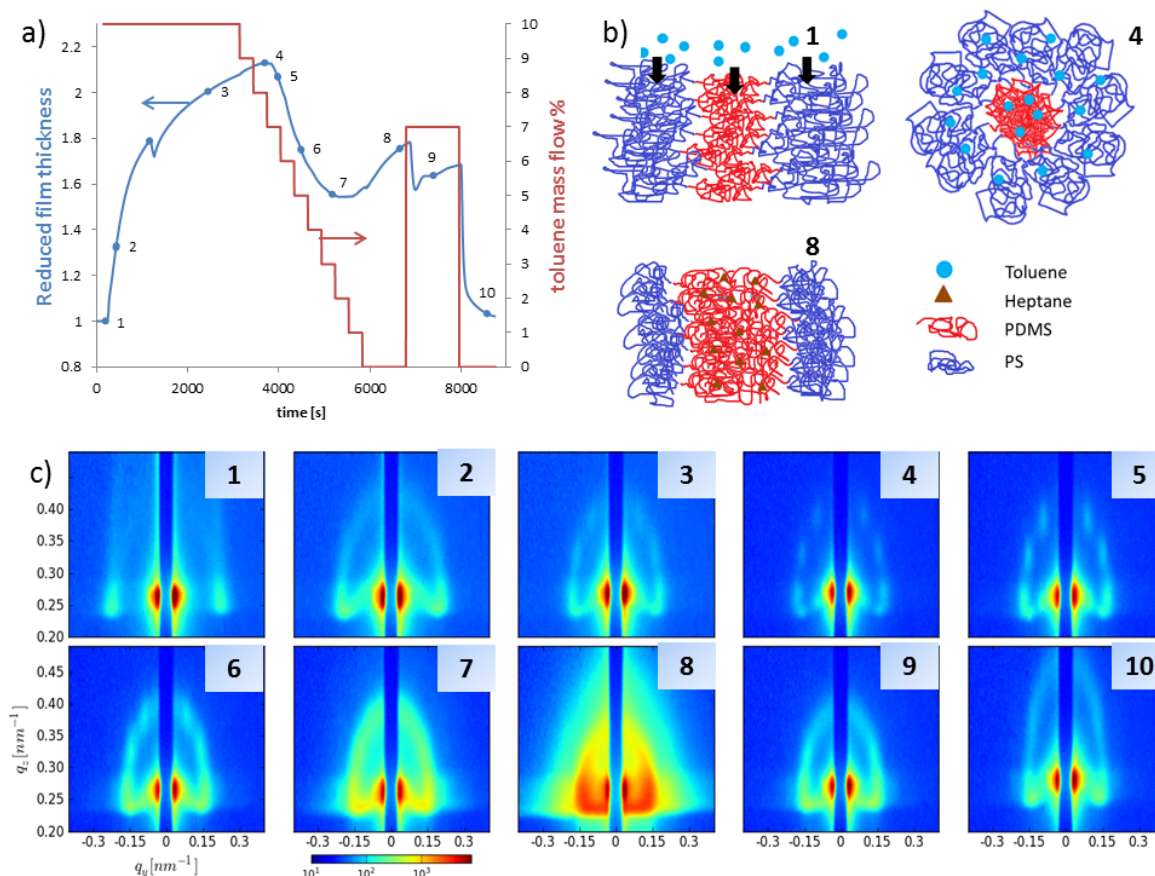


Figure 3.2:

SVA during which the vapor composition was varied. (a) Reduced film thickness (left axis) and fraction of toluene in the vapor mixture (right axis, 10 % corresponds to pure toluene). (b) Schematic of the annealing process. (c) 2D GISAXS images at certain points during swelling as marked in a).

of the Debye-Scherrer ring in (Fig. 3.2c, 6), and eventually the ring disappears and translates into a strong diffuse scattering that shows Bragg rods (Fig. 3.2b/c, 8). The effective volume fraction is estimated to be in the range of 0.4 – 0.45, which means that an order-order transition is expected to happen. This is confirmed by the appearance of the Bragg rods, indicating perpendicular lamellae. After one cycle of going from high toluene to high *n*-heptane fraction in the mixture, we tried to reconstruct the lying cylinders observed at a toluene/*n*-heptane ratio between 10:0 and 7:3 by instantly setting the flow to a ratio of 7:3 as indicated in Fig. 3.2a. The film appears to collapse as the thickness decreases rapidly for a short time. However, after collapse and reswelling, the expected lying cylinder structure is not observed again. This might hint at a path-dependent morphology. A reverse experiment (not shown), where the film was swelled in pure *n*-heptane and the fraction of toluene was increased stepwise seems to confirm this. Longer equilibration times may be required.

SVA with two selective solvents and a stepwise exchange of solvents gives a wealth of information on the structural changes in dependence on vapor composition.

The project is funded by DFG (Pa771/10-2) and the Russian Foundation for Basic Research.

[1] K.W. Gotrik, A.F. Hannon, J.G. Son, B. Keller, A. Alexander-Katz, C.A. Ross, *ACS Nano* **6**, 8052 (2012)

### 3.3 Towards an equilibrium structure in lamellar diblock copolymer thin films using solvent vapor annealing – an in-situ time-resolved GISAXS study

A. Sepe, J. Zhang, J. Perlich<sup>1</sup>, D.-M. Smilgies<sup>2</sup>, D. Posselt<sup>3</sup>, C.M. Papadakis

<sup>1</sup> Deutsches Elektronen-Synchrotron DESY, Hamburg

<sup>2</sup> Cornell High Energy Synchrotron Source (CHESS), Cornell University, Ithaca, NY, U.S.A.

<sup>3</sup> Department of Science, Roskilde University, Denmark

Nanostructured block copolymer thin films find numerous applications, e.g. for creating nanoporous films and membranes. Defect-free structures are a common requirement. However, the self-assembly process of the block copolymer film during preparation—especially when using spin-coating—introduces defects and multi-domain structures. Solvent vapor annealing (SVA) has become increasingly popular to heal defects in block copolymer thin films prepared by spin-coating. It has been found that controlling the details of the SVA procedure is imperative to achieve the necessary structural control for applications. In the present work, we investigate the structural changes in thin films from symmetric, lamellae-forming polystyrene-*block*-polybutadiene (PS-*b*-PB) diblock copolymers during two cycles of SVA with cyclohexane (CHX), a good and slightly PB selective solvent. In-situ, real-time structural investigations by in-situ and real-time grazing-incidence small-angle X-ray scattering (GISAXS) allows to investigate the mechanisms.

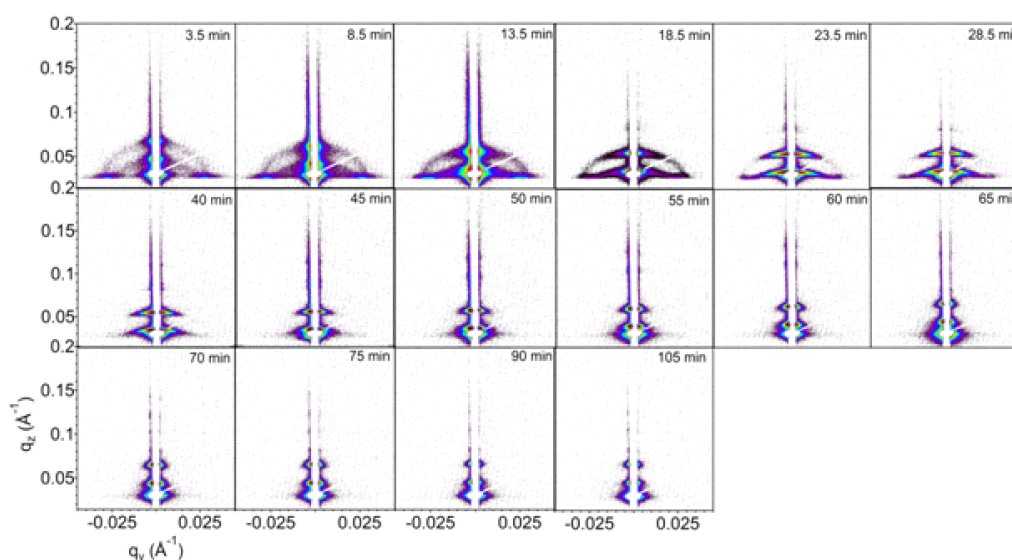


Figure 3.3: Representative 2D GISAXS maps during the first SVA cycle. The times after the solvent vapor starts entering the cell are given in each map. Drying starts after 40 min.

The sample was a lamellae-forming PS-*b*-PB diblock copolymer having block molar masses of 15.0 kg/mol and 13.0 kg/mol. The block copolymer was dissolved in toluene at a concentration of 40 mg mL<sup>-1</sup>. Films were prepared by spin-coating Si(100) wafers. The film was dried at RT in vacuum and had a thickness of 2150 ± 20 Å. GISAXS experiments were performed at beamline BW4, DORIS III at DESY in Hamburg, Germany. The wavelength was 1.3808 Å and the incident angle 0.18°. As a detector, a MarCCD camera was installed at a sample-detector distance of 1.93 m. A custom-made sample cell including a bubbler and a gas handling system were used for SVA. Swelling of the film was accomplished by letting CHX vapor flow into the sample cell. Drying of the film was performed by gradually increasing the flow of dry N<sub>2</sub> gas

directly into the cell and by decreasing the flow of CHX vapor. GISAXS measurements were taken continuously with measuring times of 30 s.

Initially, the 2D GISAXS maps (Fig. 3.3) show diffuse Bragg sheets (DBSs), i.e., a significant fraction of the lamellae is parallel with respect to the Si substrate. First-order diffuse Debye-Scherrer rings (DDSRs) from randomly oriented lamellae are present as well, indicating a minor fraction of randomly oriented lamellae. The lamellar thickness in the dry state is  $D_{lam}^{par} = 145 \pm 1 \text{ \AA}$ , which is significantly lower than the bulk value ( $220 \pm 1 \text{ \AA}$ ).

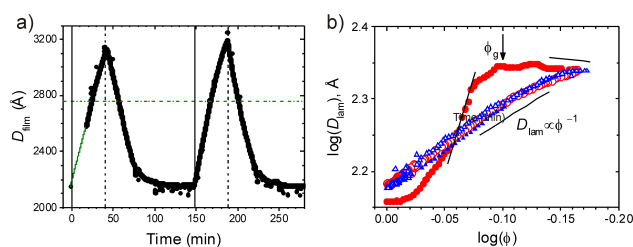


Figure 3.4:

(a) Film thickness during the SVA cycles. (b)  $D_{lam}^{par}$  as a function of  $\phi$ . Red circles: first cycle, blue down triangles: second cycle. Closed symbols: swelling, open symbols: drying.

The film was swollen twice in CHX vapor and dried (Fig. 3.4a). At this, the glass transition of PS is presumably crossed when the polymer volume fraction,  $\phi$ , decreases below  $\phi_g = 0.78$ . Representative 2D GISAXS maps measured during the first SVA cycle are shown in Fig. 3.3. During the first  $\sim 30$  min of swelling, the DDSRs become weaker and finally vanish, i.e. only parallel lamellae persist. A large-scale structural reorganization evident from the shape of the DBSs is accompanied by a streak of high intensity along the film normal which points to large-scale roughness of the film surface. In the remaining time of the first swelling, the 1st order DBSs become straighter and sharper, i.e. the lamellae become thinner, and the lamellar interfaces become flat and smooth. During the first drying, the DBSs rapidly narrow down, i.e. the lamellar interfaces become flat, and they move upwards again, as expected for decreasing lamellar thickness. The lamellae are now mainly parallel with few defects. During the second swelling, the structural changes are much less pronounced, mainly the lamellae swell and shrink again. The bulk lamellar thickness is not recovered. We suggest that this value reflects the balance of interfacial interactions and the degrees of swelling of the PS and the PB domains at the time when PS becomes glassy again.

We now focus on the behavior of the lamellar thickness of the parallel lamellae in dependence on the polymer volume fraction. Plotting the  $D_{lam}^{par}$  values vs.  $\phi$  in a double-logarithmic representation reveals the scaling behavior and helps to identify the structural reorganization processes (Fig. 3.4b). Two regimes are identified during the first swelling: In the high-concentration regime ( $\phi < 0.88$ ),  $D_{lam}^{par}$  increases steeply, whereas it decreases for  $\phi < 0.79$  which is compatible with theoretical predictions. Initially, PS is still in the glassy state, and the swelling implies strong stretching of the PB blocks. Finally, additional lamellae form which allow for more interfacial area per chain and more Gaussian chain conformations in the swollen state. During the subsequent drying and during the second SVA cycle,  $D_{lam}^{par}$  first decreases smoothly and is later (after PS is glassy again) compatible with affine behavior most of the time, i.e. the lamellar thickness scales with the film thickness. Comparing with a thicker film from the same polymer, we find that the behavior is different during the first swelling, but very similar during drying. Swelling a PS-*b*-PB thin film slowly with a good, slightly selective solvent (CHX) up to a degree of swelling of 1.5 – 1.6 and subsequently drying it again slowly thus constitutes a protocol to obtain well-ordered lamellar thin films.

The project was funded by the International Graduate School “Materials Science of Complex Interfaces” and by DFG (Pa771/7).

[1] A. Sepe, J. Zhang, J. Perlich, D.-M. Smilgies, D. Posselt, C.M. Papadakis, *Eur. Polym. J.* (2016), DOI:10.1016/j.eurpolymj.2015.12.013

### 3.4 In-situ GISAXS microfluidics investigation of the sorption, diffusion and swelling processes of thin hydrophilic polymer films

M. Philipp, V. Körstgens, D. Magerl, C. Heller, Y. Yao, W. Wang, G. Santoro<sup>1</sup>, S. V. Roth<sup>1</sup>, P. Müller-Buschbaum

<sup>1</sup> DESY, Hamburg, Germany

For many fields of application, it is essential to understand and to control the sorption and diffusion processes of low-molecular penetrants interacting with polymer films [1-4]. Significant changes in structure, dynamics and properties are typically provoked within swelling or dissolving polymer films. Sorption and swelling of nano- to micrometer thin films are essential for the reproducible uptake and release of penetrants in case of microfluidics devices, sensors, separation membranes, drug carriers, and actuators. Another example stems from the field of the fabrication of microelectronics, namely the swelling and reactive dissolution of photoresist films [2].

Diffusion of penetrants within the polymer bulk and within polymer sheets has been studied since long, both theoretically and experimentally. Multiple reasons can lead to the usually observed deviations from classical Fickian diffusion, for instance variable concentrations of the penetrant at the surface of the polymer, space- or time-dependent distributions of the diffusion coefficient within the polymer, or mechanical stresses between parts of the polymer swollen to different degrees. The uptake of the penetrant also often leads to phase transformations within the polymer, like partial crystallization, crystal melting, phase separation or devitrification. Physicochemical interactions between the penetrant and the polymer, the shape, the structural homogeneity, the amorphous or semi-crystalline nature and the elastic properties of the investigated polymer thus codetermine its swelling behavior. For thin films, geometrical confinement of the macromolecules, their dynamics and their interactions at surfaces or buried interfaces might also influence the diffusion and swelling process.

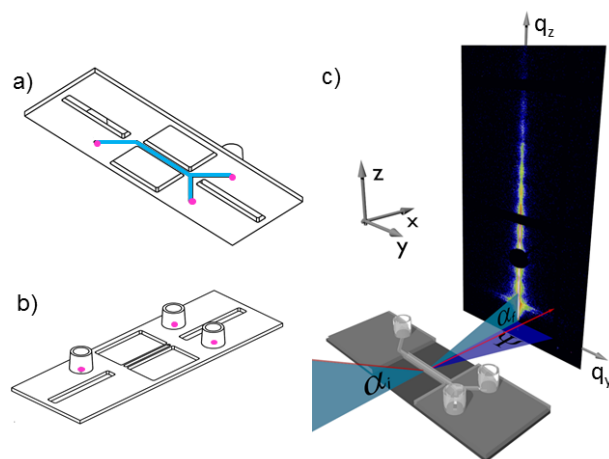


Figure 3.5:

a) Bottom view and b) top view of the microfluidics cell made of the X-ray transparent polymer TOPAS. Dots: indicate the position of the two inlets and the outlet of the microfluidics channel. c) Scheme of the in-situ GISAXS microfluidics experiment. The incident X-ray beam impinges under a shallow angle on the polymer film, exactly below the microfluidics channel. A two-dimensional scattering pattern of the hydrophilic polymer film is shown.

Sorption, diffusion and swelling processes are usually probed by recording the changes in mass, dimensions, or chemical composition of the polymer. Well-established techniques for investigating these processes in case of thin films are the quartz crystal microbalance, ellipsometry,

X-ray reflectivity, and infrared spectroscopy. For gaining a complementary perspective on the structural changes induced by the penetrant-polymer interactions, we propose a novel technique, namely in-situ grazing incidence small-angle X-ray scattering (GISAXS) microfluidics [3, 5]. Fig. 3.5 schematically represents how the experiment was carried out at the MiNaXS beam-line P03 at the PETRA III synchrotron of DESY in Hamburg.

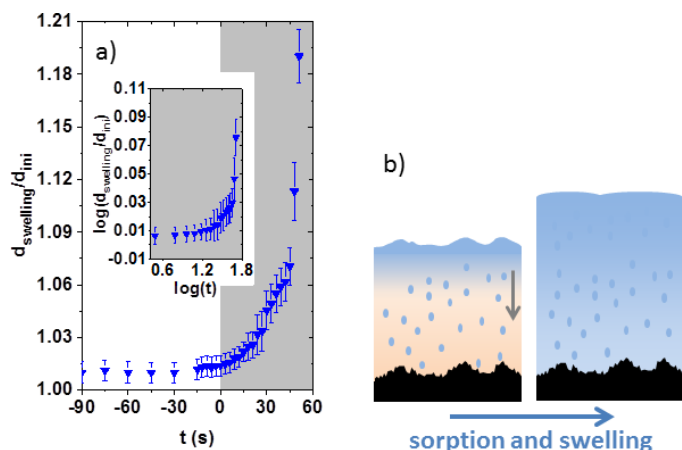


Figure 3.6:

a) Normalized increase in film thickness during the exposure of the 50 nm thin, hydrophilic film to liquid water after  $t=0$ s. Inset: log-log representation of the swelling process, prior to the dissolution of the film's surface. b) Illustration of the swelling and surface restructuring in the course of the swelling of the initially glassy, thin substrate-supported film. b) Liquid water is sorbed by the film, fills accessible free volumes and leads to the devitrification of the near-surface layer. Swelling of the polymer film occurs as the gel-glass phase boundary propagates into the depth of the film. In the meantime, the surface of the film flattens as the mobility of the macromolecules gets sufficient.

As shown in Fig. 3.6, the initial stages of water uptake, swelling and restructuring of the initially 50 nm thin, glassy hydrophilic polymer film could be resolved before the dissolution of the surface of the film sets in. Consistently, the most pronounced changes of surface restructuring occur simultaneously to the strongest swelling of the near-surface layer. The initial stages of swelling could tentatively be described by anomalous swelling induced by a time- and space-dependent diffusion coefficient [3].

To conclude, we introduced a promising GISAXS microfluidics technique, which is highly complementary to the established experimental techniques in the field of sorption, diffusion and swelling of thin polymer films. While the latter techniques focus on the changes in mass, volume or chemical composition, GISAXS allows to investigate the structural changes provoked in the bulk and at the surface and interfaces of thin films. The study of the initial stages of the swelling of a hydrophilic polymer film could be interpreted in terms of anomalous diffusion, involving a space- and time-dependent diffusion coefficient.

- [1] M. A. Cole, N. H. Voelcker, H. Thissen, H. J. Griesser, *Biomaterials* **30**, 1827-1850 (2009)
- [2] W. Hinsberg, F. A. Houle, S. W. Lee, H. Ito, K. Kanazawa, *Macromolecules* **38**, 1882-1898 (2005)
- [3] M. Philipp, V. Körstgens, D. Magerl, C. Heller, Y. Yao, W. Wang, G. Santoro, S. V. Roth, P. Müller-Buschbaum, *Langmuir* **31**, 9619-9627 (2015)
- [4] M. Koenig, D. Magerl, M. Philipp, K.-J. Eichhorn, M. Müller, P. Müller-Buschbaum, M. Stamm, P. Uhlmann, *RSC Advances* **4**, 17579-17586 (2014)
- [5] V. Körstgens, M. Philipp, D. Magerl, M. A. Niedermeier, G. Santoro, S. V. Roth, P. Müller-Buschbaum, *RSC Advances* **4**, 1476-1479 (2014)

### 3.5 Lithium-salt-containing PS-*b*-PEO block copolymer films

E. Metwalli, M. Rasool, S. Brunner, P. Müller-Buschbaum

Materials for high energy density, solid-state batteries have been tremendously explored in the last decade. In particular, recent research efforts demonstrated the utility of the lithium-ion/BC hybrid materials as membranes in lithium-ion battery applications. DBC electrolytes consist of two polymer blocks; one block enables ion-conducting pathways, while the other implements a relatively high shear modulus. The main challenge is to understand the effect of salt incorporation on the phase behavior of the PS-*b*-PEO diblock copolymer (DBC), which in turn significantly influences the conductivity performance of the ion-conducting membrane. Here, we report on the phase behavior/conductivity of a relatively high-molecular-weight DBC (91.5 kg/mol) upon lithium salt incorporation. The possible PEO chain folding in the high-content PEO of the DBC is a strong driving force that can lead to crystallization and thereby a destruction of the mesophase patterns. Thus, we additionally studied the effect of possible crystallization of lithium salt doped DBC membranes. A series of LiTFSI-doped PS-*b*-PEO DBC films was prepared by a solution casting method without any post-treatment steps, and probed using small/wide-angle X-ray scattering (SAXS/WAXS) [1]. The effect of morphology on the ionic conductivity of these ion-conducting membranes was investigated using impedance spectroscopy [1]. The temperature dependence of the WAXS profiles for the lithium-doped PS-*b*-PEO DBC at four different Li/EO ratios is plotted in Fig. 3.7. At low temperatures, two Bragg peaks at  $13.6$  and  $16.7 \text{ nm}^{-1}$  were observed and assigned to PEO crystallites. For the lithium-doped DBC at Li/EO ratios  $\leq 0.08$ , the intensities of both Bragg peaks gradually diminish and then vanish at high temperatures (Figs. 3.7a–c). An entire inhibition of the crystallization was observed for lithium-doped samples at a Li/EO ratio of 0.1 (Fig. 3.7d). Despite the WAXS profiles at Li/EO ratios of 0.1 revealing crystalline-free samples for all probed temperatures, a very broad and halo-like peak at  $14.2 \text{ nm}^{-1}$  can be observed at low temperatures (Fig. 3.7d). This halo-like peak is discriminated from the background intensity. From these results, the competition between the high tendencies of PEO to crystallize and the need to solvate the incorporated lithium salt leads to the formation of local disorder of the chain conformation. In other words, the amorphous molecular conformation is able to accommodate the lithium ions in a manner that is less disruptive to the local molecular crystalline structure. This tendency may lead to a morphological transition from those predicted by BC thermodynamics.

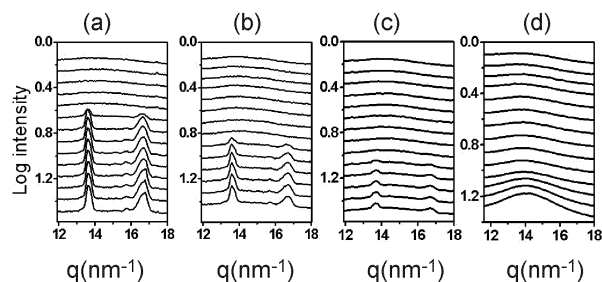


Figure 3.7: Temperature dependence of the WAXS profiles for lithium doped PS-*b*-PEO DBC at different Li/EO ratios (a) 0, (b) 0.04, (c) 0.08, and (d) 0.1. From bottom to top the temperature increases from  $25^\circ\text{C}$  to  $90^\circ\text{C}$  in steps of  $5^\circ\text{C}$ .

The temperature dependence of the SAXS profiles for all lithium-doped PS-*b*-PEO samples was acquired. The SAXS profiles of all samples indicated a lamellar structure with intensity maxima located at positions that satisfy  $q/q^* = 1, 2, \text{ and } 3$ . The scattering profiles were fitted using the “Scatter” software with a model based on a disk-like lamella of thickness  $L_a$ , radius  $R$ , and lamella spacing  $D$ . The inter-domain spacing  $D$ , as obtained from the fittings of the SAXS data, versus the temperature at all salt-doping levels is plotted in Fig. 3.8. Our results strongly emphasize that the pronounced increase of the domain spacing is not solely driven by the increase

of the effective interaction parameter  $\chi_{eff}$  upon salt doping. Generally, for salt-free BCs, an increase of N and a decrease of temperature T (an increase of  $\chi$ ) were found to increase the chain stretching (inter-domain spacing), getting the system into a strong-segregation regime (high  $\chi_N$  value). The current observation, however, showed that upon salt incorporation, an increase of domain spacing was observed with increasing temperature. From these results, we assume that the incorporation of the lithium salt results in a pronounced change of the PEO chain conformation rather than an increase of the  $\chi_{eff}$ , which leads to a stretching of the PEO chain upon coordinating the lithium ions.

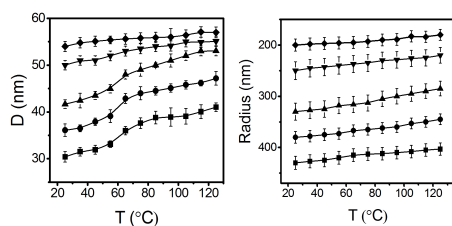


Figure 3.8:  
a) Lamella spacing D, b) lamella radius, R, versus temperature for the salt-doped PS-*b*-PEO DBC with various Li/EO ratios viz., 0.04, 0.06, 0.08, 0.1 and 0.15 from bottom to top.

For the as-prepared Li/DBC hybrid material containing the PEO crystallites, a pronounced increase of the domain spacing was consistent with those observed by recent investigation [2], assuming an amorphous nature of the PEO domains. The competition between the strong tendency of the PEO chain folding to form crystallites and the necessity of the chain to solvate the incorporated lithium ions has been overlooked in many previous related studies. Our study indicates that the strong crystallization behavior of the PEO chain may drive the incorporated salt in a Li/DBC hybrid system to reside at the PS-PEO interface, deteriorating the salt dissociation and, hence, the conductivity performance. Upon increasing the lithium salt content up to a certain threshold (Li/EO = 0.1), the samples are crystal free. Thus, the observed increase of the domain spacing with temperature is related to the melting of the PEO crystallites forming a disordered chain conformation.

At temperatures higher than the melting point of the PEO crystals, the random walk of the  $\text{Li}^+$  ions along the chain proceeds by loosening from an EO on one end of the coordination sphere and forming a new EO bond at another end, which may explain the extended domain spacing of the Li/DBC hybrid film.

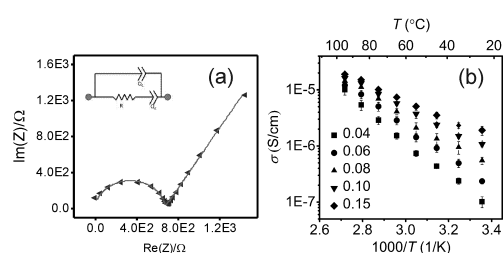


Figure 3.9:  
a) Exemplary impedance spectrum (triangle symbol) fitted (line) using the equivalent circuit given in the inset, b) Conductivity versus temperature for the lithium-doped PS-*b*-PEO DBCs.

At high temperatures, the conductivity was improved due to improved mobility of the PEO domains. Combining both the improved mobility and dissociation of the salt in the DBC membrane, a pronounced progressive increase of the conductivity is observed (Fig. 3.9b). Further studies on various types of DBCs with ion-dissolving blocks are necessary to understand the effect of the type of the various salts on the phase behavior of DBCs in a more general manner. Moreover, the fabrication of long-range ordered nanostructured materials containing ordered dispersion of inorganic salts offers a route for further applications beyond solid state batteries, such as luminescent and nonlinear optical materials.

[1] E. Metwalli, M. Rasool, S. Brunner, P. Müller-Buschbaum, *ChemPhysChem* **16**, 2882-2889 (2015)

[2] I. Gunkel, T. Thurn-Albrecht, *Macromolecules* **45**, 283-291 (2012)

### 3.6 Structure of the PLMA-*b*-PMAA diblock copolymer electrolyte

B. Springer, E. Metwalli, S. Pispas<sup>1</sup>, P. Müller-Buschbaum

<sup>1</sup> Theoretical and Physical Chemistry Institute, NHRF, Athens, Greece

The increasing demand for renewable energies, in particular wind and solar energy, gives rise to an increased interest in energy storage. Lithium-ion batteries are very attractive energy storage media due to their remarkable characteristics, like high energy densities, low self-discharge rates [1]. One of the most important component of Li-ion battery is the membrane. Liquid electrolytes are instable and highly flammable. Block copolymers (BCPs) are a possible alternative due to their ability to self-assemble into nanostructures. This self-assembly can be tuned in many different ways. For example, the fraction of one block is a very important factor that can determine the evolved morphologies. But also the nanostructures could be modified by bringing charges into one of the blocks [2]. This charged polymers give rise to an additional modification than that predicted by conventional BC phase diagrams, due to electrostatic interactions.

Here, we employed poly(lauryl methacrylate-*b*-methacrylic acid) (PLMA-*b*-PMAA) diblock copolymer (DBC) with two different PLMA weight fractions. The PLMA-*b*-PMAA DBC, with total molecular weight 8500 kg/mol and PLMA weight percentage of 0.74, as well as PLMA-*b*-PMAA with molecular weight of 12600 kg/mol and a PLMA weight fraction of 0.50. The samples were prepared using the solution-casting method with THF as the solvent. A solution of 5 wt% was prepared for each of the polymer and then pipetted on a mica window to prepare samples for small-angle X-ray scattering (SAXS) measurements. Between each drop of solution we waited 10 minutes. After a complete drying, we assembled the sample holder for the SAXS measurements. All preparation steps were conducted at ambient conditions. Following, the samples were annealed overnight under vacuum at 155°C. The PLMA-*b*-PMAA DBC with  $f_{PLMA} = 0.74$  was also measured prior and after the thermal annealing step. For the SAXS measurements, we used two different measurement protocols. For instance, we heated the samples in-situ during the heating-protocol from 25°C to 155°C in 20°C steps. For each step the measurement lasted 30 minutes. After that, eight additional measurements at 155°C were carried out at a sample-detector distance of 1051 mm. Then we cooled the samples from 155°C to 35°C in 20°C steps. Also test measurements in WAXS and SAXS configuration were conducted to probe scattering characteristics at higher  $q$  values. These test measurements showed, that there are additional peaks to see in the SAXS configuration measurements at a relatively short sample-detector distance (451 mm), which were non-resolvable at 1051 mm.

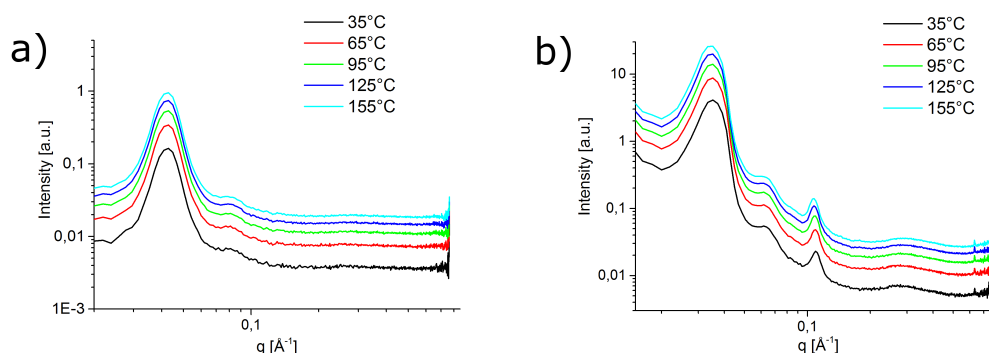


Figure 3.10: SAXS data for diblock copolymer with a weight fraction of a)  $f_{PLMA} = 0.74$  and b)  $f_{PLMA} = 0.5$  at different temperatures.

Fig. 3.10 shows the SAXS profiles of both DBC samples at different temperatures. For PLMA-b-PMAA DBC with  $f_{PLMA} = 0.74$ , two main scattering peaks are observed. While, for DBC with  $f_{PLMA} = 0.5$ , four main scattering peaks are observed.

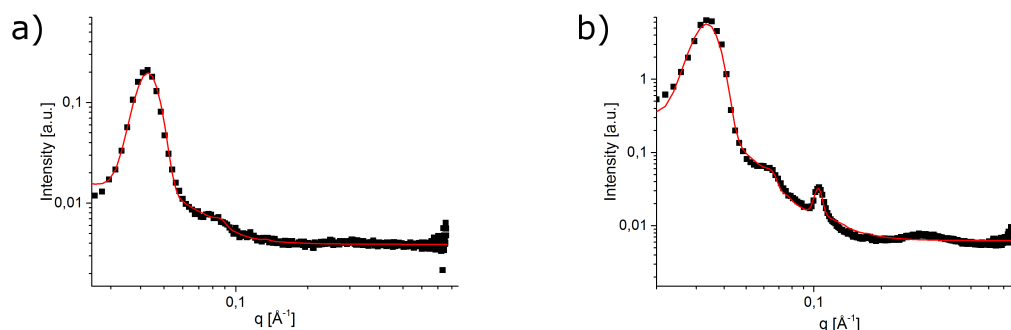


Figure 3.11:

Lamella fit for the SAXS data for diblock copolymer with a weight fraction of a)  $f_{PLMA} = 0.74$  and b)  $f_{PLMA} = 0.5$  at  $155^{\circ}\text{C}$ .

The data in Fig. 3.11 was fitted using Scatter software with a lamella model. One can see that the lamella model fits reasonably well for both polymers. The results shows that the phase diagrams of the block copolymers with high PLMA weight fraction (0.74) behave in an unconventional way as those predicted from conventional block copolymer phase diagrams. According to the fitting the polymers have slightly different periodic distances  $D$ . For the polymer with a weight fraction of 0.74 PLMA the periodic distance  $D$  is about 14.1 nm, for the polymer with a weight fraction of 0.5 PLMA we observe a periodic distance of 17.9 nm.

In further work, we are going to investigate more on this particular system. A special emphasis will be set on the observation of the electrostatic cohesion effect, predicted by Sing et al. [2]. Electrostatic cohesion effect means that the polar groups in our polymer will assemble around salt ions, for example lithium-ion. According to Sing et al. [2] this cohesion will lead to a shift in the phase diagram in a more complex way as predicted by classical BC theory, leading to structures, which else would not be expected. According to Sing et al. [2] one is able to set a new parameter  $\Gamma$ , which, similar to the Flory  $\chi$ -parameter, expressed the strength of the electrostatic cohesion.  $\Gamma$  is given by:

$$\Gamma = \frac{e^2}{8\pi\epsilon_0\epsilon_r k_B T a} \quad (3.1)$$

Here,  $\epsilon_0$  is the relative dielectric constant of vacuum,  $\epsilon_r$  is the relative permittivity of the polymer,  $a$  is the radius of the added ions and  $T$  is the temperature. Therefore we are going to investigate the phase changes in our polymer system upon salt incorporation, in particular lithium salt. We will use lithium, because in a further step, we want to investigate the suitability of the system as a polyelectrolyte for lithium-ion batteries. This will be conducted by impedance measurements and, as a last step, in a full battery assemble to measure the characteristics of a lithium-ion battery with this particular BC electrolyte.

[1] W. S. Young, W. F. Kuan, T. H. Epps III, *J. Polym. Sci. B Polym. Phys.* **52**, 1-16 (2014)

[2] C. E. Sing, J. W. Zwanikken, M. Olvera de la Cruz, *Nat. Mater.* **13**, 694-698 (2014)

[3] E. Metwalli, M. Rasool, S. Brunner, P. Müller-Buschbaum, *ChemPhysChem* **16**, 2882-2889 (2015)

### 3.7 Structure of thermoresponsive polystyrene-*b*-poly(N-isopropylacrylamide) / cobalt oxide nanocomposite thin films

H. Xu, E. Metwalli, P. Müller-Buschbaum

Nanostructured polymer-metal oxide composites are a current research area of great importance due to its highlight applications in sensors, optics and catalysts [1, 2]. In particular, the use of thermoresponsive polymers gives more flexibilities and possibilities in the design and construction of polymer templates [3]. In the present investigation, the structure and properties of hybrid films composed of a polystyrene-*b*-poly(N-isopropylacrylamide) ((PS-*b*-PNIPAM), Fig. 3.12a) diblock copolymer (DBC) and cobalt metal salt are investigated. The thermoresponsive poly(N-isopropylacrylamide) (PNIPAM) has a lower critical solution temperature (LCST) in aqueous solution at 32°C [4], which enables the controllable volume ratio of PS and PNIPAM in the structure of PS-*b*-PNIPAM. Thus, the magnetic properties and structures of PS-*b*-PNIPAM/cobalt salt nanocomposites can be tailored via structural changes introduced from the thermoresponsive behavior [5, 6].

We have studied the influence of both thermal and vapor annealing on the structure of PS-*b*-PNIPAM DBC using small-angle X-ray scattering (SAXS). The thermal annealing of the samples was performed at 90°C and 150°C for 48 hours, respectively. Also, in another experiment a vapor annealing was employed in an atmosphere of tetrahydrofuran (THF) solvent for 48 hours. One sample is used as reference directly after solution-casting without any thermal or vapor annealing. The SAXS measurement results are presented in Fig. 3.12b.

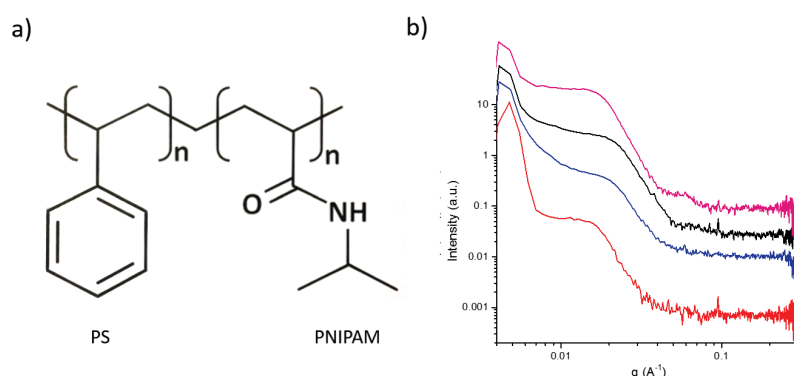


Figure 3.12:

a) Chemical structure of PS-*b*-PNIPAM DBC. b) SAXS data of thermally annealed samples at 90°C (purple line) and 150°C (red line) for 48 hours respectively, THF vapor annealed sample for 48 hours (blue line) and as-prepared sample without any post-treatment step (black line). The curves are shifted along the y axis for clarity of the presentation.

As shown in Fig. 3.12b, in the SAXS measurements a relatively broad scattering peak is present for the thermal and vapor annealed as well as the as-casted samples. This indicates that the samples did not reach an equilibrated ordered structure upon thermal or vapor annealing process. Thus, further investigations are required to explore the proper annealing conditions of the current DBC system to enable the micro-phase/self-assembly processes.

Furthermore, in order to study the influence of temperature on the structure during the thermal annealing step, we did the in-situ temperature dependent SAXS measurements for the sample which was pre-annealed at 90°C. The results are presented in Fig. 3.13.

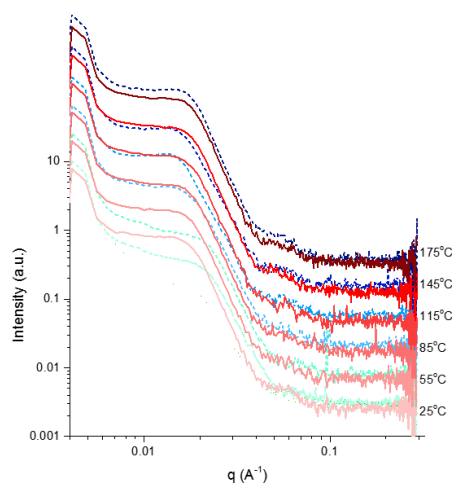


Figure 3.13:

In-situ temperature dependent SAXS measurement profiles of PS-*b*-PNIPAM DBC that pre-annealed at 90°C (red solid line) and as-prepared without any post-treatment step (blue dash line) during the heating up from 25°C to 175°C. The curves are shifted along the y axis for clarity of the presentation.

According to Fig. 3.13, with increasing the temperature, the thermal annealed sample shows relatively more defined peaks, which means that ordered structures are developed at high temperatures. We will continue the temperature-resolved investigation to figure out the suitable annealing protocol to attain the desired highly ordered structures.

The next stage of this study will focus on the magnetic properties and structure of hybrid polymer-metal oxide nanocomposite. Cobalt metal salt oxidation in the polymer matrix will be probed with UV/vis and FTIR spectroscopies during the thermal treatment step. The inter-domain lamella spacing  $D$  will be evaluated using GISAXS for thin film samples as a function of cobalt salt concentration. Both, paramagnetic and superparamagnetic behavior of the heat-treated hybrid films will be explored at different cobalt metal contents using superconducting quantum interference device magnetometer.

- [1] E. Metwalli, I. Krisch, I. Markovits, M. Rawolle, M. A. Ruderer, S. Guo, S. Wyrzgol, A. Jentys, J. Perlich, J. A. Lercher, P. Müller-Buschbaum, *ChemPhysChem* **15**, 2236-2239 (2014)
- [2] Y. Li, M. J. Yang, Y. She, *Talanta* **62**, 707-7012 (2004)
- [3] Y. Yao, E. Metwalli, M. A. Niedermeier, M. Opel, C. Lin, J. Ning, J. Perlich, S. V. Roth, P. Müller-Buschbaum, *ACS Appl. Mater. Interfaces* **6**, 5244-5254 (2014)
- [4] X. D. Ye, J. Y. Fei, J. Guan, X. C. Zhou, G. Z. Zhang, *Journal of Polymer Science Part B: Polymer Physics* **48(7)**, 749-755 (2010)
- [5] Y. Yao, E. Metwalli, B. Su, V. Körstgens, D. Mosegui Gonzalez, A. Miasnikova, A. Laschewsky, M. Opel, G. Santoro, S. V. Roth, P. Müller-Buschbaum, *ACS Appl Mater Interfaces* **7**, 13080-13091 (2015)
- [6] E. Metwalli, V. Körstgens, K. Schlage, R. Meier, G. Kaune, A. Buffet, S. Couet, S. V. Roth, R. Röhlberger, P. Müller-Buschbaum, *Langmuir* **29**, 6331-6340 (2013)

### 3.8 Optical and morphological investigation of photoactive, low band gap polymer films

F. C. Löhner, V. Körstgens, P. Zhang<sup>1</sup>, S. V. Roth<sup>1</sup>, P. Müller-Buschbaum

<sup>1</sup> DESY, Hamburg, Germany

With a wide range of potential applications, polymer-based photovoltaics have taken the spotlight as an interesting alternative to conventional solar cells. However, they are not yet able to compete in terms of their power conversion efficiency. In order to enhance the solar cell performance, recent research efforts focus on identifying new high-efficiency materials. This has led to the development of low band gap polymers such as PTB7 and its derivatives with solar cell efficiencies surpassing 10%. [1] These materials can absorb photons of lower energies and thereby show an increase of light absorption over a larger range of wavelengths compared to typically used photoactive polymers.

In order to acquire a better understanding of the underlying fundamental mechanisms in different low band gap polymers, we investigate thin films of one of their most promising examples, PTB7-Th, in blend with the electron acceptor ICBA. PTB7-Th is a derivative of the high-efficiency polymer PTB7 and is combined with ICBA, a fullerene similar to the well-known PCBM. Fig. 3.14 a) illustrates the chemical structures of the applied materials in comparison to the typically used materials PTB7 and PC<sub>71</sub>BM. The monomer units of the two polymers differ in their side chains. PTB7 has ether groups connecting the side chains to its benzodithiophene part of the backbone, while in PTB7-Th, these ether groups are substituted by thiophene rings, thereby increasing the side chain planarity. This is expected to result in an enhanced ordering of the polymer domains. The acceptor molecules both consist of a fullerene unit (C<sub>60</sub> and C<sub>70</sub> respectively) with small side groups. They mainly differ in their energy levels, which are sketched in fig. 3.14 b).

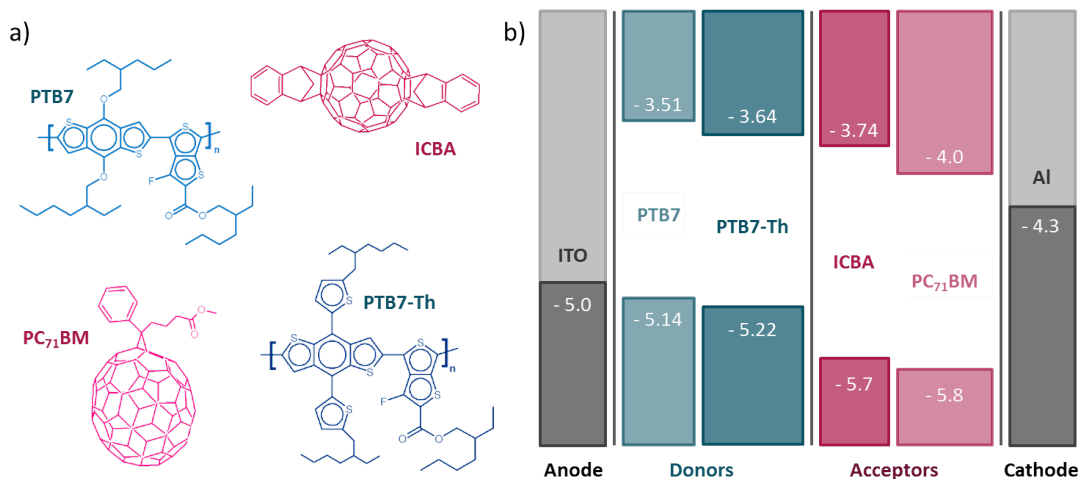


Figure 3.14:

a) Chemical structures of the applied donor and acceptor materials in comparison to PTB7 and PC<sub>71</sub>BM and b) electronic HOMO and LUMO levels of the materials and resulting band gaps in a typical solar cell.

Illustrated are the HOMO and LUMO levels of the aforementioned active materials as well as the work functions of typical electrodes for potential photovoltaic applications. [2] ICBA exhibits increased energy levels with a larger band gap compared to the commonly used PC<sub>71</sub>BM, which, in combination with a donor material, is expected to lead to a higher potential difference and thereby a higher open-circuit voltage in solar cells. PTB7-Th shows slightly decreased energy

levels with an even smaller band gap than PTB7, enabling the absorption of photons with lower energy, which in turn could lead to a higher overall absorption and photocurrent.

For characterization, thin films are prepared via spin coating out of a solution consisting of the two active materials mixed in an organic solvent. These films can be characterized using their absorption behavior, which is directly correlated to the created photocurrent and the respective solar cell performance. UV-visible absorbance measurements performed on films of varying PTB7-Th : ICBA ratios are shown in fig. 3.15 a). The absorbance values are normalized to the value of maximum absorption of pure PTB7-Th at about 720 nm to enhance their comparability. Two clear absorption maxima at higher wavelengths – and therefore lower energies – can be distinguished for the polymer, while the fullerene absorbs at lower wavelengths due to its larger band gap. With increasing amount of ICBA, the absorption at wavelengths below 550 nm is increased, which in turn should increase the created photocurrent and thereby the cell efficiency.

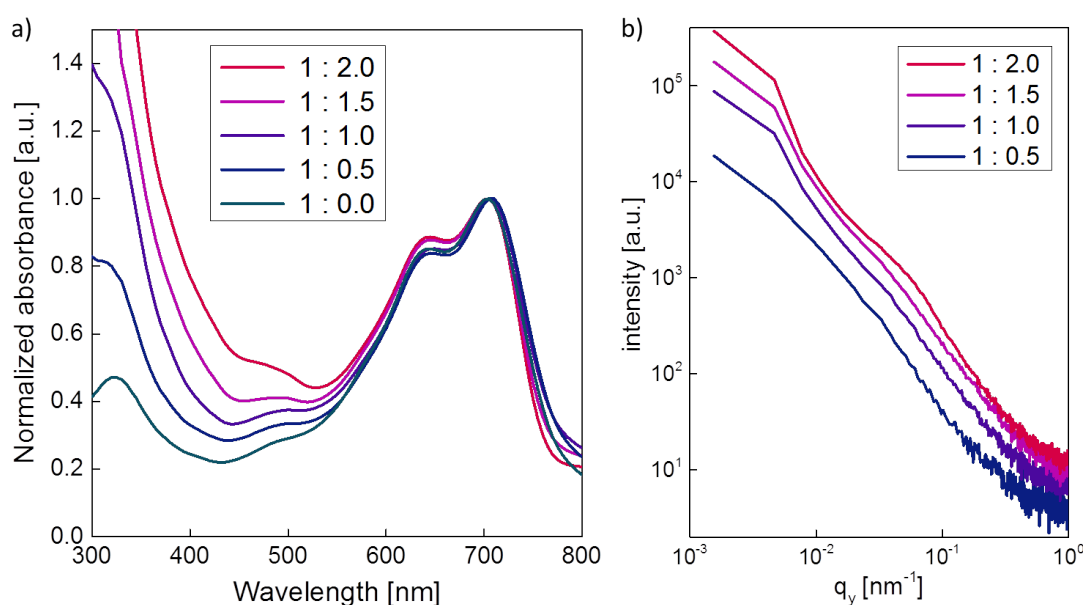


Figure 3.15:

a) Normalized UV-visible absorption spectra of thin films of varying PTB7-Th : ICBA ratios and b) horizontal line cuts of 2D GISAXS data of the respective PTB7-Th : ICBA films

The thin film morphology was investigated using GISAXS measurements performed at the Mi-NaXS beamline P03 at the DESY in Hamburg. 2D data were taken for the respective PTB7-Th : ICBA films of varying ratios. Fig. 3.15 b) shows horizontal line cuts performed at the Yoneda peak position of PTB7-Th. The detected intensity is plotted in arbitrary units for a range of  $q_y$  values. The intensity values for the different ratios are stacked for better visibility. With an increasing amount of ICBA, a shoulder emerges at a  $q_y$  value of about 0.05 nm<sup>-1</sup>. This shoulder can be explained by an increased phase separation between the two active materials and higher ordering of the polymer in its domains of about 20 nm size. From model fitting more structure information will become available.

Future work will further focus on the thin film morphology, applying characterization techniques such as electron microscopy as well as X-ray scattering methods.

[1] S.-H. Liao, H.-J. Jhuo, P.-N. Yeh, Y.-S. Cheng, Y.-L. Li, Y.-H. Lee, S. Sharma, S.-A. Chen, *Sci. Rep.* **4**, 6813 (2014)

[2] S.-H. Liao, H.-J. Jhuo, Y.-S. Cheng, S.-A. Chen, *Adv. Mater.* **25**, 4766–4771 (2013)

### 3.9 Full thermoelectric characterization of highly conducting PEDOT:PSS thin films

N. Saxena, A. Greppmair<sup>1</sup>, M. S. Brandt<sup>1</sup>, P. Müller-Buschbaum

<sup>1</sup> WSI, TU München, Garching, Germany

Imminent global climate change largely affects humanity, due to drastic fluctuations in meteorological phenomena. In order to overcome the manifold consequences of these phenomena, research on energy conversion systems based on renewable energy sources has become very appealing over the past years. While extensive research is carried in the field of photovoltaics, in order to convert the energy of visible solar radiation into electrical power, it is feasible to think about alternative ways of harvesting energy.

Heat is lost in almost any forms of chemical and physical processes which are important in everyday life. Thermoelectric materials have the ability to make use of this low-quality form of energy by transforming temperature gradients into electrical voltages by letting charge carriers flow from the hot to the cold side of the material. The conversion efficiency is dependent on both, the thermal and electrical conductivity ( $\kappa$  and  $\sigma$ , respectively), and also a material property called the Seebeck coefficient  $S$ , which relates to the generated voltage as a function of a given temperature difference. These quantities are combined in the dimensionless so-called figure of merit  $ZT$ , seen in Formula 3.2, which relates to the thermodynamic conversion efficiency.

$$ZT = \frac{\sigma S^2}{\kappa} T \quad (3.2)$$

One major bottleneck for the increase of the  $ZT$  is the interdependence of these three quantities. We wish to overcome the limitations given by inorganic thermoelectrics, such as high cost and expensive and/or toxic raw materials, by employing conjugated polymers and making use of their electrical transport properties. The possibility of facile fabrication of thin polymer films through solution-based processing techniques, such as spin-coating or printing, further increases the feasibility of this approach. Apart from the abundance of raw material, thermoelectric devices based on polymer thin films are expected to work considerably well at low temperatures, which makes them especially interesting for daily-life application.

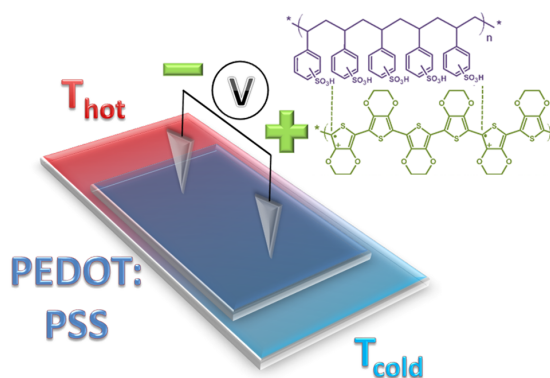


Figure 3.16: Sketch of PEDOT:PSS thin film subjected to a temperature gradient. Positive charge carriers flow along the gradient, and create a positive charge excess.

PEDOT:PSS, seen in Fig. 3.16, is a conducting, water-soluble polymer blend, and has been extensively investigated over the past years, due to its tunable conductivity by simple chemical treatments [1]. Therefore, it is well-suited for application as a thermoelectric material. However, before we can try to improve the thermoelectric parameters of PEDOT:PSS thin films, we need to be able to determine all three parameters, which are put into the equation for  $ZT$ , systematically. For this reason, we have adapted a procedure developed by Greco *et al.* in 2011, in which PEDOT:PSS is applied on thin poly(dimethyl siloxane) (PDMS) films by spin-coating, and over-coated with an aqueous solution of poly(vinyl alcohol) (PVA) [2]. The low interfacial energy of

PDMS allows for removal of the PEDOT:PSS film using tweezers. The top layer consisting of PVA gives mechanical stability of the PEDOT:PSS film after the removal. In addition, PVA is water-soluble and immersion of the PEDOT:PSS/PVA bilayer in water leads to the dissolution of PVA while the PEDOT:PSS film remains intact. In principle, using this technique, PEDOT:PSS can be transferred to a variety of different substrates. As described below, this is a crucial point regarding our systematic analysis.

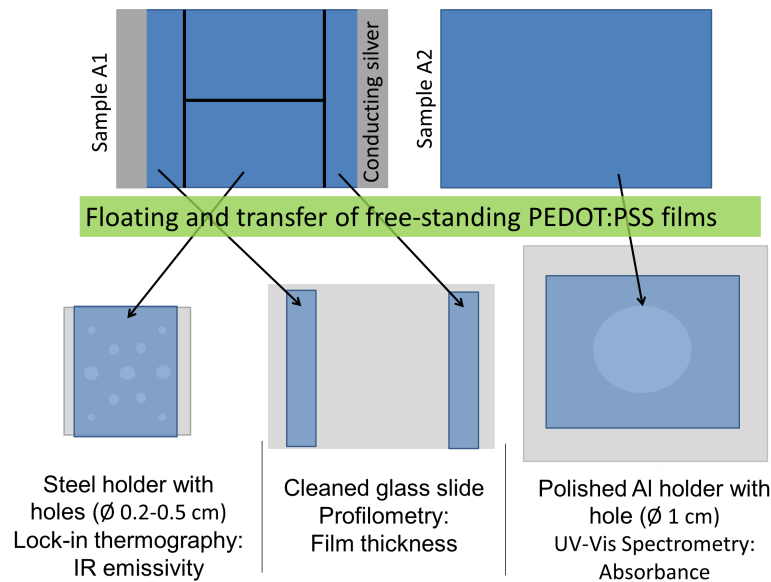


Figure 3.17:

Full thermoelectric characterization of a pair of PEDOT:PSS thin films on PDMS using IR thermography: transfer of parts of films to different substrates for IR thermography, film thickness, UV-Vis absorbance.

The Seebeck coefficient of our PEDOT:PSS thin films is determined using a home-made setup, which allows for the generation of a temperature gradient, and simultaneous monitoring of the thermovoltage as function of the respective temperature gradient. The electrical conductivity is measured using a standard four-point probe measurement setup. Determination of the thermal conductivity of thin films has proven to be very difficult, due to orders of magnitude difference in thickness between film and glass substrate. In our collaboration, we have successfully implemented IR thermography, in order to determine the film's thermal conductivity without influence of the substrate. Using the procedure by Greco *et al.* described above, we transfer different parts of the PEDOT:PSS films to different substrates, in order to carry out the measurements for IR emissivity [2] (Al holder with small holes), film thickness (glass substrate) and absorbance (Al holder with large hole). This can be seen in Fig. 3.17. The film resting on the Al holder with small holes is thermally excited by a red LED, while the emission of IR radiation is measured by a IR camera resting on top and records the emitted radiation. With this technique, we have calculated a thermal conductivity of about 1.1 W/K·m. Thus, we demonstrated the systematic determination of an ZT of  $4 \cdot 10^{-3}$  at an average temperature of 323 K.

- [1] H. Shi, C. Liu, Q. Jiang, J. Xu, *Adv. Electronic Mater.* **1**, 1500017 (2015)
- [2] F. Greco, A. Zucca, S. Taccola, A. Menciassi, T. Fujie, H. Haniuda, S. Takeoka, P. Dario, V. Mattoli, *Soft Matter* **7**, 10642 (2011)
- [3] A. Greppmair, B. Stoib, N. Saxena, P. Müller-Buschbaum, M. Stutzmann, M. S. Brandt, *submitted*.

### 3.10 Artificial nanostructuring of thin polymer films

A. Özkü, F. C. Löhner, M. A. Trunk, P. Müller-Buschbaum

The world's growing energy need is and will be one of the greatest challenges that humanity has to face for the next decades. Considering global warming, it is obvious that the growing energy need has to be covered by environment-friendly technologies. Thus, the development of green-energy technology is receiving an increasing interest.

Conjugated polymers have received great attention due to many potential applications in organic electronics, as for example organic solar cells. In addition to that, novel low band gap polymers have shown to give rise to high power conversion efficiencies exceeding the 10% limit [1]. However, their performance is still not comparable to that of state of the art inorganic solar cells. Thus, current research aims for increasing the efficiency of thin film organic solar cells by several different approaches. Among these approaches the use of artificial nanostructuring of the polymer films can add benefit with regard to solar cell applications, as for example the reflection of light can be reduced.

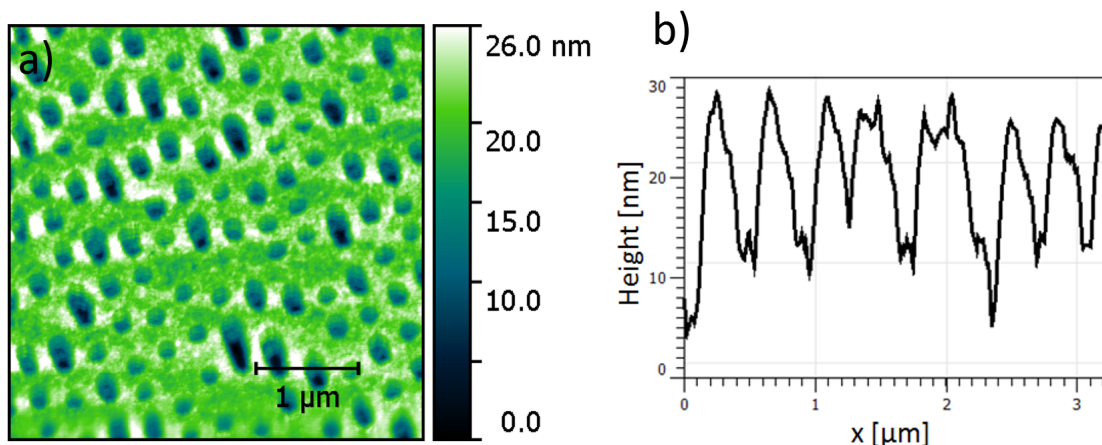


Figure 3.18: a) AFM image of imprinted surface of active layer b) Cut through pits and islands

In the present investigation, we combine low band gap polymers with an artificial nanostructuring of the polymer film by the soft embossing method. Due to its properties suited for imprinting of wet surfaces, molds are made of polydimethylsiloxane (PDMS). Commercially available Blu-Ray movie discs serve as masters for the transfer of a negative imprint of the Blu-Ray nano-pattern onto the PDMS molds. It has been reported, that the nanostructuring of quasi-randomly distributed islands and pits on a Blu-Ray disc is well suited for photon management over the entire solar spectrum [2]. Incident light is trapped between the cones leading to multiple scattering effects and enhanced absorption. With such approach an increase in the device efficiency was realized for PTB7 based organic solar cells [2].

The active layer of our solar cells consist of a blend of an electron donor polymer and the electron acceptor fullerene PC<sub>71</sub>BM. The applied donor material is a derivative of the low band gap polymer PTB7. The active layer thickness is varied between 100 and 150 nm depending on the polymer concentration in the blend and the used spin coater settings. The imprinted surface of thin films is further investigated by images taken by atomic force microscopy (AFM) in order to verify the successful transfer of the nanostructure. In Fig. 3.18a the imprinted

surface topology of a thin film can be seen. From a line cut of the AFM data through the islands and pits shown in Fig. 3.18b it is observed that the heights of the cones are reaching 15 nm.

Optical characterization of the imprinted thin polymer films is performed via UV/VIS- spectroscopy. Angulardependent absorbance measurements are carried out in an integrating sphere to ensure that transmitted as well as reflected light is detected in absorbance mode. Measurements in reflection mode are carried out for perpendicular impinging light and in absorbance mode for the measurements of samples tilted to the perpendicular impinging beam direction. Fig. 3.19 shows the spectra of films measured at normal incidence (not tilted sample Fig. 3.19a) and for a small tilt angle of  $5^\circ$  (Fig. 3.19b). Caused by multiple scattering of light that is trapped in the active layer between the cones, active layers imprinted with the Blu-Ray disc nano-pattern show an enhanced absorbance from 400 nm to 800 nm, compared to nonstructured thin films. The total increase over the spectrum from 300 nm to 800 nm is 7.1 % for the tilted samples and 4.5 % for the samples probed under normal incidence of light. Due to the increase in absorbance, we expect an increase in the short circuit current of solar cells with an imprinted active layer and therefore an increase in the power conversion efficiency.

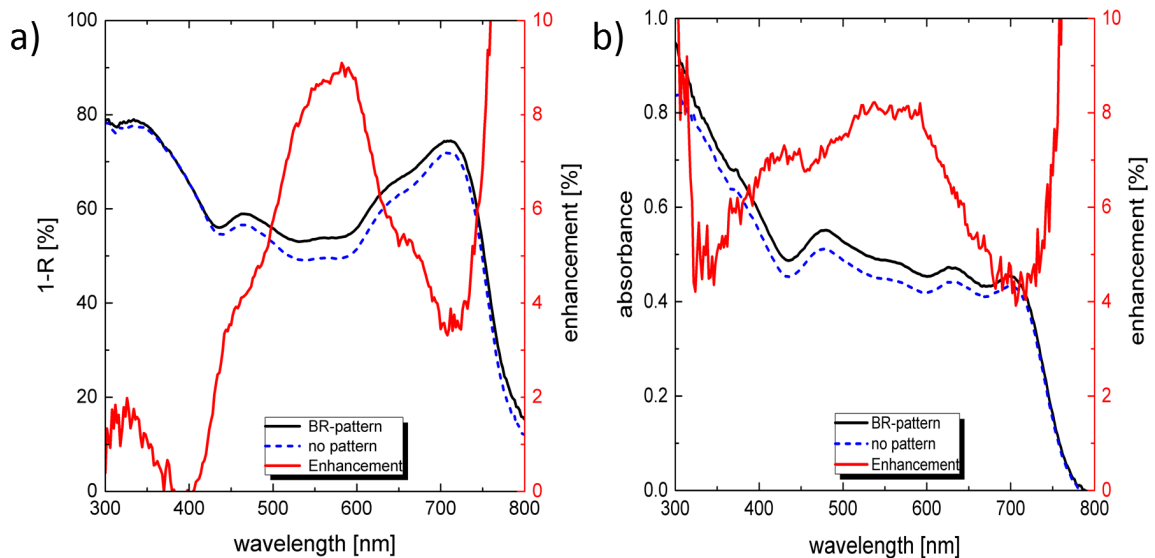


Figure 3.19:

a) Reflection spectrum of untreated and imprinted active layer and b) absorbance spectra of untreated and imprinted active layer tilted  $5^\circ$  to normal incidence of the light

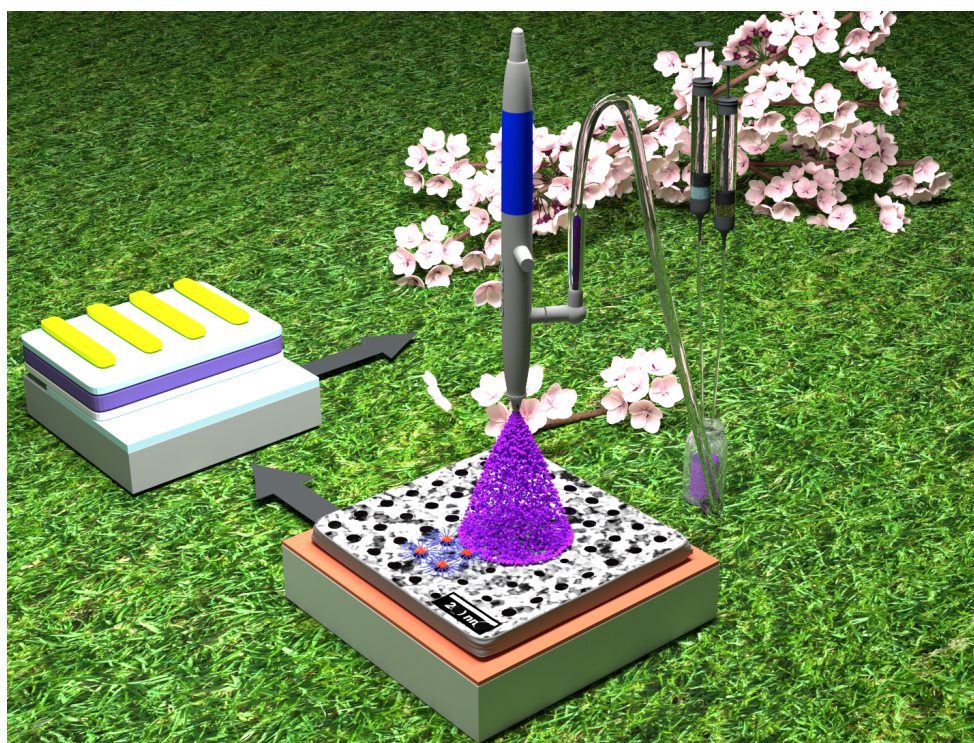
One of the next steps is to improve the imprinting process in order to get features reaching deeper into the active layer and to allow light to be guided deeper in between the cones. The film thickness dependency of the light management effect will be further investigated as well as its effect on the solar cell parameters like short circuit current and open circuit voltage.

[1] J. D. Chen, C. Cui, Y. Q. Li, L. Zhou, Q. D. Ou, C. Li, Y. Li, J. X. Tan, *Advanced Materials* **27**, 1035-1041 (2015)

[2] J. Smith, C. Wang, D. Guo, C. Sun, J. Huang, *Nature Communications* **5**, 5517 (2014)



## 4 Polymer films for applications in photovoltaics



#### 4.1 Light-induced degradation in the active layer of high-efficiency organic solar cells

C. Senfter, F. C. Löhner, C. J. Schaffer, P. Müller-Buschbaum

Organic photovoltaics are a promising technique to use the energy of the sun in order to generate electricity. The application of polymers has several advantages over conventional silicon solar cells. Organic materials are typically cheap in production (roll-to-roll process), flexible and lightweight. However, since their efficiencies and long-term stabilities are far below the ones of silicon, a deeper understanding of the fundamental processes in organic solar cells is necessary.

In the last years, research has been focusing on the identification of new high-efficiency polymers with lower band gaps, so that light can be absorbed over a larger wavelength scale. Examples of these low band gap materials are PTB7 (polymer poly[[4,8-bis[(2-ethylhexyl)oxy]benzo[1,2-b:4,5-b']dithiophene-2,6-diyl][3-fluoro-2-[(2-ethylhexyl)carbonyl]thieno[3,4-b]thiophenediyl]]) and its derivatives. In blends with PC<sub>71</sub>BM, power conversion efficiencies of over 10% have been reached on a laboratory device scale [1]. However, little is known about the long-term stability of these polymers and their blends. Since for a profitable large-scale production the lifetime is an important parameter, such studies are of importance.

In Fig. 4.1, the UV/Vis absorbance spectrum of an active layer of a PTB7-derivate high-efficiency solar cell is plotted. The absorbance of this material already decreases dramatically within a few days under ambient conditions in the dark (in a light-tight box). The absorbance decreases over the entire wavelength spectrum. For shorter wavelengths the decrease is more pronounced, which indicates a stronger degradation of PCBM than of the PTB7-derivate, which mainly absorbs at higher wavelengths. The decrease in absorbance of the polymer is mainly caused by bleaching.

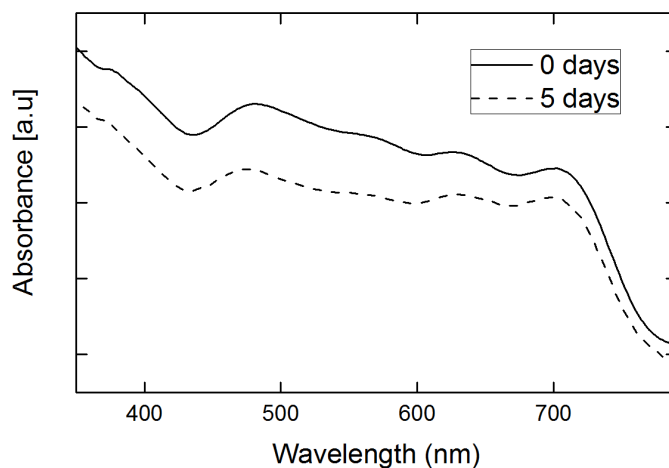


Figure 4.1:  
Example of UV/VIS absorption spectrum of a thin film of PTB7-derivate blended with PC<sub>71</sub>BM in a mixing ratio of 1 : 1.5

Degradation processes in organic solar cells can be split into chemical processes, like photo-oxidation or photo-bleaching, and physical processes caused by morphological changes. To investigate chemical degradation, changes in the molecular structure of the active materials have to be analyzed. This can be done by looking at the infrared (IR) absorption spectrum of the

used active material. The excitation energy of vibrational molecular motions between parts of the molecule lie in the infrared regime, so every molecule has a characteristic infrared spectrum with absorption peaks corresponding to the frequencies of vibrations between the atoms. If a chemical degradation process takes place in the active layer, the organic molecules change, which leads to changes in their IR-spectra.

In first investigations, we measured the infrared absorption spectrum of a drop casted PTB7-derivate:PC<sub>71</sub>BM film on silicon for different lifetimes. The measurements were done with an FT-IR (Fourier transformed infrared) spectrometer. With this instrument, it is possible to measure all infrared frequencies simultaneously, which results in fast measurements for the whole frequency range. Between the measurements, the sample was illuminated simultaneously with visible and UV light to simulate sun radiation. The associated illumination device was built by Julian Fischer during his Bachelor thesis [2] and allows us to illuminate the sample directly in the IR spectrometer, which makes it easier to compare the results. Because of the strong absorption of CO<sub>2</sub> and H<sub>2</sub>O, the instrument was purged with CO<sub>2</sub>- and H<sub>2</sub>O-free air to ensure constant measurement conditions.

In Fig. 4.2 a the infrared spectrum of an active layer for different illumination times is plotted. The changes in the spectrum within the measurement time are very small, so one peak is discussed in more detail. In Fig. 4.2 b, the peak corresponding to the CH<sub>2</sub> asymmetrical stretching is shown in more detail. The absorption decreases with time, which indicates a change in the molecular structure of some molecules in the active layer. A peak shift could not be examined for this peak, as the binding energy stays constant.

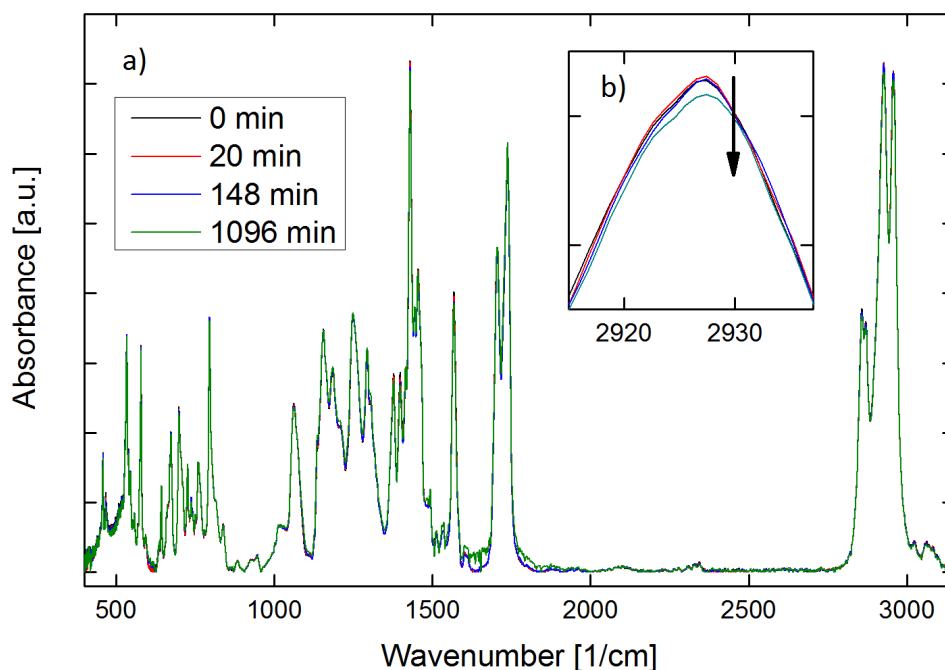


Figure 4.2:

a) FT-IR absorption spectrum of PTB7-derivate:PC<sub>71</sub>BM blend measured at different illumination times, b) enlarged CH<sub>2</sub> asymmetrical stretching peak in the spectrum.

In further investigations, we will match the changes in the IR-absorption spectrum with the associated change in the molecular structure.

[1] J.-D. Chen, C. Cui, Y.-Q. Li, L. Zhou, Q.-D. Ou, C. Li, Y. Li, J.-X. Tang, *Adv. Mater.* **10**, 664-671 (2014)

[2] J. Fischer, *Bachelor thesis, Physik-Department TU München*, (2015)

## 4.2 In operando morphology investigation of inverted P3HT:PCBM solar cells by GISAXS

W. Wang, C. J. Schaffer, L. Song, V. Körstgens, S. Pröllner<sup>1</sup>, E. D. Indari, T. Wang, A. Abdelsamie, S. Bernstorff<sup>2</sup>, P. Müller-Buschbaum

<sup>1</sup> MSE, Garching, Germany

<sup>2</sup> Elettra-Sincrotrone Trieste, Basovizza, Italy

Solar power as a renewable energy source has received great attention over last decades. It is abundant, clean, and free, and is becoming as important as conventional fossil fuels. Nowadays, photovoltaic devices have been integrated into daily life. Most photovoltaic products are based on silicon, which possess very high power conversion efficiency of over 15% for the commercial modules and over 25% for the laboratory cells. However, silicon solar cells have the limitations in the application for flexibility, light weight and semi-transparency. Thus, organic solar cells (OSCs) have emerged as another branch of photovoltaic devices due to their unique properties like flexible and easiness of manufacture. With massive research on OSCs in the last years, the efficiencies of OSCs have been pushed over 10%. Nevertheless, short lifetimes are the major obstacle for the commercial breakthrough. Therefore, solutions for enhancing the stability of OSCs are an urgent demand.

Poly(3-hexylthiophene-2,5-diyl) (P3HT): phenyl-C61-butyric acid methyl ester (PCBM) organic solar cells are one of the most mature systems in OSCs. They are frequently used to explore the structure-performance correlations. Standard geometry is commonly utilized, where the electrons flow from PCBM to the top electrodes and the holes transport from P3HT to the bottom electrodes. Previous work has demonstrated that the degradation of standard P3HT:PCBM solar cells is mainly caused by the morphological degradation. [1] In present work, we fabricated inverted P3HT:PCBM solar cells which collect the electrons and holes in an opposite directions as compared to the standard geometry. In order to make comparison with the standard solar cells, the active layer of the inverted device was prepared following the same route as detailed in reference [2].

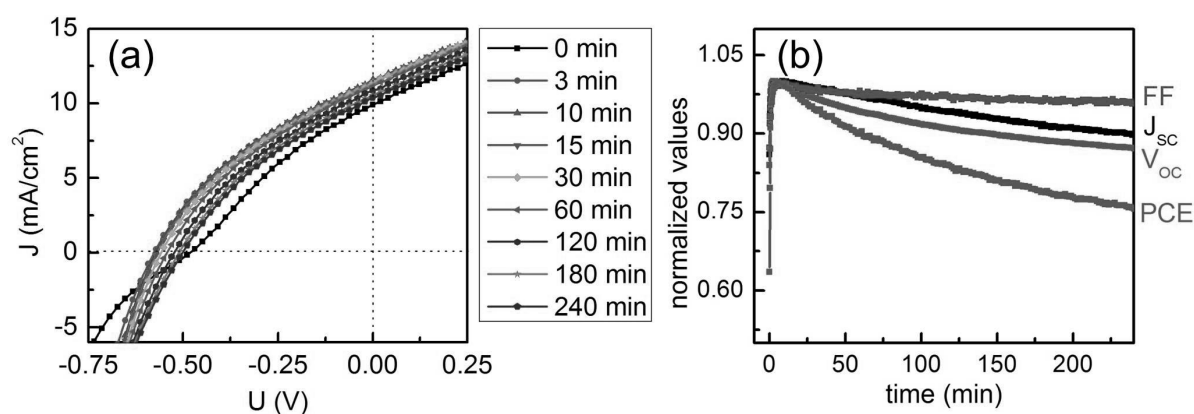


Figure 4.3:

a) J-V curves of inverted P3HT:PCBM solar cells with different illumination time recorded every 16 seconds until 240 min. Only the J-V curves are recorded at the same time as the GISAXS measurements are selected for illustration (0 min, 3 min, 10 min, 15 min, 30 min, 60 min, 120 min, 180 min and 240 min). b) Time evolution of normalized photovoltaic parameters.

We found that the inverted P3HT:PCBM solar cells are more stable than the standard devices. To understand the reason behind the better stability, the correlation between the morphological

evolution and the change of the solar cell performance during continuous operation under illumination is explored. In operando GISAXS measurements are carried out. J-V sweeps of the device are recorded simultaneously to the GISAXS study as shown in Fig. 4.3a. The initial curve (0 min) exhibits an S-shape, and displays the smallest short circuit current ( $J_{sc}$ ) and open circuit voltage ( $V_{oc}$ ) as compared to all the other measurements. Afterwards, the J-V curves transits towards a more rectangle-like-shape, suggesting a self-healing process. Performance decay is observed after 10 min. Surprisingly, the power conversion efficiency (PCE) of the inverted solar cell is preserved to 75% as compared to its maximum value after 240 min continuous operations, which is roughly 10% increase as compared to the standard solar cell. In order to clearly illustrate the contributions of  $J_{sc}$ ,  $V_{oc}$  and fill factor (FF) to the decay of PCE, each parameter is extracted from J-V measurement and normalized to their maximum values, as depicted in Fig. 4.3b. The  $V_{oc}$  and FF follows the same trend as in standard solar cell, whereas the  $J_{sc}$  shows around 10% enhancement after 240 min of operation. Therefore, the improvement of the PCE stability mainly benefits from the stabilization of  $J_{sc}$ .

The in operando GISAXS measurements give the morphological evidence for this device stability. By analyzing the vertical and horizontal line cuts of the in operando 2D GISAXS data, it is revealed that the P3HT:PCBM active layer in an inverted solar cell maintains a stable morphology during the device operation (Fig. 4.4a and b). In contrast, in a standard solar cell P3HT domains increase in size along with illumination time, regarded as morphological degradation and responsible for the efficiency decay. Therefore, the stabilization of the P3HT:PCBM layer with an inverted geometry is directly correlated to the improved stability of the  $J_{sc}$  and PCE as seen in our study for the first time.

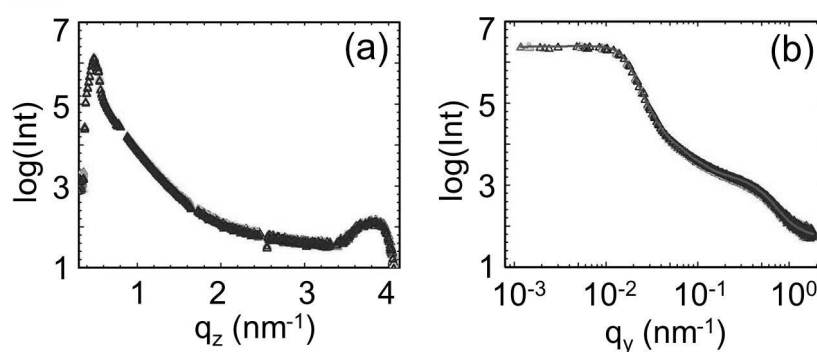


Figure 4.4:

a) Vertical and b) horizontal line cuts obtained from 2D GISAXS data. In order to visualize the differences in the line cuts as a function of operation time, all the vertical or horizontal line cuts are plotted on top of each other. All the horizontal line cuts can be fitted with the same curve shown as a line in b).

In summary, the inverted P3HT:PCBM solar cells show high stability as compared to its standard geometry. By performing in operando GISAXS measurements, we attribute the enhanced stability to a stable morphology of active layer during continuous operation.

The images and contents are adapted from W. Wang et al., *J. Mater. Chem. A* 3, 8324 (2015) with permission from the Royal Society of Chemistry.

- [1] C. J. Schaffer, C. M. Palumbiny, M. A. Niedermeier, C. Jendrzewski, G. Santoro, S. V. Roth, P. Müller-Buschbaum, *Adv. Mater.* **25**, 6760-6764 (2013)
- [2] W. Wang, C. J. Schaffer, L. Song, V. Körstgens, S. Pröllner, E. D. Indari, T. Wang, A. Abdelsamie, S. Bernstorff, P. Müller-Buschbaum, *J. Mater. Chem. A* **3**, 8324-8331 (2015)

### 4.3 Printing high efficiency solar cells

D. Yang, W. Wang, P. Müller-Buschbaum

Nowadays renewable energies are one of the most important components of the global new energy strategy. Among them, biomass, wind power, solar energy and fuel cells are the most promising resources. Furthermore, the power of the sun is supposed to one of the most viable ways to solve the foreseeable world's energy crisis. Therefore, photovoltaic (PV) technology becomes the object of a steadily growing interest from both academy and industry. Meanwhile semiconducting organic materials have established themselves as a new class of materials for PV technology besides the very well developed silicon based PV devices. Particular interest in these new materials arises from the fact that they can be solution processed and cheap. As a consequence, large scale production will become possible with a very low payback time of the PV devices. In addition, the mechanical flexibility of organic materials makes a variety of new applications feasible, e.g. PV modules can be realized on three-dimensionally shaped surfaces or as solar fibers. To date, the most successful polymer solar cell is based on the bulk heterojunction (BHJ) architecture, where an electron donating polymer and an electron acceptor (usually fullerene derivative) are mixed together to form nanoscale phase separation with a bicontinuous interpenetrating network morphology within the active layer of the PV device. However, a further increase in the power conversion efficiency (PCE) of polymer-based single junction PV devices might be still necessary. To understand the structure-function relationship of organic solar cells is challenging because the performance of these solar cells is determined by many factors such as the active layer materials, the device morphology and the interfacial energy level alignment. The future development of this technology will require significant advances in both, material synthesis and device design, to enhance the efficiency for enabling commercial applications [1-3].

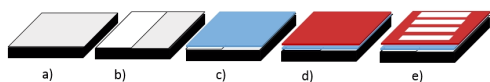


Figure 4.5:

Schematic representation of the main steps during organic solar cell preparation: a) ITO substrate as received, b) patterned ITO substrate, c) with the blocking layer PEDOT: PSS, d) after deposition of the active layer and e) the entire organic solar cell with the top electrode.

Today the perhaps best studied model system for organic solar cells consists of active layers composed out of poly(3-hexylthiophene-2,5-diyl) (P3HT) and phenyl-C61-butyric acid methyl ester (PCBM). A very simple solar cell layout comprises already several individual layers: indium tin oxide (ITO)/poly(3,4-ethylenedioxythiophene): poly(styrenesulfonate) (PEDOT: PSS)/P3HT: PCBM/Al [4]. Thus, for the solar cell preparation the deposition of these layers is required. Typically, the basics steps involved are at first to prepared a blended solution of P3HT and PCBM (e.g. at a weight ratio of 1: 1) in chlorobenzene. Frequently, indium tin oxide (ITO) coated glass slides are selected as transparent substrates (see Fig. 4.5 a). In the etching process, the ITO substrates partly were covered with an adhesive tape. The uncovered parts were coated with a mixture of zinc powder and water. Hydrochloric acid was dripped on the zinc paste and the ITO was etched away (Fig. 4.5 b). The substrate was subsequently rinsed with deionized water. The successful removal of the ITO was checked by measuring the resistance of the substrate surface with an ohmmeter. In the following procedure, the ITO substrates were cleaned with an alconox solution, ethanol, acetone and isopropanol. The substrates were immersed into each solvent separately and put into an ultrasonic bath for 10 min. Afterwards the substrates were rinsed with the same solvent and blown dry with dry, oil-free nitrogen. After the final drying, the substrates which were used for solar cell preparation were treated with oxygen plasma at a power of 240 W. The pressure was set to 0.1 mbar and the working pressure to 0.4 mbar. Later, a thin layer of PEDOT: PSS was spin cast (3000 rpm for 60 s) as an electron blocking layer on top of the ITO (Fig. 4.5 c). For further drying, the PEDOT: PSS layer was thermally annealed on a hot-plate at 150 °C for 10 min in air. When the substrates were completely cold, the active layer of P3HT: PCBM was spin cast at 2000 rpm for 30s (Fig. 4.5 d). In the end, the top electrode material, aluminum, was thermally evaporated onto the active

layer (Fig. 4.5 e). As a final step the solar cells were thermally annealed at 140 °C for 10 min in nitrogen atmosphere to avoid degradation.

Using such very simple procedure for standard device geometry in the measured J–V characteristics we usually achieve efficiencies of all solar cells which are larger than 3.0%. In case of the particular test samples the highest efficiency is about 3.26%.

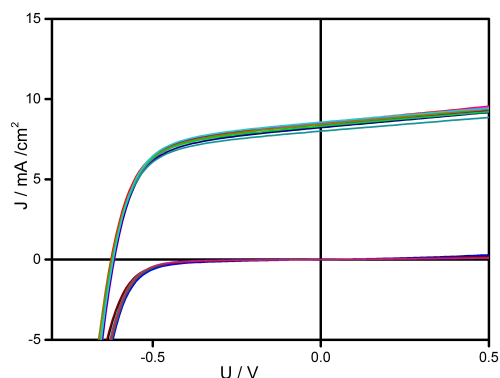


Figure 4.6:  
Example of eight J-V curves of P3HT:PCBM based solar cells prepared with spin coating of the active layer. Different curves are shown with individual colors.

In Fig. 4.6 the example of the J-V curves of eight P3HT:PCBM based solar cells are shown, which were prepared in one batch on individual substrates. The related characteristic parameters are shown in Fig. 4.7 and demonstrate a rather moderate spread of the device characteristics.

	$J_{sc} / \text{mA} / \text{cm}^2$	$V_{oc} / \text{V}$	FF / %	PCE / %
Solar cell 1	8.42	0.60	63.5	3.21
Solar cell 2	8.54	0.60	62.6	3.23
Solar cell 3	8.48	0.59	62.7	3.15
Solar cell 4	8.23	0.60	63.2	3.10
Solar cell 5	8.56	0.6	63.6	3.26
Solar cell 6	8.43	0.60	62.8	3.20
Solar cell 7	8.00	0.60	63.7	3.05
Solar cell 8	8.31	0.60	63.7	3.17

Figure 4.7:  
Characteristic parameters of solar cells devices: short circuit current ( $J_{sc}$ ), open circuit voltage ( $V_{oc}$ ), fill factor (FF) and PCE.

In a next step to printed solar cells, the active layer will be deposited by printing instead of spin coating. In such approach all the steps to assemble a solar cell as described above can be maintained, despite the change in the deposition method for the active layer. As all involved morphologies are typically non-equilibrium morphologies, the change in the deposition method from spin coating to printing will strongly affect the morphology and in turn also the device performance. Such changes can be easily probed with advanced scattering techniques as for example grazing incidence small angle x-ray scattering (GISAXS) and grazing incidence wide angle x-ray scattering (GIWAXS). To achieve fully printed organic solar cells, all individual layers need to be printed, not only the active layer. Thus, the typically used ITO needs to be replaced with printable bottom electrode materials. Again, changes of the film morphology have to be expected as for example the surface topology of underlying layers can influence the nanostructure of the active layer. The possibility to control the morphology in active layers is a key to improve organic solar cell performance. Thus, insights gained for spin cast film devices will only be of very limited benefit for the understanding of printed solar cells. However, printing techniques hold a very promising future for thin organic film devices [5,6].

- [1] H. Azimi, Y. Hou, C. J. Brabec, *Energy Environ. Sci.* **7**, 1829-1849 (2014)
- [2] T. Ameri, N Li, C. J. Brabec, *Energy Environ. Sci.* **6**, 2390-2413 (2013)
- [3] T. Ameri, G. Dennler, C. Lungenschmied, C. J. Brabec, *Energy Environ. Sci.* **2**, 347-363 (2009)
- [4] M. T. Dang, L. Hirsch, G. Wantz, *Adv. Mater.* **23**, 3597–3602 (2011)
- [5] S. Pröllner, F. Liu, C. H. Zhu, C. Wang, T. P. Russell, A. Hexemer, P. Müller-Buschbaum, E. M. Herzig, *Adv. Energy. Mater.* **6**, 1501580 (2016)
- [6] C. M. Palumbiny, F. Liu, T. P. Russell, A. Hexemer, C. Wang, P. Müller-Buschbaum, *Adv. Mater.* **27**, 3391-3397 (2015)

#### 4.4 Light absorption and inner morphology of the active layer: Influence of blend ratio of bulk heterojunction organic solar cells

E. Barabino, W. Wang, P. Müller-Buschbaum

Efficiencies of organic solar cells (OSC) broke 10% edge in bulk heterojunction (BHJ) morphology employing the low band gap polymer PTB7-Th (donor) and fullerene derivative PC<sub>71</sub>BM (acceptor) blended as active layer [1]. In OSC, the light is absorbed in the active layer resulting in the creation of an excited electron-hole pair, called exciton. In order to collect the external current, the exciton needs to be separated by the difference in working function between the two materials. This offset in potential occurs at the interface of polymer-fullerene rich domains. When the charge carriers are unbound, the electron is transported through the acceptor material, while the hole travels in the donor. The current is harvested if the intermixed materials form, via self-assembling, percolation pathways towards respective electrode. Aim of this work is to correlate light absorption properties to the performances of solar cells with five different polymer:fullerene blend ratios. From literature a best performing solar cell was reported for a blend ratio of 1:1.5 with a total concentration of 25 mg/ml [2]. To achieve that, the concentration of PTB7-Th is kept at 10 mg/ml for all the samples, while 5, 10, 15, 20, 25 mg/ml of PC<sub>71</sub>BM are added, resulting in the ratios: 1:0.5, 1:1, 1:1.5, 1:2 and 1:2.5.

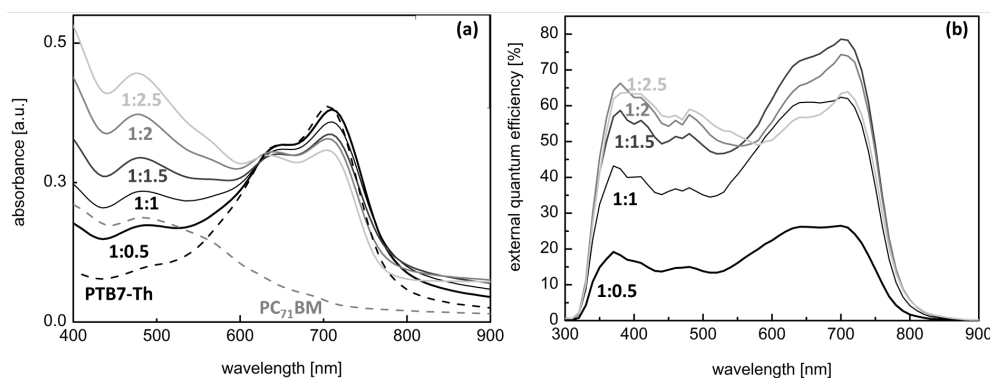


Figure 4.8:

a) UV-Vis absorbance for the five blend ratios and the pure materials. b) EQE measurements of five different photovoltaic devices employing the five different blend ratios.

UV-Vis spectroscopy is utilized to gain information about light absorption of different samples. The results are shown in Fig. 4.8a. With increasing content of PC<sub>71</sub>BM, the absorption of light with wavelengths in the range from 400 to about 530 nm is clearly increased, in accordance with the absorbance spectrum of pure PC<sub>71</sub>BM. For wavelengths in the range from 530 to 800 nm, a higher percentage of PTB7-Th corresponds to higher absorbance, in agreement with the pure polymer curve. In fact, low band gap polymers have the peculiarity to extend light absorption toward infrared region, taking advantage from a broad solar radiance spectrum.

In order to discriminate the optimized solar cell among different blend ratios, photovoltaic devices are fabricated and tested via external quantum efficiency (EQE) and *J-V* curves characterizations. The solar cells are realized in inverted geometry: Above cleaned FTO coated substrates which provide as front electrodes, a titanium oxide (TiO<sub>2</sub>) layer is deposited with hole blocking function. Above the active layers with different blend ratios are spin coated. Subsequently, a thin layer of molybdenum oxide (MoO<sub>3</sub>) is thermally evaporated as electron blocking layer before gold back electrode deposition.

In EQE measurement, the solar cell is illuminated under preset light spectrum with sweeping wavelength and the correspondent photo-generated current is recorded in function of the in-

coming light wavelengths. The integration of the EQE curves, gives the short circuit current density ( $J_{SC}$ ) harvested by the solar cell. Fig. 4.8b shows the results for our systems. In agreement with the absorption characterization, an increased response with increasing PC<sub>71</sub>BM content is evident in the range from 350 to about 530 nm. Whereas, in the range from 530 to 800 nm, where PTB7-Th shows high absorption, the signal is not directly related to the polymer percentage. The ratios 1:0.5 and 1:1 show reduced EQE in the range from 530 to 800 nm, despite the higher absorption in this interval. This is due to the fact that the charges need to be collected at the electrodes, traveling through percolation pathways in the donor and acceptor materials. Therefore, low EQE signal together with high light absorption indicates the poor phase separation between the two materials. The ratio 1:1.5 presents the best EQE signal, while the 1:2 and 1:2.5 decrease in accordance with reduced light absorption. Finally,  $J_{SC}$  values derived from EQE are shown in Fig. 4.9a as square symbols, presenting the highest result for the ratio 1:1.5.

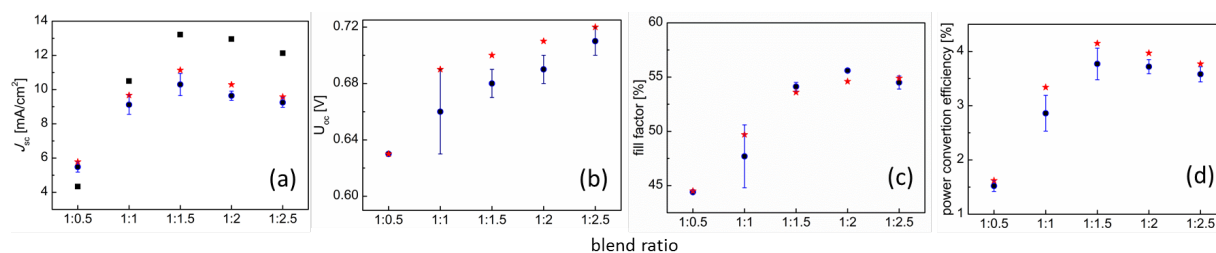


Figure 4.9:

Photovoltaic parameters: average values (dots) and best device value (star). a) Short circuit current density also shows the EQE value (squares), b) open circuit voltage, c) fill factor and (d) power conversion efficiency.

The  $J$ - $V$  curves of solar cells with different PTB7-Th: PC<sub>71</sub>BM ratio are probed under simulated solar light AM1.5, from which  $J_{SC}$ , open circuit voltage ( $V_{OC}$ ), fill factor (FF) and power conversion efficiency (PCE) are calculated. The results are presented in Fig. 4.9a-d respectively: the average values depicted as dots with their maximal value as stars. The  $J_{SC}$  increases steeply up to the ratio of 1:1.5 and then decreases slightly, in good agreement with the trend as observed in EQE. Discrepancies in the absolute values are explained to be due to different light intensity in the two measurements (lower for EQE). Moreover, the simulated solar spectrum does not correspond to constant intensity for all the wavelengths as the one employed in EQE. The  $V_{OC}$ , on the other hand, increases with increasing PC<sub>71</sub>BM content. The same behavior is explained in reference [2]. Higher PC<sub>71</sub>BM percentage leads to reduced energy disorder. Therefore, the energy levels between the donor and acceptor materials are more neat, providing better exciton separation and resulting in higher  $V_{OC}$ . The FF is index of low recombination between separated charge carriers. It reaches high values up to the ratio 1:1.5, evidence of efficient charge extraction. The measured overall PCE confirms the above illustrated best results for the ratio of 1:1.5 (4.15%). In conclusion, in BHJ solar cells power extraction derives from the balanced interplay between high light absorption and formation of suitable pathways for charges transport in the active layer. For PTB7-Th:PC<sub>71</sub>BM system, the blend ratio of 1:1.5 is found to provide the highest  $J_{SC}$  and PCE, respect to the other tested ratios. The success of this ratio arises from a high value of absorbance (but not the highest) over the whole tested spectrum. In addition, the highest EQE signal in the range from 530 to 800 nm indicates that charge carriers travel through the active layer and are efficiently collected by respective electrodes.

[1] S. Liao, H. Jhuo, Y. Cheng, S. Chen, *Adv. Mater.* **26**, 4766-4771 (2013)

[2] Z. He, B. Xiao, F. Liu, H. Wu, Y. Yang, S. Xiao, C. Wang, T. P. Russell, Y. Cao, *Nat. Photonics* **9**, 174-179 (2015)

## 4.5 Characterization of thiophene-selenophene-tellurophene copolymer thin films for OPV applications

F. Dreher, D. Moseguí González, G. He<sup>1</sup>, E. Rivard<sup>1</sup>, P. Müller-Buschbaum

<sup>1</sup> Department of Chemistry, University of Alberta, Alberta, Canada

Organic photovoltaic (OPV) devices are promising candidates to deal with the future energy supply due to several advantages over their inorganic counterparts such as semi-transparency, flexibility, light-weight, and low production costs. The so-called bulk heterojunction (BHJ) is one of the most investigated architectures of organic solar cells as it gives rise to high efficiencies. [1]

Due to the fact that the arrangement and typical length scales of the donor and the acceptor phases within the bulk heterojunction mainly limits the exciton splitting efficiency, the attainment of an optimized morphology of the active layer is of capital importance for the performance of the final OPV devices.

One novel approach for improving the morphology the exciton lifetime is achieved by increasing the intersystem crossing for the excitons. Thereby, the singlet excitons switch to the triplet state through a spin flip. As a consequence the probability of radiative recombination in the device is lowered, which in turn yield longer exciton lifetimes. As a consequence, the performance of the solar cells is improved without affecting the film morphology. One example is a study on poly(3-hexylthiophene):[6,6]-phenyl-C60-butyric acid methyl ester (P3HT:PCBM) doped with  $Fe_3O_4$  nanoparticles (NPs). The presence of the nanoparticles relaxes the spin selection rules by the incremented spin-orbit coupling in the vicinity of the NPs and therefore increases the probability for intersystem crossing in the films. [2] Theoretically, the same effect can be achieved with polymers which exhibit heavy elements embedded in the monomers. In this respect a new thiophene-selenophene-tellurophene copolymer is investigated. The present study aims on a general characterization. [3]

We study the influence of the annealing temperature on the copolymer. Films were prepared with spin coating on cleaned glass substrates. Subsequently the films were annealed in a glove box in nitrogen atmosphere from room temperature (20 °C) up to 140 °C in 10 °C steps. With UV/VIS spectroscopy and X-ray reflectivity measurements the absorbance and film thickness were probed.

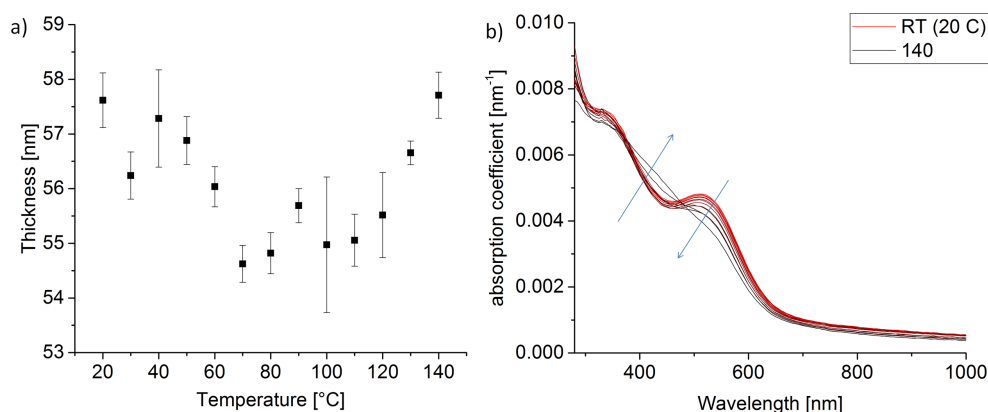


Figure 4.10:

a) Evolution of the film thickness for different annealing temperatures from 20 °C to 140 °C in 10 °C steps measured with X-ray reflectivity. b) Absorption coefficient spectra measured for different annealing temperatures from 20 °C (red curve) to 140 °C (black curve) in 10 °C steps with UV/VIS. The temperature dependence is shown with the color-code using in a red-black gradient.

Fig. 4.10 shows the evolution of the film thickness and the absorption coefficient as a function of the annealing temperature. The thickness decreases monotonously until it reaches a minimum at around 80 °C. At higher temperatures the thickness increases back to the original starting value. The absorption coefficients (Fig. 4.10 b) are analyzed by fitting the data with 3 Gaussian distribution functions. Their centers are located at 320 nm, 415 nm and 530 nm.

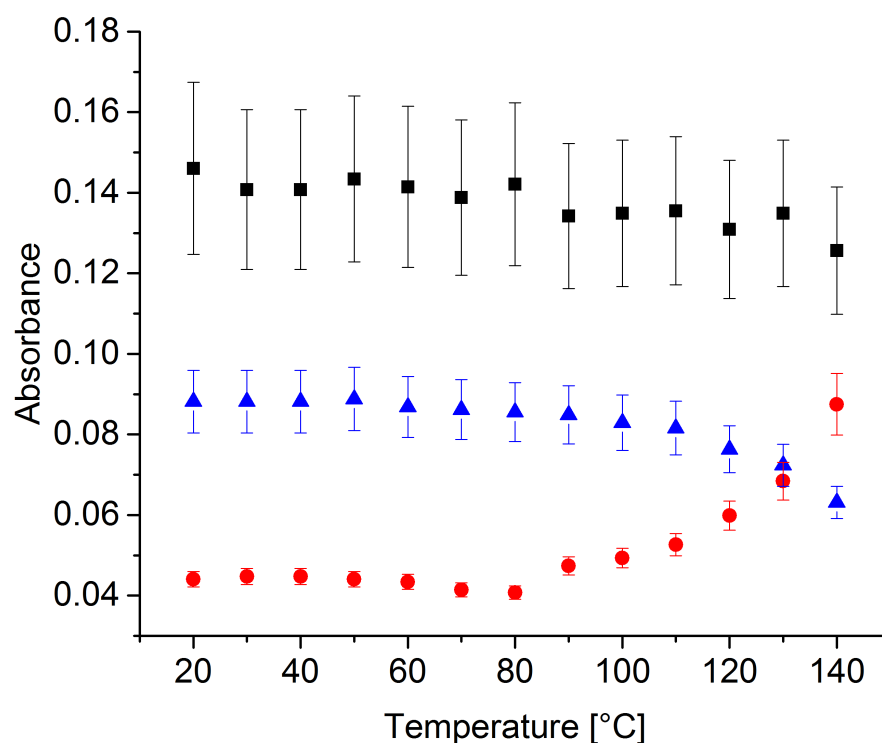


Figure 4.11:  
Temperature dependence of the three contributions identified in the absorbance spectra positioned at 320 nm (black), 415 nm (red) and 530 nm (blue).

The temperature dependence of the intensities of the 3 peaks is shown in Fig. (4.11). The contribution of the peak at 320 nm remains basically unchanged with temperature. In contrast, the intensity of the peak at 415 nm increases at 80 °C, whereas that of the peak at 530 nm decreases at the same temperature. Thus, both peaks change their intensity at the same temperature at which the film thickness exhibits its minimum. We assume, that crystal transitions are possible at 80 °C and cause the changes in the vibronic peaks as well as the film thickness.

The presented investigations give a first insight in the behavior of the thiophene-selenophene-tellurophene copolymer films. The comprehensive characterization aims for a fundamental understanding of a promising material for future organic electronic applications.

- [1] G. Yu, J. Gao, J. C. Hummelen, F. Wudl, A. J. Heeger, *Science* **270**, 1789 (1995)
- [2] D. Moseguí González, V. Körstgens, Y. Yao, L. Song, G. Santoro, S. V. Roth, P. Müller-Buschbaum, *Adv. Energy Mater.* **5**, 1401770 (2015)
- [3] G. He, L. Kang, W. Torres Delgado, O. Shynkaruk, M. J. Ferguson, R. McDonald, E. Rivard, *J. Am. Chem. Soc.* **135**, 14 (2013)

#### 4.6 Degradation in printed polymer:fullerene thin films as active layers for organic photovoltaic devices

J. R. Stockhausen, C. J. Schaffer, P. Müller-Buschbaum

Clean and renewable energy sources gain more and more importance. Among them, solar energy has the largest growth potential. In comparison to conventional silicon solar cells, organic photovoltaics (OPVs) offer several advantages, like cheap and energy-saving production or the possibility to produce flexible, transparent and portable solar cells. Nevertheless, their efficiency is below that of conventional solar cells. Up to now, OPVs reached a maximum efficiency of over 10 % for the champion solar cells in laboratory device scale [1]. However, a further increase in device efficiency might be realistic due to the ongoing improvement in tailoring the applied polymer materials. Beside the overall efficiency another challenge for the research of OPVs exists in the fast device degradation, which lowers the efficiency with time. In comparison to silicon solar cells fast degradation occurs. Hence, the lifetime needs to be prolonged, so that a profitable large-scale production becomes feasible. Therefore, a detailed understanding of the degradation mechanisms is necessary. The possibility of printing OPVs enables large-scale fabrication, e.g. by roll-to-roll printing, in contrast to laboratory-scale techniques, such as spin-coating. So far, a lot of research has been focusing on OPV devices produced by spin-coating. Less research was addressing printed films. The morphology of the active layer will likely be affected by the preparation process, e. g. printed and spin-coated films will have different morphologies. As a consequence, it is not clear how the method of film application affects the aging behavior. In the present investigation, we address UV and visible light induced aging of P3HT:PCBM active layers, printed with a home-made positive shim mask slot dye coater. This printing machine was constructed by S. Günther in the context of his master thesis. More information about the working principle and the manual can be found in his thesis [2]. For the degradation experiments, six irradiation chambers were built. One of these chambers is shown in Fig. 4.12. Each one allows the irradiation of one printed sample with a certain wavelength in the visible or UV range. It is equipped with a water cooling system to control the temperature and a gas exchange system, that allows the degradation exposition in different atmospheres. Changes in the morphology of the films due to accelerated aging are investigated by means of atomic force microscopy (AFM), X-ray reflectivity (XRR) and UV/Visible light spectroscopy (UV/Vis).

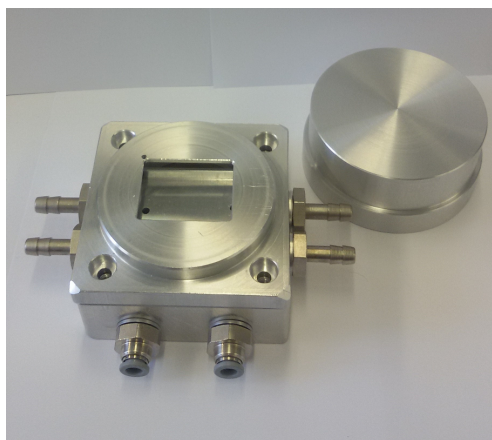


Figure 4.12:  
Example of the irradiation chambers with the connectors for the water cooling and the gas exchange on the left. The illumination source is integrated in the cap at the right.

Additionally, the influence of different printing heights and printing solution concentrations on film thickness and homogeneity was investigated. The aim is to find the right combination of printing parameters, which enable the fabrication of homogenous films with a thickness between 200 nm and 300 nm[3]. Such active layer thickness is expected to allow for solar cells with

optimum efficiency. As displayed in Fig. 4.13, the film thickness shows a linear dependence on the printing height. In accordance to that, the absorption spectra show an increase of the absorbance with the printing height (see Fig. 4.14). However, the film homogeneity increases for decreasing printing heights. Thus, by the variation of the printing solution concentrations at the lowest practicable printing height, the optimum concentration will be calculated, as the film thickness has a linear relation to the concentration.

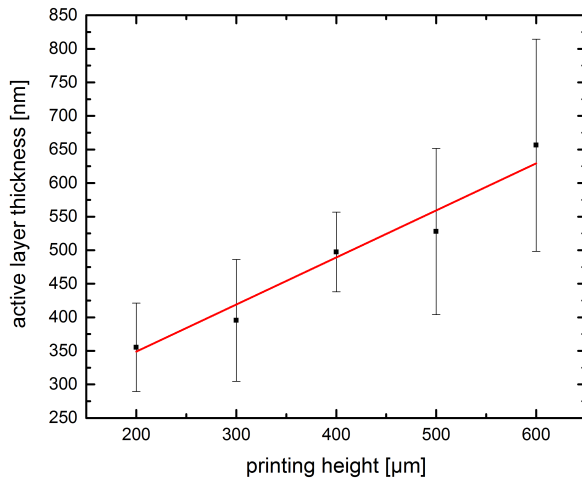


Figure 4.13: Active layer thickness versus printing height. The red line indicates the linear fit to the data with a slope of  $0.701 \pm 0.079$ . Because of the high variation of the film thickness within the films, the error bars are large in this graph.

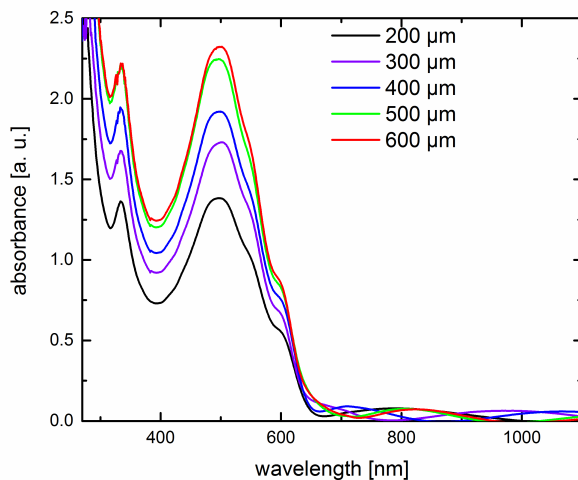


Figure 4.14: Increase in absorbance with printing height due to an increase in the film thicknesses

In the following experiments, reproducible and homogenous films will be printed with the optimum thickness as determined before. These active layer films will be exposed to the radiation of different wavelengths in the UV chambers under a defined atmosphere, such as e. g. nitrogen atmosphere. The impact of the radiation induced degradation will be analyzed as a function of irradiation time and wavelength. Changes in the absorbance will be probed as well as changes in the film morphology or film thickness.

- [1] Chen, Jing-De, C. Cui, Y.-Q. Li, Q.-D. Ou, C. Li, Y. Li, J.-X. Tang, *Adv. Mater.* **27**, 1035-1041 (2015)
- [2] S. Günther, master thesis, *Physik-Department TU München* (2014)
- [3] A. J. Moulé, J. B. Bonekamp, K. Meerholz, *J. App. Phys.* **9**, 094503 (2006)

#### 4.7 Effect of solvent additives on the morphology and stability of polymer-fullerene blend thin films for organic photovoltaics

C. J. Schaffer, J. Schlipf, B. Su, E. D. Indari, S. Bernstorff<sup>1</sup>, P. Müller-Buschbaum

<sup>1</sup> Elettra-Sincrotrone Trieste, Basovizza, Italy

Since the power conversion efficiency of polymer-fullerene bulk-heterojunction solar cells by now exceed the milestone of 10 % [1], long-term stability remains the last unsolved issue that hinders a launch of organic photovoltaics (OPVs). This technology could, however, open a large field of application and cost-effective generation of electricity due to their fundamental advantages as compared to conventional Si-based PV. Among these advantages are the mechanical flexibility, the low production cost at a large-scale processability as well as their optical tunability, which even allows for semitransparent photovoltaic modules.

The stabilization of OPV, however, rises a challenge to be overcome. In order to extend OPV lifetimes, which are typically on the order of a few thousand operation hours, all degradation mechanisms must be well understood first. These include, among others, (photo) oxidation, contact oxidation and delamination or the diffusion of impurities. Last but not least, it has been evidenced in our earlier work that the bulk-heterojunction morphology is not necessarily stable [2]. Morphological changes in the bulk-heterojunction thereby drive device degradation which is referred to as morphological degradation. Novel approaches towards highly efficient polymer-fullerene solar cells use solvent additives to tune the morphology of the bulk-heterojunction for enhancing photovoltaic efficiencies [3]. However, the immediate question arises if this optimization is morphologically stable. Therefore, we aim to investigate the morphological stability of PCPDTBT : PC<sub>70</sub>BM thin films processed with and without 1,8-octanedithiol (ODT) as solvent additive. As a first step, the influence of solvent additive to the bulk-heterojunction morphology of the blend system has been thoroughly investigated. The complete study is published in reference [4].

Fig. 4.15 shows GIWAXS patterns of PCPDTBT : PC<sub>70</sub>BM films with different film compositions processed with and without ODT. The data reveal that ODT increases the polymer crystallinity which is indicated by the scattering reflex at  $q_z \approx 5.5 \text{ nm}^{-1}$ .

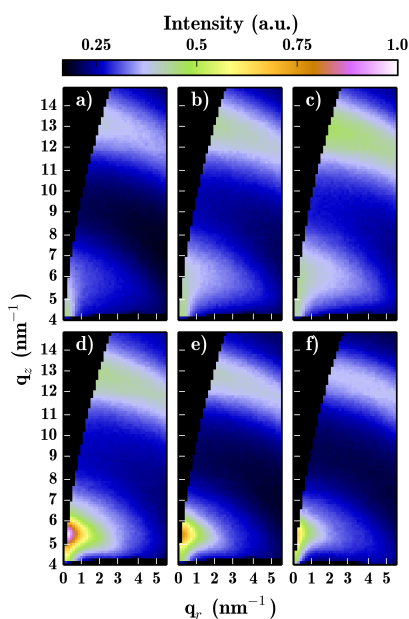


Figure 4.15:

GIWAXS patterns of PCPDTBT : PC<sub>70</sub>BM thin films with different film compositions. (a,d: 1:1.5, b,e: 1:2.0, c,f: 1:2.7). a)-c) represent GIWAXS patterns of films processed without the use of ODT, d)-f) corresponds to the films processed with the use of 3 vol% ODT in CB as solvent. All data are mapped to a  $q_r$ - $q_z$  representation using GIXSGUI [5]. The figure is taken from the original ACS Author-Choice open access publication [4].

As a consequence of polymer crystallization, a generally enhanced phase separation is found in films with ODT (based on GISAXS investigations, not shown here [4]). This phase separation is

probably caused by a reduction of the solubility limit of fullerene in the polymer matrix which is induced by the presence of ODT. As a result, excess fullerene molecules are pushed to the film surface while the composition of the main blend layer becomes independent of the mixing ratio, as evidenced by X-ray reflectivity measurements ([4], not shown here). As a summary, the use of 3 vol% ODT as solvent additive in chlorobenzene leads to enhanced phase separation of the polymer and fullerene moieties. The phase separation is accompanied by improved polymer crystallization and the formation of a partially covered, rough fullerene-topping. In the case of PCPDTBT : PC<sub>70</sub>BM the morphological coarsening due to the use of solvent additive leads to the formation of percolating pathways for charge carriers in the film. The enhanced crystallinity gives rise to a better charge carrier transport while the forming fullerene-rich topping acts as a built-in electron-blocking layer. These effects are summed up and illustrated in Fig. 4.16. All these effects lead to improvement of the photovoltaic efficiency.

First UV/Visible-light absorption spectrographs (see Fig. 4.17) have shown that on a timescale of several weeks, the absorption spectrum of PCPDTBT : PC<sub>70</sub>BM films transits from its original state towards the one without ODT. This implies that the polymer crystallinity decreases over time. We suggest that this mechanism provides a new pathway of morphological degradation that can occur in OPV fabricated with use of solvent additives. However, a detailed study is due and topic of our current research.

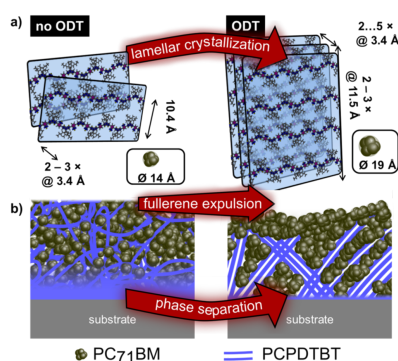


Figure 4.16:

The mechanism of bulk-heterojunction morphology tuning using ODT as solvent additive. a) ODT increases the polymer crystallinity particularly along the lamellar stacking direction. b) With enhanced crystallinity comes an enhanced micro phase separation. Larger polymer domains form as the solubility limit of fullerene in the polymer matrix is lowered due to ODT. A fullerene-rich topping forms. The figure is taken from the original ACS AuthorChoice open access publication [4].

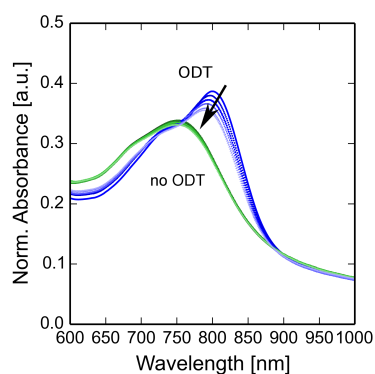


Figure 4.17:

UV-Vis spectra of a PCPDTBT : PC<sub>70</sub>BM films (1:2.7) processed with and without ODT after different times. The absorption spectrum of the film without ODT stays constant while the absorption peak around 800 nm vanishes with time. Both films were measured subsequently just after preparation and after 1, 2, 3 10 and 36 days.)

- [1] Z. He, C. Zhong, S. Su, M. Xu, H. Wu, and Y. Cao, *Nat. Photon.* **6**, 591-595 (2012).
- [2] C. J. Schaffer, C. M. Palumbiny, M. A. Niedermeier, C. Jendrzewski, G. Santoro, S. V. Roth, P. Müller-Buschbaum, *Adv. Mater.* **25**, 6760 - 6764 (2013).
- [3] J. Peet, J. Y. Kim, N. E. Coates, W. L. Ma, D. Moses, A. J. Heeger, G. C. Bazan, *Nat. Mater.* **6**, 497-500 (2007).
- [4] C. J. Schaffer, J. Schlipf, B. Su, E. D. Indari, S. Bernstorff, P. Müller-Buschbaum, *ACS Appl. Mater. Interfaces* **7**, 21347 - 21355 (2015).
- [5] Jiang, Z. *J. Appl. Crystallogr.* **48**, 443 - 448 (2015).

#### 4.8 In-situ tracking of crystalline evolution in P3HT:PCBM organic solar cells

D. Moseguí González, C. J. Schaffer, S. Pröller<sup>1</sup>, J. Schlipf, L. Song, S. Bernstorff<sup>2</sup>, E. M. Herzig<sup>1</sup>, P. Müller-Buschbaum

<sup>1</sup> MSE, TU München, Garching, Germany

<sup>2</sup> Elettra-Sincrotrone Trieste, Basovizza, Italy

Organic electronics features one of the currently most rapidly-growing research fields. In particular, organic photovoltaics is gaining its own space and reputation as a solid candidate for addressing the important problem of future energy supply. The many advantages they present in comparison to their inorganic correspondents, like light-weight, flexibility, semi-transparency and low energy and cost requirements for fabrication have opened a new dimension on the implementation possibilities of renewable energy generation devices.

Fully organic solar cells have already overcome the barrier of the 10 % efficiency, thus, becoming functional devices for applications in daily live [1]. However, compared to classic inorganic semiconductors, the more complex nature of the materials involved and the electronic and energetic picture of organic solar cells still hold some shadowed areas that are vaguely understood, feature that hinders the fundamental grasp of the physical mechanisms underlying the working principle of such devices.

One very common approach in the construction of organic solar cells consists of the mixture of two phases in the active layer. One type of donor and one type of acceptor molecules are mixed, forming a so-called bulk heterojunction (BHJ). The concept of BHJ was introduced about two decades ago featured a revolution in the efficiencies of organic solar cells [2]. The BHJ dramatically increases the interface area between donor and acceptor phases available for aiding the separation of photo-generated excitons. At the same time, the mixtures and their processing define parameters like aggregation or crystallinity, which subsequently will have a direct impact on device properties, like recombination or charge transport. Thus, the morphology of organic domains, their arrangement at the mesoscale, as well as their crystalline behavior are determining in the overall performance of organic solar devices.

Scattering techniques, especially those featuring grazing incidence geometry, have proven to be the approach of choice, when addressing morphology and crystallinity of thin films [3]. This, together with the high time resolution provided by the high X-ray fluxes of synchrotron radiation facilities has enabled in-situ scattering experiments, which allow for real time characterization [3]. In the present study, we will apply in-situ scattering experiments to follow the crystalline evolution of films being active layers of organic solar cells simultaneously to tracking the performance of the solar device with time.

In greater detail, the current-voltage characteristics of organic solar cells made of poly(3-hexylthiophene-2,5-diyl):phenyl-C<sub>60</sub>-butyric acid methyl ester (P3HT:PCBM) are monitored during operation at the same time that the evolution of the P3HT crystallinity is recorded with grazing incidence wide angle X-ray scattering (GIWAXS). Fig. 4.18 presents the evolution of the intensity and the anisotropy (depicted as a Full Width at Half Maximum) of the edge-oriented [100] P3HT crystalline family for approximately 5.5 h. It can be seen how generally the amount of crystalline material decreases with time, as well as the signal corresponding to the remaining crystalline grains continuously increase in its Full Width at Half Maximum (FWHM), indicating worse oriented crystals and, thereby, worse topologic and energetic pathways for the charge carriers to be transported.

Fig. 4.19 depicts the evolution of the solar cell parameters recorded in-situ during GIWAXS experiment. It can be seen how the efficiency of the studied solar cell decays as well with time, reaching the half of its initial value after approximately 2 hours (non-encapsulated devices). The decrease in efficiency is mainly driven by the decrease in short-circuit current density ( $J_{SC}$ ),

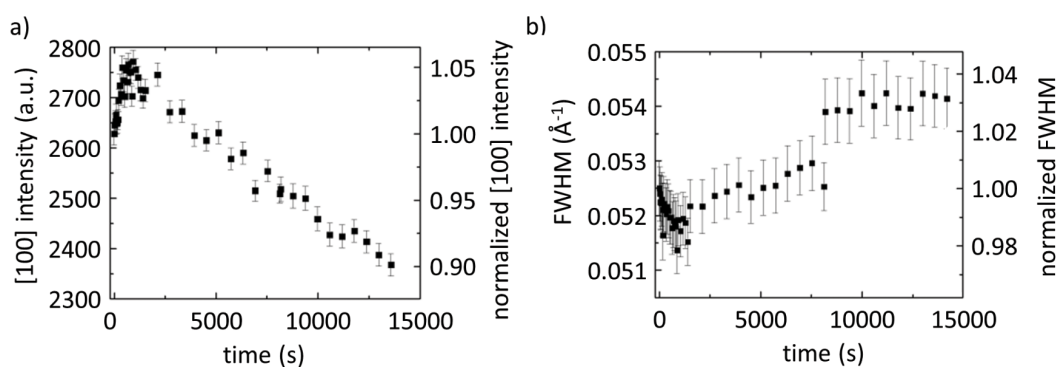


Figure 4.18:

Temporal evolution of the P3HT edge-on [100] crystalline family. As a function of time, a) the peak intensity and b) the peak center position are displayed. Left axes display the absolute values of the plotted quantities. Right axes represent the variations relative to the initial values.

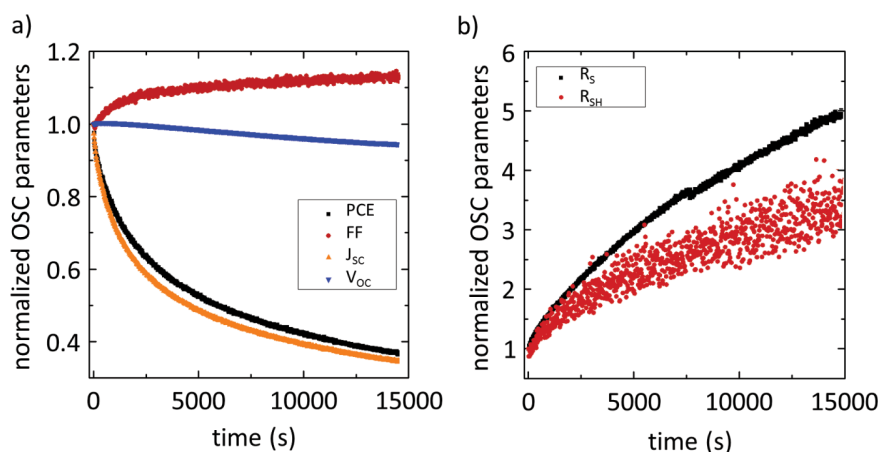


Figure 4.19:

Time evolution of a) power conversion efficiency (PCE), fill factor (FF), short-circuit-current density (JSC), open-circuit-voltage (VOC), b) series ( $R_S$ ) and shunt resistances ( $R_{SH}$ ). Ordinate axes represent the variations normalized to the initial values.

which is in a good agreement with the reduced crystallinity amount and anisotropy observed in GIWAXS. Moreover, a less efficient charge carried transport derived as well from a reduced crystallinity can be read from the increasing series resistance ( $R_S$ ) observed in Fig. 4.19b. In summary, this new approach of understanding the fundamental physical mechanisms governing the functioning of organic solar cells featuring time-resolved GIWAXS experiments provides a step further towards a comprehensive understanding of the physics behind novel organic solar cells.

- [1] M. A. Green, K. Emerzy, Y. Hishikawa, W. Warta, E. D. Dunlop, *Prog. Photovolt: Res. Appl.* **23(1)**, 1-9 (2015)
- [2] G. Yu, J. Gao, J. C. Hummeken, F. Wudl, A. J. Heeger, *Science* **270**, 1789 (1995)
- [3] P. Müller-Buschbaum, *Adv. Mater.* **26**, 7692-7709 (2014)

#### 4.9 Following the morphology formation in situ in printed active layers for organic solar cells

S. Pröllner<sup>1</sup>, F. Liu<sup>2,3</sup>, C. Zhu<sup>4</sup>, C. Wang<sup>4</sup>, T. P. Russell<sup>2,3</sup>, A. Hexemer<sup>4</sup>, P. Müller-Buschbaum, E. M. Herzig<sup>1</sup>

<sup>1</sup> MSE, TU München, Garching, Germany

<sup>2</sup> University of Massachusetts Amherst, Amherst, USA

<sup>3</sup> LBNL, MSD, Berkeley, USA

<sup>4</sup> LBNL, ALS, Berkeley, USA

Organic solar cells are a promising alternative to silicon based inorganic modules. Latter ones require more material for the same absorption and a high energy input for the production of the solar cell modules increasing the energy payback time magnificently. In organic solar cells, on the other hand, highly absorbing materials are used reducing the needed amount of materials. Furthermore, a key advantage of organic photoactive layers is the processability out of solution. Using this property opens the opportunity to produce the active layer of the solar cell via printing methods and allows for up-scaling to industrial-oriented scales which is not the case for laboratory techniques like spin coating. Thus, roll-to-roll processing on flexible substrates is the goal of production techniques for organic solar cells. Several methods of printing and coating techniques can be used to reach this goal, among others knife coating, slot-die coating, screen printing or spray coating.

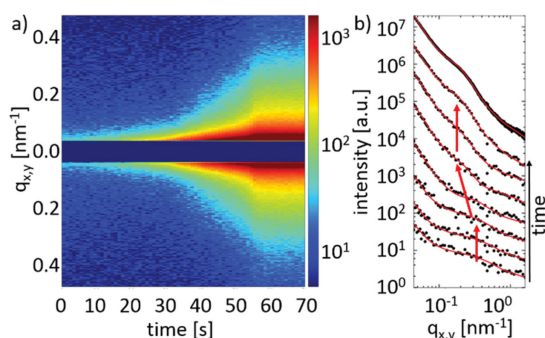


Figure 4.20:

Data of the GISAXS measurements performed at room temperature: a) Horizontal line cuts of the GISAXS data versus the time showing the structure evolution at  $q_{x,y} \approx 0.25\text{-}0.3 \text{ nm}^{-1}$ . b) Binned data obtained from the horizontal line cuts (black dots) for every 10 s from 0 to 60 s along with the respective modeled data (solid red lines), as well as the unbinned data obtained from the final film (top curve). The data are shifted along the intensity axis for clarity. From reference [4], reprinted with permission from WILEY-VCH Verlag GmbH & Co. KGaA, Weinheim.

However, the inner morphology has an enormous impact on the charge transport and therefore on the device performance. [1] Tuning and influencing the assembling of the materials in the organic thin film is still challenging and a better knowledge of the structure determining parameters is of utmost importance. Useful techniques for investigating the inner morphology of a thin organic active layer are grazing incidence wide and small angle X-ray scattering GIWAXS and GISAXS, respectively. [2] While there are investigations on the development of nanoscale morphology in polymer:fullerene photoactive layers during solvent casting [3], not much is known about the appropriate development in printed systems. We performed in situ GIWAXS and GISAXS measurements on slot-die printed photoactive blends of poly(3-hexylthiophene-2,5-diyl) and phenyl-C61-butyric acid methyl ester (P3HT:PCBM). The experiments were performed at the Advanced Light Source (ALS) at the Lawrence Berkeley National Laboratory in Berkeley, California, USA. From the GIWAXS pattern we obtain information on the polymer crystal development and see initially a strong scattering signal at  $q_y \approx 14 \text{ nm}^{-1}$ , which can be attributed to the evaporating solvent. With the decrease of the solvent signal, the characteristic (100) signal of the P3HT backbone spacing appears at  $q_y \approx 3.9 \text{ nm}^{-1}$ . Additionally contributions of the (200) and (010) signals can be seen after evaporation of solvent. This development clearly

shows the crystallization of the P3HT. We see that the crystals initially form in a well aligned edge-on orientation and later in stage III get less aligned. Towards the end of the structure formation process, the distance between neighboring P3HT backbones decreases which is referred to as self-annealing of the crystals.

The GISAXS experiments allow us to observe another length scale at which we can follow the aggregation of PCBM clusters. Fig. 4.20 a) shows a color plot of the obtained horizontal scattering intensities with time. A clear structure evolution at  $q_{x,y} \approx 0.25\text{-}0.3 \text{ nm}^{-1}$  can be seen. To further analyze the data, an advanced evaluation procedure is applied to obtain information with a high time resolution at low scattering intensities. The data are binned logarithmically along  $q_{x,y}$  without the loss of information. The binned data are shown in Fig. 4.20 b) for every 10 seconds along with an untreated plot of the horizontal cut of the final film in order to show the reliability of the data treatment. The red curves show the data obtained from modeling the scattering data.

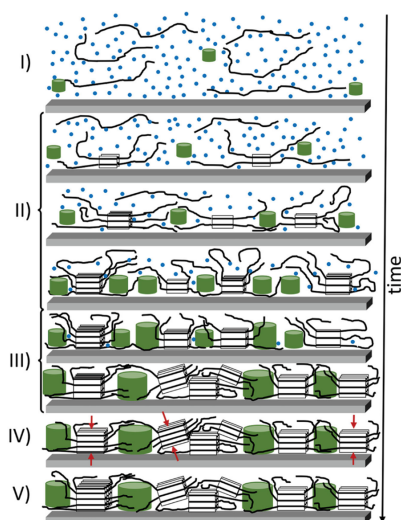


Figure 4.21:

Schematic of the structure development with time obtained from the combination of the GIWAXS and GISAXS experiments at different temperatures. The five stages are indicated on the left. The stages in which happens the most are split into initial to final phases. Most of the structure evolution happens in stage III. Blue dots represent the solvent, green cylinders the PCBM aggregates, black lines the P3HT chains, and the rectangles the crystalline P3HT domains. For simplicity, only a single layer out of the bulk film is shown for each stage. From reference [4], reprinted with permission from WILEY-VCH Verlag GmbH & Co. KGaA, Weinheim.

By combining the results from the GIWAXS and GISAXS experiments, we are able to propose a model of the structure evolution which can be divided into five stages. The proposed model is depicted in Fig. 4.21, in which the blue dots represent the solvent which initially evaporates. With time the first P3HT crystals form in a well aligned edge-on orientation (stage II). Most of the structure evolution happens in a short time step in stage III, after which end the crystals become less oriented. In stage IV the P3HT crystals undergo a self-annealing process in which they pack denser until the final structure is obtained in stage V. The performed experiments give an insight into the crystallization kinetics and fullerene aggregation dynamics of a slot-die coated P3HT:PCBM active layer. With the performed experiments we are able to picture the structure formation process with time. This knowledge is important for further influencing the inner nanoscale morphology in printed films to optimize the device performance of organic solar cells in an up-scalable technique.

- [1] R. Noriega, J. Rivnay, K. Vandewal, F. P. V. Koch, N. Stingelin, P. Smith, M. F. Toney, A. Salleo, *Nat. Mater.* **12**, 1038-1044 (2013)
- [2] P. Müller-Buschbaum, *Adv. Mater.* **26**, 7692-7709 (2014)
- [3] T. Wang, A. D. F. Dunbar, P. A. Staniec, A. J. Pearson, P. E. Hopkinson, J. E. MacDonald, S. Lilliu, C. Pizzey, N. J. Terrill, A. M. Donald, A. J. Ryan, R. A. L. Jones, D. G. Lidzey, *Soft Matter* **6**, 4128-4134 (2010)
- [4] S. Pröllner, F. Liu, C. Zhu, C. Wang, T. P. Russell, A. Hexemer, P. Müller-Buschbaum, E. M. Herzig, *Adv. Energy Mater.*, **6**, 1501580 (2016)

#### 4.10 Effect of a medium boiling point selective solvent additive on P3HT:PCBM based solar cells

J. F. Martínez Grisales, E. M. Herzig<sup>1</sup>, P. Müller-Buschbaum

<sup>1</sup> MSE, TU München, Garching, Germany

The use of selective solvent additives with high boiling point such as 1,8-diiodooctane have been used to improve the performance of organic photovoltaics based on P3HT:PCBM blends, from 3.4% to 5.1% [1]. These solvent additives work by favoring separation mechanisms in drying films. These effects have been shown to have an impact on the conductivity and the morphology of thin films. However, the drying time is increased due to the slow evaporation rate [2] making the fabrication process much more extensive. Cyclohexanone (CHX) is used as a candidate with a medium boiling point to replace such solvents, enabling shorter times in drying times, while retaining the desired effects. The effects of CHX were studied using different techniques such as UV-Vis spectroscopy, Grazing Incident Wide Angle Scattering (GIWAXS), and in the current-voltage characteristic curve (IV curve).

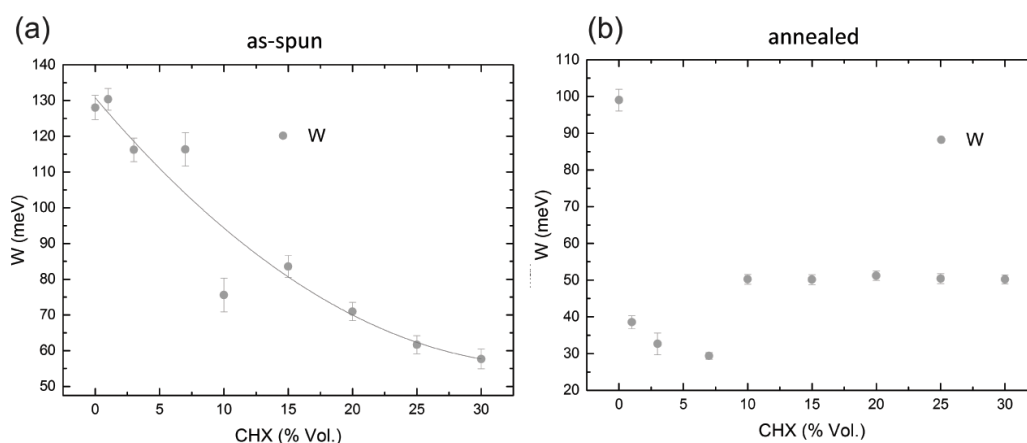


Figure 4.22:

Exciton bandwidth of thin films as-spun (a) and annealed (b). Line found at (a) is guide to the eye. For as-spun this value shows a dependence to the amount of CHX; once annealed this value becomes independent of  $W$  for samples with higher quantities of CHX

To study the effect of CHX on the morphology the absorption curves were fitted and the exciton bandwidth ( $W$ ) of the P3HT was determined for samples as-spun and annealed. This parameter is related to the tilt of the transition dipole, located along the molecular plane, with respect to the  $\pi - \pi$  stacking direction [3]. Hence, it grants information on the alignment of the backbone throughout the whole molecule, which is important in the process of charge transportation along the molecule. This is also an important condition for good alignment of  $\pi - \pi$  stacking for the crystalline polymer regions. As shown in the Fig. 4.22a, there is a decrease of  $W$  on the as-spun films indicating alignment of the P3HT molecules with the increased amount of CHX on the solutions. However, for the annealed films (Fig. 4.22b), the value of  $W$  does not show a relation to the presence of CHX, as it becomes stable for films with ratios higher than 10 vol% CHX, while displaying a minimum of 30 meV at 10 vol% CHX.

In order to infer if the P3HT crystals have a preferred orientation GIWAXS images were used, and the ratio of intensity of the peaks (100) and (010) (corresponding to the  $\pi - \pi$  and the lamellar stacking, respectively) was calculated and it is displayed in Fig. 4.23. It is found that the edge-on orientation is predominant as it is expected from P3HT crystals [4]. For as-spun samples, there is a slightly higher face-on/edge-on orientation, which decreases and stabilizes rapidly

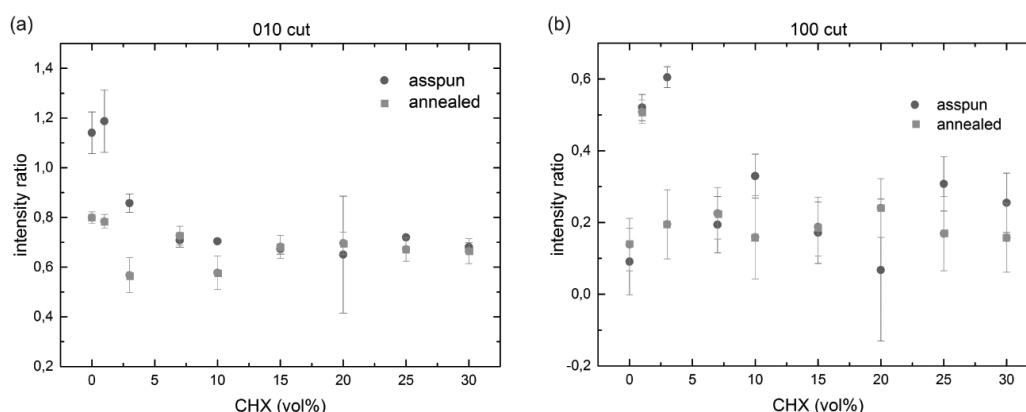


Figure 4.23:

Ratio of the face-on/edge-on orientations. This measurement was performed using a glass substrate in order to mimic the roughness of the surface below the active layer. The difference between ratios calculated corresponds to a difference of ordering between both type of stackings.

with higher content of CHX; once annealed, the ratio remains steady. This discrepancy for low CHX content may occur since the low content of the solvent additive in the solutions might not be enough to promote the formation of crystals. In films with a larger content, as well to the annealed samples, self-ordering of the molecules is promoted and the ratio does not change.

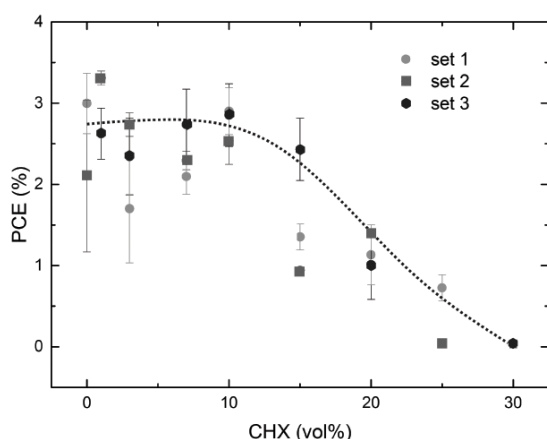


Figure 4.24:

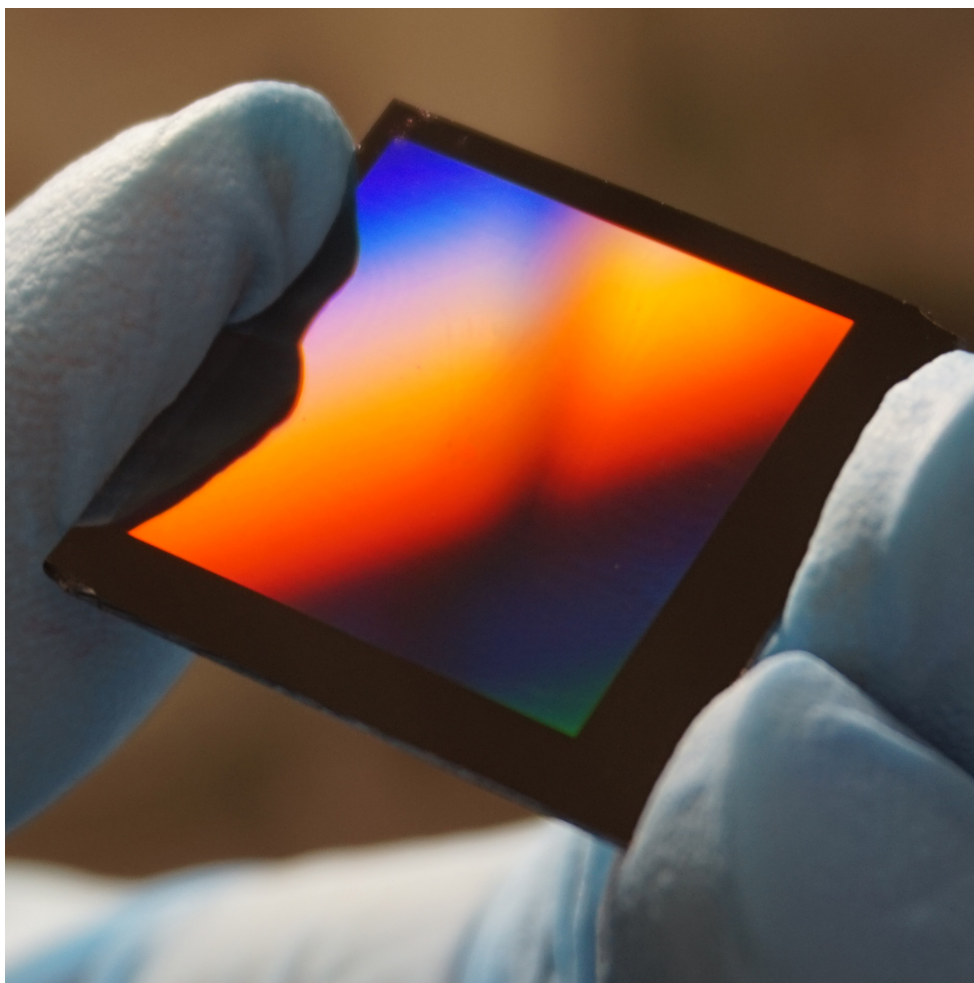
PCE of three different solar cells sets fabricated under the same conditions, using an inverted architecture and illuminated under 1.5AM conditions. The line is a guide for the eye.

To measure the effect of the selective solvent on photovoltaic devices, three different ensembles were fabricated in order to compare their behaviour. The power conversion efficiency (PCE) seems to have a maximum for the solar cells with CHX under 10 vol%. However, the exact point for the maximum is not apparent due to the fluctuation of efficiency between sets and devices. Samples with higher amount of CHX show a steady decline on the PCE, which may be related to geminate recombination [5], with the devices with the highest content presenting short-circuits which may be induced due to the size of the aggregates.

- [1] E. M. Herzig, P. Müller-Buschbaum, *Acta Futura* **6**, 17-24 (2013)
- [2] M. Scharber, N. Sariciftci, *Prog. Polym. Sci.* **38**, 1929-1940 (2013)
- [3] M. A. Ruderer, P. Müller-Buschbaum, *Soft Matter* **7**, 5482-5493 (2011)
- [4] E. Verploegen, et al. *Adv. Funct. Mater.* **20**, 3519-3529 (2010)
- [5] C. Scharsich, et al. *J. Polym. Sci. Part. B* **6**, 442-453 (2012)



## 5 Polymer-hybrid systems



## 5.1 Aqueous processed hybrid solar cells with laser-ablated titania nanoparticles

V. Körstgens, S. Pröller<sup>1</sup>, S.V. Roth<sup>2</sup>, H. Iglev<sup>3</sup>, R. Kienberger<sup>3</sup>, P. Müller-Buschbaum

<sup>1</sup> MSE, TU München, Garching, Germany

<sup>2</sup> DESY, Hamburg, Germany

<sup>3</sup> LS Laser- und Röntgenphysik, TU München, Garching, Germany

In the development of non-conventional solar cells not only the achievements of highest power conversion efficiencies and maximum lifetime of devices is of interest. Also the sustainability of the production process of the devices comes into focus. In order to achieve an all-embracing green technology, the materials applied and the required energy for device fabrication are of importance. Materials in terms of functional components or as additives in the processing should be non-toxic and environmentally friendly. In an optimum approach no organic solvents should be used for the coating of any of the layers of the device. High temperature processing steps should be reduced or avoided to increase the energy payback times of the solar cells. Following this idea, we developed hybrid solar cells with an active layer based on low temperature processed titania and a water-soluble polymer [1]. For this approach we produced titania nanoparticles with the process of laser ablation in liquid. One of the main advantages of this technique is that nanoparticles of various compositions and morphologies can be produced in dispersion of a desired liquid. In order to functionalize the fabricated nanoparticles, the aqueous suspension of the laser-ablated titania was removed from the laser beam and an aqueous poly[3-(potassium-6-hexanoate)thiophene-2,5-diyl] (P3P6T) solution was added. The resulting P3P6T:TiO<sub>2</sub> compound serves as the active layer in hybrid solar cells. The main steps of the solar cell fabrication are depicted in Fig. 5.1. In the chosen inverted cell geometry the electrons are extracted via a transparent conductive oxide (TCO) electrode. As TCO-substrates fluorine doped tin oxide (FTO) is used, since the blocking layer has to be calcined and FTO has better temperature stability as compared with indium tin oxide. A compact titania layer is selected as the hole blocking layer, which reduces the contact of the hole conductor with the FTO and therefore prevents charge recombination (Fig. 5.1a). The active layer made of the P3P6T:TiO<sub>2</sub> compound prepared from laser-ablated titania from a titania powder suspension is deposited by spin coating (Fig. 5.1b).

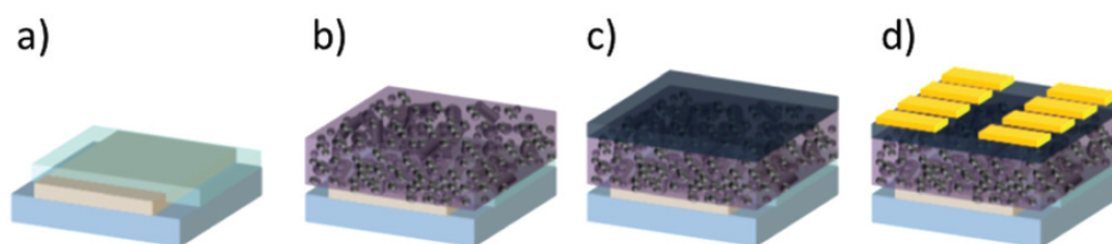


Figure 5.1:

Built-up of inverted solar cells: (a) the glass substrate with the FTO top layer partially etched away and added compact titania blocking layer; (b) adding the active layer consisting of laser-ablated titania and P3P6T; (c) adding an electron blocking layer; (d) evaporation of gold contacts. Reproduced from Ref. [1] with permission from the Royal Society of Chemistry

An electron blocking layer of poly(3,4-ethylene dioxythiophene):poly(styrenesulfonate) (PEDOT:PSS) is applied from a dilution of PEDOT:PSS with isopropyl alcohol in the volume ratio 1:10 (Fig. 5.1c). The last step before characterizing the solar cell is the evaporation of gold top contacts (Fig. 5.1d) followed by annealing. An annealing step at 140 °C for 10 min is chosen as this treatment showed an improvement in crystallinity of the hole-conducting polymer and thus

in the performance of solar cells based on poly(3-hexylthiophene) (P3HT), which is similar to the used P3P6T. All obtained hybrid solar cells are functional. However, the power conversion efficiencies achieved for solar cells containing laser-ablated titania out of aqueous titania powder suspension reached only  $(0.12 \pm 0.03)\%$  so far. In particular the low short circuit current density  $I_{SC} = (0.36 \pm 0.05) \text{ mA cm}^{-2}$  causes the low efficiency, since open circuit voltage  $U_{OC} = (0.68 \pm 0.03) \text{ V}$  and fill factor  $FF = (46 \pm 7)\%$  are both in a very promising range.

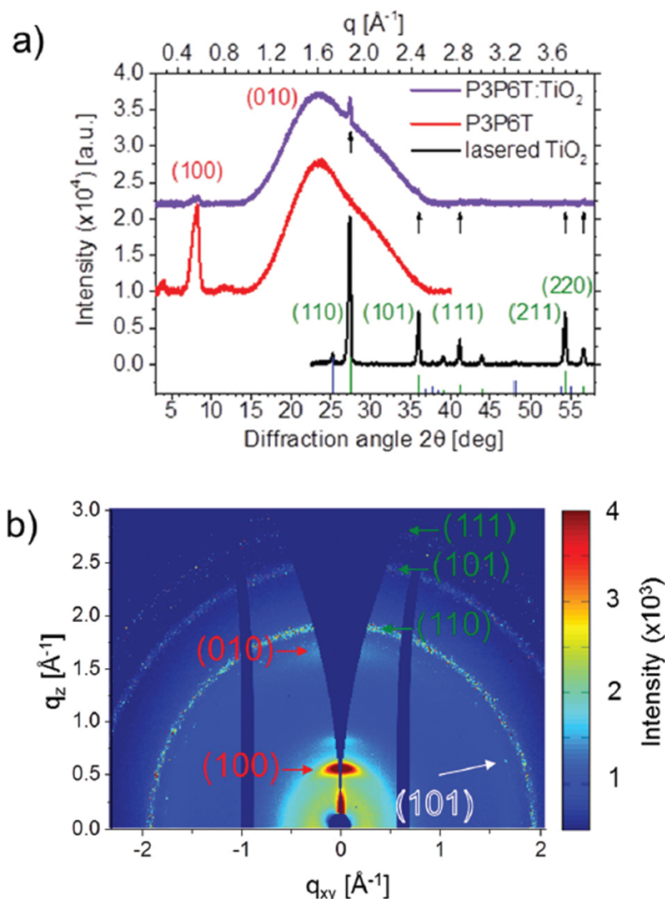


Figure 5.2:

(a) XRD patterns of laser-ablated TiO<sub>2</sub> (bottom black curve), P3P6T (centered red curve) and the P3P6T:TiO<sub>2</sub> compound (top purple curve). Theoretical positions of TiO<sub>2</sub> in anatase and rutile phases are plotted in green and blue, respectively. The main rutile peaks, which are observed in the P3P6T:TiO<sub>2</sub> blend are denoted by black arrows. The data are shifted along the y-axis for clarity. (b) Two-dimensional GIWAXS pattern of a film of P3P6T:TiO<sub>2</sub> compound. The crystal planes for the polymer are denoted on the left side (red letters), whereas the attribution of the observed crystalline phases of TiO<sub>2</sub> is noted on the right side by green and outlined white letters for the anatase and rutile phase, respectively. Reproduced from Ref. [1] with permission from the Royal Society of Chemistry

To understand the reasons which limit the efficiencies of the aqueous processed hybrid solar cells, the crystalline structure of the titania nanoparticles is investigated. X-ray diffraction (XRD) measurements are performed on spin-coated films of P3P6T and the P3P6T:TiO<sub>2</sub> compound based on laser ablation of the titania powder annealed at 120 °C (Fig. 5.2). Additionally, a pure film of laser-ablated TiO<sub>2</sub> is cast on a glass substrate and investigated for comparison. The titania film shown in Fig. 5.2a is not calcined. For the pure titania film, the main crystal phase is rutile. However, a certain amount of anatase phase can be found. For comparison, the material as purchased (without laser ablation) is mainly in its rutile phase.

A further key factor for the active layer is the functionalization of the titania with the polymer P3P6T, which is indicated by FTIR-spectroscopy. The obtained high fill factors and open circuit voltages show the potential of the novel material. As current investigations show, alternative processing of the active layer by spray-coating and printing techniques can improve the applicability of the proposed system.

[1] V. Körstgens, S. Pröllner, T. Buchmann, D. Mosegui Gonzalez, L. Song, Y. Yao, W. Wang, J. Werhahn, G. Santoro, S. V. Roth, H. Iglev, R. Kienberger, P. Müller-Buschbaum, *Nanoscale* 7, 2900-2904 (2015)

## 5.2 Superstructuring titania films via nanoimprinting for photovoltaic applications

B. Su, T. Haeberle<sup>1</sup>, M. Trunk, P. Lugli<sup>1</sup>, P. Müller-Buschbaum

<sup>1</sup> Institute for Nanoelectronics, TU München, Germany

Solid state dye-sensitized solar cells are promising alternative candidates in photovoltaic applications, due to their low costs and moderate device efficiencies. For example, Snaith and coworkers compared a series of molecular sensitizers in dye-sensitized solar cells containing the organic hole transporter 2,2',7,7'-tetrakis(N,N-di-p-methoxyphenyl-amine)-9,9'-spirobifluorene (spiro-MeOTAD) and reported record power conversion efficiencies of 5.1% by replace Au electrodes with reflective Ag electrodes to enhance the light absorption in the devices [1]. However, recombination losses in disordered mesoporous titania films prevented to achieve higher efficiency solar cells. In the present investigation, mesoporous titania films are obtained by a sol-gel process, which combines block copolymers as a structure directing template with superstructuring via nanoimprint lithography [2]. Superstructures are used to enhance light trapping in the solar cells. For a comparison, the commonly used commercial paste is used in the preparation instead of the tailored sol-gel.

The sample preparation consists of several steps: The substrates were soda-lime glasses which were cleaned in an ultrasonic bath with alconox, DI water and ethanol, respectively. The amphiphilic diblock copolymer polystyrene-block-polyethylene oxide (PS-*b*-PEO) was used as a template in the sol-gel solution. PS-*b*-PEO was dissolved in 1,4-dioxane, which is a good solvent for both blocks. Afterwards, HCl was added as a selective solvent (the PS block is hydrophobic and the PEO block is hydrophilic) to induce a micro-phase separation and obtain a micellar solution. In the meantime, titanium tetraisopropoxide (TTIP) was added as a titania precursor. The weight ratios for 1,4-dioxane, HCl and TTIP were 0.94, 0.01 and 0.05, respectively. After stirring the final solution for 45 mins, the mesoporous film were fabricated by 3 times spin coating with 2000 rpm, 60 s. The commercial paste 18NR-T from dyesol company was diluted with terpinol in a 1:1 weight ratio for reference samples. The films were fabricated with the doctor blade method.

To obtain superstructures tailored imprint stamps were used. These stamps were coated with an anti-sticking layer to prevent the adhesion of the titania film on the imprint stamps during the imprint process. Fig. 5.3 a) and b) show the surface structure of the stamps as probed by atomic-force microscopy (AFM). The size of pillar structure is 360 nm × 360 nm with a height of 260 nm. The pillars are arranged periodically on a square lattice. The nanoimprint was realized via soft embossing using an Obducat NIL-2.5. The titania film samples were placed inside the imprint chamber with the stamps on top. After heating to 130 °C, a pressure of 20 bar was applied for 10 minutes to imprint the superstructure. To crystallize the titania films and remove the polymer matrix, the samples were transferred into the furnace and heated slowly to 450 °C for 30 mins.

The scanning electron microscopy (SEM) images were taken with a Zeiss Gemini NVision 40 field emission scanning electron microscope (5.0 kV, working distance 3 mm). Fig. 5.4 shows the SEM images of the samples before and after calcination. Directly after the soft embossing the amorphous titania films, which are obtained from the sol-gel route and from the commercial paste, are shown in Fig. 5.4 a) and c), respectively. The inverted pillar structure is converted from the master stamp to the amorphous titania films with the size of 335 nm × 335 nm. Fig. 5.4 b) and d) compare the structures of calcined titania films from the sol-gel route with the commercial paste. In case of the block copolymer based sol-gel sample, compared to the stamp,

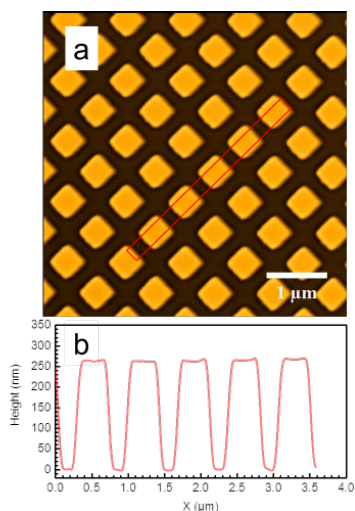


Figure 5.3:

a) AFM topography image of the imprinting stamp and b) height profile of the pillars taken across the red rectangular regime.

the height of the pillars is dramatically decreased to 30 nm. This loss in structure height is attributed to polymer evaporation during calcination. Importantly, the foam like structure is conserved in the inverted pillar structure, which emphasizes the elevated pressure and temperature during imprint step do not affect the nanostructure originating from the copolymer's phase separation. Furthermore, the foam-like morphology maintained its bicontinuous nature, which is essential to photovoltaic applications. In contrast, the imprinted superstructure is destroyed on the commercial paste film during the calcination step.

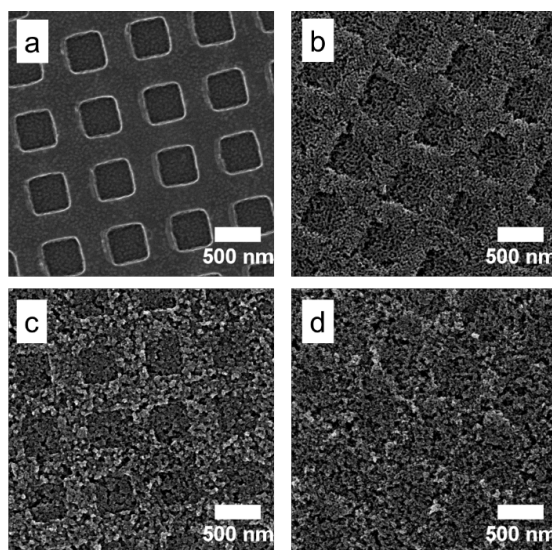


Figure 5.4:

SEM images of a) titania films from sol-gel route before calcination and b) after calcination in comparison with c) titania films from commercial paste before calcination and d) after calcination.

In conclusion, the titania films, which are obtained from the sol-gel route, demonstrate advantages for the soft embossing process. Moreover, the bicontinuous foam-like morphology remains mostly unchanged inside the inverted pillar structure.

- [1] H. J. Snath, A. J. Moule, C. Klein, K. Meerholz, R. H. Friend, M. Gratzel, *Nano Lett.* **7**, 3372 (2007)
- [2] M. A. Niedermeier, G. Tainter, B. Weiler, P. Lugli, P. Müller-Buschbaum, *J. Mater. Chem. A* **1**, 7870 (2013)

### 5.3 Superstructuring of mesoporous titania thin films via wet-imprinting

M. A. Trunk, B. Su, P. Müller-Buschbaum

Mesoporous titania scaffolds are used as a electrode-transport material (ETM) in a whole bench of solar cells, such as dye-sensitized solar cells (DSSC), its solid-state version ssDSSC and their derivatives [1]. Typically, mesostructured titania films are obtained from commercial titania pastes. Spherical granular form an interconnected network. In an alternative approach, nanostructured titania films are created e.g. from a sol-gel synthesis approach. Superstructuring of these nanostructured titania thin film can increase the efficiency of the final solar cells [2].

In order to superstructure the nanoporous titania films first we manufactured a silicon chip via optical lithography (silicon master), which features the desired lateral superstructure on its surface. On top of the master a PDMS mold is formed, which mimics the inverse of the silicon structure. Using this mold the original structure is imprinted by a wet-imprinting method to the nanoporous titania films.

In the optical lithography method the silicon substrate is coated by a photoresist. To improve the adhesion of the resist on the silicon, initially the silicon surface is functionalized by a chemical vapor deposition. Then the film is soft-baked to achieve an uniform and dense resist film on top. After soft-baking the resist is exposed to UV-light. In order to expose foreordained areas a photomask is used. This mask can be arbitrary designed so that the final superstructure fulfills any given purpose. The only limitation arises from the diffraction limit of light with respect to the smallest possible feature size (in the nanometer regime). After exposure, the photoresist film is developed. This process selectively removes the resist depending whether the region of the photoresist has been exposed.

Normally the developed resist is hard-baked to achieve a higher stability of the film. Then the master is etched via ion etching. In this step the depth of the superstructure on the master can be engineered for a given use. After removal of the remaining resist the silicon master exhibits the desired superstructure in the micrometer regime on top. An example is shown in the optical microscope image in Fig. 5.5 b). Another advantage of this lithography method is the relatively large area in which homogeneous structuring can be realized. For imprinting the titania scaffold we fabricated the superstructure on a (2x2) cm<sup>2</sup> area, shown in Fig. 5.5 a).

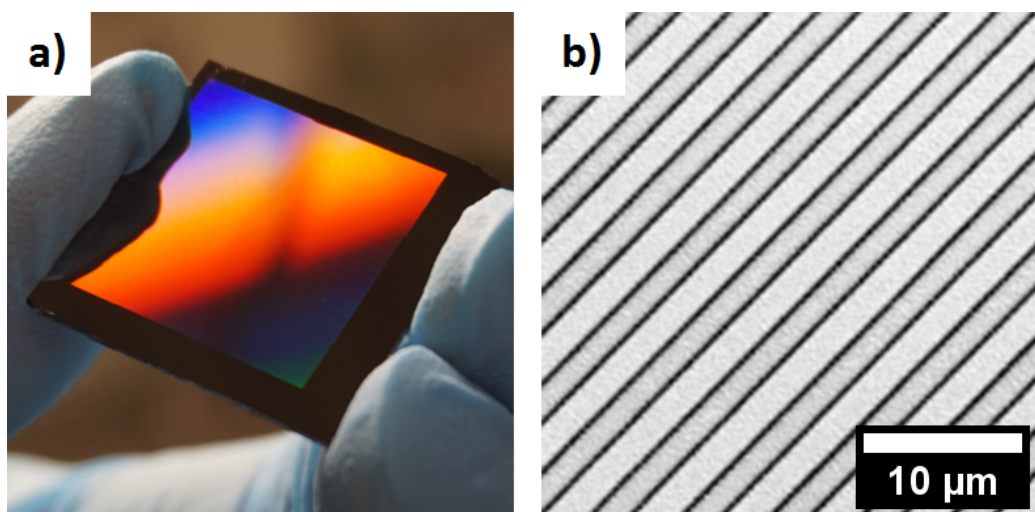


Figure 5.5:

a) Photograph and b) optical microscope image of the silicon master surface with a line grating superstructure.

After the silicon master manufacture process we mold a PDMS replica of this structure. PDMS is a cheap and easy-to-fabricate material. After molding this replica exhibits the inverse structure of the master and therefore can be used to transfer the original structure from the master to the titania scaffold.

Finally, the mesoporous titania scaffold is superstructured by a wet-imprinting process [2]. An schematic sketch of the used wet-imprint procedure is shown in Fig. 5.6 a). After preparation of the sol-gel solution we covered the top surface of the PDMS stamp. Thus, the sol-gel solution can fully fill the superstructure of the stamp, thereby ensuring a good capability of superstructuring the final titania films. Then we placed our substrate on the covered stamp, pressed the substrate on the stamp by placing a weight on top and let it dry. After drying we lift off the stamp carefully. Fig. 5.6 b) shows an optical microscope image of the successfully superstructured sol-gel solution film with a line grating morphology on a silicon substrate. After the final calcination the polymer part in the sol-gel solution is removed, yielding the successfully superstructured mesoporous titania template on our substrate. Of course the pattern collapse of the original superstructure needs to be avoided by a well designed calcination procedure. This technique is an easy way to superstructure porous titania scaffolds on almost any given flat and compact substrate.

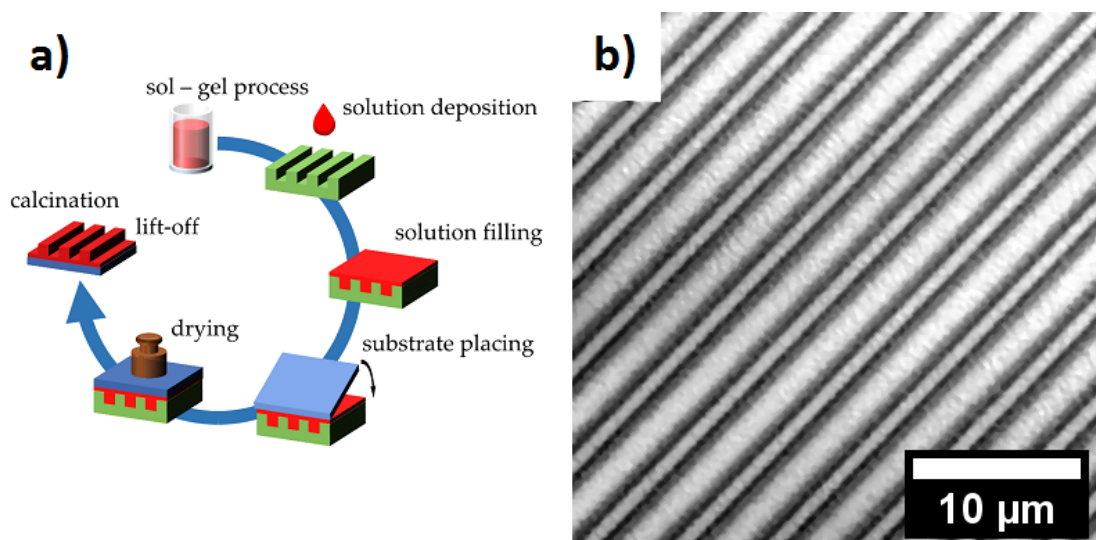


Figure 5.6:

a) Schematic sketch of the wet-imprinting process. b) Optical microscope image of the superstructured amorphous titania thin film with a line grating structure before calcination.

- [1] P. Docampo, S. Guldin, T. Leijtens, N. K. Noel, U. Steiner, H. J. Snaith, *Adv. Mater.* **26**, 4013 (2014)
- [2] M. A. Niedermeier, I. Gross, P. Müller-Buschbaum, *J. Mater. Chem. A* **1**, 13399 (2013)

## 5.4 Nanostructured zinc oxide films for application in hybrid photovoltaics

K. Wang, L. Song, P. Müller-Buschbaum

Hybrid solar cells, a combination of conventional inorganic and organic photovoltaic systems, offer outstanding potential due to their minor investment compared to inorganic solar cells and higher stability compared to organic solar cells. For this kind of solar cells, nanostructured inorganic metal oxides with tunable morphologies are of great importance. Among the inorganic metal oxides, zinc oxide (ZnO) has been widely explored due to its outstanding electrical and optical properties and rich variety of morphologies [1-4]. To date, many different routes towards ZnO nanostructures have been reported, such as hydrothermal synthesis, metal-organic chemical vapor deposition, sol-gel process and others. The sol-gel process is one of the most widely used methods in solar cells due to the production of a homogeneous material and fabrication of ceramic coatings from solutions by chemical means. However, the structures obtained by the sol-gel process are limited, regarding both morphologies and structure sizes. A possible way to improve the film structure is to introduce amphiphilic block copolymers into sol-gel process. The hydrophilic and hydrophobic polymer blocks of amphiphilic block copolymers are covalently bound, which could induce a micro-phase separation via a so-called good-poor solvent pair. Herein, the diblock copolymer of polystyrene (PS) and polyethylene oxide (PEO), PS-*b*-PEO template assisted sol-gel technique is used to prepare ZnO films.

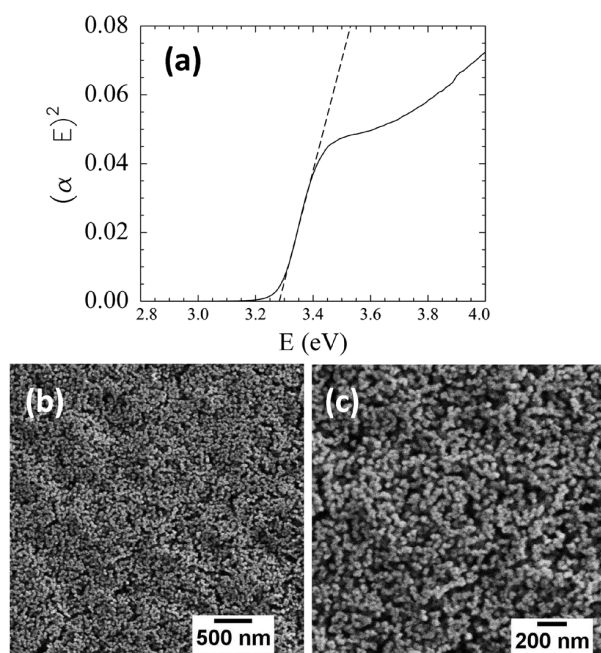


Figure 5.7:

a) Tauc plot of the ZnO film to determine the band gap of the material present in the film, by linear extrapolation of the data to the energy axis; b) and c) SEM images showing the surface structures of the ZnO nanocomposite films produced by spray deposition.

To synthesize the nanocomposite films, DMF is used as a good solvent to dissolve both PS and PEO blocks. This is followed by the addition of appropriate amounts of water, which acts as a good solvent for the PEO block but a poor solvent for the PS block. As the chain length of the PEO block is much shorter than that of PS block in the present work, so-called crew-cut micelles are expected to form with hydrophobic PS cores and hydrophilic PEO coronas. The morphologies of the micelles are controlled by the balance of steric and electrostatic forces among the hydrophilic segments as a result of protonation of the PEO block by water. The shape and size of the micelles in solution are determined by the degree of the PS block stretching and by the PS domain interactions with the surrounding solvent and the surrounding PEO domains. A zinc oxide precursor, namely, zinc acetate dihydrate (ZAD), is then incorporated into the micelles.

As a result of this complex thermodynamic and kinetic energy balance, various morphologies can be obtained through the different chain lengths of the hydrophilic and hydrophobic

polymer blocks, as well as the weight fractions of DMF, water, and ZAD in the solution. In the present work, PS-*b*-PEO (50 mg) is dissolved in DMF (1 mL). The corresponding amount of ZAD is mixed with DMF (1 mL) separately. Afterwards both solutions are filtered with a PTFE filter with a pore size of 0.45  $\mu\text{m}$  to get rid of the undissolved parts. The required amount of deionized water is then added to the polymer solution. Next, the polymer and precursor solutions are mixed together with the aid of a syringe pump (PHD 2000 infuse/withdraw, Harvard Apparatus) by using a constant infuse rate of 1 mL  $\text{min}^{-1}$ . The syringe pump ensured uniform mixing of the two solutions. The final solution is directly transferred on pre-cleaned silicon (100) substrates to prepare films by spray- and spin-casting, respectively. A final calcination step at 673 K was carried out for 30 min in order to combust the diblock copolymer and crystallize ZnO.

For spray-casting, the weight fraction for the sol-gel solution is  $\omega$  (DMF):  $\omega$  ( $\text{H}_2\text{O}$ ):  $\omega$  (ZAD)=0.96:0.02:0.02. On linear extrapolation of the data to the energy axis (as shown by the dashed line in Fig. 5.7 a)), the direct band gap of the material is calculated to be 3.28 eV, which corresponds well with literature [5]. Moreover, the foam-like ZnO structure seen from Fig. 5.7 b) and c), is considered to be promising for photovoltaic device performance due to the higher surface-to-volume ratio, which provides a larger effective area for interfacial reactions [6].

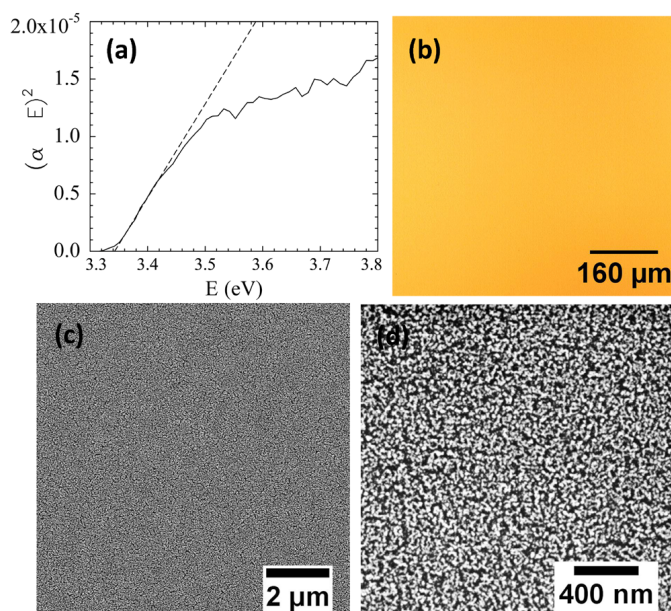


Figure 5.8:  
a) Tauc plot of the ZnO film to determine the band gap of the material present in the film; b) Optical microscope image of spin coated ZnO film; c) and d) SEM images showing the surface structures of the ZnO nanocomposite films produced by spin coating.

For spin-coating,  $\omega$  (DMF):  $\omega$  ( $\text{H}_2\text{O}$ ):  $\omega$  (ZAD) is 0.96:0.01:0.03. From the UV-Vis measurements (Fig. 5.8 a)), we can calculate the ZnO band gap energy  $E_g$  to be 3.34 eV. The optical microscope (Fig. 5.8 b)) illustrates the homogeneous ZnO surface structure. For more clear observation, SEM images are performed under 20K and 100K (Fig. 5.8 c) and d)). A foam-like morphology is found over a large sample area. Such type of film morphology is very promising for improving the power conversion efficiency of hybrid solar cells.

- [1] S. Cho, J. Jang, A. Jung, A. S. Lee, J. Lee, J. S. Lee, K. Lee, *Langmuir* **27**, 371-378 (2011)
- [2] H. Yu, Z. Zhang, M. Han, X. Hao, F. Zhu, *J. Am. Chem. Soc.* **127**, 2378-2379 (2005)
- [3] W. Peng, S. Qu, G. Cong, Z. Wang, *Cryst. Growth Des.* **6**, 1518-1522 (2006)
- [4] H. Zou, Y. Luan, J. Ge, Y. Wang, G. Zhuang, R. Li, Z. Li, *Cryst. Eng. Comm.* **13**, 2656 (2011)
- [5] Y. Zhang, Y.-H. Wen, J.-C. Zheng, Z.-Z. Zhu, *Appl. Phys. Lett.* **94**, 113114 (2009)
- [6] K. Sarkar, M. Rawolle, E. M. Herzig, W. Wang, A. Buffet, S. V. Roth, P. Müller-Buschbaum, *Chem. Sus. Chem.* **6**, 1414-1424 (2013)

## 5.5 Hybrid based thermoelectrics

A. K. Maurya, N. Saxena, P. Müller-Buschbaum

As energy demand around the world increases and the amount of non-renewable fossil fuels decreases, the need for sustainable renewable energy sources is evident. In addition to the growing demand for energy, there is also a push for reducing the amount of emitted pollution, in the form of greenhouse gasses, by using clean energy sources.

Thermoelectric materials (TE) convert heat directly into electricity. This clean energy technology has advantages over other renewable technologies in that it requires no sunlight, has no moving parts, and is easily scalable. With the majority of the unused energy in the world being wasted in the form of heat and the recent mandates to reduce greenhouse gas emissions, thermoelectric devices could play an important role in our energy future by recovering this wasted heat and increasing the efficiency of energy production. Thermoelectric generators also can be used to increase the lifetime and capability of the wireless sensor networks (WSNs). Integration of energy harvesters into sensor nodes of WSNs can realize self-powered systems, providing the possibility for maintenance free WSNs.

However, low conversion efficiencies and the high cost of crystalline inorganic thermoelectric materials have restricted their implementation into modern society. Previous studies of TE materials have mainly investigated inorganic materials such as bismuth-telluride (Bi-Te) and metal oxides [1, 2]. Most of these inorganic TE materials show their optimum performance at temperatures higher than 200° C. However, there is a huge amount of waste heat that occurs at temperatures lower than 150° C. At such low temperatures, the energy conversion efficiency is low because of the small achievable temperature difference suggested by the Carnot cycle. To combat these issues, composite materials that use conductive polymers have been under investigation due to their low cost, manufacturability, and malleability. These new composite materials could lead to cheaper thermoelectric devices and even introduce the technology to new application areas. Unfortunately, polymer composites have been plagued by low operating efficiencies due to their low figure of merit. The figure of merit (ZT) is given by the following relation:

$$ZT = \frac{\sigma S^2}{\kappa} T. \quad (5.1)$$

S is the Seebeck coefficient,  $\sigma$  is the electrical conductivity,  $\kappa$  is the thermal conductivity and T is the mean temperature. To maximize the efficiency of a thermoelectric device, one needs to maximize the dimensionless figure of merit. Therefore, when investigating thermoelectric materials, the primary goal, and indeed the focus of this research, is to increase the thermoelectric ZT of the material.

In this research, we deposit a thin film of poly(3,4-ethylenedioxythiophene):poly(styrenesulfonate) (PEDOT:PSS) by spin coating of various thicknesses on the glass substrate. We also post-treat these films with ethylene glycol (EG) for enhancing conductivity. For characterization, we use four point probe method to measure the electrical conductivity, thickness profilometry to measure film thickness and a home-made setup to measure the Seebeck coefficient, as illustrated in the left part of Fig. 5.9. We find an enhanced electrical conductivity of the PEDOT:PSS film exposed to a post treatment by EG. The maximum electrical conductivity measured was 1051.4 S/cm. We also observed that the Seebeck coefficient does not change significantly on post treatment with EG while it increases upon decreasing the thickness of the film. A linear variation of the thermovoltage with the temperature difference is measured for

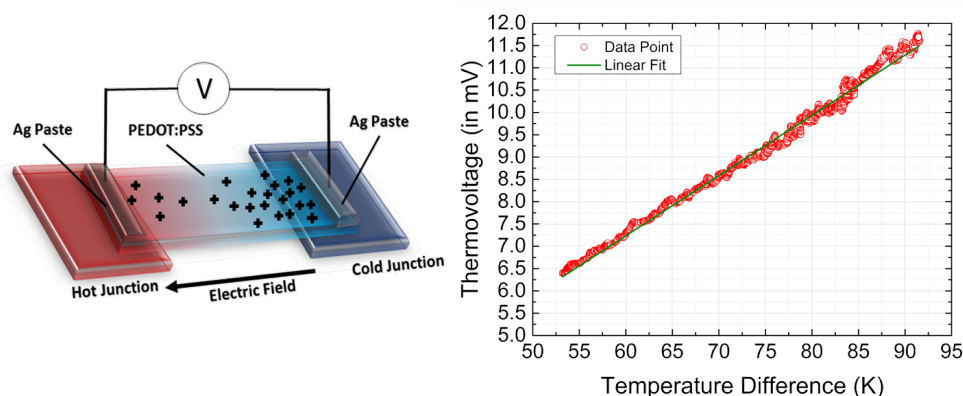


Figure 5.9:  
left: Schematic of the Seebeck coefficient measurement setup; right: thermovoltage versus temperature difference.

the PEDOT:PSS films as seen in Fig. 5.9. Electrical conductivity and Seebeck coefficient for two different PEDOT:PSS film thicknesses are presented in table 1. A Seebeck coefficient (S) of  $18 \mu\text{V}/\text{K}$  is achieved for a PEDOT:PSS film thickness of 50.1 nm.

Table 1: Thermoelectric properties of PEDOT:PSS thin films with and without EG treatment.

Thickness (nm)	$\sigma$ without EG (S/cm)	$\sigma$ with EG (S/cm)	S without EG ( $\mu\text{V}/\text{K}$ )	S with EG ( $\mu\text{V}/\text{K}$ )
$50.1 \pm 5.1$	-	$1037.8 \pm 14.9$	$17.8 \pm 0.2$	$18.0 \pm 0.2$
$119.1 \pm 10.3$	$2.3 \pm 0.1$	$1051.4 \pm 17.2$	$12.1 \pm 0.1$	$11.9 \pm 0.2$

Continuing research in this area will attempt to enhance the Seebeck coefficient even further by optimizing the thickness and post treatment of the PEDOT:PSS thin film. Further, we plan for creating a composite material of PEDOT:PSS with metal and inorganic nanoparticles. It has been reported that composites [3-5] and hetero-junctions [5-8] can offer effective approaches to control thermal and electrical conductivities in the development of thermoelectric functions. Specifically, polymer composites can also limit the thermal conductivity while still permitting electrical conductivity via combining materials that exhibit high electrical conductivity with insulating polymers that have a low thermal conductivity. Hetero-junctions can be effectively used to lower thermal conductivity by phonon scattering at the interfaces of separate materials due to boundaries and imperfections. This interface also causes Kapitza resistance due to the acoustic mismatch model.

- [1] G. J. Snyder, E. S. Toberer, *Nat. Mater.* **7**, 105 (2008)
- [2] M. Zebarjadi, K. Esfarjani, M. S. Dresselhaus, Z. F. Ren, G. Chen, *Energy Environ. Sci.* **9**, 395 (2002)
- [3] L. D. Hicks, M. S. Dresselhaus, *Phys. Rev. B* **47**, 12727 (1993)
- [4] C. Yu, Y. Kim, D. Kim, J. Grunlan, *Nano Lett.* **8**, 4428 (2008)
- [5] D. Kim, Y. Kim, K. Choi, J. Grunlan, C. Yu, *ACS Nano* **4**, 513 (2010)
- [6] B. S. W. Kuo, J. C. M. Li, A. W. Schmid, *Appl. Phys. A* **55**, 289 (1992)
- [7] M. Asheghi, Y. K. Leung, S. S. Wong, K. E. Goodson, *Appl. Phys. Lett.* **71**, 1798 (1997)
- [8] P. Reddy, S. Jang, R. Segalman, A. Majumdar, *Science* **315**, 1568 (2007)

## 5.6 Investigating the energy-level alignment at hybrid interfaces between ZnO and p-doped organic semiconductors

M. H. Futscher, J. Frisch<sup>1</sup>, E. Metwalli, M. V. Nardi<sup>1</sup>, N. Koch<sup>1</sup>, P. Müller-Buschbaum

<sup>1</sup> HU Berlin, Germany

Since the first successful demonstration in the late 1980s, organic light emitting diodes (OLEDs) have been intensively investigated due to the potential fabrication of low-cost, high-brightness and light-weight lighting applications. OLEDs require a transparent conductive electrode for charge carrier injection and the out-coupling of light. Typically, these electrodes are made of transparent conductive oxides such as gallium nitride (GaN), indium tin oxide (ITO) or zinc oxide (ZnO). ZnO is particularly well suited as an electrode for OLEDs because it is abundant in nature, cheap and features a high exciton binding energy of 60 meV [1].

Both the operating voltage and the luminance efficiency of OLEDs strongly depend on effective charge injection from electrodes to organic semiconductors (OSCs) and charge transport in the organic material [2]. A promising solution to reduce the bias voltage in OLEDs is the use of doped organic semiconductors as electron and hole transport materials. However, the underlying mechanisms of doping in organic semiconductors are only little understood compared to their inorganic counterparts [3]. Here, the energy-level alignment between ZnO and the hole transport material  $\alpha$ -NPD p-doped with the strong molecular acceptor F<sub>6</sub>TCNNQ is investigated by means of photoelectron spectroscopy (PES). Furthermore, the morphology of the p-doped molecular organic semiconductor is investigated using grazing incidence small angle X-ray scattering (GISAXS). For this purpose,  $\alpha$ -NPD films with and without F<sub>6</sub>TCNNQ doping are prepared via sublimation at pressures < 10<sup>-6</sup> mbar on ex-situ thermally annealed ZnO(0001) substrates.

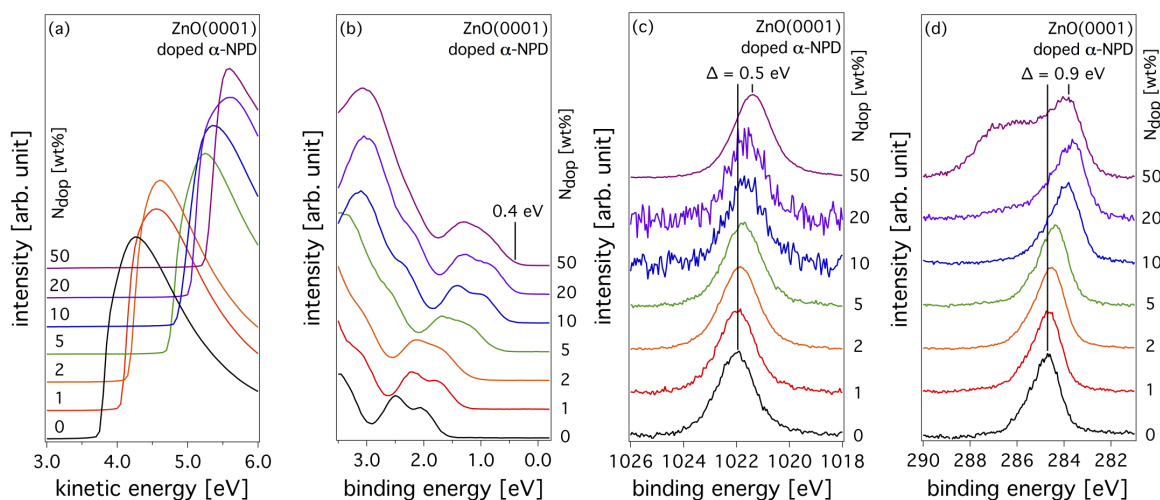


Figure 5.10:

PES data of pristine and F<sub>6</sub>TCNNQ-doped  $\alpha$ -NPD films with increasing doping concentrations ( $N_{\text{dop}}$ ) measured with respect to the Fermi level. a) Secondary electron cut-off b) Valence electronic structure c) Zn2p<sub>3/2</sub> core level region spectra d) C1s core level region spectra

Fig. 5.10 shows PES data obtained at the Humboldt-University of Berlin of  $\alpha$ -NPD films with and without F<sub>6</sub>TCNNQ doping with a film thickness of (5 ± 2) nm. The secondary electron cut-off (SECO) and the valence electronic structure are obtained using a photon energy of 21.2 eV and a pass energy of 2 eV and 5 eV, respectively. In order to clear the analyzer work function a constant negative bias of 10 V was applied to the sample during the measurement of the

SECO. Core level region spectra are obtained using a photon energy of 1486.6 eV and a pass energy of 20 eV. With increasing doping concentration, a work function increase and clear shift of the Fermi level towards the highest occupied molecular orbital (HOMO) is observed, showing the expected effect for p-type doping in standard semiconductor theory. Shifts of the valence electronic structure are accompanied by shifts of the  $\text{Zn}2p_{3/2}$  and the C1s core level positions towards lower binding energies. At high doping ratios, molecular features of pristine  $\text{F}_6\text{TCNNQ}$  emerge at higher binding energies. Shifts of the  $\text{Zn}2p_{3/2}$  core level positions are attributed to a change in surface near band bending in the inorganic substrate. Shifts of the C1s core level position on the other hand are attributed to originate from band bending in the organic thin film and a contribution of an interface dipole which may exist due to adsorbed  $\text{F}_6\text{TCNNQ}$  molecules on the ZnO surface. Consequently, the overall behavior of the energy alignment of electronic bands of the hole transport material with controlled p-doping on intrinsically n-doped ZnO can be described by accounting for a change in surface near band bending in the inorganic substrate, band bending in the organic thin film and an interface dipole.

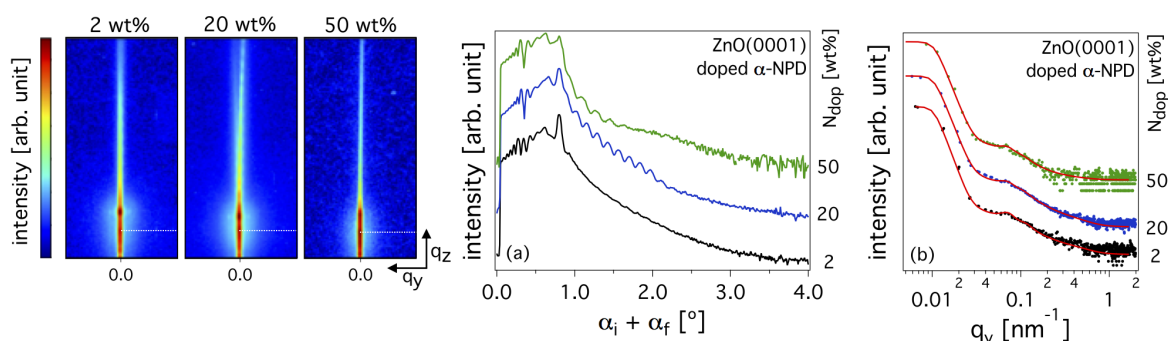


Figure 5.11:

GISAXS data of  $\text{F}_6\text{TCNNQ}$ -doped  $\alpha$ -NPD films with increasing doping concentrations ( $N_{\text{dop}}$ ). Images on the left side display the acquired two-dimensional GISAXS data. White dashed lines indicate the positions of the horizontal line cuts. a) Vertical line cuts performed at  $q_y = 0 \text{ nm}^{-1}$  b) Horizontal line cuts together with their fits

Fig. 5.11 shows GISAXS data of  $\alpha$ -NPD films with and without  $\text{F}_6\text{TCNNQ}$  doping obtained with a sample-detector distance of 1056.2 mm and a wavelength of 1.5408 Å. In order to perform quantitative analysis of the data, horizontal and vertical line cuts are performed. Horizontal line cuts performed at the material-sensitive Yoneda peak position together with their fits are shown in Fig. 5.11(b). This analysis reveals a similar bulk morphology of  $\text{F}_6\text{TCNNQ}$ -doped  $\alpha$ -NPD films with different doping concentrations. Vertical line cuts performed at  $q_y = 0 \text{ nm}^{-1}$  are shown in Fig. 5.11(a). Intensity modulations along the  $q_y$ -direction above the specular reflection provide average depth-sensitive information. With increasing doping concentration, these intensity modulations are getting considerably more pronounced, suggesting that the surface of  $\text{F}_6\text{TCNNQ}$ -doped  $\alpha$ -NPD films gets aligned horizontally to the surface of the ZnO substrate. Furthermore, an additional large modulation is observed for high doping ratios indicating the presence of multiple correlated layers. This is attributed to derive from phase separation between  $\text{F}_6\text{TCNNQ}$ -doped  $\alpha$ -NPD and pristine  $\text{F}_6\text{TCNNQ}$  at high doping ratios. Concluding, it is found that  $\alpha$ -NPD can be efficiently p-doped with  $\text{F}_6\text{TCNNQ}$  by co-evaporation of the two molecules. Obtained results might help to reduce operating voltage and increase luminance efficiency of OLEDs.

[1] C. Wöll, *Progress in Surface Science* **82**, 55-120 (2007)

[2] L. S. Hung, C. H. Chen, *Materials Science and Engineering R* **39**, 143-222 (2002)

[3] I. Salzmänn, G. Heimel, *Journal of Electron Spectroscopy and Related Phenomena* **204**, 208-222 (2015)

## 5.7 Porous titania-based electrodes for high capacity lithium-ion batteries

T. Kaps, E. Metwalli, P. Müller-Buschbaum

Nowadays block copolymers (BCs) are used for a wide range of different applications owing to their ability to form nanostructured materials. As well, BCs can be used to direct inorganic materials into ordered nanomorphologies for application related to organic solar cells, lithium batteries and gas sensors.

A good battery characterizes safety, high capacity, good cycle stability and long lifetime. A main part of a battery is the anode, which properties strongly depend on its material characteristics. Titania is very promising as anode material, because it is known for its abundance, safety, chemical stability and low expansion during a lithiation/delithiation process. But on the downside it shows only a low capacity and energy density. In contrast silicon shows high specific capacity, high energy density and good safety, but a poor cycling and capacity fading [1]. Thus, the aim is to incorporate silicon or silica based composites into the titania structure to create hybrid electrodes with optimized performance. The electrode structure strongly influences the properties of solid-state batteries. Nanoporous structures drastically increase the electrical and electrochemical performance of titania based electrodes. By increasing the surface area more active sites are created, and for batteries a higher electron and ion flux can be achieved.

Depending on the procedure of the sol-gel process nanoparticles, fibers, films or even aerogels can be fabricated. The precursor, usually metal alkoxides, determines the resulting metal oxide. Employing BC along with the so-called good-bad solvent pair different morphologies can be obtained [2]. Hence, the polymer assisted sol-gel process enables the creation of nanostructured thin film electrodes.

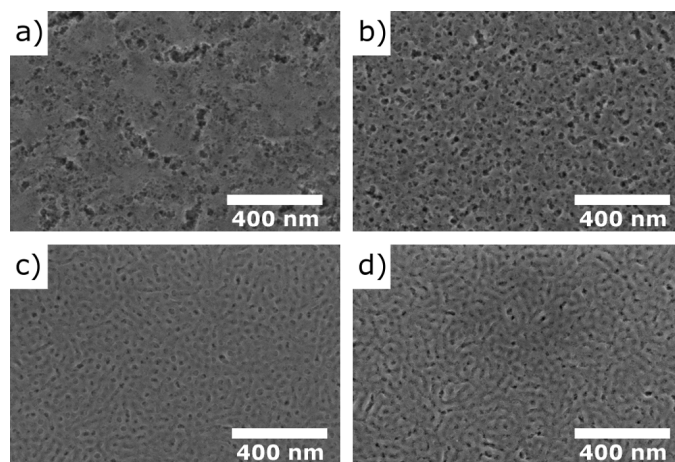


Figure 5.12:

SEM images of mesoporous structures: a) Nanostructured titania films and nanostructured hybrid films with weight ratios  $SiO_2/TiO_2$  of a) 0.7 and b) 0.3. d) Sol-gel process performed with ethanol solvent replacing isopropanol in the synthesis.

In the present work, sol-gel solutions for titania and silica were prepared separately. For the titania solution, polystyrene-block-polyethylene oxide (PS-b-PEO) diblock copolymer (DBC) was used as template for the mesoporous structure preparation. The polymer was dissolved in 1,4-dioxane under stirring. Two additional solutions were prepared and simultaneously added drop-wise to the PS-b-PEO DBC solution under stirring for one hour. The titania precursor was tetraisopropyl orthotitanate (TTIP) which was diluted in 1,4-dioxane. The hydrolyzing agent

was hydrochloric acid  $HCl$  (37%), which acts as a catalyst. It was also diluted in 1,4-dioxane and stirred. The silica sol-gel was prepared by mixing the PS-b-PEO DBC, isopropanol and tetraisopropyl orthosilicate under stirring. Afterwards drop-wise the mixture of the hydrolyzing agent, deionized  $H_2O$ , the catalyst acid  $HCl$  and the solvent isopropanol were added to the sol-gel. The silica sol-gel was stirred for three hours at  $60^\circ C$ . The sol-gels composed from both, titanium and silica precursors, were mixed and spin-coated on a pre-cleaned silicon substrate. A calcination step at  $400^\circ C$  for 4 hours was performed to create the nanostructured hybrid electrodes.

The prepared samples were analyzed using scanning electron microscopy (SEM). Fig. 5.12 compares SEM images of different preparation methods. Fig. 5.12 a) shows a mesoporous titania structure using the  $TiO_2$  sol-gel process adapted from Niedermeier et. al [3]. Nanopores with various dimensions up to 200 nm indicate that the PS-b-PEO polymer aggregates to small-like clusters during the sol-gel process. Additionally, the sharp edges suggest partly less ordered morphologies. In Figs. 5.12 b) to d) mixtures of the  $TiO_2$  and  $SiO_2$  sol-gels with  $SiO_2/TiO_2$  weight ratios of 0.7 and 0.3 are compared. In the samples shown in Figs. 5.12 c) and d) the amount of PS-b-PEO was proportional to the  $TiO_2$  ratio. In that shown in Fig. 5.12 d) ethanol was used as the solvent for the silica sol-gel replacing the isopropanol solvent. In contrast to the far less ordered morphologies (Fig. 5.12a and 5.12b) a lower amount of PS-b-PEO resulted in better ordered structures and more uniform pore sizes (Figs. 5.12c and 5.12d). Comparing the different solvents, a wormlike structure was created with ethanol as solvent (Fig. 5.12d). The size of the holes is about 20 nm for a weight ratio of 0.3, whereas for a weight ratio of 0.7 some of the holes are sufficient close to create bigger holes due to a relatively ill-defined structure.

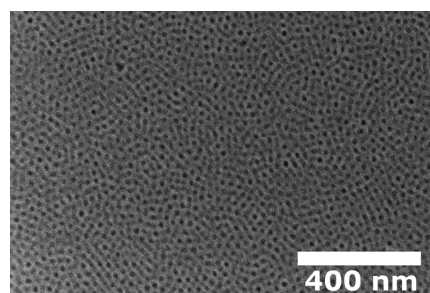


Figure 5.13:  
SEM image of a highly-ordered mesoporous  $TiO_2/SiO_2$  hybrid film at a  $SiO_2/TiO_2$  weight ratio of 0.5

An improved order of the morphology was obtained by decreasing the PS-b-PEO amount to 50% and the  $SiO_2/TiO_2$  ratio to 0.5 (see Fig. 5.13). With such sol-gel, a densely packed and ordered structure can be observed. None of the previously observed rough or wormlike structure can be seen. The diameter of the pores is more uniform in size at about an average size of 25 nm. Further investigations are in progress to quantitatively analyze the SEM data. As well, the grazing incidence small-angle scattering technique will be employed to have a more statistical relevant analysis of the evolved morphology of the hybrid nanoporous film. Additionally, X-ray diffraction will be used to investigate the crystalline structure of the prepared films.

- [1] S. Goriparti, E. Miele, F. De Angelis, E. Di Fabrizio, R. P. Zaccaria, C. Capiglia, *Journal of Power Sources* **257**, 421-443 (2014)
- [2] G. Kaune, M. Memesa, R. Meier, M. A. Ruderer, A. Diethert, S. V. Roth, M. D'Acunzi, J. S. Gutmann, P. Müller-Buschbaum, *ACS Appl. Mater. Interfaces* **1**, 2862-2869 (2009)
- [3] M. A. Niedermeier, D. Magerl, Q. Zhong, A. Nathan, V. Körstgens, J. Perlich, S. V Roth, P. Müller-Buschbaum, *Nanotechnology* **23**, 145602 (2012)

## 5.8 Nanostructured hybrid block copolymer electrolytes as a membrane for lithium-ion batteries

M. Kaepfel, E. Metwalli, P. Müller-Buschbaum

Lithium-ion batteries are the most popular energy storage system not only for electrical devices like laptops, cameras or mobile-phones, but also for electric vehicles. These batteries have a high power to weight ratio, a good cycle lifetime, low self-discharge rates and no memory effect. A typical Lithium-ion battery consists of several cells which are linked together. Each cell consists of an anode, a cathode and Li-ion conducting electrolyte. During the discharge of the cell Li-ions migrate from the anode through the electrolyte to the cathode.

Usually Lithium-salts in aprotic organic solvents are used as an electrolyte, but these liquid electrolytes render the system thermally and electrochemically unstable. One approach to overcome these problems uses solid electrolytes. Namely polymer electrolytes, which are less volatile and allow the fabrication of batteries in various shapes and configurations.

One well known polymer for this purpose is poly(ethylene oxid) (PEO), as it can be easily enriched with Lithium-salts. It is also quite cheap and easy to process.

One major disadvantage of PEO as a Li-ion electrolyte is low conductivity at room temperature in the order of  $\sigma = 10^{-8} \text{Scm}^{-1} - 10^{-4} \text{Scm}^{-1}$ . To enhance the conductivity of PEO-based electrolytes, plasticizers like ionic liquids can be added. However, a big drawback of plasticizers is the even more reduced mechanical strength of the hybrid solid state membrane [1].

To improve the mechanical stability of the electrolyte, while keeping a high conductivity, diblock copolymers (DBC) are used, namely polystyrene-block-polyethylene oxide (PS-*b*-PEO). It has a rigid PS block and a Li-ion conducting PEO block. To suppress PEO crystallites and to increase the segmental motion of the PEO chains, the DBC is also enriched with the ionic liquid [EMIMTf] [2].

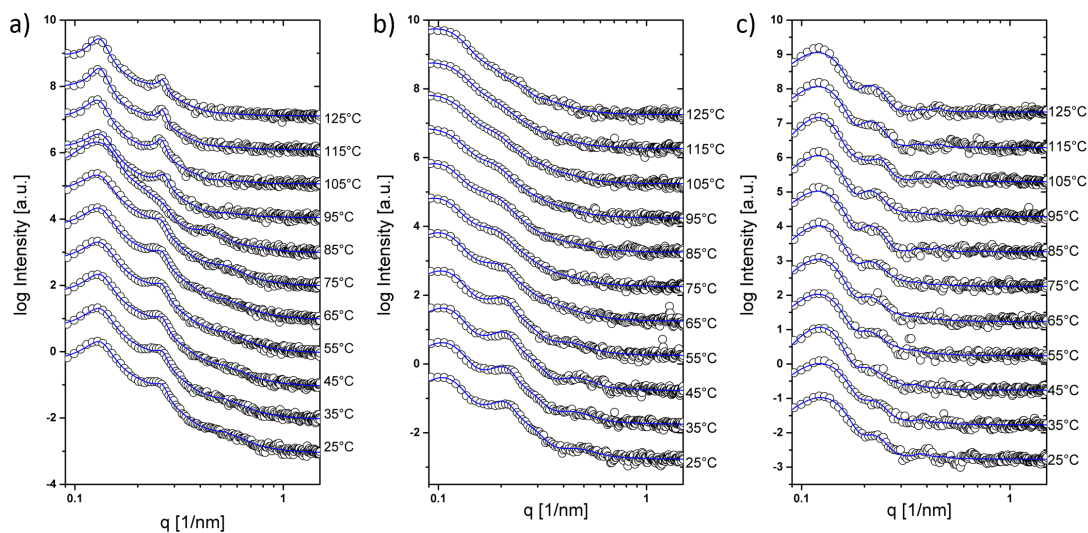


Figure 5.14:

1D SAXS profiles and the corresponding fits of a) pure polymer and b) polymer with  $[\text{Li}]/[\text{EO}] = 0.1$  and c) polymer with  $[\text{Li}]/[\text{EO}] = 0.1$  and  $[\text{EMIM}]/[\text{EO}] = 0.08$

Ionic liquids are basically salts, consisting of mostly large size organic anions and cations. They are nonflammable, chemically and electrochemically very stable and they have a negligible vapor pressure leading to a liquid state at room temperature. Ionic liquids can solve well in

PEO and lower its melting temperature [3]. To provide Li-ions to the system, the lithium-salt ( $CF_3LiO_3S$ ) is added as a third component to the system.

Samples were prepared by solution casting. Tetrahydrofuran (THF) was used as a solvent for all three components. For small angle X-ray scattering (SAXS) and wide angle X-ray scattering (WAXS) the prepared solution was put dropwise into a self-designed stainless steel sample holder. The measured SAXS data can be seen in Fig. 5.14. The pure polymer was fitted with a lamellar micro-phase separated structure (Fig. 5.14 a)). By the incorporation of LiTf salt, the periodic distance increases. But the data can still be fitted by a lamellar structure (Fig. 5.14 b)). In contrast, with ionic liquid in the system (Fig. 5.14 c)) the morphology changes to hexagonally packed cylinders. This should lead to an improved conductivity by forming a percolating path for lithium ions migration.

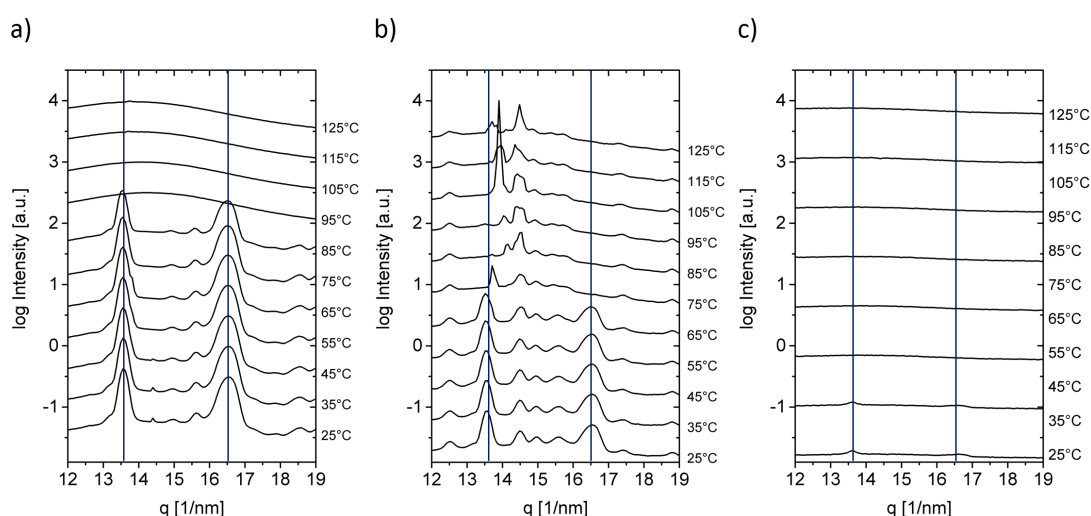


Figure 5.15:  
1D WAXS profile during a heating cycle of a) pure polymer and b) polymer with  $[Li]/[EO] = 0.1$  and c) polymer with  $[Li]/[EO] = 0.1$  and  $[EMIM]/[EO] = 0.08$

The crystalline structure of the tri-component system is probed using WAXS. In Fig. 5.15 a) one can clearly see the well-known PEO crystal peaks at  $13.6\text{nm}^{-1}$  and  $16.5\text{nm}^{-1}$ , which are depicted by the gray solid lines. With the incorporation of [LiTf] in the lithium containing DBC/IL hybrid samples, the melting temperature of the PEO is decreased but still very distinct (Fig 5.15b)). PEO crystals hinder Li-ions to migrate through the PEO leading to a significantly decreased conductivity [4]. Our preliminary conductivity measurements indicate an improved ionic conductivity for crystal-free samples (Fig. 5.15 c)).

[1] J. W. Fergus, *J. Power Sour.* **195**, 4554-4569 (2010)

[2] G. Zardalidis, E. F. Ioannou, K. D. Gatsouli, S. Pispas, *Macromolecules* **48**, 1473-1482 (2015)

[3] G. B. Appetecchi, G. T. Kim, M. Montanio, F. Alessandrini, S. Passerini, *J. Power Sour.* **196**, 6703-6709 (2011)

[4] W. S. Young, W. F. Kuan, T. H. Epps, *J. Polym. Sci., Part B* **52**, 1-16 (2014)

## 5.9 Morphology of nanocomposite copolymer electrolytes for Li<sup>+</sup>/polymer batteries

K.N. Raftopoulos, M. Rasool, E. Metwalli, P. Müller-Buschbaum, C.M. Papadakis

Long scale, effective transition to green energy and wide distribution of electric and hybrid cars, demand for batteries with high energy and power density, good mechanical stability, as well as impact and temperature resistance. Speaking of electrochemical storage, lithium is the lightest of metals, and thus the element with the theoretically best charge to mass ratio. Thus, batteries utilizing it as the charge carrier are most promising in terms of achievable power and energy density.

Of crucial importance for the power density and the mechanical stability in these batteries is the electrolyte component. Poly(ethylene oxide) (PEO) has proven itself as a reliable electrolyte, but it has two significant drawbacks: 1) Its crystallinity, while providing some stability, acts as a barrier to the mobility of the Li cations. 2) It lacks adequate dimensional stability, especially if mixed with plasticizing moieties like salts. In this project, we use a block copolymer of PEO with polystyrene (PS), which is glassy at operational temperatures, in order to provide the desired dimensional stability. Bis-trifluoromethane sulfonimide (LiTFSI) was selected as the Li<sup>+</sup> salt to serve as the electrolyte.

Furthermore, a fraction of nanoparticles in the ion-conductive PEO phase may increase the conductivity. There are several mechanisms for that, including but not limited to: (i) The nanoparticles suppress crystallinity thus raise ion conductivity barriers [1], (ii) the particles may create paths of increased molecular and ion mobility at their interfaces with the polymer [2], and (iii) they may tailor the microphase separated morphology in a form favorable for ion transport, i.e. a bicontinuous structure [3]. For this reason, and in order to further improve dimensional stability, we introduced SiO<sub>2</sub> nanoparticles in the system. In this stage, we studied the thermal properties and the morphology of these materials, by means of differential scanning calorimetry (DSC) and X-ray scattering, respectively.

The samples were prepared by solution blending in THF. The PS-*b*-PEO copolymer had  $M_{w,PEO} = 54.2$  kDa, and  $M_{w,PS} = 29.2$  kDa. The molar Li<sup>+</sup>:EO ratio was 1:10. SiO<sub>2</sub> particles of nominal radius 14 nm were added with content up to 5 wt% with respect to the copolymer.

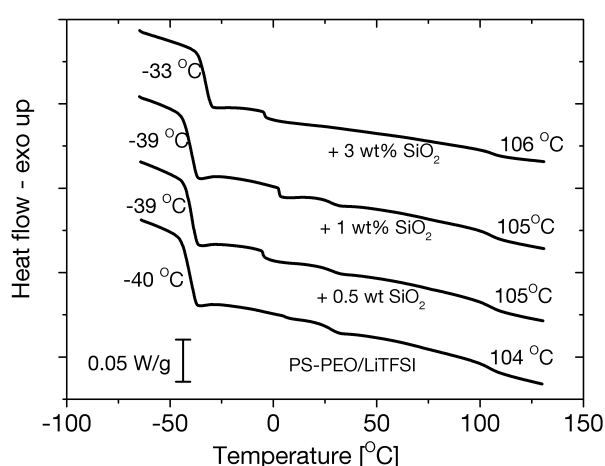


Figure 5.16: Differential scanning calorimetry curves recorded with the copolymer/Li<sup>+</sup> salt blend and selected composites, during heating. The glass transitions of the components (PEO around -40 °C, and PS around 105 °C) are indicated in the graph.

Fig. 5.16 shows the DSC curves of the unfilled copolymer electrolyte and the nanocomposites. In all cases, we observe two glass transition steps at -40 °C and 105 °C. These correspond to the PEO and PS component, respectively. This occurrence of two glass transitions is the first indication that the system is microphase-separated. The PS glass transition temperature  $T_{g,PS}$  remains unaffected by the nanoparticles. In contrast, the PEO glass transition temperature  $T_{g,PEO}$

increases moderately on addition of nanoparticles, which is interpreted as a slowing down of dynamics in the PEO-rich phase. Interestingly, no clear PEO melting peaks are observed around 60 °C, as expected for PEO. Instead, only broad end weak endotherms in the area of 20 °C are observed, indicating that the PEO crystallinity is already fully suppressed by the salt.

The combined SAXS-WAXS scattering curves are shown in Fig. 5.17. The pure copolymer shows Bragg reflections at  $q > 10 \text{ nm}^{-1}$  (wide angles) which are suppressed in the salt containing copolymer, confirming the observations by DSC. The presence of two amorphous halos in the same  $q$ -region is another indication of a microphase separated structure: the one at higher  $q$  values is related to the PEO-rich domains and the one at lower  $q$  values is related to the PS-rich domains.

The microphase-separated structure is observed in more detail at low  $q$  values (SAXS) as a pattern of diffraction maxima. The ratio of peak positions reveals the morphology of the system: the second maximum is always at a  $q$  value twice the first one ( $q^*$ ), indicating a lamellar morphology. The lamellar spacing (long period) can be calculated by the position of the peaks and is 54 nm for the pristine copolymer. The presence of the salt increases the lamellar spacing, presumably by swelling the PEO phase, but now the structures are less well defined as revealed by the broadening of the scattering maxima. 0.5 wt% of nanoparticles increases slightly the spacing, but more loading tends to decrease it to some extent. A loading of 5 wt% leads to a still microphase separated morphology, as revealed by the two amorphous halos, but the maxima are very broad, indicating less order in the microphase separation.

This work showed that 1:10  $\text{Li}^+:\text{EO}$  ratio is enough to completely suppress PEO crystallinity. The nanoparticles reside in the PEO phase and facilitate the formation of wider and well defined conductive paths.

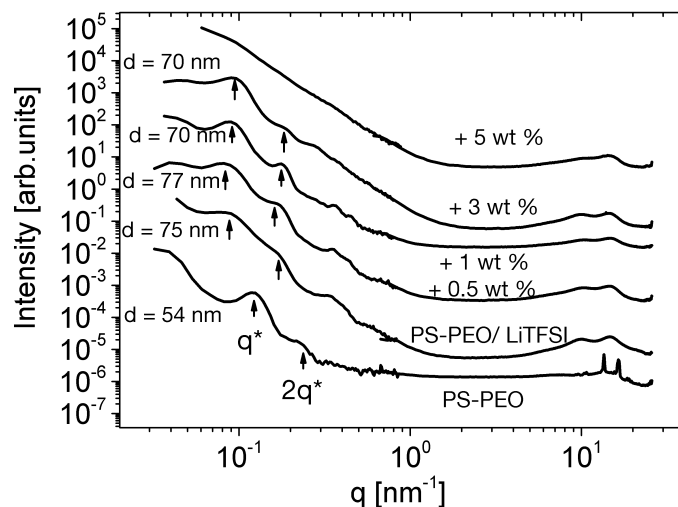


Figure 5.17:

X-ray scattering curves from PS-*b*-PEO, the PS-*b*-PEO/LiTFSI electrolyte, and the nanocomposites, at 30 °C. The  $q^*$  arrow indicates the position of the first SAXS peak and the  $q^*$  is drawn at  $q = 2q^*$ ; it coincides with a second peak indicating a lamellar structure. The calculated lamella-spacings are annotated on the plot.

K.N.R. was supported by the TUM University Foundation Fellowship.

- [1] C.-W. Nan, L. Fan, Y. Lin, Q. Cai, *Phys. Rev. Lett.* **91**, 266104 (2003)
- [2] F. Croce, G.B. Appetecchi, L. Persi, B. Scrosati, *Nature* **394**, 456-458 (1998)
- [3] I. Villaluenga, X.C. Chen, D. Devaux, D.T. Hallinan, N.P. Balsara, *Macromolecules* **48**, 358-364 (2015)

## 5.10 Self-assembled hybrid materials for lithium-ion batteries

S. Schaper, E. Metwalli, P. Müller-Buschbaum

Polymer solid electrolytes for rechargeable lithium-ion batteries have the potential to increase energy density by incorporating high Li-ions content, simplify production by just printing a battery, enhance lifetime by preventing dendrite formation and improve safety by using nonflammable materials.

In the present study, the structure conductivity relation for a high molecular weight polystyrene-*block*-poly(ethylene oxide) (PS-*b*-PEO) diblock copolymer (DBC) blended with bis(trifluoromethane)sulfonimide lithium salt (LiTFSI) is investigated.

Small and wide angle X-ray scattering (SAXS/WAXS) methods were used to probe the membrane morphology, while the conductivity was measured using potentiostatic electrochemical impedance spectroscopy (PEIS). To perform reproducible and reliable conductivity measurements we designed a new measurement cell for solution-casted films. A sketch of the cell is shown in Fig. 5.18.

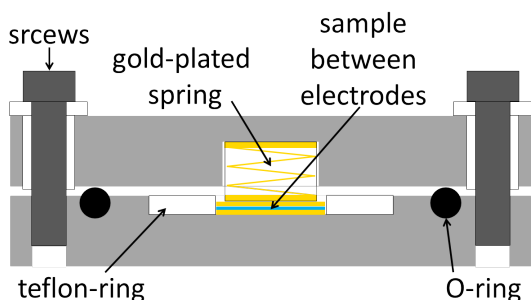


Figure 5.18:

Profile of the measurement cell for impedance spectroscopy. The sample is sandwiched between two gold-plated electrodes. The electrode/electrolyte assembly is enclosed between the two stainless steel parts of the cell.

Due to the extremely hygroscopic nature of the Li-salt, all samples were prepared in a glove box under an argon atmosphere. The PS-*b*-PEO DBC (16.4 kg/mol PS, 110 kg/mol PEO, PDI = 1.08) with a PEO fraction of 0.87 was chosen to have a large volume ion-conducting soft PEO domain. The PEO block is known to crystallize at room temperature [1] having a melting temperature and crystallization temperature of  $T_m = 64^\circ\text{C}$  and  $T_c = 40^\circ\text{C}$ , respectively. The glassy PS block provides mechanical stability in the solid electrolyte. The lithium salt LiTFSI was chosen because of the large TFSI<sup>-</sup> anion, which has a very small mobility compared to the Li-ion. Therefore we can get a better charge separation and an enhanced Li<sup>+</sup> conductivity. The polymer films were solution-casted either on a gold-plated copper electrode for conductivity measurements or on a mica window for SAXS/WAXS measurements. The samples were dried and thermally annealed overnight before the measurements.

The SAXS/WAXS measurements were performed at sample-detector distances of 1051 mm and 101 mm, respectively. Conductivity measurements were performed with a SP-150 potentiostat (Bio-logic) in a frequency range from 1 Hz to 1 MHz.

Metwalli et al. [2] recently investigated the influence of Li-salt on the structure and conductivity of a high molecular weight PS-*b*-PEO diblock copolymer (DBC) (PEO fraction of 0.67). They reported that at the Li-salt loading level of  $[\text{Li}]/[\text{EO}] = 0.1$  in the PS-*b*-PEO, the PEO crystallization was suppressed, while a self-assembled lamella microstructure for all employed temperatures was pertained. Villaluenga et al. [3] considered a DBC structure with a continuous percolating path for Li<sup>+</sup> as ideal for a good conductivity in polymer solid electrolytes.

Fig. 5.19 shows the SAXS measurements of the bare and the lithium containing PS-*b*-PEO DBC. The corresponding WAXS measurements show only peaks corresponding to PEO crystallites for

the bare DBC from 25°C to 55°C (data is not shown).

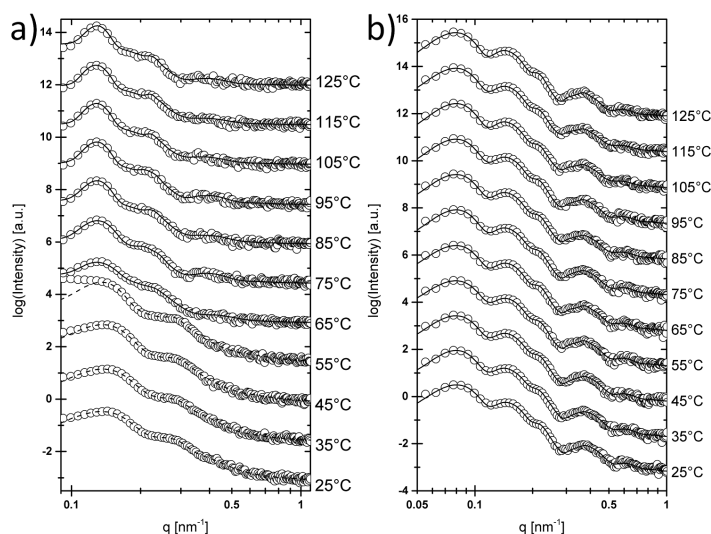


Figure 5.19: SAXS measurements for the a) bare PS-*b*-PEO DBC and b) PS-*b*-PEO with LiTFSI ([Li]/[EO] = 0.1) heated from 25°C to 125°C. Data points (circles) were fitted with either lamella (dashed line) or cylinders (line) using the scatter software.

With melting of the PEO crystals in the bare PS-*b*-PEO DBC, a change in the self-assembled morphology from a lamella to a cylinder morphology between 55°C and 65°C is observed. For lithium-salt content of [Li]/[EO] = 0.1, PEO crystallization is prohibited over the employed temperature range and the DBC forms a cylindrical structure with an increased periodic distance (86 nm) compared to the Li-free DBC (54 nm).

The transition from lamella to cylinders offers a continuous percolation path for the Li<sup>+</sup>, which leads to a large increase in the ionic conductivity shown in Fig. 5.20.

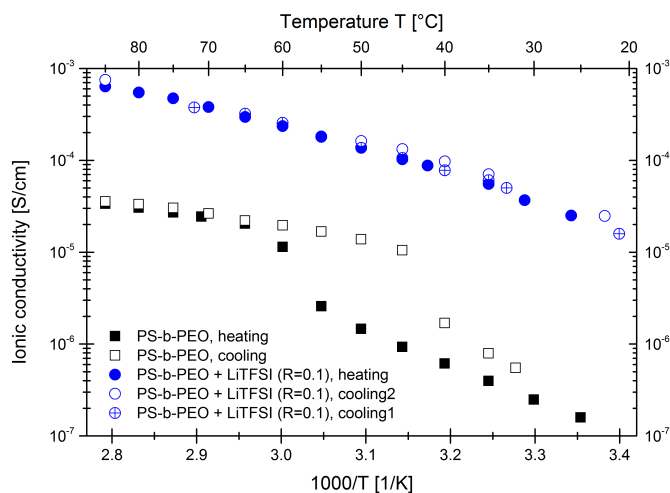


Figure 5.20: Conductivity data for bare PS-*b*-PEO (squares) and lithium-salt containing PS-*b*-PEO (circles) with [Li]/[EO] = 0.1. Heating (solid) and cooling cycles (open symbols) are presented.

For the pure DBC we see a hysteresis with a drop, which is related to the different melting and crystallization temperatures of the PEO crystals. The ionic conductivity increases with temperature due to the improved mobility of the Li<sup>+</sup>. With Li-salt at [Li]/[EO] = 0.1, the hysteresis and the drop in conductivity vanishes. As conclusions, upon lithium salt incorporation, the PEO crystallization is suppressed, while the ionic conductivity is enhanced. Such Li-containing DBC electrolyte will be further implemented as a solid-state electrolyte in Li-ion battery cell assembly, followed by a comprehensive evaluation of the battery performance.

- [1] Y. Takahashi, H. Tadokoro, *Macromolecules* **6**, 672-675 (1973)
- [2] E. Metwalli, M. Rasool, S. Brunner, P. Müller-Buschbaum, *Chem. Phys. Chem.* **16**, 2882-2889 (2015)
- [3] I. Villaluenga, X. C. Chen, D. Devaux, D. T. Hallinan, N. P. Balsara, *Macromolecules* **48**, 358-364 (2015)

### 5.11 In situ DC-sputter deposition of Al on PS templates

S. V. Roth<sup>1</sup>, M. Schwartzkopf<sup>1</sup>, G. Singh<sup>1</sup>, O. Polonskyi<sup>2</sup>, A. Hinz<sup>2</sup>, T. Strunskus<sup>2</sup>, F. Faupel<sup>2</sup>, V. Körstgens, F. Löhner, E. Metwalli, P. Müller-Buschbaum

<sup>1</sup> DESY, Hamburg, Germany

<sup>2</sup> CAU, Kiel, Germany

The nanostructure of metallic layers affects their desired functionality. This ranges from the isolated island regime in sensors [1] and organic photovoltaic cells [2], where plasmonic effects are used for detecting single molecules or to enhance light absorption, to full scale contacts well beyond the percolation threshold [3]. Therefore, it is indispensable to understand the metallic layer growth on polymeric templates during industrial relevant deposition conditions. In the present study, we focus on DC sputter deposition, being a versatile metal deposition method. We investigate the metal layer growth from the nucleation phase to the coalescence and beyond the percolation threshold. As one crucial parameter we use a bias voltage during the deposition, which enables us to tune the energy of the impinging metal atoms.

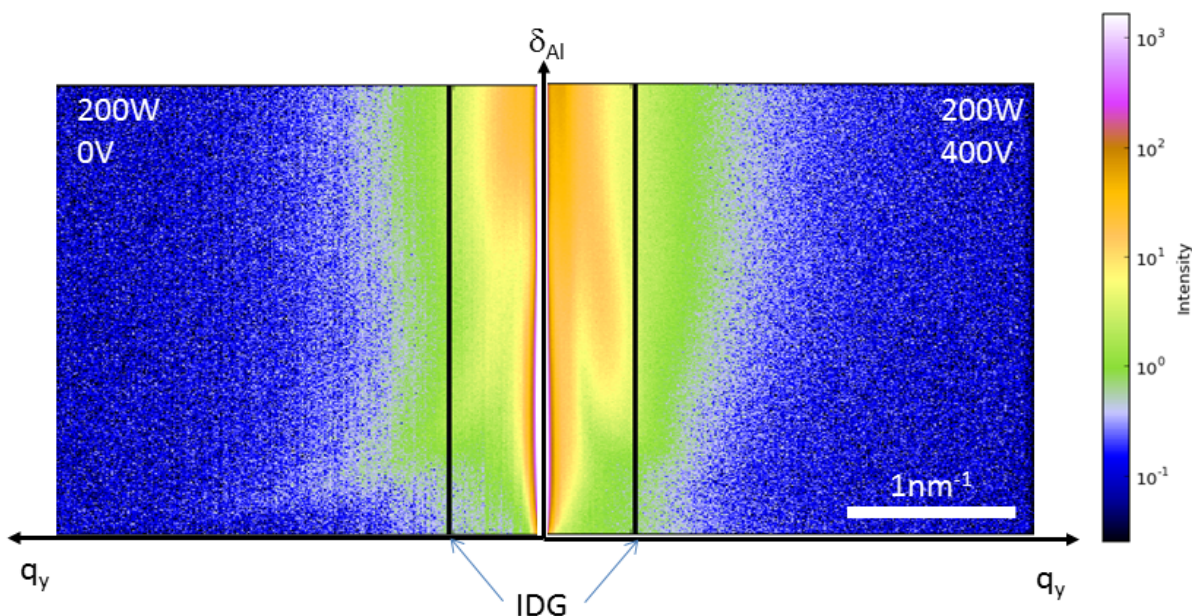


Figure 5.21:

Comparison of  $q_y$ - $\delta_{Al}$  maps of the growing Al layer on top of the PS template. The DC sputter power as well as the bias voltage are indicated.  $\delta_{Al}$  denotes the growth Al layer thickness.

As particular, but at the same time industrial relevant model system, we use aluminum (Al) as metal and polystyrene as polymer, often used as dielectric in electronics. The polystyrene (PS) template was deposited on a pre-cleaned silicon (Si) wafer using spin-coating. In order to investigate in-situ and in real time the growth of the Al layer on top of the PS template, we use the advanced scattering technique grazing incidence small-angle X-ray scattering (GISAXS) [4] at the beamline MiNaXS /P03 of DESY, Hamburg, Germany [5,6]. A DC sputter deposition chamber was incorporated into the beamline. The beam size was  $32 \times 25 \mu\text{m}^2$ , the X-ray wavelength  $0.9525 \text{ \AA}$ , and the sample to detector distance (SDD) set to 2387 mm. A two-dimensional (2D) pixel detector PILATUS 1M (Dectris, Switzerland) with a pixel size of  $172 \mu\text{m}$  was used. The sputter rate was estimated to  $4.8 \pm 0.1 \text{ \AA s}^{-1}$ . The sputter power was set to 200W. Argon (Ar) pressure was 0.005 mbar. Two bias voltages were used ( $U_B = 0 \text{ V}$  and 400

V). Data analysis was performed using DPDAK [7].

In Fig. 5.21 we present a first analysis of the growth regimes with  $U_B = 0$  V and 400 V. The maps present the intensity distribution along  $q_y$  in the so-called out-of-plane cut at the position of the Al Yoneda peak [8], thus depicting the evolution of the structure and morphology of the Al layer parallel to the substrate surface during deposition. Clearly, the use of a bias voltage alters the growth behavior. At  $U_B = 400$  V, it seems the Al nanoparticle growth starts delayed, but more pronounced. Moreover, atomic force microscopy (AFM) indicates the installation of larger nanoparticles at  $U_B = 400$  V. Additionally, we monitored the crystallinity of the growing Al layer using grazing incidence wide-angle X-ray scattering (GIWAXS) and a Lambda detector, DESY, [9] and the optical response using a custom-designed single wavelength ellipsometer (DRE GmbH, Germany) at the same time. The detailed analysis is ongoing.

To summarize, for the first time, we are able to observe the growth of Al on top of a PS template at industrial relevant rates using the unique combination of in-situ DC-sputter deposition, GISAXS, GIWAXS and ellipsometry. This enables comparative analysis of the influence of the different deposition parameters.

The authors acknowledge the Deutsche Forschungsgemeinschaft (DFG) for funding under projects RO 4638/1-1, FA 234/23-1, and MU 1487/18-1. Parts of this research were carried out at the light source PETRA III at DESY, a member of the Helmholtz Association (HGF).

- [1] G. Santoro, S. Yu, M. Schwartzkopf, P. Zhang, S. K. Vayalil, J. F. H. Risch, M. A. Rübhausen, M. Hernandez, C. Domingo, S. V. Roth, *Appl. Phys. Lett* **104**, 243107 (2014)
- [2] S. Pillai, M. A. Green, *Sol. Energy Mater. Sol. Cells* **94**, 1481-1486 (2010)
- [3] C. J. Schaffer, C. M. Palumbiny, M. A. Niedermeier, C. Jendrzewski, G. Santoro, S. V. Roth, P. Müller-Buschbaum, *Adv. Mater.* **25**, 6760-6764 (2013)
- [4] P. Müller-Buschbaum, *Anal. Bioanal. Chem.* **376**, 3-10 (2003)
- [5] A. Buffet, A. Rothkirch, R. Döhrmann, V. Körstgens, M. M. Abul Kashem, J. Perlich, G. Herzog, M. Schwartzkopf, R. Gehrke, P. Müller-Buschbaum, S. V. Roth, *J. Synchr. Radiation* **19**, 647-653 (2012)
- [6] M. Schwartzkopf, G. Santoro, C. J. Brett, A. Rothkirch, O. Polonskyi, A. Hinz, E. Metwalli, Y. Yao, T. Strunskus, F. Faupel, P. Müller-Buschbaum, S. V. Roth, *ACS Appl. Mater. Interfaces* **7**, 13547-13556 (2015)
- [7] G. Benecke, W. Wagermaier, C. Li, M. Schwartzkopf, G. Flucke, R. Hoerth, I. Zizak, M. Burghammer, E. Metwalli, P. Müller-Buschbaum, M. Trebbin, S. Förster, O. Paris, S. V. Roth, P. Fratzl, *J. Appl. Cryst.* **47**, 1797-1803 (2014)
- [8] Y. Yoneda, *Phys. Rev.* **131**, 2010-2013 (1963)
- [9] J. Perlich, J. Rubeck, S. Botta, R. Gehrke, S. V. Roth, M. A. Ruderer, S. M. Prams, M. Rawolle, Q. Zhong, V. Körstgens, P. Müller-Buschbaum, *Rev. Sci. Instr.* **81**, 105105 (2010)

## 5.12 Structure and properties of metal oxide-block copolymer nanocomposites

E. Metwalli, M. Bahr, M. Opel<sup>1</sup>, C. Himmelsbach<sup>2</sup>, E. Ember<sup>2</sup>, J. A. Lercher<sup>2</sup>, P. Müller-Buschbaum

<sup>1</sup> WMI, Garching, Germany

<sup>2</sup> Department of Chemistry and Catalysis Research Center, Garching, Germany

Metal oxide-polymer nanocomposites are important materials due to their unique electrical, optical and magnetic properties [1-5]. Diblock copolymers (BC) are the matrix of choice for providing the desired arrangement of the metal oxide nanoparticles (NPs), since they develop nanostructures via microphase separation and self-assembly processes. There are several routes for fabrication of highly dispersed, well-ordered metal-oxide nanoparticles in polymer matrix. One route is using a mixture of block copolymer and a transition metal-salt solution to prepare either bulk or thin film samples. Due to the high metal-ion selectivity to one block of the block copolymer, well-ordered metal ions within the polymer matrix can be achieved. Following the thermal decomposition of the transition metal salt within the solid polymer matrix, the desired well-ordered metal oxide nanoparticles-block copolymer nanocomposites is obtained. In the current report, diblock copolymer poly(styrene-*b*-methylmethacrylate) (PS-*b*-PMMA), which forms a lamellar structure, and a cobalt salt based on a 2,2' bipyridine ring ( $C_{10}H_8Cl_2CoN_2$ ) were employed to prepare nanoparticles-BC hybrid materials. Bulk and thin film samples were prepared with different [Co]/[PMMA] molar ratios via solution-casting and spin-coating methods, respectively. Samples were prepared at room temperature and thermally post-treated at 150°C for 4 days. The structural evolution of the bulk samples was investigated as a function of both Co salt doping level and temperature using small-angle X-ray scattering (SAXS). Additionally, the morphology of the corresponding thin film samples were probed using grazing incidence small-angle X-ray scattering (GISAXS) and atomic force microscopy (AFM). A lamellar structure was observed for all samples in both bulk and thin film formats (Figs. 5.22 & 5.23), as indicated from the emerging scattering peaks with  $q/q^*$  ratios of 1, 2, and 3.

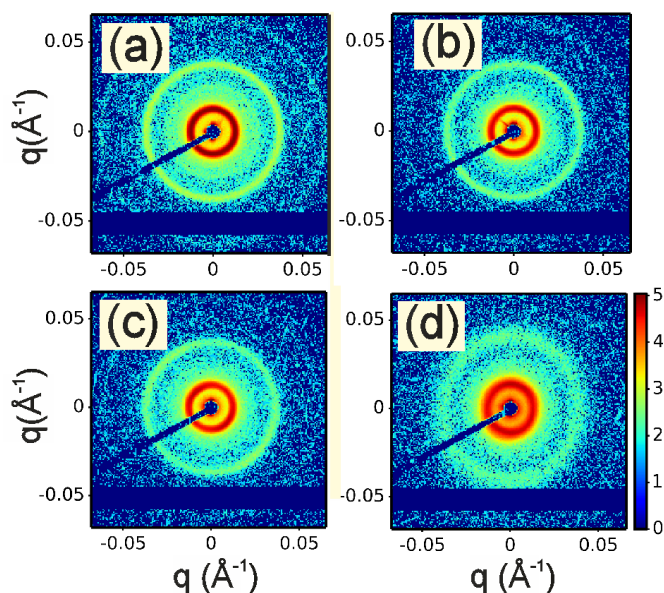


Figure 5.22: 2D SAXS patterns of metal oxide nanoparticles-BC nanocomposites with various [Co]/[PMMA] ratios: a) 0, b) 0.017, c) 0.025, d) 0.085. Three prominent scattering rings can be observed, indicating the formation of lamella morphology.

The X-ray photoelectron spectroscopy measurements indicated the formation of the metal-oxide nanoparticles in the form of  $CoO_2$  following the heat-treatment step of the metal salt-BC hybrid materials. Additionally, AFM data clearly indicated that the lamella morphology of the nanocomposite films (Fig. 5.23). Both bulk and thin film metal oxide-BC nanocomposites showed a similar trend of the inter-domain spacing  $D$  with increasing the [Co]/[PMMA] ratios.

A relatively small decrease in the lamella spacing  $D$  upon increasing the Co salt doping level is due to a possible charge cohesion effect ( $\text{Co}^{2+}$  and the carbonyl groups on the PMMA chains). At slightly higher concentration,  $[\text{Co}]/[\text{PMMA}] = 0.085$ , the FWHM of these scattering peaks became much broader, indicating the formation of less ordered morphologies.

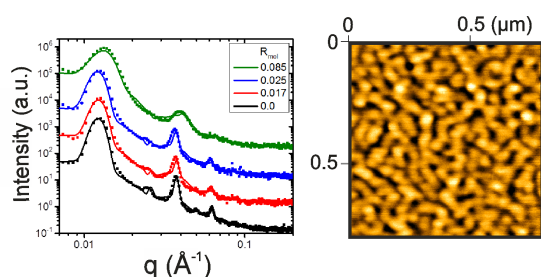


Figure 5.23: 1D SAXS profiles of metal oxide NPs-BC nanocomposites with various  $[\text{Co}]/[\text{PMMA}]$  ratios; from bottom to top viz., 0, 0.017, 0.025, and 0.085. The curves are shifted along the y axis for clarity of the presentation.

The magnetic properties of the metal oxide NPs-BC hybrid films were also investigated (Fig. 5.24) at different temperatures using superconducting quantum interference device. Consistence with our previous investigation [1] with iron oxide NPs in perforated lamella forming structures, a temperature dependent saturation magnetization is observed. At high temperatures, a hysteresis can also be detected. For super-paramagnetic material such a magnetic hysteresis behavior occurs only at low temperatures. Due to hysteresis at room temperature the thin film has ferro- or ferrimagnetic properties. This leads to sizes of cobalt complexes bigger than a magnetic domain. Further evaluation of the magnetic measurements is still in progress.

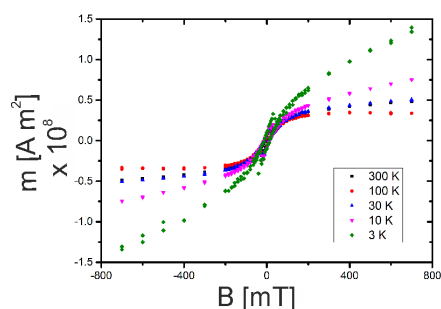


Figure 5.24: Magnetic properties of metal oxide NPs-BC hybrid films with  $[\text{Co}]/[\text{PMMA}]$  ratio of 0.10. Magnetization ( $M$ ) versus magnetic field ( $B$ ) measured at different temperatures.

In conclusion, this current simple methodology enables fabrication of metal oxide NPs-polymer hybrid nanostructured material with desirable final functionality owing to the ability to control the evolved NPs distribution in the polymer matrix. The overall combination of certain types of metal-oxide nanoparticles as well as the features of these matrices will offer a wide range of possible applications and functionalities.

- [1] Y. Yao, E. Metwalli, J.-F. Moulin, B. Su, M. Opel, P. Müller-Buschbaum, *ACS Appl. Mater. Interfaces* **6**, 18152-18162 (2014)
- [2] E. Metwalli, I. Krisch, I. Markovits, M. Rawolle, M.A. Ruderer, S. Guo, S. Wyrzgol, A. Jentys, J. Perlich, J.A. Lercher, P. Müller-Buschbaum, *ChemPhysChem* **15**, 2236-2239 (2014)
- [3] Y. Yao, E. Metwalli, M.A. Niedermeier, M. Opel, C. Lin, J. Ning, J. Perlich, S.V. Roth, P. Müller-Buschbaum, *ACS Appl. Mater. Interfaces* **6**, 5244-5254 (2014)
- [4] Y. Yao, E. Metwalli, B. Su, V. Körstgens, D. Mosegui Gonzalez, A. Miasnikova, A. Laschewsky, M. Opel, G. Santoro, S.V. Roth, P. Müller-Buschbaum, *ACS Appl. Mater. Interfaces* **7**, 13080-13091 (2015)
- [5] E. Metwalli, V. Körstgens, K. Schlage, R. Meier, G. Kaune, A. Buffet, S. Couet, S. V. Roth, R. Röhlberger, P. Müller-Buschbaum, *Langmuir* **29**, 6331-6340 (2013)

### 5.13 Printed diblock copolymer films with embedded magnetic nanoparticles

S. Xia, E. Metwalli, Y. Yao, M. Opel<sup>1</sup>, P. Müller-Buschbaum

<sup>1</sup> WMI, TU München, Garching, Germany

Nanocomposites composed of metal-oxide nanoparticles and polymers are important materials, owing to their unique optical, magnetic and electrical properties, enabling a wide range of applications such as solar cells, sensors, biomedical imaging, drug delivery and high-density magnetic storage devices [1-4]. Having been established and employed for many years, printing proves to be an easy and effective method for film preparation on various solid supports. In the present work, the printing method was applied to prepare polystyrene-*b*-polymethyl methacrylate, denoted PS-*b*-PMMA with embedded PS-coated maghemite ( $\gamma$ -Fe<sub>2</sub>O<sub>3</sub>) nanoparticles (NPs). The hybrid films are prepared and then organic solvent vapor-annealed under an applied external magnetic field. The metal oxide NPs-block copolymer nanocomposite films were investigated using optical microscopy (OM), scanning electron microscopy (SEM) and grazing incidence small angle x-ray scattering (GISAXS). Fig. 5.25 shows the formation of metal-oxide wires in the hybrid films that are highly oriented along the direction of external magnetic field. The number per unit surface as well as the width and length of the metal-oxide NP wires increases with the NP doping level.

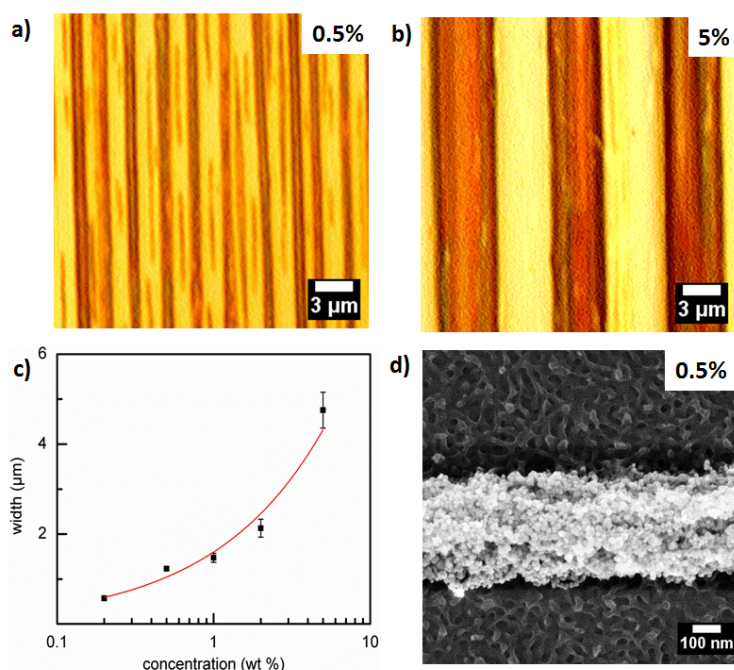


Figure 5.25:

a, b) Optical microscopy images of NPs-block copolymer hybrid films with 0.5 and 5 wt% NP concentration, c) extracted widths of NP aggregates (wires) as a function of NP concentration (the solid line serves as a guide to the eye), d) SEM images of the hybrid film with 0.5 wt% NP concentration. NP clusters and the wire-shaped NP aggregates (white) are clearly observed.

As seen in Fig. 5.25, the SEM image shows the NP aggregates forming the micro-scale sized metal oxide wires. Additionally, SEM proved the evolved nanostructure of the hybrid films due to the micro-phase separation process.

Fig. 5.26a exhibits the 2D GISAXS data of the metal oxide NPs-block copolymer hybrid films for different NP concentrations. For a quantitative analysis, horizontal line cuts from the 2D GISAXS data were plotted with the corresponding fits in Fig. 5.26b. Different main scattering features are observed, which are marked as I, II and III. The GISAXS study indicates that at low NP loading, the NPs are selectively dispersed in the PS domains due to the selective nature of the PS-coating of the NPs towards the PS block. At high NPs concentration, an increase of the inter-domain periodic distance  $D$  is observed.

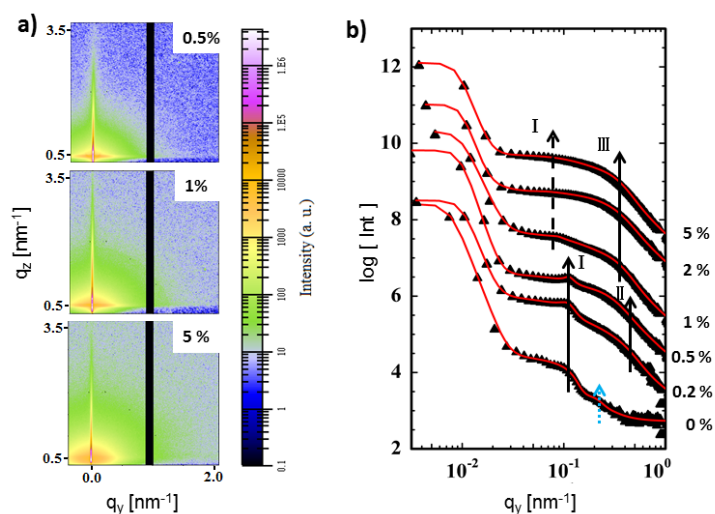


Figure 5.26: a) Selected 2D GISAXS data, b) horizontal line cuts of the 2D GISAXS data (triangle symbols) and corresponding fits (solid lines) of the metal oxide NPs-block copolymer nanocomposite films with different NP concentrations as indicated.

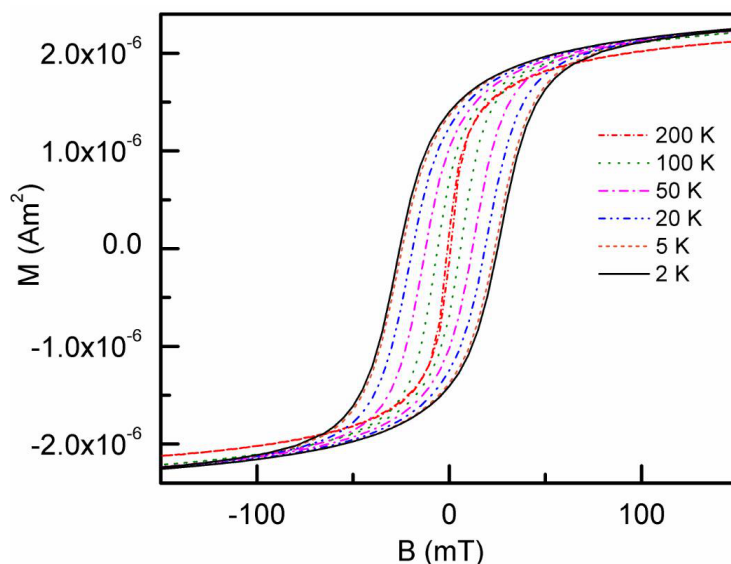


Figure 5.27: Magnetic moments measured as a function of the external magnetic field with a parallel orientation at different temperatures for a selected sample with 5 wt% NPs.

Magnetic measurements were collected using a superconducting quantum interface device (SQUID). Fig. 5.27 shows the magnetic hysteresis at low temperatures. With increasing temperature, the coercive fields become much smaller, as well as the remanence decreases. Thus, the hybrid films show a superparamagnetic behavior, which renders such materials promising in applications related to magnetic sensors.

- [1] Y. Yao, E. Metwalli, B. Su, V. Körstgens, A. Miasnikova, M. Opel, S V. Roth, P. Müller-Buschbaum, *ACS Appl. Mater. Interfaces* **7**, 13080-13091 (2015)
- [2] Y. Yao, E. Metwalli, J. F. Moulin, B. Su, M. Opel, P. Müller-Buschbaum, *ACS Appl. Mater. Interfaces* **6**, 18152-18162 (2014)
- [3] Y. Yao, E. Metwalli, M. A. Niedermeier, M. Opel, C. Lin, J. Ning, J. Perlich, S V. Roth, P. Müller-Buschbaum, *ACS Appl. Mater. Interfaces* **6**, 5244-5254 (2014)
- [4] E. Metwalli, I. Krisch, I. Markovit, M. Rawolle, M. A. Ruderer, S. Guo, S. Wyrzgol, A. Jentys, J. Perlich, J. A. Lercher, P. Müller-Buschbaum, *Chem. Phys. Chem* **15**, 2236-2239 (2014)

### 5.14 Parallel lamella via self-assembly of PSd-*b*-PBMA with embedded maghemite nanoparticles

Y. Yao, E. Metwalli, J. -F. Moulin<sup>1</sup>, M. Haese-Seiller<sup>1</sup>, P. Müller-Buschbaum

<sup>1</sup> FRM II, Garching, Germany

Diblock copolymers (DBC)s with incorporated nanoparticles (NPs) comprise one novel class of hybrid nanocomposites for potential applications of functional nanodevices. The control over the alignment of the NPs within structure directing DBC template is crucial for fabricating highly-oriented metal-polymer nanopatterns. In the current investigation, we have studied well-aligned highly-periodic hybrid films, consisting of polystyrene(*d*-deuterated)-*block*-polybutyl methacrylate (PSd-*b*-PBMA) symmetric lamellar DBC and maghemite NPs. The local surface structures of the hybrid films were characterized with AFM. The depth-dependent morphology of the micro-phase separation structures were probed with time-of-flight grazing incidence small angle neutron scattering (TOF-GISANS).

The DBC-NPs hybrid films were fabricated by spin-coating in combination with thermal annealing at 160 °C for 72 hours in N<sub>2</sub> atmosphere. The pre-cut silicon substrates were cleaned in an acid bath (H<sub>2</sub>SO<sub>4</sub> 200 mL, H<sub>2</sub>O<sub>2</sub> 70 mL and H<sub>2</sub>O 130 mL) at 80 °C for 15 min. Toluene was chosen as solvent. DBC-NPs solutions with different weight ratios of NPs vs. DBC (0, 0.1, 0.5, 1, 3, 7, and 15 wt%) were prepared. Concentration of DBC was fixed at 36 mg/mL.

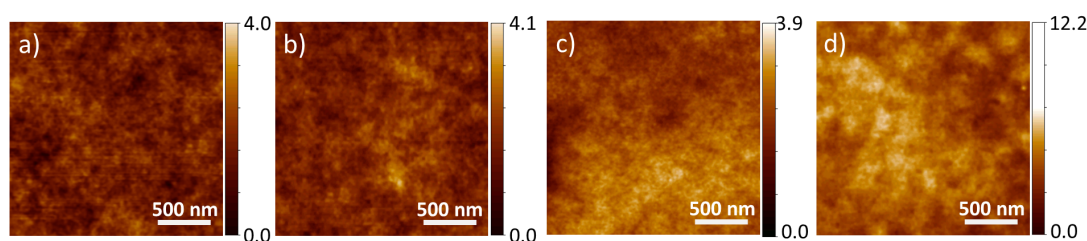


Figure 5.28: AFM topographical images of hybrid films at different NP concentrations: a) 0, b) 0.5, c) 3, and d) 15 wt%.

As the NP concentration increases from 0 to 15 wt%, the film thickness expands from 228.1 to 255.2 nm. Fig. 5.28 shows AFM topographical images of the film surfaces, where no feature of perpendicular (with respect to film surface) lamellar structure is found. At high NP concentration (15 wt%, Fig. 5.28b), large NP aggregates formed on the film surface.

In TOF-GISANS measurements, different neutron wavelengths  $\lambda$  probe different depths of the investigated hybrid film. The penetration depth of the neutron beam decreases with increasing neutron wavelength. Fig. 5.29a shows vertical line cuts made from 2D GISANS data at all probed wavelength channels for a selected sample of NP-free DBC film. In general, two distinct Yoneda peaks are observed. They increase linearly with increasing wavelength. Moreover, four different slopes for the Bragg peaks are found. To quantify the effect of NP concentration on the inner film morphology, a deeper analysis is applied. For hybrid films with different NP concentrations, vertical line cuts at all wavelength channels are made. Further, for selected films, the positions of characteristic Yoneda and Bragg peaks observed from the vertical cuts have been extracted and plotted in Fig. 5.29 b-d and e-f, respectively. The difference of the Yoneda peak positions proves the contained chemical components of the films due to their contribution of the scattering signal with a Yoneda peak. For the DBC template (Fig. 5.29b), three series of Yoneda peaks are observed, which follow the theoretical critical angles of Si, PS-*b*-PBMA and PSd from

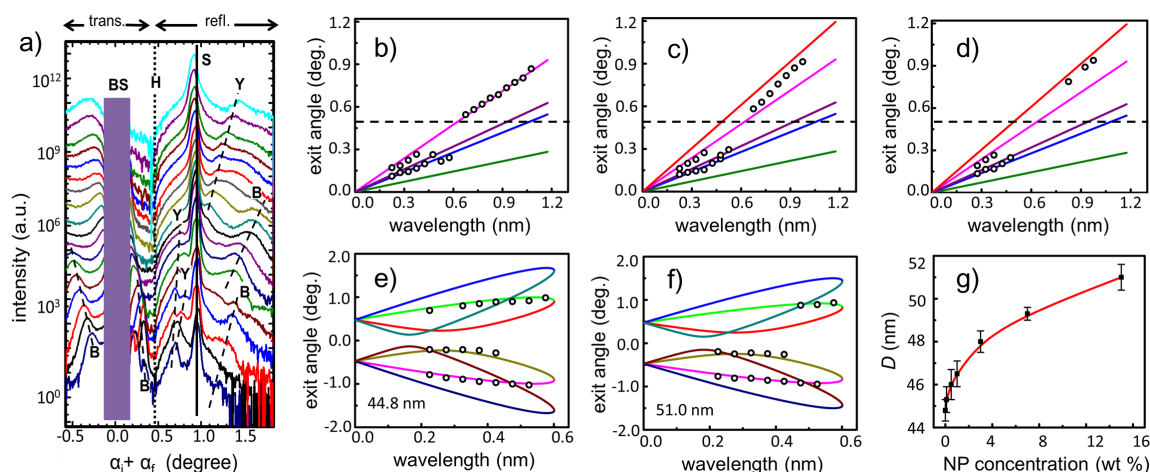


Figure 5.29:

a) Vertical line cuts made from 2D GISANS data at all measured channels for NP-free DBC film vs. angle ( $\alpha_i + \alpha_f$ ) recorded on the detector. The trend of Yoneda peaks (Y) and Bragg peaks (B) is guided with dashed lines. For clarity, all cuts are shifted against  $y$  axis as the neutron wavelength increases from bottom to top: 0.225, 0.275, 0.325, 0.375, 0.425, 0.475, 0.525, 0.575, 0.625, 0.675, 0.725, 0.775, 0.825, 0.875, 0.925, 0.975, 1.025, and 1.075 nm. Extracted Yoneda peak positions from corresponding vertical line cuts of hybrid films with different NP concentration (b) 0, c) 7, and d) 15 wt%) are plotted with open circles. Theoretical critical angles are shown for including chemical components of maghemite (red line), PSd (pink line), PSd-*b*-PBMA (purple line), Si (blue line) and PBMA (green line). The specular peak positions ( $\alpha_i = \alpha_f$ ) are pointed out with the horizontal dashed line. Extracted Bragg peak positions from corresponding vertical line cuts of hybrid films with different NP concentrations (e) 0 and f) 15 wt%) are plotted with open circles. Calculated Bragg peak positions with different inter-domain distance  $D$  (e) 44.8 and f) 51.0 nm) are plotted with solid lines. g) The inter-domain distance  $D$  extracted from corresponding fits of Bragg peaks vs. wavelength.

bottom to top. In Fig. 5.29b-d, at low and intermediate wavelengths, NP concentration has weak effect on the Yoneda peaks. However, at longer wavelengths, a significant change of the Yoneda peaks is found. In Fig. 5.29b, the Yoneda peaks follow the theoretical critical angle of PSd. It suggests that a PSd layer at the film/air interface presents in NP-free DBC film. As NP concentration increases, the Yoneda peaks move towards higher angles and approach the maghemite line. Such behavior arises from the selectively incorporated NPs in the PSd domains, since a PSd layer at the film/air interface is proven. Moreover, the Bragg peak positions obtained from the selected films are shown together with their best fits in Fig. 5.29e,f. The fits indicate the inter-domain distance of the parallel lamellar structures. In Fig. 5.29g, the inter-domain distance of each NPs/PSd-PBMA hybrid layer expands from 44.8 to 51.0 nm as the NP concentration increases from 0 to 15 wt%. The increasing trend of the inter-domain distance keeps consistent with the film thickness.

From additional horizontal line cuts (not shown) made from hybrid films at all probed NP concentrations, broadly distributed perpendicular PSd domains (250 nm) are found and slightly expands within 8 nm as NP concentration increases from 0 to 15 wt%. The expansion results from selectively incorporated NPs inside their favorable PSd domains, since only very few perpendicular PSd domains are present in the PBMA parallel lamella layers.

To conclude, a morphology of highly ordered, well parallel orientated lamellae with very few perpendicular defects is established. With a small amount of NPs incorporated, NPs are well arranged inside the PSd domains. However, at high NP concentrations, previous long-range ordered morphology has been perturbed with relatively large NP aggregates.

### 5.15 Spray deposition of titania films with incorporated crystalline nanoparticles

L. Song, W. Wang, V. Körstgens, D. Moseguí González, Y. Yao, N. K. Minar<sup>1</sup>, J. M. Feckl<sup>1</sup>, K. Peters<sup>1</sup>, T. Bein<sup>1</sup>, D. Fattakhova-Rohlfing<sup>1</sup>, G. Santoro<sup>2</sup>, S. V. Roth<sup>2</sup>, P. Müller-Buschbaum

<sup>1</sup> Department of Chemistry and CeNS, LMU, München, Germany

<sup>2</sup> DESY, Hamburg, Germany

Nanostructured titania films have been widely used in a variety of applications such as photovoltaics, photocatalysis, and gas sensing. The main advantages are related to their unique properties such as good scattering effect, high dielectric constant, chemical and biological inertness and long-term stability. The crystalline phase of titanium oxide, especially its anatase polymorph, has been studied extensively in photovoltaic applications. The optical and electrical properties could be tuned by its morphology, crystallinity and particle size. In order to obtain more efficient titania photoanodes, we modify nanostructured titania films with incorporating crystalline anatase nanoparticles into the interconnected titania network in the present work.

Titania films could be fabricated via many techniques as described in the literature, among which the block copolymer assisted sol-gel synthesis in combination with spray coating is very promising. In this approach, the block copolymer assisted sol-gel synthesis is used to produce titania nanostructures. A so-called good-poor solvent pair induced micro-phase separation of the diblock copolymer allows for controlling the titania size and mesopores of the final titania films. Moreover, the sol-gel method allows for uniformly incorporating anatase particles into the titania nanostructure. Spray-coating is used to convert titania solution into titania solid films [1]. It allows for film deposition directly from the sol-gel solution and yields mesoporous films. Furthermore, spray coating is simple, low cost and enables the production of films on almost any surface at large scale.

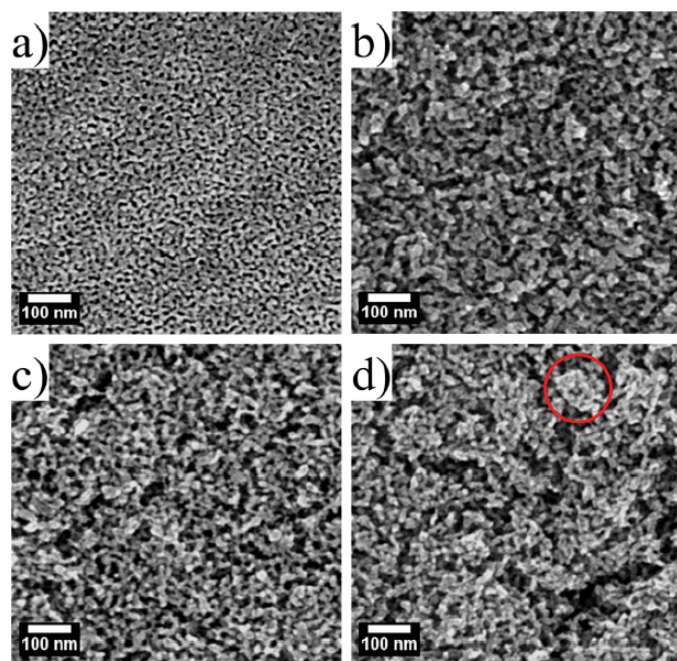


Figure 5.30: SEM images of composite titania films containing a) 0, b) 25%, c) 50% and d) 75% of titania anatase nanoparticles after 500 °C calcination.

In this work we focus on the influence of pre-synthesized crystalline titania nanoparticles on the properties of titania films. Four films with different amounts of anatase nanoparticles were manufactured. The weight ratio of sol-gel induced titania and anatase nanoparticles are 1:0,

3:1, 1:1, 1:3 (denoted as 0wt.%NPs, 25wt.%NPs, 50wt.%NPs, and 75wt.%NPs, respectively). After spray deposition the films were calcined at 500 °C for 2h. The surface morphology of the films is determined by scanning electron microscopy (SEM) and the results are illustrated in Fig. 5.30. All the SEM images demonstrate porous sponge-like morphologies, irrespective of the different amounts of anatase nanoparticles introduced, suggesting that spray deposition can also generate regular interconnected network as compared to spin coating. The 0wt.%NPs film has smallest pores with pore sizes of around 10 nm. The pore size increases with increasing the nanoparticle concentration. In both, 25wt.%NPs and 50wt.%NPs films, a 3D-mesostructural arrangement and pore sizes of about 20 nm can be observed. While less homogeneous films are achieved with a further increase of nanoparticles concentration to 75 wt.%. It is noticeable that some film areas differ in pore size. A possibility for this feature is the dominant existence of nanoparticles in the titania film, which tend to aggregate rather than being incorporated into the templated titania network structure. A nanoparticle cluster is seen clearly in Fig. 5.30 d) as indicated by a red circle, which is the evidence of nanoparticles aggregation as it only be observed at high nanoparticle loading.

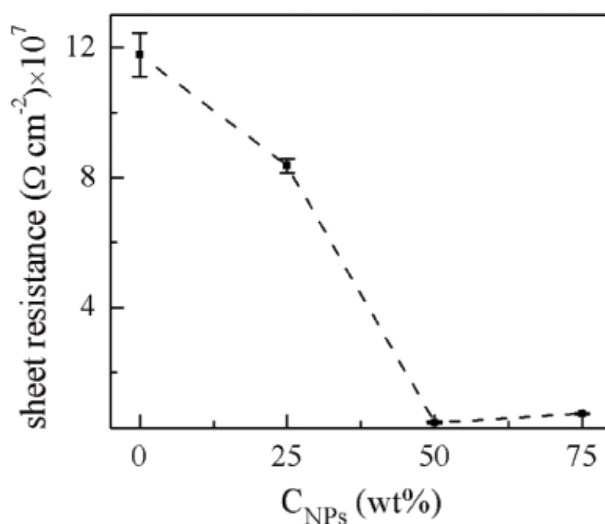


Figure 5.31: Sheet resistance of 0wt.%NPs, 25wt.%NPs, 50wt.%NPs, and 75wt.%NPs titania films.

The conductivity of titania film is very important for solar cell performance. S. Guldin et al. demonstrated that the increased titania conductivity strengthened the photovoltaic performance of solid-state dye sensitized solar cells even in the case of lower surface area and dye loading [2]. The film resistivity was determined by four points probe measurements. The nanoparticle-concentration dependence of the resistivity of mesoporous titania films is shown in Fig. 5.31. We note that increasing the nanoparticle concentration from 0 wt.% to 75 wt.% reduced the sheet resistance by over a factor of 2. Therefore, it is expected that 50wt.%NPs and 75wt.%NPs films are more efficient as solar cell photoanodes than the other two films.

- [1] L. Song, W. Wang, V. Körstgens, D. Moseguí González, Y. Yao, N. K. Minar, J. M. Feckl, K. Peters, T. Bein, D. Fattakhova-Rohlfing, G. Santoro, S. V. Roth, P. Müller-Buschbaum, *Adv. Funct. Mater.* DOI:10.1002/adfm.201504498 (2016)
- [2] S. Guldin, S. Hüttner, P. Tiwana, M. C. Orilall, B. Ülgüt, M. Stefik, P. Docampo, M. Kolle, G. Divitini, C. Ducati, S. A. T. Redfern, H. J. Snaith, U. Wiesner, D. Eder, U. Steiner, *Energy Environ. Sci.* **4**, 225-233 (2011)

## 5.16 Dynamics of nanocomposites composed of HEUR polymer and magnetite iron oxide nanoparticles

A. Campanella<sup>1</sup>, H. Frielinghaus<sup>1</sup>, P. Müller-Buschbaum<sup>2</sup>

<sup>1</sup> JCNS@FRMII, Lichtenbergstrasse 1, 85747 Garching, Germany

<sup>2</sup> Technische Universität München, Physik-Department, Lehrstuhl für Funktionelle Materialien, James-Franck-Strasse 1, 85748 Garching, Germany

A novel type of nanocomposite composed of hydrophobically modified ethoxylated urethane (HEUR) polymer and coated magnetite nanoparticles (MNP) was investigated. The preparation, the structural characterization and the magnetic response of these nanocomposites as hydrogels and as dry films was investigated in our previous work [1]. Now we focus on the dynamics of these nanocomposites as dry films and as hydrogels.

The dynamics of the nanocomposites in the dried state was investigated by Dielectric Relaxation Spectroscopy (DRS), in combination with Differential scanning calorimetry (DSC) and Thermally stimulated depolarization current (TSDC). From the DRS data, we observed three relaxation processes in different temperature ranges i)  $-20\text{ °C} < T < 25\text{ °C}$  the low-frequency process whose origin is yet unclear, but we suggest that is related to the MWS relaxation ii) at  $-65\text{ °C} < T < 25\text{ °C}$  the  $\alpha$ -process associated to the glass transition of the amorphous PEO iii) at  $T < -55\text{ °C}$  the  $\gamma$ -process, attributed to the crankshaft motion of the methylene groups. No influence of the MNP addition in the pure HEUR film on the  $\alpha$ -relaxation of the HEUR polymer was observed. This means that structural properties of the material, like the glass transition  $T_g$ , are not affected by the presence of the MNP. This result is in agreement with the structural characterization of the nanocomposites, which reveals no change in the domain spacing of the polymer network with increasing MNP concentration.

The TSDC measurements revealed the existence of two main dispersions, one at /approx  $-75\text{ °C}$  which does not depend of the polarization temperature and is attributed to the segmental relaxation of the PEO amorphous portion ( $\alpha$ -relaxation), accordingly to the fact the peak temperature coincide to the glass transition temperature found in the DSC measurements. The second dispersion observed at higher temperature, i.e. at approx  $-44\text{ °C}$ , has been found to be depended on the  $T_p$ , meaning that a dipolar-like mechanism, like the Maxwell-Wagner-Sillar polarization process may be involved. The MWS process is usually observed when a microphase separation within the sample is present, therefore we expected to observe it because of the high heterogeneity of the investigated samples.

On the other hand, the dynamics of the nanocomposite hydrogels was investigated with dielectric relaxation spectroscopy (DRS) and neutron spin echo (NSE) spectroscopy. The incorporation of the magnetic nanoparticles within the hydrophobic domains of the HEUR polymer network leads to an increase of the size of these domains and to an increase of their distance. The size increase leads to a dilution of the polymers nearby the hydrophobic domain, allowing higher mobility of the smallest polymer blobs close to the "center" [2]. This is reflected in the decrease of the activation energy of the  $\beta$ -process detected in the DRS data. The increase in distance leads to an increase of the size of the largest hydrophilic polymer blobs. Therefore, the segmental dynamics of the largest blobs is slowed down. The suppression of the segmental dynamics is reflected in the  $\alpha$ -relaxation processes detected in the DRS data and in the decrease of the relaxation rate  $\Gamma$  of the segmental motion in the NSE data with increasing the concentration of magnetic nanoparticles (see Fig. 5.32).

The glass transition temperature decreases with increasing the MNP loading. Therefore it would be possible to tune the glass transition of the hydrogels by varying the MNP concentration. The contribution of the static inhomogeneities to the total scattering function  $S_{st}(q)$  is extracted from the NSE data, revealing a more ordered gel structure than the one giving rise to the total scattering function  $S(q)$ .

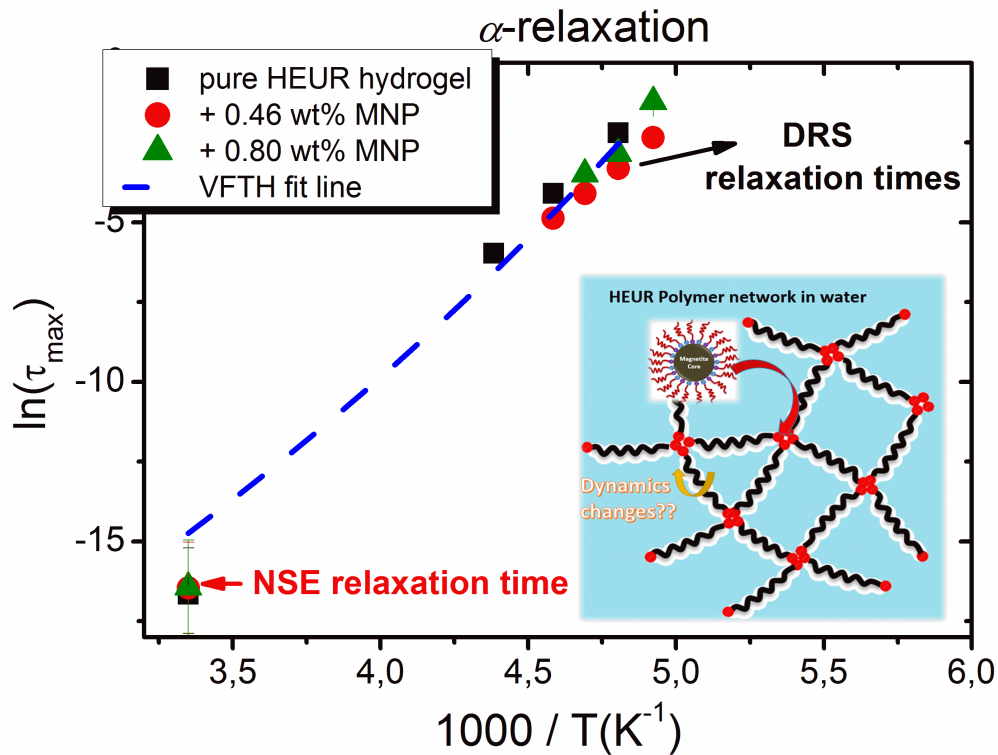


Figure 5.32: Arrhenius map showing the segmental relaxation of the HEUR polymer network

- [1] A. Campanella, Z. Di, A. Luchini, L. Paduano, A. Klapper, M. Herlitschke, O. Petracic, M. S. Ap-pavou, P. Müller-Buschbaum, H. Frielinghaus, D. Richter, *Polymer* **60**, 176-185 (2015)
- [2] A. Halperin *Macromolecules* **20**, 2943-2946 (1987)

### 5.17 Unraveling the mechanisms of 2-step perovskite synthesis for highly efficient hybrid photovoltaics

J. Schlipf, P. Docampo<sup>1</sup>, C. J. Schaffer, V. Körstgens, L. Bießmann, F. Hanusch<sup>1</sup>, N. Giesbrecht<sup>1</sup>, S. Bernstorff<sup>2</sup>, T. Bein<sup>1</sup>, P. Müller-Buschbaum

<sup>1</sup> LMU, München, Germany

<sup>2</sup> Elettra-Sincrotrone Trieste, Basovizza, Italy

The hybrid material  $\text{CH}_3\text{NH}_3\text{PbI}_{3-x}\text{Cl}_x$  with perovskite crystal structure has recently led to a revolution in thin film photovoltaics. Since its inception in 2009, solar cell power conversion efficiencies have risen up to 20 % now challenging conventional inorganic photovoltaic technologies as perovskite solar cells (PSC) promise cheap production from abundant precursor materials. This extraordinary performance by a solution-processed material is due to the favorable properties of this class of hybrid perovskites like high absorption coefficient and long diffusion length of photogenerated charge carriers even in multicrystalline thin films. However, fundamental understanding of material properties and especially the correlation of crystallization dynamics and film morphology lack behind the rapid device development. Especially in the very simple planar cell architecture these cells suffer from performance losses due to irreproducible film morphologies. A second prominent effect is a more or less severe hysteresis observed in current-voltage measurements that is in part related to film morphology. Thus, understanding and ultimately controlling the crystal morphology of perovskite thin films is of great importance to achieve a reproducible high photovoltaic performance.

A very versatile approach for the synthesis of such hybrid perovskites is a 2-step technique, where the perovskite is obtained by conversion from a crystalline precursor film, lead iodide ( $\text{PbI}_2$ ), by dipping into a solution containing the organic cations. It has been reported before that optimization of the  $\text{PbI}_2$  layer is of utter importance for good performance in photovoltaic devices.

We conducted the first successful grazing incidence small angle X-ray scattering (GISAXS) measurements on thin films of a hybrid perovskite and its respective precursor while simultaneously monitoring the crystal phase with grazing-incidence wide angle X-ray scattering (GIWAXS). With the latter we confirmed the crystal structure for our thin films. In GISAXS we made use of the fact that an incident angle below the critical angle of the material yields surface-sensitive data while higher angles penetrate the entire film and give information on the bulk morphology. Thus, by horizontal line cuts at high and low  $q_z$  positions we gather information on the lateral film morphology in the bulk and on the surface of  $\text{PbI}_2$  and perovskite thin films, respectively. Using the distorted wave Born approximation (DWBA) and assuming a local monodisperse domain distribution (LMA) we simulated the GISAXS data and extracted three form factors with a broad Gaussian distribution. First, we find a close correlation of crystal sizes in the precursor and the perovskite films. As during the conversion to perovskite these films usually exhibit a significant volume expansion due to the incorporation of  $\text{CH}_3\text{NH}_3$  into the inorganic framework, it can be concluded that crystal growth is confined laterally. In fact, by a Williamson-Hall analysis on powder X-ray diffraction measurements certain amount of crystal strain is confirmed for the perovskite film. Furthermore, from this measurement it is possible to get insight into the distribution of crystal sizes (see Fig. 5.33). Thus, it is apparent that not only does the ratio of smaller to larger crystals increase during conversion in favor of smaller crystals, but also that this effect is more severe inside the bulk.

This leads to the model of the conversion mechanism presented in Fig. 5.34: In the bulk, the crystalline  $\text{PbI}_2$  precursor layer is converted to perovskite by the intercalation of organic cations into the inorganic framework (solid-state conversion). As the crystal growth is constrained

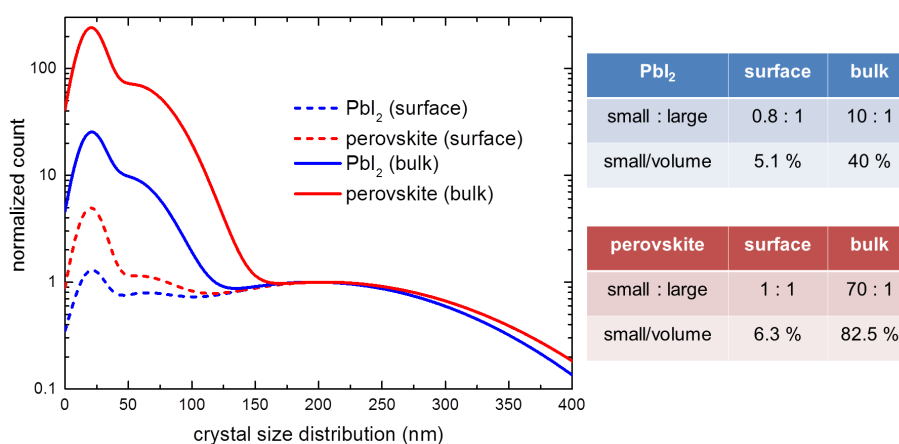


Figure 5.33:

Crystal size distribution on the surface (broken lines) and in the bulk (solid lines) of PbI<sub>2</sub> precursor (blue) and perovskite thin film (red) extracted from form factors from modeling GISAXS cuts with the DWBA. The table on the right gives the estimated volume ratio of medium sized crystals (50-100 nm) to large crystals (> 100 nm). [1]

laterally the volume expansion of the crystals during conversion of PbI<sub>2</sub> to perovskite is mainly vertical. This, however, requires a mechanical redistribution within the film, i.e. due to the observed strain larger crystals crack up into smaller units that accumulate closer to the substrate. On the surface, on the other hand, the concentration of organic compounds is higher and facilitates the complete reconstruction of the domains and smaller crystals are dissolved or incorporated into larger ones by Ostwald ripening.

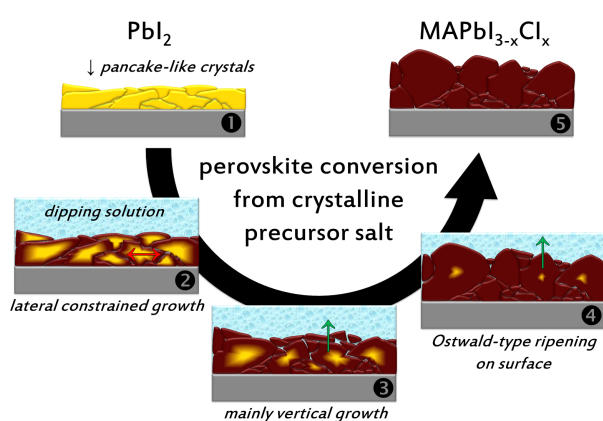


Figure 5.34:

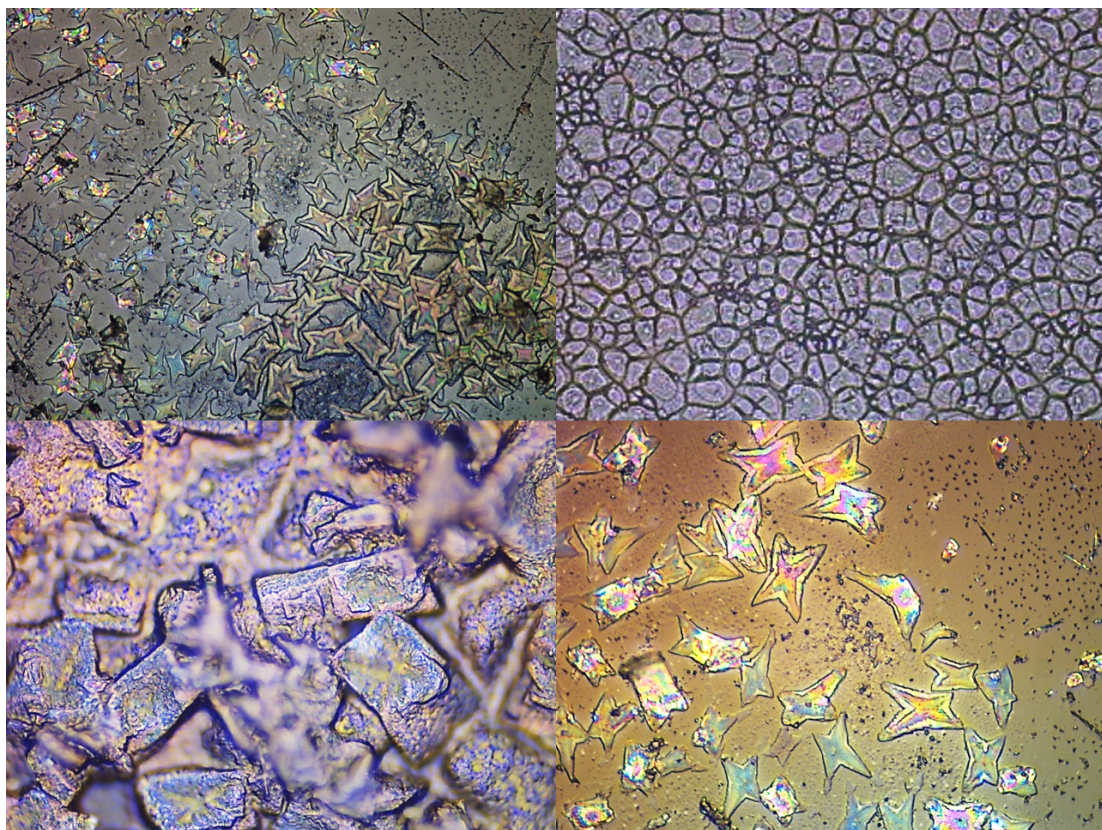
Schematic showing the conversion of PbI<sub>2</sub> into hybrid perovskite: The crystalline precursor consists of pancake-like crystals. Upon immersion into the solution containing the organic compounds, in the bulk the lateral confinement of neighboring crystals leads to a volume expansion mainly in vertical direction while the lateral strain promotes formation of smaller crystals. Additionally, at the film surface the large concentration of organic cations facilitates crystal dissolution and in combination with Ostwald ripening favors the observed preference of large crystals. [1]

In conclusion, our results help to elucidate the origin of the morphology in hybrid perovskite thin films fabricated with the aforementioned method. As this method serves as the basis for many more sophisticated protocols, our model helps in advancing the improvement of synthesis methods for hybrid perovskites which is important for reproducible high photovoltaic performance and ultimately large-scale production. Furthermore, our analysis shows that X-ray scattering methods are an essential tool for a rational development of new synthesis methods for controlled film morphology.

[1] J. Schlipf, P. Docampo, C. J. Schaffer, V. Körstgens, L. Bießmann, F. Hanusch, N. Giesbrecht, S. Bernstorff, T. Bein, P. Müller-Buschbaum, *J. Phys. Chem. Lett.* **6**, 1265-1269 (2015)



## 6 New materials



## 6.1 Metal decoration of nanoparticles attached to a substrate

V. Körstgens, S. Bernstorff<sup>1</sup>, P. Müller-Buschbaum

<sup>1</sup> Elettra-Sincrotrone Trieste, Basovizza, Italy

We produced composite films of silver decorated colloidal silica particles. Our aim was the development of a procedure for the decoration of spherical nanoparticles attached to a surface. This is the first step toward the production of nanostructured surfaces with tailored optoelectronic properties. One of the envisaged applications is the use of the structured films as a substrate for surface enhanced Raman scattering (SERS). The general scheme we followed is given in Fig. 6.1. The process of metal growth on a particle consists in principal of two steps: First metal ions adhere to the surface of colloidal particles and in a second step metal ions are reduced to the metallic state. By choosing the suitable reducing agent and adjusting the concentration the finite size and distribution of the metal nanoparticles decorating the colloids can be controlled [1]. The scheme in Fig. 6.1 shows the metal decoration with silver. In the first step particles are immersed in a solution of silver complex ions  $[\text{Ag}(\text{NH}_3)_2]^+$ . Due to the negative charge of particles the attachment of complex ions is facilitated. In the second step shown in Fig. 6.1 the silver ions are reduced to metallic silver by immersion in a solution of a reducing agent.

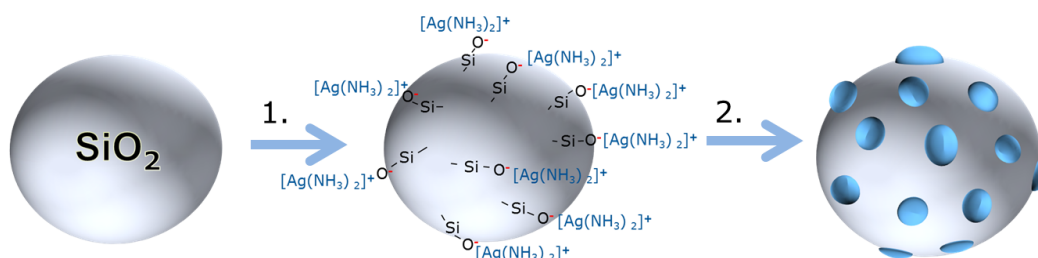


Figure 6.1:

General scheme for the decoration process of particles with silver nanoparticles with the two steps: 1) Attachment of silver ions, here complex ions  $[\text{Ag}(\text{NH}_3)_2]^+$  and 2) application of a reducing agent for the generation of metallic silver

In the procedure we developed, the decoration of colloids is not performed with particles in suspension, but with structured substrates. A layer of silica nanospheres is attached to a glass substrate via a thin coating of polyethyleneimine (PEI). These films are the source material for the metal decoration process. With this method we achieved the production of hierarchical structures with metallic nanoparticles distributed on the surface of spherical nanoparticles attached to a surface, representing well-defined strawberry-like composite particles. An aqueous solution containing silver ions and a reduction agent is applied in a custom-built reaction vessel. In the reaction vessel several samples of glass slides coated with  $\text{SiO}_2$  nanospheres are exposed to the solution  $[\text{Ag}(\text{NH}_3)_2]^+$  under gentle stirring conditions. For the common approach with the growth process of particles in suspension [1] usually an elaborate washing and concentration procedure is necessary to remove residual silver ions from the solution before adding the reduction agent. The advantage of our procedure with coated substrate is that the washing step can be simplified to a single dipping process. Following that using the custom-built reaction vessel, coated substrates are immersed in a freshly prepared aqueous solution of the reduction agent. Silica nanoparticles in different sizes and different concentration of the reduction agent  $\text{NaBH}_4$  were investigated. In Fig. 6.2 the results for coatings on a glass substrate with  $\text{SiO}_2$  nanospheres with a diameter of 142 nm is shown for different concentrations of  $\text{NaBH}_4$ . The SEM-images in Fig. 6.1a and Fig. 6.1b show the layer of nanoparticles after immersion in  $\text{NaBH}_4$ -solution of

0.33 mg/ml for 15 min. It is observed that silver nanoparticles of about 5 nm size are distributed on each individual silica nanoparticle.

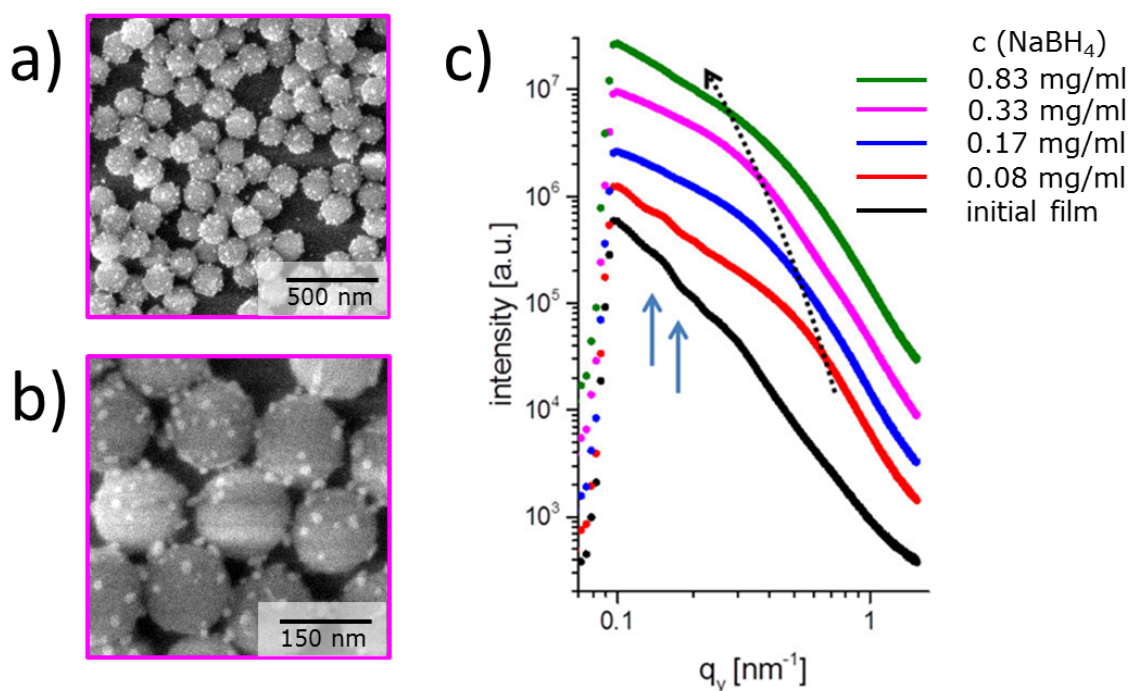


Figure 6.2:

a) SEM image of silver-decorated silica nanospheres of 142 nm diameter attached to a PEI coated glass substrate after the reduction process with  $\text{NaBH}_4$  in a concentration of 0.33 mg/ml b) SEM in larger magnification to emphasize on the size and distribution of silver particles c) Horizontal line cuts of the 2D GISAXS data measured from bottom to top for a film of untreated silica nanospheres and films after the reduction process with 0.08, 0.17, 0.33 and 0.83 mg/ml aqueous  $\text{NaBH}_4$ -solution. The curves are shifted along the y-axis for clarity of the presentation.

We investigated the composite films of silver decorated silica nanoparticles with grazing incidence small angle x-ray scattering (GISAXS) at an energy of 8 keV with a sample-to-detector distance of 1992 mm and a Pilatus 1M Detector with  $172 \mu\text{m} \times 172 \mu\text{m}$  pixel size at the Austrian SAXS beamline of the Elettra synchrotron in Italy. Horizontal line cuts extracted from 2D GISAXS data of the initial film and the films after silver nanoparticle growth with the reduction agent  $\text{NaBH}_4$  are shown in Fig. 6.2c (from bottom to top initial film, 0.08, 0.17, 0.33 and 0.83 mg/ml  $\text{NaBH}_4$  in aqueous solution). We were able to resolve the structure of the base colloidal layer (bottom black curve of Fig. 6.2c; form factor oscillations from spheres denoted with blue arrows in Fig. 6.2c) for the initial films denoted with blue arrows in Fig. 6.2c. For the films after metal decoration with increasing concentration of reduction agent  $\text{NaBH}_4$ , the scattering of the silver nanoparticles becomes more dominant with increasing concentration of the reduction agent. With lower concentrations of the reduction agent smaller silver nanoparticles on the silica spheres are obtained. The dotted arrow in Fig. 6.2c indicates the change of silver nanoparticle size with the increasing concentration of the reduction agent  $\text{NaBH}_4$ . In summary with the two-step process the size of silver nanoparticles decorating surface-attached silica spheres can be controlled. The kinetics of the silver nanoparticle growth in the reduction step is currently under investigation.

[1] J. Zhang, J. Liu, S. Wang, P. Zhan, Z. Wang, N. Ming, *Adv. Funct. Mater.* **14**, 1089-1096 (2004)

## 6.2 Mesostructured ZnO scattering layer

L. Bießmann, P. Müller-Buschbaum

During the last decade organic light emitting diodes (OLEDs) became more and more important for every day applications like smartphones and displays applications in general. This is not only related to the implementation of active matrix technology which allowed the construction of high resolution displays, but also, even more importantly, was the production of efficient and long-life emitter materials. The development of colored displays raised since the fabrication of stable blue, green, yellow and red organic emitter materials was possible. The combination of these emitting materials enables the design of white OLEDs with specific color temperature as well. Even if the enhanced efficiency and life expectancy made OLEDs suitable for commercial applications, the use of white OLEDs in room lighting is still behind its potential. In the recent years, research was mainly focused on the increase of the energy conversion of OLEDs and thus aimed to make them more efficient. Baldo et al. showed that one can triple the internal quantum efficiency and reach values close to 100 % by using phosphorescent emitting materials [1]. However, especially for white OLEDs the extraction of photons out of the device is still a limiting factor. For conventional device architecture, roughly 80% of the photons are trapped in substrate and organic modes and eventually will be absorbed [2]. Therefore, there is still a high potential for enhancing the luminance of OLEDs by increasing the photon extraction.

There are several approaches to overcome this problem which are based on inserting scattering centers in the device. Besides the direct structuring of the substrate surface, e.g. with micro lenses [3], or different refractive index materials [4], the attachment of a transparent layer on the substrate is a very promising approach. Such layers were produced by simply attaching nanoparticles on the substrate surface or attaching a polymer film included some nanoparticles [5]. Nanostructures made from metal oxides provide another promising approach, because they combine high stability with a high refractive index. An optical band gap of 3.3 eV and a refractive index of 2.0 makes zinc oxide (ZnO) a suitable material for optical transparent scattering layers, which are employed in this work. In Fig. 6.3 the working principle of the scattering layer

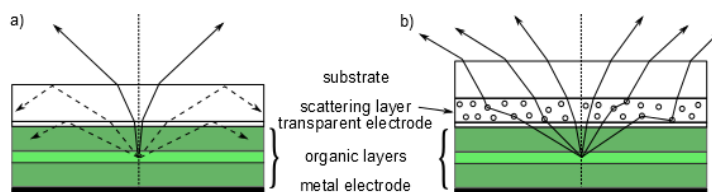


Figure 6.3:

a) Working principle of an additional scattering layer in comparison to b) a standard device architecture of. The illustrated light propagation shows the escaping modes as solid lines. The trapped modes are represented by dashed lines. Upon introduction of a scattering layer, more modes are able to escape the device and thus the efficiency is increased.

is illustrated. The photons generated in the emitting part of the organic layers are directed to the forward hemisphere of the OLED. The standard device architecture suffers from low photon extraction caused by trapped light due to substrate modes and total reflection on the high refractive ITO (transparent electrode) and lower refractive glass interface and glass to air interface, respectively. An additional scattering layer positioned in between the glass substrate and the transparent electrode yields two advantages. Firstly, the high refractive metal oxide reduces total reflection caused by the smaller jump of refractive indices. Secondly, the scattering centers of the layer yield a redirection of the generated light and suppress substrate modes. The combination of both effects can increase the light-outcoupling of the device significantly.

In this work porous ZnO scattering layers are produced by combining a structure giving diblock copolymer template with sol-gel chemistry. Using this method the nano- and micro-structure of the thin ZnO films can be designed to fit the needs for such a scattering layer. In detail, zinc acetate dihydrate (ZAD) is used as a precursor for ZnO, whereas polystyrene-block-polyethylene oxide, abbreviated as P(S-b-EO), is used as the structure giving template. Due to its wide range of accessible film thicknesses, the spray deposition technique is chosen for the deposition of ZnO on pre-cleaned glass substrates.

The surface structure of the obtained thin films was investigated by electron microscopy whereas UV-Vis spectroscopy was used to understand the scattering behavior in the visible light spectrum. To compare the complete transmitted and reflected light intensity through the film, an integrating sphere was used for the UV-Vis measurements. The nano- and micro-structured surface provides good scattering behavior which is supported by the following UV-Vis measurements. The comparison of the absolute transmitted intensity shown in Fig. 6.4 a) and the reflected intensity depicted in Fig. 6.4 b) shows a clear difference between the prepared films. For further investigations of the visible light scattering behavior of the ZnO layers a self-made

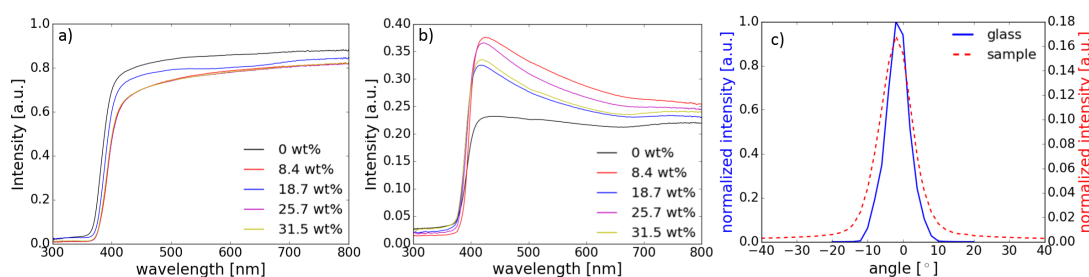


Figure 6.4:

a) UV-Vis transmittance, b) reflectance measured for different sol-gel concentrations and c) exemplary measurement of angle resolved scattered sum intensity. The intensities in (c) are normalized to their maximum intensity respectively to emphasize the enhanced scattering for larger angles. The maximum intensity for the scattering layer is reduced to 1/6 of the reference intensity by increased reflectance.

goniophotometer was constructed which allows the measurement of the wavelength resolved intensity in dependence of the scattering angle. An exemplary measurement in comparison to a glass substrate is depicted in Fig. 6.4 c). The scattering pattern of the ZnO film shows a decreased maximum intensity by about 1/6, but a higher intensity for larger angles. The reduced maximum intensity is rather related to the increased amount of reflected light than to absorption by the ZnO film which means that these films show an enhanced scattering behavior. As a next step the scattering will be further investigated to verify the structure-function relation and finally the performance of such a scattering layer in a working OLED device will be investigated.

- [1] M. A. Baldo, D. F. O'Brien, Y. You, A. Shoustikov, S. Sibley, M. E. Thompson, S. R. Forrest, *Nature* **395**, 151-154 (1998)
- [2] S. Reineke, F. Lindner, G. Schwartz, N. Seidler, K. Walzer, B. Lüssem, K. Leo, *Nature* **459**, 234-238 (2009)
- [3] J. Sun and S. R. Forrest, *Journal of Applied Physics* **100**, 073106 (2006)
- [4] J. Sun and S. R. Forrest, *Nature Photonics* **2**, 483-487 (2008)
- [5] H.-W. Chang, Y. H. Kim, J. Lee, S. Hofmann, B. Lüssem, L. Müller-Meskamp, M. C. Gather, K. Leo, C.-C. Wu, *Organic Electronics* **15**, 1028-1034 (2014)

### 6.3 Two dimensional organometal halid perovskite nanosheets in light emitting application

R. Wang<sup>1</sup>, H. Frielinghaus<sup>1</sup>, A. Koutsoumpas<sup>1</sup>, S. Mattauch<sup>1</sup>, P. Müller-Buschbaum

<sup>1</sup> JCNS at MLZ, Garching, Germany

The breakthrough of organometal halid perovskite attracts intensive research interests due to its potential for high efficiency solar cells. Recently, low dimensional perovskite nanocrystals, such as 2D perovskite nanosheets have been reported to possess reduced fluorescence decay times, an increased exciton binding energy and low conductivity in certain crystallographic directions. Consequently, these lower dimensional perovskites can be utilized for light emitting applications. In the present work, 2D nanosheet organometal bromide perovskites are formed by using octylamine bromide (OABr) as capping ligands. A one-step solution based preparation route is used to fabricate the samples. The achieved structures are investigated by SEM, photoluminescence (PL) spectroscopy and neutron reflectivity (NR).

All samples are synthesized under a fixed mole ratio of the  $PbBr_2$  and the organic ammonium salts. Three different fractions of OABr are selected from 20% to 50%. The film thickness revealed by Dektak surface profilometer is around 200 nm. The resulting surface morphology as probed with SEM is shown in Fig. 6.5. Irregular perovskite grain with dimensions on micrometer scale is achieved for an OABr ratio of 20%. The surface uniformity decreases with increasing OABr content. Comparing with XRD results, the round white spots on the surface are residue of the precursor material. For the sample with an OABr content of 50%, larger grains are formed by the stacking of different dimensions of 2D structures, which originates from the capping effect. 3D bulk crystals have been confined into low dimensionality. Another interesting observation is the degradation of perovskite crystal under the electron beam. The structure shown in Fig. 6.5 e) corresponds to that of the sample shown in Fig. 6.5 d) but probed after 2 minutes electron beam exposure. Gaps appear on the perovskite crystals and expand even broader. This result is comparable with previous report for perovskite nanoparticles [1].

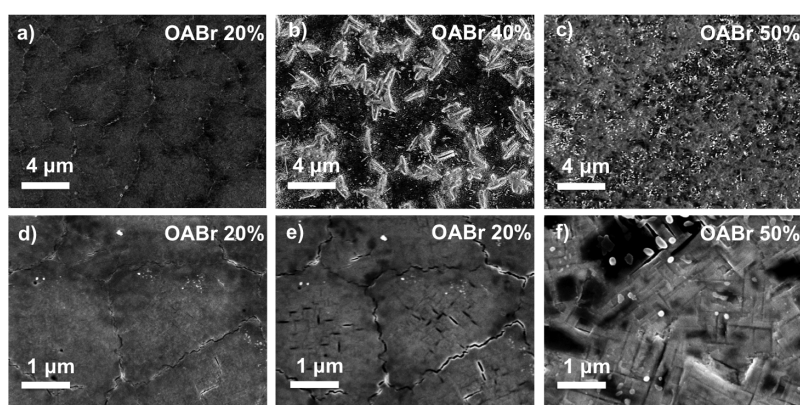


Figure 6.5:

SEM images of spin-coated organometal bromide perovskite samples with different OABr fractions. a), d) and c) are the SEM images of samples with 20% OABr content under different magnifications. b) SEM image of sample with 40% OABr content and c) and f) with 50% OABr content.

Photoluminescence (PL) spectroscopy shows a blue shift of the signal from the perovskite samples with increasing OABr concentration. In Fig. 6.6, the emission peak of the sample with an OABr content of 20 % locates at 537 nm, which is comparable with literature values reported for

bulk perovskite samples [2]. Additional features appear at higher energies in samples having a larger OABr fraction. These features can be assigned to the quantum size confinement occurring for these morphologies. When the decreased structure size is similar to the size of exciton Bohr radius, quantum size effects will be induced into the system [3]. A similar picture is depicted in the SEM images, the micrometer scale perovskite nanocrystals are shrinking into 2D nanocrystals in case of higher OABr content. For the sample with 20% OABr content, another two higher energy peaks appeared at 457 nm and 477 nm as well. This reveals that low dimensional perovskite nanocrystals are existing in the sample as well. However, the structure information of several nanometers is below the SEM resolution limit and therefore needs to be confirmed with other techniques.

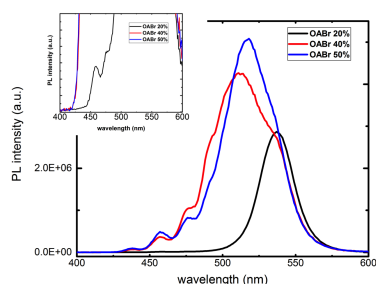


Figure 6.6:  
PL measurements of organometal bromide perovskite samples with different OABr fractions as indicated. The inset shows the existence of features on the PL data of 20% sample as well.

Structural information is gained with neutron reflectivity (NR) measurements at the MARIA instrument. As a result of the large surface roughness of the perovskite thin films, no distinct Kiessig fringes are observed in the NR data (Fig. 6.7). In the NR data only distinct Bragg peaks are found, which evolve with increasing OABr concentration. The presence of such Bragg peaks in the NR data confirms the existence of periodic structures along the surface normal. The periodic distance increases from 2.6 nm (40% OABr sample) to 3.2 nm (50 % OABr sample). Moreover, off-specular scattering is seen in the 2D data measured at MARIA. The data analysis of the diffuse scattering is undergoing.

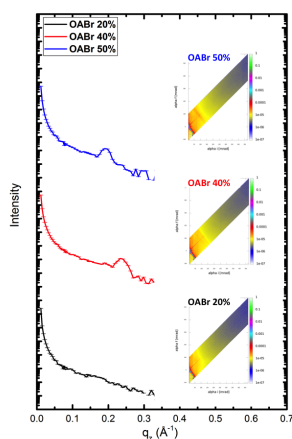


Figure 6.7:  
NR measurements of organometal bromide perovskite samples with different OABr fractions as indicated. The corresponding 2D off-specular data are shown in the insets.

- [1] J. A. Sichert, Y. Tong, N. Mutz, M. Vollmer, S. Fischer, K. Z. Milowska, R. G. Cortadella, B. Nickel, C. Cardenas-Daw, J. K. Stolarczyk, A. S Urban, J. Feldmann, *Nano Lett.* **10**, 6521-6527 (2015)
- [2] R. Sheng, A. Ho-Baillie, S. Huang, S. Chen, X. Wen, X. Hao, M. A. Green, *J. Phys. Chem. C* **119**, 3545-3549 (2015)
- [3] P. Tyagi, S. M. Arveson, W. A. Tisdale, *J. Phys. Chem. Lett.* **6**, 1911-1916 (2015)

## 6.4 The morphology and formation chemistry of solution-processed MAPbI<sub>3</sub> films

L. Oesinghaus, J. Schlipf, N. Giesbrecht<sup>1</sup>, Y. Hu<sup>1</sup>, L. Song<sup>1</sup>, T. Bein<sup>1</sup>, P. Docampo<sup>1</sup>, P. Müller-Buschbaum

<sup>1</sup> LMU, München, Germany

Over the last few years, the power conversion efficiencies (PCE) of perovskite solar cells based on methylammonium lead iodide (MAPbI<sub>3</sub>) have increased rapidly from 3.9 % in 2009 to 20.1 % in 2015, with the latter value rivaling the typical PCE of commercially sold single crystal silicon solar cells [1,2]. This rapid increase in efficiency in combination with the abundant and cheap precursor materials, possible cheap fabrication by solution-processing and good environmental sustainability make MAPbI<sub>3</sub> a promising material to replace silicon as a solar cell material [3]. To transfer the success in lab-based devices to large-scale applications, a number of problems have to be solved, the most critical of which are material stability and process control for reproducibility. In order to achieve reproducibility, the crystallization and formation mechanisms of solution-processed MAPbI<sub>3</sub> films have to be understood.

There is a large variety of different methods to prepare MAPbI<sub>3</sub> films for efficient solar cells. We studied films prepared by five typical preparation methods with scanning electron microscopy (SEM) and grazing-incidence wide-angle x-ray scattering (GIWAXS). We chose two one-step methods, labeled chlorobenzene method (CB) and lead acetate method (LA), and three two-step methods, labeled solution conversion method (SC), evaporation method (EV) and interdiffusion method (ID). In the chlorobenzene method, PbI<sub>2</sub> and MAI are mixed and dissolved in DMF and spin-coated together, and chlorobenzene is dropped on the sample while it is still spinning to wash out remaining solvent. In the lead acetate method, lead acetate (Pb(CH<sub>3</sub>COO)<sub>2</sub>) and MAI are used as the precursors and mixed in a common solution. For the SC, EV and ID methods, a crystalline PbI<sub>2</sub> film is first applied by spin-coating, and then brought into contact with the organic cation to convert the film into MAPbI<sub>3</sub>. In the solution conversion method, the film is immersed into a mixed solution of 95 wt% MAI and 5 wt% MAI. In the evaporation method, the film is placed into a MAI vapor. In the interdiffusion method, a MAI solution is spin-coated.

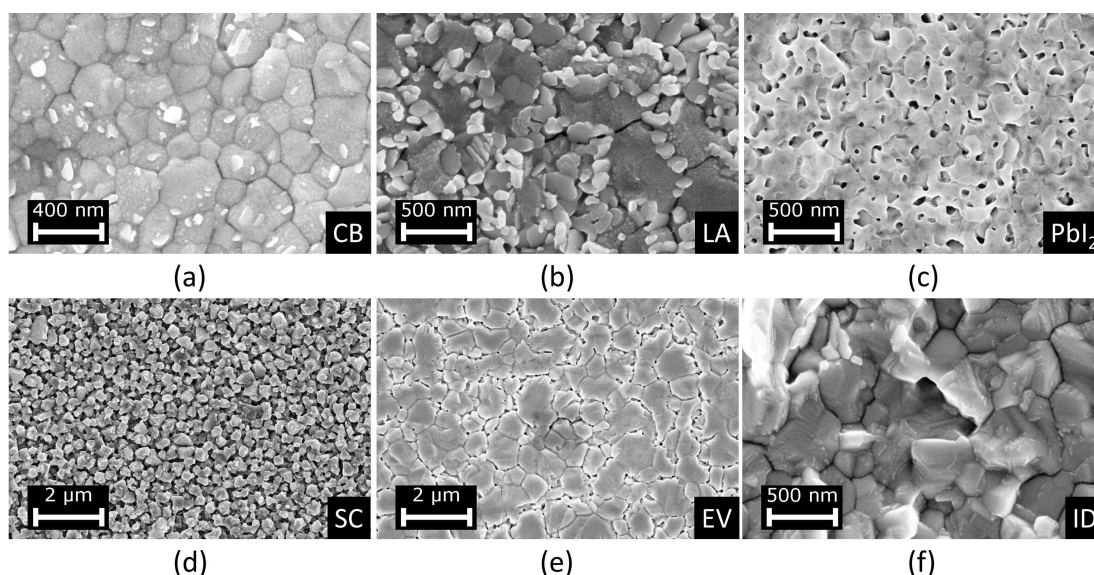


Figure 6.8: SEM pictures of samples prepared by the five methods: a) chlorobenzene, b) lead acetate, d) solution conversion, e) evaporation and f) interdiffusion. c) The lead iodide precursor film is shown for comparison.

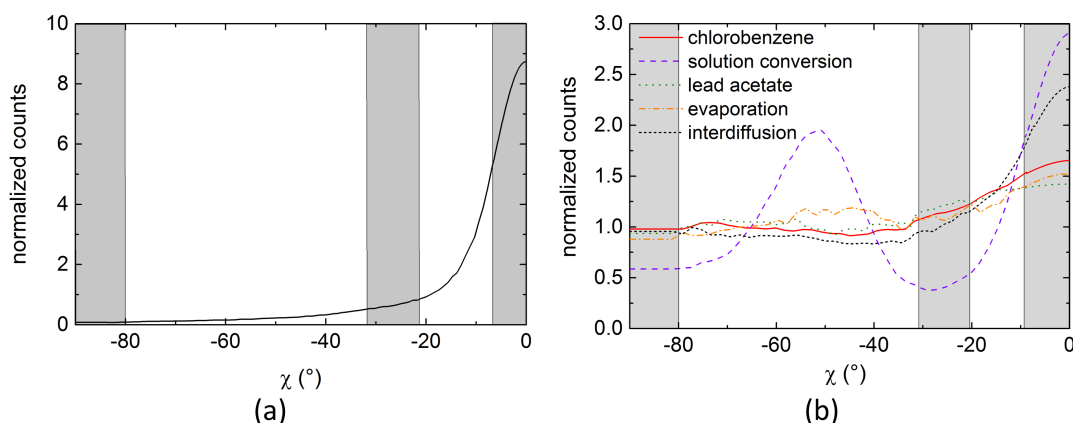


Figure 6.9:  
GIWAXS line cut of the (002)/(110) peak for a) a  $\text{PbI}_2$  film and b) films from the five investigated methods as indicated.

Fig. 6.8 shows SEM measurements for films prepared by the five methods as explained above and the lead iodide precursor film. The one step methods produce flat films consisting of densely packed grains. The crystallites produced by the LA method are larger and typically of the order of 500 nm, while the crystallites of the CB method are typically around 200 nm. The LA method also has quite a bit of smaller crystallites on top due to secondary nucleation. The lead iodide precursor film is flat with pores of roughly 50 nm size. The SC method produces very rough film of individual crystallites, the larger ones of which are typically 400-500 nm in size. The EV method produces flat films with large crystallites often over 1  $\mu\text{m}$  in size, which are not densely packed and exhibit many pinholes. The ID method produces film similar to the one-step methods, consisting of very densely packed grains roughly 500 nm in size.

Fig. 6.9 shows GIWAXS line cuts of the intensity of the first peak from films prepared by the five investigated methods and a  $\text{PbI}_2$  film as used in the two-step methods prior to conversion. The one-step methods are found to produce largely isotropic films, while we find a variety of orientations for two-step methods. The solution conversion method produces strongly oriented films with preferential orientations along (002) and (202), the interdiffusion method produces weakly oriented films with (002) preferential orientation and the evaporation methods produces largely isotropic films similar to the one-step methods. Based on the strong preferential (001) orientation of the  $\text{PbI}_2$  precursor film, which corresponds to  $\text{PbI}_6^{4-}$  octahedra tilted at  $55^\circ$  to the substrate, the (202) preferential orientation is assigned to an in-situ conversion process, while the (002) preferential orientation is assigned to a dissolution-recrystallization process. The film produced by the SC method is thus hypothesized to be a combination of in-situ conversion and dissolution-recrystallization, and the ID method is hypothesized to produce films based in the dissolution of a layer on the top, which acts as a seed layer for the remaining film. The complete lack of orientation of the films produced by the EV method requires a dissolution of the  $\text{PbI}_2$  film to destroy the preferential orientation of the precursor layer.

In conclusion, the comparison of the orientation of the precursor film to the orientations the resulting  $\text{MAPbI}_3$  films provides direct evidence for fundamentally different conversion mechanisms.

- [1] A. Kojima et al., *J. Am. Chem. Soc.* **131**, 6050-6051 (2009)
- [2] W. S. Yang et al., *Science* **348**, 1234-1237 (2015)
- [3] J. Gong et al., *Energy Environ. Sci.* **8**, 1953-1968 (2015)

## 6.5 Increasing achievable states of order in Heusler systems by quenched-in vacancies

M. Leitner, P. Neibecker, W. Petry

For most of the phenomena that are in the focus of contemporary solid-state physics, the large family of Heusler compounds harbours a representative. Properties displayed by specific Heusler systems include for instance half-metallic ferromagnetism, superconductivity, shape-memory effects, magneto-caloric and thermo-electric properties, as well as unconventional metallic states [1]. This wide array of properties is due to, first, the large number of possibilities to choose elements as constituents, and second, the additional freedom with respect to the actual elemental make-up of the distinct sublattices.

On the other hand, the wide regions of phase stability imply low ordering energies, which can also pose problems from the point of view of applications. Specifically, the  $\text{Ni}_2\text{MnZ}$  Heusler systems are the most promising examples for the ferromagnetic shape-memory effect. Here ferromagnetism coincides with a martensitic instability, and a large magneto-crystalline anisotropy in the martensite phase in combination with a low stress threshold for twin boundary movement allows to switch the domains and therefore effect macroscopic shape changes by applying an external field. The most promising example is the  $\text{Ni}_2\text{MnGa}$  system, where strains of 10 % in fields of 1 T have been reported [2]. The isoelectronic system  $\text{Ni}_2\text{MnAl}$  is being considered as a substitute for  $\text{Ni}_2\text{MnGa}$  due to its more favourable mechanical properties, but its ferromagnetic shape-memory performance has been found to be inferior to  $\text{Ni}_2\text{MnGa}$ , which is thought to be due to the low degree of  $L_{21}$  order achievable in the  $\text{Ni}_2\text{MnAl}$  system [3].

This example constitutes the motivation for the endeavour considered here: What can be done if theoretical calculations predict a specific ordered compound to display some desirable properties, but in experimental reality the necessary order cannot be achieved due to low ordering energies? This is a question of kinetics: For correlations on the local scale to relax to their equilibrium value, each concerned atom has to jump a few times, while it will take on the order of a few thousand jumps for the domains to coarsen so that sizeable long-range order is developed. Therefore, the highest degree of order that is experimentally achievable is determined by the lowest temperature where atomic mobility is sufficient for a given number of jumps to occur within practicable timescales, and any endeavour to extend this window towards lower temperatures has to be concerned with accelerating atomic diffusion at a given temperature.

In metallic systems, the random motion of vacancies drives atomic diffusion. The vacancies' jumping is due to cooperative anharmonic excitations of the neighbouring atoms and as such strictly connected to the instantaneous local temperature. Therefore, enhancing ordering kinetics by accelerating the vacancy jump rate is in principle not possible without simultaneously decreasing the degree of achievable order. In contrast, the vacancy concentration can equilibrate only at imperfections of the crystal such as dislocations, grain boundaries, and surfaces. As a consequence, its concentration is governed by a relaxation time which essentially is the mean time it takes a vacancy to reach such an imperfection. Specifically, the vacancy concentration is not directly given by the instantaneous temperature.

We exploited these circumstances in the following way: As mentioned above, in the nominal Heusler system  $\text{Ni}_2\text{MnAl}$  the tendency for Mn and Al to separate onto distinct sublattices is weak. We prepared samples of these systems by quenching from 1273 K into water (in the following denoted as *quenched*) and subsequently annealing part of them for one hour at 853 K followed by slow cooling (called *annealed*). By way of the direct correlation between state of order and magnetic transition temperature  $T_c$  (specifically, the interplay of antiferromagnetic interactions between close Mn moments and ferromagnetic Mn-Ni nearest-neighbour interactions leads to a destabilization of magnetic order under disorder) we followed the evolution of

the state of order during low-temperature annealing in a differential scanning calorimeter [4]. The associated kinetics are presented in Fig. 6.10. Turning our attention first to the *annealed* samples, we observe, as expected, a significant increase of order during annealing. However, contrary to the naive expectation, at the lower annealing temperature (623 K) a lower state of order can be achieved compared to the higher annealing temperature. This shows that we are here in a regime of severe kinetic limitation: Even though the thermodynamic driving force for ordering is lower at the higher annealing temperature, the faster kinetics allow higher states of order to be achieved *during the timescales accessible here*.

The curves for the *quenched* samples show a vastly differing behaviour, both quantitatively and qualitatively: Even though they start from a lower degree of order (evidenced by the slightly lower initial value of  $T_c$ ), they quickly surpass the curves corresponding to the *annealed* samples. Both the curves for 673 K and 623 K show a clear convergence, and the respective limiting values behave as expected (i.e., lower annealing temperatures correspond to higher order), while here the 573 K-curve is still below its limiting value.

These findings can be understood by assuming a sizeable excess concentration of vacancies to be present after quenching, which would be consumed during the annealing at 853 K and the following slow cooling. In effect, the atomic jumps would be due to thermal vacancies (with migration and vacancy formation enthalpies determining the activation enthalpy of diffusion) in the *annealed* samples and due to excess vacancies (where the activation enthalpy is only given by the migration part) in the *quenched* samples. The acceleration of kinetics corresponds to a 300-fold increase of excess vacancies over the thermal vacancy concentration.

Preliminary measurements of positron lifetimes correlated to the evolution of  $T_c$  corroborate this view and show that the relaxation times of the vacancy concentrations and order are on the same order of magnitude, which is also suggested by detailed studies of the evolution of  $T_c$  under non-constant annealing temperatures [4].

In conclusion, our findings demonstrate a way to increase achievable states of order in chemical compounds: after annealing at high temperature to promote grain growth and thereby remove vacancy sinks, a rapid quenching to low temperature leads to a vacancy excess which can be utilized to promote ordering during low-temperature annealing.

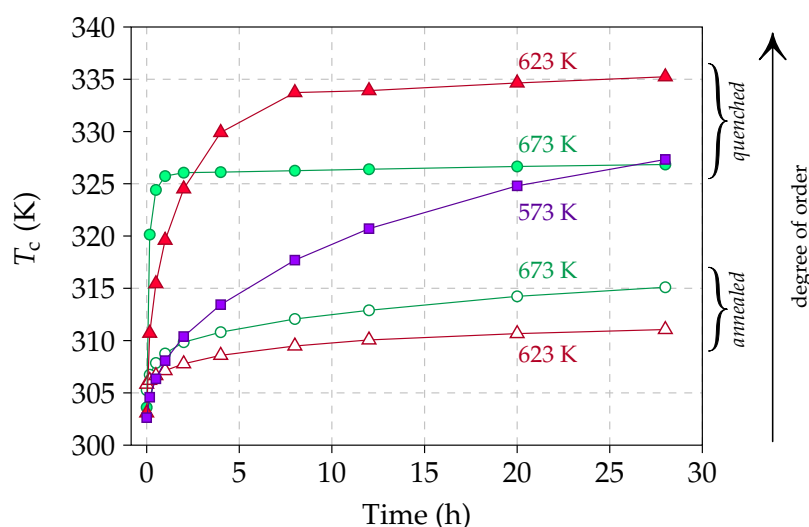


Figure 6.10: Evolution of magnetic phase transition temperature during annealing at different temperatures for *quenched* (filled symbols) and *annealed* (empty symbols) samples.

- [1] T. Graf, C. Felser, S. S. Parkin, *Prog. Solid State Chem.* **39**, 1–50 (2011)
- [2] A. Sozinov, A. A. Likhachev, N. Lanska, K. Ullakko, *Appl. Phys. Lett.* **80**, 1746 (2002)
- [3] M. Acet, E. Duman, E. F. Wassermann, L. Mañosa, A. Planes, *J. Appl. Phys.* **92**, 3867 (2002)
- [4] P. Neibecker, M. Leitner, G. Benka, W. Petry, *Appl. Phys. Lett.* **105**, 261904 (2014)

## 6.6 Magnesium battery electrolytes: $\text{Mg}(\text{BH}_4)_2$ in tetrahydrofuran studied by quasielastic neutron scattering

W. Lohstroh, J. F. Mora Cardozo, L. Silvi, W. Petry

E13 and MLZ, Garching, Germany

An alternative pathway for electrochemical energy storage which has been explored only little so far, are secondary batteries based on polyvalent ions, as magnesium ions. A limitation for magnesium based batteries is the lack of a suitable electrolyte compatible with a magnesium metal anode [1]. Recently, it has been demonstrated that  $\text{Mg}(\text{BH}_4)_2$  salt solution in ethereal solvents such as tetrahydrofuran (THF), dimethoxyethane (DME) or diglyme (DGM) [2] could be a viable alternative for a Mg-battery electrolyte and more promising results were obtained for mixed salt solutions comprising  $\text{LiBH}_4$  and  $\text{Mg}(\text{BH}_4)_2$ . The solvation structure and the coordination chemistry are strongly correlated with the coulombic efficiency of the cells [3] and therefore the inner structure and dynamic processes in the electrolyte solutions needs to be better understood to shed further light on the charge transfer processes.

In this study, we investigated the diffusion processes in THF and in its salt solutions with  $\text{Mg}(\text{BH}_4)_2$ ,  $\text{LiBH}_4$  and the mixture  $\text{Mg}(\text{BH}_4)_2 + \text{LiBH}_4$  on a microscopic scale using quasielastic neutron scattering. The technique mainly probes the incoherent cross section of the hydrogen atoms and thus it is sensitive to the dynamics of the THF solvent. Anhydrous tetrahydrofuran (THF, Sigma Aldrich, 99.8 %, used as received) was added to  $\text{LiBH}_4$  (Alpha Aesar, 95%),  $\text{Mg}(\text{BH}_4)_2$  and the mixtures 1 mol  $\text{LiBH}_4$ : 1 mol  $\text{Mg}(\text{BH}_4)_2$  (see reference [4]) and thoroughly mixed. Each solution had a 0.2 mol salt concentration. Handling of the materials took place in an Argon filled glovebox ( $\text{O}_2 < 1$  ppm,  $\text{H}_2\text{O} < 1$  ppm). Quasielastic neutron scattering experiments have been done at the cold Time-of-Flight spectrometer TOFTOF at the Forschungsneutronenquelle Heinz Maier-Leibnitz (FRM II) in Munich, Germany. The incoming neutron wavelength was 6 Å which gave an energy resolution of 23  $\mu\text{eV}$  (FWHM) at the elastic peak and an accessible momentum transfer,  $Q$  in the range 0.2 - 1.7  $\text{\AA}^{-1}$ . Measurements were taken at temperatures between 253 K and 323 K. The measured signal was analysed using

$$S(Q, \hbar\omega) = F e^{-\frac{\langle u^2 \rangle Q^2}{3}} [A_0 L_1(\Gamma_{\text{global}}) + (1 - A_0) L_2(\Gamma_{\text{local}})] \otimes \text{Res} + bg \quad (6.1)$$

where  $F$  is a general scaling factor,  $e^{-\frac{\langle u^2 \rangle Q^2}{3}}$  the Debye-Waller-factor that takes into account fast vibrations,  $\text{Res}$  the instrument resolution function,  $bg$  the background that summarizes all motions faster than the observation time window of the instrument. For simplicity, the local motions are summarized in one Lorentzian only,  $L_2$ . The obtained  $S(Q, \hbar\omega)$  is exemplarily shown in

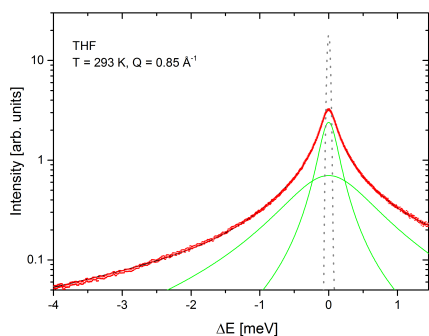


Figure 6.11:

Analysis of the data of THF measured at 293 K,  $Q = 0.85$  Å. Open symbols are the experimental data, solid lines are the overall fit (red), and the contributions of the smaller and the broader Lorentzian (green), respectively, convoluted with the experimental resolution function. The resolution function measured using the vanadium standard measurement is shown as dashed grey line.

Fig. 1 for THF at 293 K at  $Q = 0.85$  Å. Using two Lorentzians proved to be sufficient to describe the data satisfactorily at all temperatures and for all salt solutions investigated in this study. In

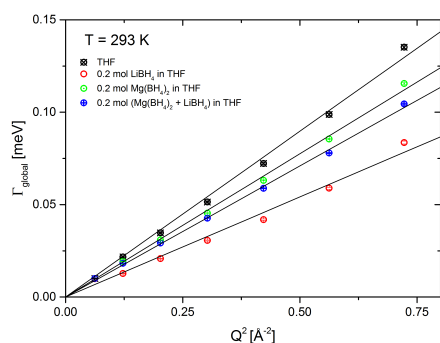


Figure 6.12:  
 $\Gamma_{local}$ , plotted as function of  $Q^2$  and the linear fits to calculate  $D_{eff}$ .

the limit of low  $Q$ ,  $\Gamma_{global}$  follows the  $Q^2$ -law, as expected for stochastic diffusion (see Fig. 2). For pure THF, a self diffusion coefficient  $D_{eff} = 2.72 \pm 0.05 \cdot 10^{-5} \text{ cm}^2 \text{ s}^{-1}$  was obtained at 293 K which is in good agreement with published data (which are in the range of  $2.84 \cdot 10^{-5} \text{ cm}^2 \text{ s}^{-1}$  at 298 K [5] to  $3.0 \cdot 10^{-5} \text{ cm}^2 \text{ s}^{-1}$  at 293 K [6]). The addition of the borohydride salts effectively slows down the long range translational diffusion as visible from the smaller values of  $\Gamma_{global}$  shown in Fig. 2. It is noteworthy to remark that all salt solutions could be fitted using the same model as given in eq. 6.1, i.e. there was no separation into different THF populations, such as molecules tightly bound to the solutes and free THF. The average diffusion coefficient  $D_{eff}$  are summarized in Fig. 3. Adding the salts yielded a considerable slowing down and at 293 K, the average value of  $D_{eff}$  are  $2.36 \pm 0.03$ ,  $2.16 \pm 0.02$ , and  $1.65 \pm 0.05 \cdot 10^{-5} \text{ cm}^2 \text{ s}^{-1}$  for the solutions with  $\text{Mg}(\text{BH}_4)_2$ ,  $\text{LiBH}_4 + \text{Mg}(\text{BH}_4)_2$  and pure  $\text{LiBH}_4$ , respectively. The thermal dependence of  $D_{eff}$  is very similar for all samples, independent from the kind of salt.

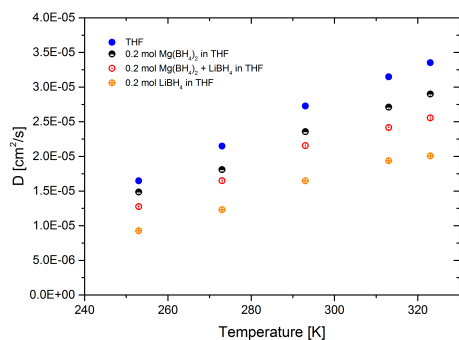


Figure 6.13:  
 Effective self diffusion coefficient  $D_{eff}$  of THF and borohydride - THF solutions as function of temperature. Error bars inside symbol size.

- [1] J. Muldoon, C.B. Bucur, A.C. Oliver et al., *Energy & Environmental Science* **5**, 5941 (2012)
- [2] (a) R. Mohtadi, M. Matsui T.S. Arthur, and S.-J. Hwang, *Ang. Chem. Int. Ed.* **51**, 9780 (2012); (b) O. Tutusaus, R. Mohtadi, *ChemElectroChem* **2**, 51 (2015)
- [3] Y. Shao, T. Liu, G. Li et al., *Scientific Reports* **3**, (2013)
- [4] E. G. Bardají, Z. Zhao-Karger, N. Boucharat et al., *J. Phys. Chem. C* **115**, 6095 (2011)
- [5] M. Holz, X.-A. Mao, D. Seiferling, A. Sacco, *J. Chem Phys.* **104**, 669 (1996)
- [6] G.J. Krüger, R. Weiss, *Zeitschrift für Naturforschung A* **25**, 777 (1970)

## 6.7 Strain induced martensitic transformation in austempered ductile iron (ADI)

X.H. Li, P. Saal<sup>1</sup>, W. M. Gan<sup>2</sup>, M. Landesberger<sup>1</sup>, M. Hoezel<sup>3</sup>, M. Hofmann<sup>3</sup>

<sup>1</sup> UTG, Garching, Germany

<sup>2</sup> German Engineering Materials Centre at MLZ, Garching, Germany

<sup>3</sup> FRM2, Garching, Germany

Austempered ductile iron (ADI) is a nodular ductile iron which has undergone a special heat treatment to enhance mechanical properties to a great extent. The heat treatment process of ADI consists of austenitization followed by quenching to a temperature typically between 250 and 450 °C and isothermal austempering [1,2]. After such a heat treatment the microstructure of ADI consists of acicular ferrite and high carbon enriched retained austenite. The microstructure strongly depends on the austenitization and austempering temperatures. Details on dependence of microstructure and temperature can be found in [1-3].

The high carbon enriched austenite is metastable and several reports exist indicating a transformation induced plasticity effect (TRIP) when ADI is subjected to deformation [4,5]. During the plastic deformation the high carbon enriched retained austenite can transform to martensite. Austenitization temperature, austempering temperature ( $T_{Aus}$ ), austempering time and alloying composition can influence the retained austenite fraction, its grain size and stability [3], which in turn will affect the possible martensitic transformation. The relationship between heat treatment parameters and phase fractions in ADI has been extensively studied by Meier et al. using in-situ neutron powder diffraction on non-textured samples [1].

On the other hand in case of the deformation induced martensitic transformation in ADI quantitative phase analysis is hindered due to texture formation and standard Rietveld analysis fails to produce reliable results. In the current work we used a method where the texture information is directly incorporated into Rietveld refinements to extract quantitative phase information. Using this approach we studied the influence of different treatments and composition parameters on the martensitic transformation using high resolution neutron powder diffraction and texture measurements on samples after compression to different plastic strains [6]. The results from these experiments allow us to relate the martensitic transformation kinetics in ADI with austempering temperature and plastic strains.

Fig. 6.14a and b show the martensite phase fractions in deformed ADI extracted using the recalculated ODFs as input in the Rietveld refinements of the lattice constants, peak shape parameters and phase contents. The strain induced martensite transformation in ADI during plastic deformation is not proportional to the retained austenite content at the beginning of plastic deformation. For the sample treated with  $T_{Aus} = 400\text{ °C}$  and also similar  $T_{Aus} = 350\text{ °C}$  a linear dependence of the martensite phase content with strain is found. Thus at each strain level the same amount of martensite is formed regardless of the initial retained austenite content. However, at around 20 pct plastic strain the increase in martensite phase fraction deviates from a linear behavior in the sample with the lowest austempering temperature  $T_{Aus} = 300\text{ °C}$  leveling out to about 20 pct martensite at 40 pct plastic strain. At this point about 80 pct of the retained austenite is transformed to martensite in this sample. To visualize this effect in Fig. 6.14b the martensite phase fractions are normalized to the initial retained austenite content from [2]. This shows clearer the dependence on heat treatment parameters, with the highest amount of transformation for the lowest austempering temperature (Fig. 6.14b). Fig. 6.14b shows that at 40 pct compressive deformation a total amount of 65 to 80 pct retained austenite transformed into martensite. Due to sample breakage higher strain levels cannot be achieved

using compression and further experiments allowing a higher degree of deformation, for instance cold rolling, are needed to clarify whether the trend seen in the sample austempered at  $T_{Aus}=300\text{ }^{\circ}\text{C}$  becomes apparent in samples heat treated at higher temperatures.

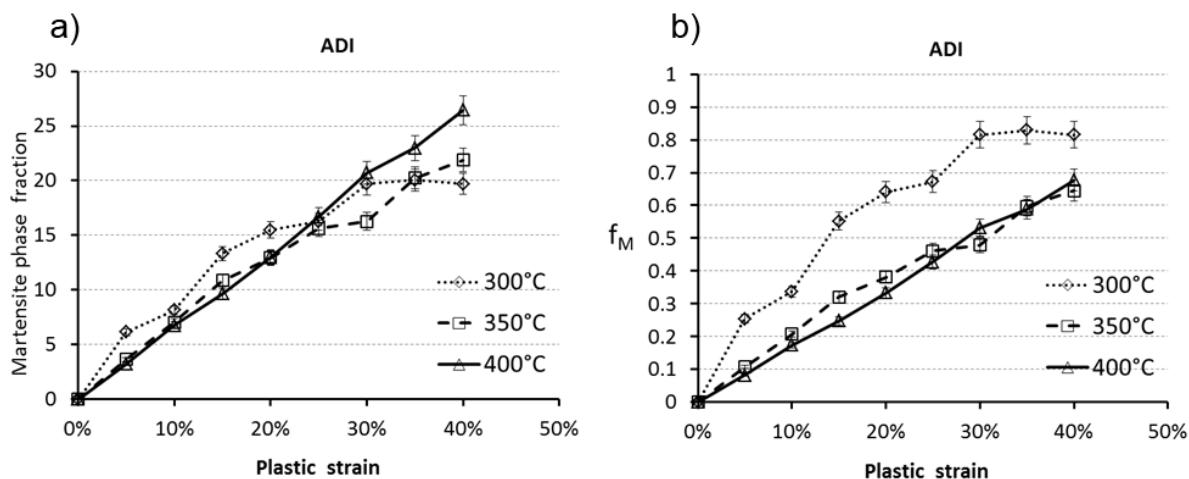


Figure 6.14:

(a) Martensite phase fraction in ADI (austempered at 300, 350 and 400 °C) after compressive deformation vs. plastic strain. (b) Normalized martensitic phase fraction  $f_M$  in ADI after compressive deformation vs. plastic strain.

Combining texture information and Rietveld refinements of neutron powder diffraction patterns allows extracting quantitatively phase fractions in ADI. The results of the quantitative analysis of the martensite phase fractions as a function of deformation shows a dependence of transformation rates with heat treatment parameters with up to 80 pct of the retained austenite being transformed to martensite for samples heat treated at  $T_{Aus} = 300\text{ }^{\circ}\text{C}$ .

- [1] L. Meier, M. Hofmann, P. Saal, W. Volk, H. Hoffmann, *Mater. Char.* **85**, 124-133 (2013)
- [2] P. Saal, L. Meier, X. H. Li, M. Hofmann, M. Hoebel, J. N. Wagner, W. Volk, *Metal. Mat. Trans.* **47**, 661-671 (2016)
- [3] M. Daber, P. Prasad Rao, *J. Mat. Sci.* **43**, 357-367 (2008)
- [4] M. R. Berrahmoune, S. Berveiller, K. Inal, A. Moulin, E. Patoor, *Mat. Sci. Eng. A* **378**, 304-307 (2004)
- [5] W. J. Dan, S. H. Li, W. G. Zhang, Z. Q. Lin, *Mater. Design* **29**, 604-612 (2008)
- [6] X. H. Li, P. Saal, W. M. Gan, M. Landesberger, M. Hoebel, M. Hofmann, *ECNS 2015 Conference Proceedings*, accepted (2015)

## 6.8 Synthesis and morphological characterization in PDMS-polythiophene segmented polyureas

M. Grübel<sup>1</sup>, K.N. Raftopoulos, S. Meister<sup>1</sup>, U. Schulze<sup>1</sup>, C.M. Papadakis, B. Rieger<sup>1</sup>

<sup>1</sup> Chemistry Department, TU München, Garching, Germany

In this work, we combine a flexible polydimethylsiloxane (PDMS) with an ordered structure of oligothiophenes. In order to achieve this, we use a polyaddition reaction between amine terminated PDMS and diisocyanate functionalized oligothiophenes, which form urea bonds with each other (Fig. 6.15). These urea groups form hydrogen bonds with each other, leading to a phase separation and enhanced mechanical stability. This elegant route combines the hydrogen bond supported stacking of conjugated chromophores with the introduction of secondary interactions into a thermoplastic silicon elastomer. The latter is thus provided with both optical functionality and mechanical integrity.

The lengths of the oligothiophene and PDMS segments can be easily varied in order to tailor the physical properties of the final system, as described in detailed in ref. [1]. As part of an ongoing research, we investigated the effect of PDMS segment length on the morphology of these copolymers and its stability upon melt processing. The small-angle X-ray scattering method provides a comprehensive insight in this kind of materials, as it follows the structure in a wide range of length scales. We selected two compounds with a rather short oligothiophene segment with three thiophene units ( $k = 1$  in Fig. 6.15). A short ( $n = 15$ ) and a long ( $n = 150$ ) PDMS length were chosen.

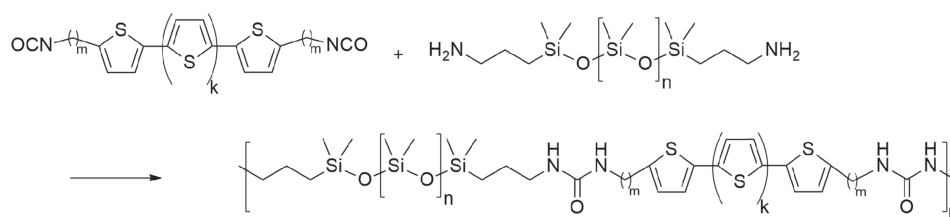


Figure 6.15: Schematic reaction route and chemical structure of the final compounds. Reproduced with permission from [1], copyright John Wiley and sons, 2015.

We performed X-ray scattering experiments in a wide range of momentum transfers  $q$ , ranging from  $10^{-2} \text{ \AA}^{-1}$  (SAXS) to  $2 \text{ \AA}^{-1}$  (WAXS). The two compounds were studied as received and after melting at  $80 \text{ }^\circ\text{C}$  followed by cooling to room temperature. The resulting scattering curves are shown in Fig. 6.16.

Starting from *wide angles* (large  $q$  values), for all samples, we observe two amorphous halos at  $q = 0.85 \text{ \AA}^{-1}$  and  $1.5 \text{ \AA}^{-1}$ . The presence of two amorphous halos is characteristic of phase separated copolymers, and correspond to distances of the order of several angstroms. The  $1.5 \text{ \AA}^{-1}$  halo (corresponding roughly to distances of  $4.4 \text{ \AA}$ ) occurs in several urea and urethane systems [2] and is here attributed to the distances between urea units in the “hard” thiophene domains. The  $0.85 \text{ \AA}^{-1}$  (distance  $7.5 \text{ \AA}^{-1}$ ) is due to PDMS, as confirmed by its relative intensity enhancement in the system with long PDMS segments. As expected, the halos persist to the melt processing.

Proceeding to the *small-angle* region, strong scattering structures with peaks in the region  $0.03 \text{ \AA}^{-1}$  to  $0.1 \text{ \AA}^{-1}$  confirm the microphase-separated morphology, which now differs substantially between the two samples.

A form factor of polydisperse homogeneous spheres combined with a hard sphere structure factor and a Porod forward scattering describes very well the scattering profile of the material

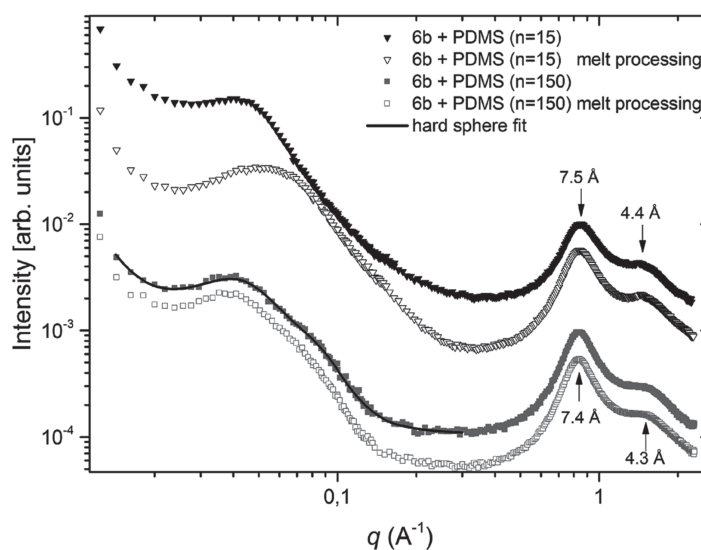


Figure 6.16:

X-ray scattering curves of the samples with  $n = 15$  and  $n = 150$ , before and after melt processing. The curves have been translated for clarity. Reproduced with permission from [1], copyright John Wiley and sons, 2015.

with long PDMS segments (solid line in Fig. 6.16). The fit gives an average radius of the spheres of  $24 \pm 1 \text{ \AA}$ , a polydispersity of  $0.30 \pm 0.06$ , and an average distance of  $67 \pm 4 \text{ \AA}$ .

Despite the smoother scattering curve of the sample with short PDMS segments, the morphology is much more complex. No simple model fits adequately to the curve. This is a common challenge in polyurethane and polyurea systems with high hard segment content as pointed out in ref. [3], which describes the morphology of similar systems as randomly dispersed hard segment nanodomains which turn more periodic and interconnected with increasing hard segment content. A Gaussian random field describes adequately curves similar to ours.

While a detailed analysis is beyond the scope of this project, we would like to point out a qualitative observation: the maxima of the scattering profiles of both materials (before melt processing) are located at very similar  $q$  values, and thus we believe that the irregular domains in the short PDMS segment material are at comparable distances with the long PDMS segment one. In other words, with decreasing PDMS length, the oligothiophene domains grow in size, rather than increase in number, which would lead to a decrease of the average distance between each other. With respect to the effect of melt processing on the morphology of the short PDMS segment material, we would like to point out that the scattering maximum moves to higher  $q$  values. This may be interpreted as an approach of the hard structures, possibly accompanied by a reduction in their size. This suggests a finer morphology upon melting and cooling down. The kinetics of microphase separation determine to a large extent the final micromorphology which can be tuned by the cooling rates applied after melting.

**Acknowledgement:** K.N.R. was supported by the TUM University Foundation Fellowship.

- [1] M. Grübel, S. Meister, U. Schulze, K.N. Raftopoulos, F. Baumer, C.M. Papadakis, T. Nilges, B. Rieger, *Macromol. Chem. Phys.* **217**, 59-71 (2015)
- [2] T. Choi, D. Fragiadakis, C.M. Roland, J. Runt, *Macromolecules* **45**, 3581 (2012)
- [3] S. D'hollander, C.J. Gommers, R. Mens, P. Adriaensens, B. Goderis, F. Du Prez, *J. Mater. Chem.* **20**, 3475 (2010)

## 6.9 Crystallization and mesophase formation of bottle brush copolymers with poly(propylene oxide)-*b*-poly(ethylene oxide) side chains

C. Psylla, K. Kyriakos, J. Zhao<sup>1</sup>, S. Pispas<sup>1</sup>, S. Kripotou<sup>2</sup>, A. Kyritsis<sup>2</sup>,  
C. M. Papadakis

<sup>1</sup> Theoretical and Physical Chemistry Institute, National Hellenic Research Foundation, Athens, Greece

<sup>2</sup> National Technical University of Athens, Physics Department, Athens, Greece

Graft copolymers with densely grafted side chains (also called bottle brush copolymers) behave differently from linear polymers because of their multibranching molecular structure. We have been studying a series of bottle brush copolymers where the side chains are diblock copolymers from poly(propyleneoxide) (PPO) and poly(ethyleneoxide) (PEO). These are grafted on a poly(*p*-hydroxystyrene) (PHOS) backbone with a grafting density of virtually one [1]. Varying the composition and the sequence of PEO and PPO in the side chains allows investigating the effect on the crystallization behavior and mesophase formation. We report here on small- and wide-angle X-ray scattering experiments (SAXS and WAXS) on bottle brush systems of various architectures and molecular compositions, focusing on the crystallization and the microphase separation.

At this, WAXS and SAXS experiments were carried out using the instrument Ganesha 300XL with a wavelength  $\lambda = 1.54 \text{ \AA}$  and sample-detector-distances of 101 and 401 mm. The samples were mounted between mica sheets. Prior to the measurements, they were heated to 80 or 100 °C and cooled down after 5 min to -80 °C with a cooling rate of -10 K/min. The measurements were taken during stepwise heating with equilibration times of 5 min after each step of 5-10 K. The measuring times were 10-30 min. Lorentz functions were fitted to the peaks in the WAXS and the SAXS curves to determine their positions and thus the crystal structure and the mesophase.

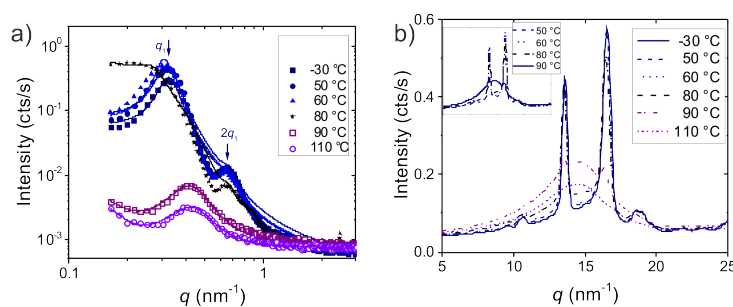


Figure 6.17:

Representative SAXS (a) and WAXS curves (b) of sample gEP. The lines in (a) are model fits.

The inset in (b) shows WAXS curves from the temperature region above  $T_m$ .

A sample with PEO (weight fraction 84.9 %) near the PHOS backbone and PPO at the end of the side chains reveals in differential scanning calorimetry (DSC) the usual melting point,  $T_m$ , of PEO of 54 °C. Up to 50 °C, the SAXS curves feature a strong diffraction peak at  $\sim 0.31\text{-}0.33 \text{ nm}^{-1}$  (Fig. 6.17a). A second-order reflection is present at  $\sim 2.1q_1$ , pointing to an asymmetric lamellar structure with a repeat distance 18.8-19.7 nm. Between 60 ° and 80 °C, the peak moves to smaller  $q$  values ( $0.25 \text{ nm}^{-1}$ ), and forward scattering appears, which may be due to large domains, possibly due to a restructuring. The second-order peak moves to values of  $2.5q_1$ ; the morphology cannot be determined in this temperature range. At 90 °C and above, the peak becomes much weaker and broader and moves to higher  $q$  values. The sample becomes disordered at these temperatures.

The changes between 50 °C and 60 °C reflect the melting of the PEO domains observed in DSC. In the WAXS measurements, two strong Bragg reflections are observed at 13.6 nm<sup>-1</sup> and 16.5 nm<sup>-1</sup> (Fig. 6.17b) which are close to the (120) and (032) reflections known from the PEO lattice (13.58 nm<sup>-1</sup> and 16.60 nm<sup>-1</sup>) [2]. Interestingly, the diffraction peaks do not vanish at the melting point from DSC, but persist up to 80 °C (inset of Fig. 6.17b) and vanish only at 100 °C. Thus, crystalline order persists even above the melting point determined by DSC. We speculate that, due to the dense grafting of the PEO blocks to the PHOS backbone, the crystalline order is maintained up to 80 °C.

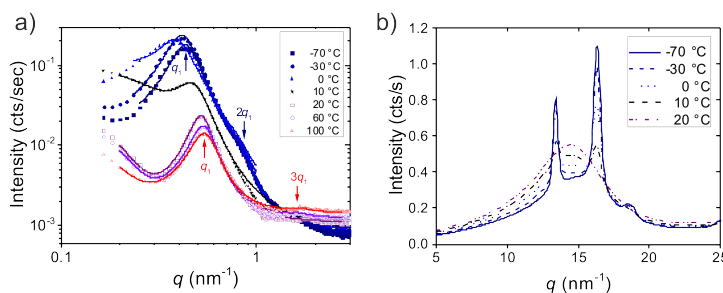


Figure 6.18:  
Representative SAXS (a) and WAXS curves (b) of sample gPE. The lines in (a) are model fits.

A sample with PPO near the PHOS backbone and PEO (62.5 %) at the end of the side chains (gPE) behaves differently. DSC revealed that the melting point of PEO is at 11 °C, thus, strongly suppressed with respect to bulk PEO. The SAXS curves feature a strong diffraction peak which moves from 0.43 nm<sup>-1</sup> at -70 °C to 0.38 nm<sup>-1</sup> at 0 °C (Fig. 6.18a). In this temperature range, the main peak features a shoulder, which is a second-order reflection at  $\approx 2q_1$ . The morphology is thus lamellar with asymmetric lamellae. Between 0 °C and 20 °C, the main reflection becomes weaker and narrower and moves to 0.52 nm<sup>-1</sup>. A higher-order reflection is present at  $\sim 3q_1$ ; this points to the formation of symmetric lamellae (for symmetric lamellae, the even-order reflections are extinct). The lamellar morphology is thus assumed both in the crystalline and the amorphous state of PEO, even though the volume fraction of PEO is far from 50 %. In the WAXS curves, the (120) and (032) Bragg reflections from the crystalline PEO lattice are observed up to 10 °C at 13.4 nm<sup>-1</sup> and 16.3 nm<sup>-1</sup> (Fig. 6.18b). These positions are lower than the expected ones (13.58 nm<sup>-1</sup> and 16.60 nm<sup>-1</sup>); thus, the lattice constants, i.e. the distances between the parallel PEO chain stems are slightly larger than in bulk PEO. The area of the reflections decreases with increasing temperature and goes to zero above -20 °C, which is again consistent with the  $T_m$  value from DSC.

Thus, two regimes are discerned: (i) up to 10 °C, a lamellar phase where PEO is crystalline with a distorted PEO crystal structure and (ii) a lamellar morphology with symmetric lamellae above. Melting of the PEO domains leads to a strong shrinkage of the repeat distance, which points to breakout crystallization.

We conclude that the architecture and the composition of the bottle brushes play an important role for the crystallization and the resulting mesophase formation.

The project is funded by DAAD in the framework "Hochschulpartnerschaften mit Griechenland".

[1] J. Zhao, G. Mountrichas, G. Zhang, S. Pispas, *Macromolecules* **43**, 1771 (2010)

[2] H. Tadokoro, Y. Chatani, T. Yoshihara, S. Tahara, S. Murahashi, *Makromol. Chem.* **73**, 109 (1964)

## 6.10 Quasielastic neutron scattering on $\alpha$ -Mg(BH<sub>4</sub>)<sub>2</sub>

L. Silvi, W. Lohstroh<sup>1</sup>

<sup>1</sup> MLZ, Garching, Germany

Energy storage is one of the most important issue of present days. For automotive application using renewable energy, hydrogen has become one of the candidate alternative to fossils. The major key in hydrogen based automotive is storage, and therefore metal borohydrides got interest due to their relative high volumetric and gravimetric hydrogen densities.

Among borohydrides, magnesium borohydride is characterized by a gravimetric and volumetric storage density of 14.9 mass% H<sub>2</sub> and 90 kg/m<sup>3</sup>. The decomposition temperature around 300 °C makes the material less suitable as a hydrogen storage compound, although it is interesting due to its gravimetric capacity. Many polymorphs of Mg(BH<sub>4</sub>)<sub>2</sub> have been observed, namely  $\alpha$ ,  $\beta$ ,  $\gamma$  and  $\delta$ -phase, the low-temperature (LT)  $\alpha$ -phase and the high-temperature (HT)  $\beta$ -phase are the most commonly investigated for hydrogen storage applications. The structure of  $\alpha$ -Mg(BH<sub>4</sub>)<sub>2</sub> has been identified by X-ray and neutron scattering techniques to be a hexagonal lattice with P6<sub>1</sub>22 space group symmetry, as shown in Fig. 6.19. Above 490 K it transforms into the  $\beta$ -phase, which is metastable when cooled down to room temperature (and below). The investigation of hydrogen dynamics could shed light on the understanding of borohydrides, especially in the picosecond timescale and in an extended momentum transfer ( $Q$ ) range.

Quasielastic neutron scattering (QENS) has been performed on  $\alpha$ -Mg(BH<sub>4</sub>)<sub>2</sub>, and due to the natural boron high absorption cross-section, the isotope <sup>11</sup>B has been used. Measurements have been performed at the cold time-of-flight spectrometer TOFTOF (Maier-Leibnitz Zentrum), at two different energy resolutions (and therefore two different timescales):  $\lambda_1 = 2.5$  Å yielding an energy resolution of 450  $\mu$ eV (FWHM) of the elastic line and an accessible elastic  $Q$  from 0.5 to 4.2 Å<sup>-1</sup>, the second at  $\lambda_2 = 6$  Å, with an energy resolution of 48  $\mu$ eV (FWHM) and an elastic momentum transfer from 0.2 to 2 Å<sup>-1</sup>.

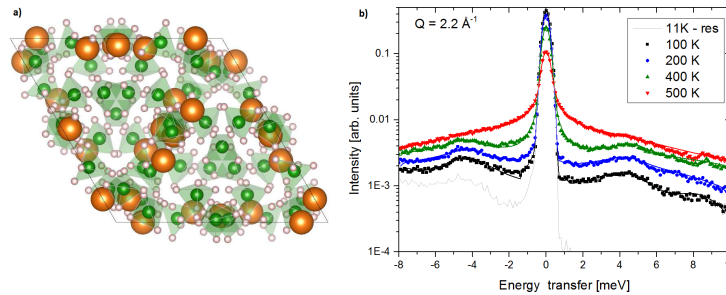


Figure 6.19:

a) crystal structure of  $\alpha$ -Mg(BH<sub>4</sub>)<sub>2</sub> along the  $c$  axis: magnesium atoms are represented by orange spheres, boron by green and hydrogen by grey spheres. b)  $S(Q, \omega)$  measured at 2.5 Å and at 11, 100, 200, 400 and 500 K. The solid lines represent the fit of the data according to  $S(Q, \omega) = S_{\text{rot}}(Q, \omega) \otimes S_{\text{vib}}(Q, \omega)$ . (see text).

Due to the large hydrogen cross section, the experiment almost exclusively probes hydrogen dynamics. Possible movements for the [BH<sub>4</sub>] units are long range diffusion, rotations around a specific axis, libration or vibrations. The scattering function for rotational motions can be written as a sum of a  $\delta$ -function and a series of Lorentzian. In case a fraction  $p$  of atoms are not moving, but the rest is, then:

$$S_{\text{rot}}(Q, \omega) = [p + (1 - p)A_0(Q)]\delta(\omega) + (1 - p) \sum_{n>0} A_n(Q)L_n(\Gamma_n, \omega), \quad (6.2)$$

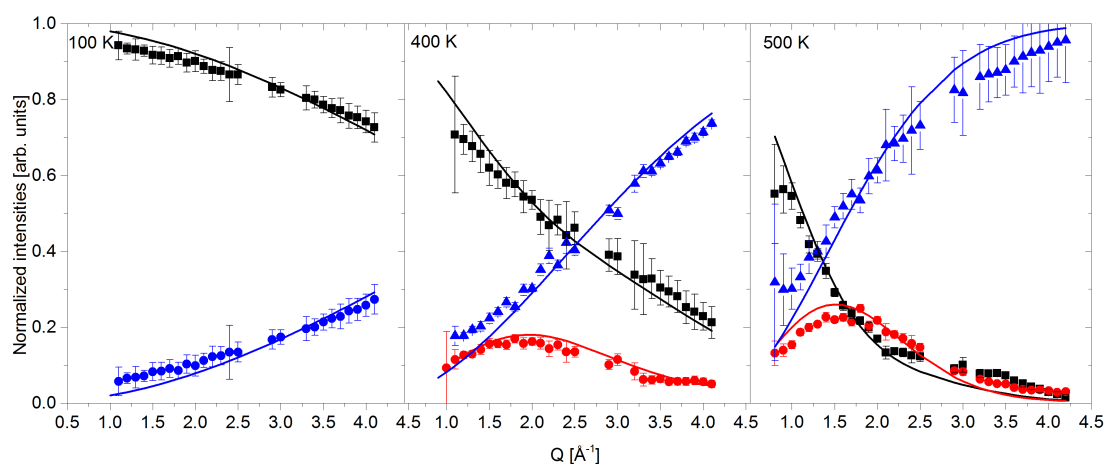


Figure 6.20:

EISF and QISF at different temperatures: EISF (black squares),  $\text{QISF}_{L_1}$  (red circles) and  $\text{QISF}_{vib}$  (blue triangles). Solid lines represent the simultaneous fit of the EISF and QISFs extracted from the scattering function  $S(Q, \omega)$ .

where the half-width-half-maximum  $\Gamma_n$  is related to the medium residence time between two successive steps, and the factor  $A_0$  is related to the geometry of reorientational dynamics. The vibrational part can be modelled separating the elastic contribution from the inelastic one:  $S_{vib}(Q, \omega) = B(Q)\delta(\omega) + [1 - B(Q)]S_{vib}^{inel}(Q, \omega)$ , where the factor  $B(Q)$  is the Debye-Waller Factor. In the harmonic approximation, it becomes:  $B(Q) = \exp(-u^2Q^2/3)$ , where  $u^2$  is the mean-square displacement of the H atoms. The inelastic scattering function used to model the data was chosen to be a damped harmonic oscillator (DHO). If motions occur in the same time scale, a convolution is used to model the scattering function:  $S(Q, \omega) = S_{rot}(Q, \omega) \otimes S_{vib}(Q, \omega)$ . Inelastic scattering have been modelled using two DHO up to 400 K, whereas for the QE part a Lorentzian is required from 300 K and above. At 500 K the  $\alpha$ -phase transforms into the  $\beta$ , and only two Lorentzian are sufficient to model the experimental data. The fraction of elastically scattered neutron (EISF) and can be evaluated directly from the measured elastic and quasielastic integrated intensities, independent of any specific model. Its dependence on the momentum transfer  $Q$ , presented in Fig. 6.20, reflects the spatial distribution of the hydrogen atoms in the long time average. The complementary of EISF is called QISF, and both quantities have been analysed independently.

From the 6 Å-data two reorientational motions are found, possible ascribed to  $C_{2/3}$  rotations. The width of the QE signal though is not showing any dependence from temperature T.

From the 2.5 Å-data, the inelastic peaks are visible up to 400 K, whereas at 500 K the DHO is supposed to be overdamped and therefore the inelastic signal falls in the QE region. Up to 400 K, only a fraction  $p = 0.55$  of  $[\text{BH}_4]$  units is undergoing on reorientational motions around one of the symmetry axis  $C_{2/3}$ , whereas as soon the  $\beta$ -phase is reached, all units are participating to the rotations.

In conclusion, a QENS experiment on  $\alpha$ - $\text{Mg}(\text{BH}_4)_2$  has been performed. A vibrational dynamics is found to be close (in energy) to the quasielastic region, and a global fit of the EISF and QISFs shows a interdependence between local reorientations (rotations around  $C_{2/3}$  axis) and vibrational dynamics (lattice vibrations).

[1] Y. Yaroslav, B. Richter, T. R. Jensen, V. Dimitriev, D. Chernyshov, H. Hagemann, *Angew. Chem. Int. Ed.* **50**, 11162 (2011)

## 6.11 A quantum dot array to template gold nanostructure growth

N. Paul<sup>1</sup>, E. Metwalli, Y. Yao, M. Schwartzkopf<sup>2</sup>, S. Yu<sup>2</sup>, S. V. Roth<sup>2</sup>, P. Müller-Buschbaum, A. Paul<sup>3</sup>

<sup>1</sup> MLZ, Garching, Germany

<sup>2</sup> DESY, Hamburg, Germany

<sup>3</sup> E21, Garching, Germany

We investigate gold nanostructure growth on a tailored CdSe quantum dot array to probe the templating possibilities. Real-time GISAXS experiments are used to follow the different stages of gold nanomorphology evolution during sputter deposition. This well-organized quantum dot array serves as a model template for investigating growth of gold nanostructures with in-situ and real-time GISAXS experiments.

*Quantum dot array before and after completing gold deposition.* Fig. 6.21(a) shows the two-dimensional GISAXS data of the bare quantum dot array where some pronounced features such as Yoneda peak, peaks due to lateral and vertical correlations are highlighted. The 1<sup>st</sup> order lateral correlation peak, indicated by a white arrow (i), arises from the in-plane nearest-neighbor short-range ordering of the CdSe quantum dots. A faint 1<sup>st</sup> order vertical correlation peak, indicated by the dashed white ellipse (iii), can be noticed directly above this peak due to a vertical correlation in the dots. This is usually an indication of a nearly uniform height of the quantum dots with only small variances. The weaker 2<sup>nd</sup> order lateral correlation peak, indicated by a white arrow (ii), shows the extension of the short range ordering to the next-nearest-neighbor level. For this lateral correlation peak as well, a faint 2<sup>nd</sup> order scattering maximum (iv) in the vertical direction (but at a lower  $Q_y=1.62 \text{ nm}^{-1}$ ) value can be seen. The most reasonable agreement between the experimental data and the simulated two-dimensional GISAXS pattern is observed for a spheroidal shape geometry as can be seen by the simulated image in Fig. 6.21(b). The most prominent size distribution extracted from this model corresponds to an average quantum dot diameter of  $5.2 \pm 0.2 \text{ nm}$ , an average inter-dot spacing of  $6.7 \pm 0.3 \text{ nm}$  and a height of 5 nm. The two-dimensional GISAXS data of the quantum dot array after gold deposition is shown in Fig. 6.21(c). As compared to the GISAXS data of the bare quantum dot array, the 1<sup>st</sup> order lateral correlation peak has shifted to a lower  $Q_y$  position, indicated by a white arrow (v). This shift is attributed to the formation of a new surface morphology during the gold deposition. Above the circular beam stop, the intensity increases due to the Kiessig oscillation, which originate from the finite thickness of the thin gold film on the quantum dot array. Based on IsGISAXS, the simulated two-dimensional GISAXS pattern for the quantum dot array after gold deposition is shown in Fig. 6.21(d). The model assumes a mixed gold-CdSe (50:50) layer having a high roughness with thick gold hemispherical clusters on top. The most prominent size distribution extracted from this model corresponds to an average particle diameter of  $5.4 \pm 0.3 \text{ nm}$ , an average inter-particle spacing of  $10.0 \pm 1.2 \text{ nm}$  and a height of 16 nm.

*Intermediate morphologies during gold sputtering.* The mappings in Fig. 6.22 have been extracted from the two-dimensional GISAXS data, obtained during gold growth. With them, the temporal evolution of vertical and horizontal structures can be seen pictorially. Fig. 6.22(a) shows the time evolution of the vertical cuts taken at a constant  $Q_y = 0.92 \text{ nm}^{-1}$ . These exhibit the temporal evolution of structures perpendicular to the sample surface, which translates into its evolution with thickness ( $d_{Au}$ ). The thickness oscillations give rise to the oscillating intensity waves in this figure.

Fig. 6.22(b) represents the time evolution of the horizontal line cuts taken at the Yoneda peak with the full time resolution of the real-time experiment. In general, horizontal line cuts are sensitive to structural features parallel to a quantum dot array. Thus, this figure represents the temporal lateral structure evolution which translates into changes with increasing thickness

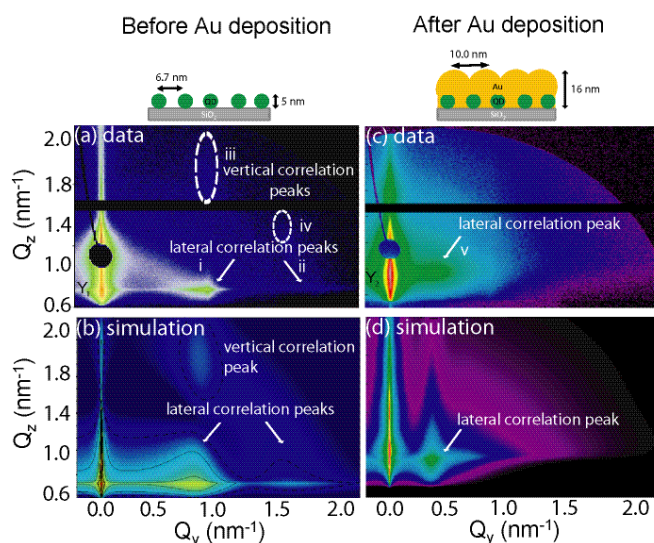


Figure 6.21:

Two-dimensional GISAXS data of the quantum dot array (a) before and (c) after gold deposition are shown along with simulated GISAXS patterns (b) before and (d) after gold deposition. Characteristic structures are highlighted and explained in the text. At the top, a schematic shows the side-view morphology of the quantum dot array before and after gold deposition.

$d_{Au}$ . The peak due to lateral correlation or intensity maxima at  $Q_y = 0.92 \text{ nm}^{-1}$ , is very intense in the initial stages till  $d_{Au} \approx 3.6 \text{ nm}$ , due to short range ordering of CdSe quantum dots. For larger  $d_{Au}$ , its intensity gradually decreases and the scattering is dominated by the scattering from the compact gold layer which has formed on the template by this time.

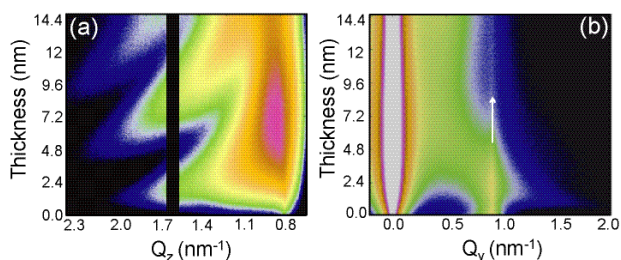


Figure 6.22:

(a) Mapping of vertical line cuts from the time-resolved two-dimensional GISAXS data (b) and mapping of horizontal line cuts from the time-resolved two-dimensional GISAXS data taken at the Yoneda maximum position. The solid white arrow follows the Au growth at quantum dots characteristic peak due to lateral correlation position.

As a consequence, we have worked out a condition to have gold metal nanocontacts positioned directly on top of quantum dots only. For such local contact formation in the nanoscale, a clever combination of a low deposition rate and a gold film thickness less than  $d_{Au} \approx 0.48 \text{ nm}$  is required. These structures will be of interest for the next generation quantum dots based nano-electronic devices serving as stable metal contacts for local charge transfer or for interconnecting the dot array. For further details on this work, please read [1].

- [1] N. Paul, E. Metwalli, Y. Yao, M. Schwartzkopf, S. Yu, S. V. Roth, P. Müller-Buschbaum, A. Paul, *Nanoscale* 7, 9703-9714 (2015)



## 7 Teaching and outreach

### 7.1 Lectures, seminars and lab courses

#### Spring semester 2015

Prof. Dr. Christine Papadakis, *Höhere Physik 2*

Prof. Dr. Peter Müller-Buschbaum, *Experimentalphysik 2 für MSE*

Prof. Dr. Christine Papadakis, *Angewandte Physik: Polymerphysik 2*

Prof. Dr. Peter Müller-Buschbaum, Dr. Ezzeldin Metwalli Ali,  
*Nanostructured Soft Materials 2*

Prof. Dr. Peter Müller-Buschbaum, Prof. Dr. Christine M. Papadakis,  
*Seminar über Struktur und Dynamik kondensierter Materie*

Prof. Dr. Peter Müller-Buschbaum, Prof. Dr. Christine M. Papadakis,  
*Seminar: Polymere*

Prof. Dr. Peter Müller-Buschbaum, Prof. Dr. Christine M. Papadakis,  
*Studentenseminar: Grundlegende Phänomene der Physik der weichen Materie*

Prof. Dr. Peter Müller-Buschbaum, Prof. Dr. Christine M. Papadakis,  
*Bachelor-Seminar: Funktionelle weiche Materialien*

Prof. Dr. Peter Müller-Buschbaum, *Seminar: Aktuelle Probleme der organischen Photovoltaik*

Prof. Dr. Winfried Petry, Prof. Dr. Peter Böni, Dr. Tobias Schrader, Dr. Thorsten Schröder,  
*Seminar über Neutronen in Forschung und Industrie*

Prof. Dr. Winfried Petry, *Blockseminar Erasmus Mundus MaMaSELF Summerschool*

#### Fall semester 2015/2016

Prof. Dr. Christine Papadakis, *Höhere Physik 1*

Prof. Dr. Peter Müller-Buschbaum, *Experimentalphysik 1 für MSE*

Prof. Dr. Winfried Petry, Dr. Michael Leitner, *Materialphysik auf atomarer Skala 1*

Prof. Dr. Winfried Petry, *MSC Radiation Biology*

Prof. Dr. Christine Papadakis, *Angewandte Physik, Polymerphysik 1*

Prof. Dr. Peter Müller-Buschbaum, Dr. Martine Philipp, *Nanostructured Soft Materials 1*

Prof. Dr. Peter Müller-Buschbaum, Prof. Dr. Christine M. Papadakis,  
*Seminar über Struktur und Dynamik kondensierter Materie*

Prof. Dr. Peter Müller-Buschbaum, Prof. Dr. Christine M. Papadakis, *Seminar: Polymere*

Prof. Dr. Peter Müller-Buschbaum, Prof. Dr. Christine M. Papadakis,  
*Studentenseminar: Grundlegende Phänomene der Physik der weichen Materie*

Prof. Dr. Peter Müller-Buschbaum, *Seminar: Aktuelle Probleme der organischen Photovoltaik*

Prof. Dr. Winfried Petry, Prof. Dr. Peter Böni, Dr. Tobias Schrader, Dr. Thorsten Schröder,  
*Seminar über Neutronen in Forschung und Industrie*

#### Lab courses 2015

*Theoretische und praktische Einführung in AFM (Fortgeschrittenenpraktikum)*

*Thermische Analyse (Fortgeschrittenenpraktikum)*

*Neutronenstreuung am FRM II (Fortgeschrittenenpraktikum)*

*JCNS Laboratory Course - Neutron Scattering (Forschungspraktikum)*

## 7.2 Conferences and public outreach

P. Müller-Buschbaum, W. Petry

Lehrerfortbildung 'Laser- und Quantenphysik'

39. Edgar-Lüscher-Seminar

Zwiesel, 24 – 26 April 2015

Programm	Organisation	39. Edgar-Lüscher-Seminar										
<p><b>Freitag, 24. April 2015</b></p> <p>13.00 - 14.30 Studienberatung der TUM</p> <p>15.00 - 15.30 Begrüßung</p> <p><b>15.30 - 16.45 Attosekundenspektroskopie an Molekülen und Festkörpern</b>  <i>Prof. Dr. Reinhard Kienberger, TUM, Physik-Department</i></p> <p>16.45 - 17.30 Diskussion und Kaffeepause</p> <p><b>17.30 - 18.45 Materiewelleninterferenz auf schnellsten Zeitskalen</b>  <i>Prof. Dr. Peter Hommelhoff, Universität Erlangen-Nürnberg, Lehrstuhl für Laserphysik</i></p> <p>18.45 - 19.00 Diskussion</p> <p><b>Samstag, 25. April 2015</b></p> <p><b>09.00 - 10.15 Quantencomputing</b>  <i>Prof. Dr. Rudolf Gross, TUM, Walther-Meißner-Institut</i></p> <p>10.15 - 11.00 Diskussion und Kaffeepause</p> <p><b>11.00 - 12.15 Schmetterlinge und Photonen: Halbleiterbasierte Bauelemente für die Quantentechnologien</b>  <i>Prof. Dr. Jonathan Finley, TUM, Walter-Schottky-Institut</i></p> <p>12.15 - 12.30 Diskussion</p> <p><b>14.30 - 15.45 Quanteninternet</b>  <i>Prof. Dr. Gerhard Rempe, Max-Planck-Institut für Quantenoptik, Garching</i></p> <p>15.45 - 16.30 Diskussion und Kaffeepause</p> <p><b>16.30 - 17.45 Teilchenbeschleunigung mit Licht</b>  <i>Prof. Dr. Jörg Schreiber, LMU München, Fakultät für Physik</i></p> <p>17.45 - 18.00 Diskussion</p> <p>im Anschluss Empfang in der Mensa des Gymnasiums Zwiesel</p> <p><b>Sonntag, 26. April 2015</b></p> <p><b>09.00 - 10.15 Relativistische Optik</b>  <i>Prof. Dr. Gerhard G. Paulus, Universität Jena, Institut für Optik und Quantenelektronik</i></p> <p>10.15 - 11.00 Diskussion und Kaffeepause</p> <p><b>11.00 - 12.15 Biomolekulare Optik mit ultra-kurzen Lichtpulsen</b>  <i>Prof. Dr. Wolfgang Zinth, Ludwig-Maximilians-Universität, Lehrstuhl für BioMolekulare Optik</i></p> <p>12.15 - 13.00 Diskussion, Themenfindung für das 40. Edgar-Lüscher-Seminar</p>	<div style="display: flex; flex-direction: column;"> <div style="display: flex; align-items: center;">  <div style="margin-left: 10px;"> <p><b>Prof. Dr. Peter Müller-Buschbaum</b> TUM</p> <p>Prof. Müller-Buschbaum ist Sprecher für das Netzwerk „Regenerative Energien (NRG)“ in der Munich School of Engineering (MSE) der TU München, Leiter des KeyLabs „TUM.solar“ im Forschungsnetzwerk „Solar Technologies Go Hybrid“, Deutscher Vertreter bei der European Polymer Federation (EPF) für den Bereich Polymerphysik und Associate Editor der Zeitschrift „ACS Applied Materials &amp; Interfaces“ der „American Chemical Society“ (ACS). Er befasst sich in seiner Forschungsarbeit mit der Entwicklung polymerbasierter Materialien mit neuartigen Struktur-Eigenschaftsbeziehungen.</p> </div> </div> <div style="display: flex; align-items: center; margin-top: 10px;">  <div style="margin-left: 10px;"> <p><b>Prof. Dr. Winfried Petry</b> TUM</p> <p>Prof. Petry ist Ordinarius am Lehrstuhl für Funktionelle Materialien (E13) des Physik Departments der TU München, Betreuungsprofessor für die Bayerische Ethikakademie und Wissenschaftlicher Direktor der Forschungsneutronenquelle Heinz Maier-Leibnitz (FRM II). Er forscht auf dem Gebiet der Materialwissenschaften mit Neutronen.</p> </div> </div> </div> <p><b>Organisatorische Hinweise</b></p> <p><b>Organisation vor Ort:</b></p> <table border="0"> <tr> <td>OSTD Heribert Strunz,</td> <td>Gymnasium Zwiesel</td> </tr> <tr> <td>OSTR Christian Stoiber,</td> <td>Gymnasium Zwiesel</td> </tr> <tr> <td>SIR Claus Starke,</td> <td>Gymnasium Zwiesel</td> </tr> <tr> <td>SIR Josef Müller,</td> <td>Gymnasium Zwiesel</td> </tr> <tr> <td>SIR Thomas Kufner,</td> <td>Gymnasium Zwiesel</td> </tr> </table> <p><b>E-Mail:</b> luescherseminar@gymnasium-zwiesel.de</p> <p><b>Hinweise:</b></p> <ul style="list-style-type: none"> <li>Alle Veranstaltungen finden in der Aula des Gymnasiums Zwiesel statt. Die Teilnehmer erhalten am Ende des Seminars für 5,- € eine CD mit sämtlichen freigegebenen Vorträgen.</li> <li>In den ausgewiesenen Kaffeepausen wird in der Mensa des Gymnasiums Kaffee und Kuchen gegen eine freiwillige Spende angeboten.</li> <li>Am Rande der Aula findet eine Ausstellung verschiedener Lehrmittelausstatter und Verlage statt.</li> </ul> <p style="font-size: small; text-align: right;">Foto: Thorsten Nöcker</p>	OSTD Heribert Strunz,	Gymnasium Zwiesel	OSTR Christian Stoiber,	Gymnasium Zwiesel	SIR Claus Starke,	Gymnasium Zwiesel	SIR Josef Müller,	Gymnasium Zwiesel	SIR Thomas Kufner,	Gymnasium Zwiesel	<p><b>Laser- und Quantenphysik</b></p>  <p>am Gymnasium Zwiesel Freitag, 24. April 2015, bis Sonntag, 26. April 2015</p> <p><b>Schirmherr:</b> Prof. Dr. Dr. h.c. mult. Wolfgang A. Herrmann, Präsident der TUM</p> <p><b>Veranstalter:</b> Ltd. OStD Anselm Räder, Ministerialbeauftragter für die Gymnasien in Niederbayern</p> <p><b>Wissenschaftliche Leitung:</b> Prof. Dr. Peter Müller-Buschbaum, TUM Prof. Dr. Winfried Petry, TUM</p> <div style="display: flex; justify-content: space-around; align-items: center;">    </div>
OSTD Heribert Strunz,	Gymnasium Zwiesel											
OSTR Christian Stoiber,	Gymnasium Zwiesel											
SIR Claus Starke,	Gymnasium Zwiesel											
SIR Josef Müller,	Gymnasium Zwiesel											
SIR Thomas Kufner,	Gymnasium Zwiesel											

W. A. Herrmann, T. Hamacher, N. Adams, H. Gasteiger, W. Lang, M. Lienkamp, P. Müller-Buschbaum, H. Spliethoff, W. Wall  
*5th Colloquium of the Munich School of Engineering 'Innovations for Energy Systems, Mobility, Buildings and Materials'*  
 Garching, 9 July 2015

**MSE** Munich School of Engineering  
 Technische Universität München **TUM**

Prof. Dr. Dr. h.c. mult. Herrmann,  
 Prof. Dr. Hamacher, Prof. Dr.-Ing. Adams,  
 Prof. Dr. Gasteiger, Prof. Dr.-Ing. Lang,  
 Prof. Dr.-Ing. Lienkamp, Prof. Dr. Müller-Buschbaum,  
 Prof. Dr.-Ing. Spliethoff, Prof. Dr.-Ing. Wall

5th Energy Colloquium of the Munich School of Engineering  
**Innovations for Energy Systems,  
 Mobility, Buildings and Materials**

09.07.2015 – 8.30 am to 9.00 pm

**8.30 - 9.00 am**  
**Registration**

**9.00 - 9.15 am**  
**Opening**  
 Klaus Diepold, Senior Vice President TUM  
 Thomas Hamacher, Director Munich School of Engineering

**9.15 - 9.45 am**  
**Keynote: The Energiewende as a Business Case**  
 Clemens Hoffmann, Director Fraunhofer Institute for Wind Energy and Energy System Technology (IWES)

**9.45 - 11.00 am**  
**Session Chair: Markus Lienkamp, WZE MSE**

**Energy Storage System Management and Design Space Exploration of Public Electric Vehicle Charging Stations**  
 Sangyoung Park, Institute for Real-Time Computer Systems

**From Model Surfaces to Nanostructured Catalysts for Oxygen Electroreduction in Fuel Cells**  
 Viktor Colic, Physics of Energy Conversion and Storage

**Visio.M - Light Vehicle Concept for Urban Electric Mobility**  
 Patrick Stenner, Institute of Automotive Technology

**11.00 - 11.45 am**  
**Poster Presentation, Coffee Break**

**11.45 - 1.00 pm**  
**Session Chair: Werner Lang, ZNB MSE**

**Design-Engineering-Based and Material-Based Improvement of Precast Concrete Facade Elements**  
 Matthias Pätzold, Chair of Building Construction and Material Science

**Non-Residential Buildings - Modelling the Long-Term Development of Energy Demand**  
 Laura Franke, Center for Sustainable Building

**The CityGML Energy ADE - An International Standardization Effort for the Extension of 3D City Models to Support Energetic Building Analysis**  
 Robert Kaden, Chair of Geoinformatics

**1.00 - 2.30 pm**  
**Poster Presentation, Lunch Break**

**2.30 - 2.50 pm**  
**Teaching at MSE**  
 Nikolaus A. Adams, Dean for Academic Affairs MSE

**2.50 - 4.05 pm**  
**Session Chair: Peter Müller-Buschbaum, NRG MSE**

**Optimization of Carbon Nanotubes Networks for Organic Photovoltaics by Femtosecond Laser Structuring**  
 Jürgen Sotrop, Institute for Nanoelectronics in cooperation with University of Applied Sciences Munich

**Metal Cluster Semiconductor Hybrid Materials in Photocatalysis for Chemical Energy Conversion**  
 Constantin Walenta, Chair of Physical Chemistry

**Hybrid Thermoelectrics Based on a Polymer-Nanoparticle Composite**  
 Nitin Saxena, Chair of Functional Materials

**4.05 - 4.50 pm**  
**Poster Presentation, Coffee Break**

**4.50 - 6.05 pm**  
**Session Chair: Hartmut Spliethoff, CPG MSE**

**Heat Transfer at Supercritical Pressures in Power Applications - Physics and Experimental Methods**  
 Gerrit Schatte, Institute for Energy Systems

**Optimal Planning of Urban Infrastructure Networks for Multiple Energy Carriers**  
 Johannes Dorfner, Institute for Renewable and Sustainable Energy Systems

**Small-Scale Wind Turbine Systems with Efficient and Inexpensive Generator Topology for Micro-Grids**  
 Christoph Hackl, Research Group MSE

**6.05 - 6.35 pm**  
**Keynote: Building and Energy Research in Singapore**  
 Priya Pawar, Energy Research Institute, Nanyang Technological University, Singapore

**6.35 - 6.50 pm**  
**Summary of the Day**

**6.50 - 9.00 pm**  
**Poster and Presentation Award, Colloquium Dinner**

**Location:**  
**TUM - Institute for Advanced Study, Garching**

**Registration:**  
<http://www.mse.tum.de>

W. Petry  
 35th Symposium on Dynamical Properties of Solids (DYPROSO)  
 Bildungszentrum Freising, 17 – 19 September 2015



35th Symposium on Dynamical Properties Solids (DyProSo 2015), 13 to 17 September 2015, at the Bildungszentrum Freising near Munich  
 Programme

Sunday, 13 September	Monday, 14 September	Tuesday, 15 September	Wednesday, 16 September	Thursday, 17 September
	9:00 10 Welcome: W. Petry Chair: W. Schranz	8:30 40 Z. Lodziana 9:10 25 Z. Evenson 9:35 25 M. Stana 10:00 25 P. Fouquet	8:30 40 A. Sacuto 9:10 40 M. Le Tacon 9:50 25 J. Park 10:15 25 T. Forrest	8:30 40 S. Jahn 9:10 25 B. Wehinger 9:35 40 S. Kamba 10:15 25 U. Wdowik
	9:10 40 A. Chumakov 9:50 25 J. Krawczyk 10:15 25 M. Philipp 10:40 30 Coffee break 11:10 40 I. Musevic	10:25 30 Coffee break Chair: J. Hlinka 10:55 40 B. Fultz 11:35 25 F. Weber	10:40 30 Coffee break Chair: T. Keller 11:10 40 J. Chang 11:50 25 A. Boris	10:40 30 Coffee break Chair: M. Arai 11:10 40 A. Pimenov 11:50 25 A. Bussmann-Holder
	11:50 25 F. Ziegler 12:15 75 Lunch Chair: A. Almeida	12:00 90 Lunch Chair: M. Leitner 13:30 40 J. Neugebauer 14:10 25 M. Pasciak 14:35 25 S. de Brion	12:15 75 Lunch Chair: J. Kulda 13:30 25 F. Damay 13:55 25 S. Petit 14:20 25 P. Neibecker	12:15 75 Lunch Chair: P. Boni 13:30 25 C. Ulrich 13:55 25 P. Ondrejko 14:20 25 J. Banys
	13:30 40 I. Kezsmarki 14:10 25 A. Loidl 14:35 25 S. de Brion	14:35 25 J. Hlinka 15:00 30 Coffee Break/End Guided tours: Cathedral and Prince Bishop's Residence, Research Reactor FRM II	14:45 30 Coffee break Chair: G. Eckold 15:15 25 W. Schranz 15:40 25 M. Majka	14:45 Close of conference and Coffee
	15:00 30 Coffee break Chair: A. Almeida R. Vilarinho Silva Chair: S. Petit 15:55 40 E. Lhotel 16:35 40 L. Eng 17:15 25 F. Pforr		Chair: J. Neuhaus 16:05 40 A. Paul 16:45 25 K.H. Michel 17:10 25 A. Tröster 17:35 25 A. Piovano 18:00 End	
17:00 Registration	17:40 End	Dinner or snack at FRMII		
19:00 Welcome Reception (Fingerfood buffet)	18:00 Dinner 19:00 Chair: B. Fultz Poster session wine/beer	18:00 Advisory Board Meeting	19:30 Conference Dinner at Bräustüberl Weißenstephan	

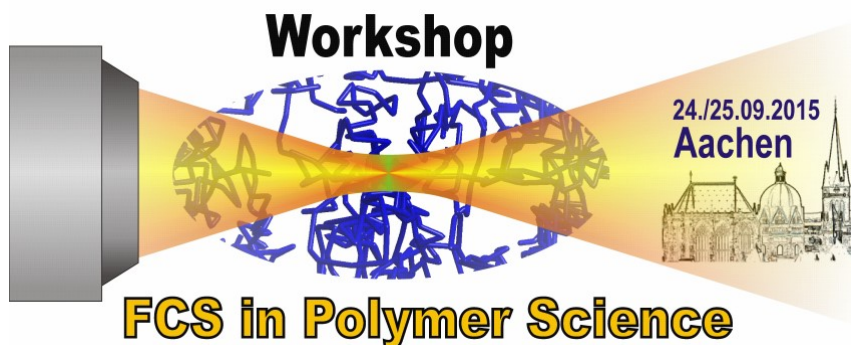
Amorphous and soft matter
Theoretical and experimental methods
Excitations of strongly correlated electrons
Diffusive dynamics
Two-dimensional systems
Electrons and Spins
Materials under high pressure
Multiferroics and ferroelectrics
Phonons and magnons
Poster session/Advisory Board Meeting
Social events

D. Wöll, C. M. Papadakis

2nd Workshop 'Fluorescence Correlation Spectroscopy in Polymer Science'

Rheinisch-Westfälische Technische Hochschule Aachen

Aachen, 24 – 25 September 2015



Thursday, September 24, 2015	
13:00–13:10	<b>Welcome address</b>
13:10–14:10	<b>Robert Holyst (invited)</b> The Length-Scale Dependent Viscosity: From Polymer Solutions to Living Cells
14:10–14:40	<b>Peter Košovan</b> MSD from FCS?
14:40–15:10	<b>Stefan Krause</b> Temperature Dependent Single Molecule Rotational Diffusion in Polymer Melts Probed by Fluorescence Correlation Spectroscopy
15:10–15:40	<b>Coffee break</b>
15:40–16:00	<b>Sergey I. Druzhinin</b> Detection and Characterization of Surface Nanobubbles with Time Correlated Single Photon Counting Imaging
16:00–16:20	<b>Simone Bonetti</b> Monitoring the Kinetics of Nanoparticles Formation by Fluorescence Correlation Spectroscopy with Molecular Rotor Tracers
16:20–17:20	<b>Jörg Enderlein (invited)</b> Fluorescence Correlation Spectroscopy: Fundamentals and Applications
17:20–18:20	<b>Poster session</b>
19:00–	<b>Dinner im Aachener Brauhaus</b>

Friday, September 25, 2015	
09:00–10:00	<b>Martin Hof (invited)</b> Hydration, Mobility, and Nanodomain Formation in Lipid Membranes Studied by Fluorescence
10:00–10:30	<b>Stefan Walta</b> Dynamics of tracer molecules in complex environments investigated by two-focus fluorescence correlation spectroscopy
10:30–10:50	<b>Antsijs Nollis</b> Dynamics of fluorescent proteins encapsulated in complex coacervate micelles
10:50–11:10	<b>Coffee break</b>
11:10–11:30	<b>Jing Xie</b> Fluorescence Correlation Spectroscopy Monitors the Hydrophobic Collapse of pH-responsive Hairy Nanoparticles at Individual Particle Level
11:30–11:50	<b>Deborah Sandrin</b> Quantitative Experimental and Theoretical Investigation of Diffusion of Macromolecules through Gel Matrices by Fluorescence Methods
11:50–12:20	<b>Daryan Kempe</b> Accurate Fluorescence Quantum Yield Determination by Fluorescence Correlation Spectroscopy
12:20–12:50	<b>Felix Koberling</b> STED-FCS for the Direct Observation of Nanoscale Dynamics
12:50–13:00	<b>Closing Remarks and Poster Prize</b>

#### Posters session (Thursday, 17:20-18:20)

**Alyazan Albarghash**, FCS on proteins in crowded environments

**Micael Gouveia**, Collapse Behavior of a Thermo- and pH-Responsive Block Copolymer in Water

**Bart-Jan Niebuur**, HPMA-Based Micelles as Drug Carriers: Influence of Chain Architecture and Molar Mass

**Romy Schachoff**, Twin Focus Photothermal Correlation Spectroscopy

**Simone Bonetti**, Monitoring the kinetics of nanoparticles formation by fluorescence correlation spectroscopy with molecular rotor tracer

**Xiaohan Zhang**, A Fluorescence Life-time Study of the Drug Delivery System Based on HPMA Copolymers

**Martin Tress**, Glassy dynamics of condensed isolated polymer chains

**Robrecht Vergauwe**, Effect of shear flow on the dynamics of polymer chains with specific intrachain associations

**Oleksii Nevskiy**, Superresolved fluorescence localization microscopy in nonpolar systems

**Alex Oppermann**, Fluorescence microscopy on microgels

P. Müller-Buschbaum

*Lehrerfortbildung 'Großgeräte und Projekte in der Physik'*

Edgar-Lüscher-Lectures

Akademie für Lehrerfortbildung Dillingen, 28 – 30 September 2015

EDGAR-LÜSCHER-LECTURES DILLINGEN/DONAU 2015

Thema: Großgeräte und Projekte in der Physik

Datum: Montag, 28. September bis Mittwoch, 30. September 2015

Tagungsort: Akademie für Lehrerfortbildung Dillingen

Veranstalter: Akademie für Lehrerfortbildung Dillingen und TU München

wissenschaftliche Leitung: Prof. Dr. Peter Müller-Buschbaum,

Technische Universität München.

Programm

**Montag, 28. 09. 2015**

15:00 – 15:30 Begrüßung

StD Werner Ettinger / Prof. Dr. Peter Müller-Buschbaum (Physik-Department TUM)

15:30 – 17:00 Dr. Thomas Tschentscher, XFEL, Hamburg

Der Molecular Movie - Das Filmen von chemischen oder biochemischen Reaktionen am European XFEL

18:30 – 20:00 Prof. Dr. Arno Hiess, European Spallation Source AB, Lund (Schweden)

Neue wissenschaftliche Möglichkeiten zur Untersuchung kondensierter Materie durch die innovative Instrumentierung der Europäischen Spallationsquelle ESS

**Dienstag, 29. 09. 2015**

8:30 – 10:00 Prof. Dr. Fritz Bosch, GSI Helmholtzzentrum für Schwerionenforschung GmbH, Darmstadt

Aktuelle Projekte bei GSI und zukünftige Möglichkeiten bei FAIR

10:00 – 10.30 Kaffeepause

10:30 – 12:00 Dr. Hans Meister, Max-Planck-Institut für Plasmaphysik, Garching  
Das International Thermonuclear Experimental Reactor (ITER) Projekt

15:30 – 17:00 Prof. Dr. Bastian Märkisch, Physik-Department, TUM, Garching  
Fundamentale Physikgroßexperimente mit Neutronen

18:30 – 20:00 Dr. Edith Maurer, DRL, Oberpfaffenhofen

Erdbeobachtung und wissenschaftliche Missionen am Deutschen Raumfahrt-Kontrollzentrum

**Mittwoch, 30. 09. 2015**

8:30 – 10:00 Dr. Sascha Schmeling, CERN, Genf (Schweiz)

Historie und aktueller Zustand

10:00 – 10.30 Kaffeepause

10:30 – 12:00 Dr. Sascha Schmeling, CERN, Genf (Schweiz)

Geplante Experimente und die Zukunft

Ab 12:00 Lehrgangsabschluss

Prof. Dr. Peter Müller-Buschbaum / StD Werner Ettinger

C. M. Papadakis, A. Kyritsis

*Greek-German Workshop 'Structural investigation and molecular dynamics of nanostructured polymeric materials'*

Athens, 28 September – 1 October 2015

**GREEK - GERMAN Workshop 2015**  
*"Structural investigation and molecular dynamics of nanostructured polymeric materials"*

	<b>Monday</b> September 28, 2015 Teleteaching room	<b>Tuesday</b> September 29, 2015 Multimedia Amphitheater	<b>Wednesday</b> September 30, 2015 Multimedia Amphitheater	<b>Thursday</b> October 1, 2015
09:00-10:00	<b>P. Pissis:</b> Polymer nanocomposites and interfacial effects	<b>S. Pispas :</b> Block copolymer nanostructures for the encapsulation and delivery of hydrophobic drugs, proteins and nucleic acids	<b>L. Tsetseris:</b> First-principles calculations of materials properties: theory and applications	<b>Lab course:</b> – DRS spectroscopy – Differential Scanning Calorimetry /TMDSC – Synthesis of polystyrene nanospheres via radical polymerization – Nanoindentation of engineering materials and structures – Dynamic Mechanical Analysis
10:00-11:00	<b>C.M. Papadakis:</b> Phase behavior of thermoresponsive polymers	<b>E. Metwalli :</b> Self-Assembly of soft hybrid materials	<b>C. Tzoumanekas:</b> Multiscale simulations of polymer systems	
11:00-11:30	<b>Coffee break</b>	<b>Coffee break</b>	<b>Coffee break</b>	
11:30-12:00	<b>K. Tsitsilianis:</b> Self-assembling hydrogels: from conventional block copolymers to peptide-based amphiphilic gelators	<b>I.A. Kartsonakis:</b> Synthesis of multifunctional coatings through polymerization techniques for corrosion protection of metals	<b>E. Kontou:</b> Thermomechanical behavior of bio-based matrix nanocomposites. Modeling of elastic properties	
12:00-12:30		<b>D.A. Dragatogiannis:</b> Nanomechanical and nantribological properties of copolymers for tissue regeneration		
12:30-13:00	<b>N. Vishnevetskaya :</b> Orthogonally responsive block copolymers	<b>K. Raftopoulos:</b> Small-angle scattering	<b>D. Georgopoulos :</b> DSC, TMDSC and Heat Capacity Spectroscopy	
13:00-13:30	<b>Lunch break</b>	<b>Lunch break</b>  <i>Visit of the archaeological site of Acropolis of Athens and the new Acropolis Museum, <b>Workshop Dinner</b></i>	<b>Lunch break</b>	<b>Lunch break</b>
13:30-14:00	<b>S. Kripotou :</b> Dielectric spectroscopy as a tool for molecular dynamics study			<b>Lab course:</b> – DRS spectroscopy – Differential Scanning Calorimetry /TMDSC – Dynamic Mechanical Analysis
14:00-15:00	<b>D. Aravopoulou:</b> Dielectric and calorimetric studies on thermoresponsive block copolymers			
15:00-15:30			<b>A. Kyritsis:</b> Hydration of macromolecules. What can we learn from dielectric measurements?	
15:30-16:00	<b>X. Krokidis, M. Kavousanakis:</b> Model, Simulate, Analyze complex materials on a multiscale level		<b>M. Philipp:</b> Studying hydration of polymers by quasi-elastic neutron scattering	
16:00-16:30	<b>Coffee break</b>			
16:30-17:30	<b>Poster session</b>			



### 7.3 Service to the community

**Prof. Dr. Peter Müller-Buschbaum:**

- Since 3/2015 member of “Advanced Light Source (ALS) Review Panel”
- Since 9/2014 member of “Heinz Maier-Leibnitz Zentrum (MLZ) Review Panel”
- From 11/2012 until 6/2015 member of “Peer Review Panel 3 – Surfaces & Interfaces” of “Diamond Light Source Ltd”
- Since 9/2012 Associate Editor of journal “ACS Applied Materials & Interfaces” of the American Chemical Society
- Since 3/2012 Head of keylab “TUM.solar” in the Bavarian Collaborative Research Project “Solar Technologies Go Hybrid” (SolTech)
- Since 1/2012 member of the Scientific Selection Panel of the Helmholtz-Zentrum Berlin für Materialien und Energie (HZB)
- Since 2011 member of European Spallation Source (ESS) Scientific Advisory Panel (Reflectivity)
- Since 2011 German representative at the European Polymer Federation (EPF) for polymer physics
- Since 2010 managing director of “Network of Renewable Energies” (NRG) at the Munich School of Engineering (MSE) of TU Munich
- Since 2010 member of TUM.Energie at TU Munich
- Since 2010 spokesman of the energy section at the Physics Department/TU Munich
- Since 2010 German representative at the European Synchrotron User Organization (ESUO)
- Since 2008 chairman of “DESY Photon Science User Committee ‘DPS-UC’” at the synchrotron radiation laboratory DESY in Hamburg

**Prof. Dr. Christine Papadakis:**

- From 9/2014 to 3/2015 Regional Editor Europe for Colloid & Polymer Science, Springer
- Since 4/2015 Editor-in-Chief for Colloid & Polymer Science, Springer
- Member of the subcommittee “College 9: Structure and Dynamics of Soft-Condensed Matter” at Institut Laue-Langevin (ILL), Grenoble, France
- Vice women’s representative of the Physics Department at TU München

**Prof. Dr. Winfried Petry:**

- Since 2015 member of the Neutron Scientific Advisory Committee of the National Research Center Kurchatov Institute “Petersburg Nuclear Physics Institute” (PNPI, Gatchina)
- Since 2012 member of the Scientific Advisory Board of NaWi Graz
- Since 2007 member of the Steering Committee of the Laue Langevin Institute and chairman of the instrumentation review panel of the CEA Leon Brillouin Laboratory
- Since 1999 liaison professor of Bayerische Eliteakademie (Bavarian Leadership Academy) and since May 2011 member of the Board of Trustees

## 8 Publications, talks and funding

### 8.1 Publications

- J. Adelsberger, A. M. Bivigou-Koumba, A. Miasnikova, P. Busch, A. Laschewsky, P. Müller-Buschbaum, C. M. Papadakis  
*Poly(styrene-block-(methoxy diethylene glycol acrylate)-block-styrene) triblock copolymers in aqueous solution – a SANS study of the temperature-induced switching behaviour*  
Colloid. Polym. Sci. **293**, 1515-1523 (2015)
- A. Campanella, Z. Di, A. Luchini, L. Paduano, A. Klapper, O. Petravic, M. S. Appavou, P. Müller-Buschbaum, H. Frielinghaus, D. Richter  
*Nanocomposites composed of HEUR polymer and magnetite iron oxide nanoparticles: Structure and magnetic response of the hydrogel and dried state*  
Polymer **60**, 176-185 (2015)
- S. Döge, C. Herold, S. Müller, C. Morkel, E. Gutschiedl, P. Geltenbort, T. Lauer, P. Fierlinger, W. Petry, P. Böni  
*Scattering cross sections of liquid deuterium for ultracold neutrons: Experimental results and a calculation model*  
Phys. Rev. B **91**, 214309 (2015)
- S. Dullinger, N. Dendoncker, A. Gattringer, M. Leitner, T. Mang, D. Moser, C. A. Mücher, C. Plutzar, M. Rounsevell, W. Willner, N. E. Zimmermann, K. Hülber  
*Modelling the effect of habitat fragmentation on climate-driven migration of European forest understorey plants*  
Diversity Distrib. **21**, 1375-1387 (2015)
- M. A. Dyakonova, A. V. Berezkin, K. Kyriakos, S. Gkempoura, M. T. Popescu, S. K. Filippov, P. Štěpánek, Z. Di, C. Tsitsilianis, C. M. Papadakis  
*Salt-induced changes in triblock polyampholyte hydrogels - computer simulations, rheological, structural and dynamic characterization*  
Macromolecules **48**, 8177-8189 (2015)
- J. Eckert, W. Lohstroh  
*Hydrogen storage materials*  
Neutron Application in Materials for Energy, Eds. G. J. Kearly, V. K. Peterson, 205-239 (2015)
- A. Eisele, K. Kyriakos, R. Bhandary, M. Schönhoff, C.M. Papadakis, B. Rieger  
*Structure and ionic conductivity of liquid crystals having propylene carbonate units*  
J. Mater. Chem. A **3**, 2942-2953 (2015)
- F. Essl, K. Biró, D. Brandes, O. Broennimann, J. M. Bullock, D. S. Chapman, B. Chauvel, S. Dullinger, B. Fumanal, A. Guisan, G. Karrer, G. Kazinczi, C. Kueffer, B. Laitung, C. Lavoie, M. Leitner, T. Mang, D. Moser, H. Müller-Schärer, B. Petitpierre, R. Richter, U. Schaffner, M. Smith, U. Starfinger, R. Vautard, G. Vogl, M. von der Lippe, S. Follak  
*Biological flora of the British isles: Ambrosia artemisiifolia*  
J. Ecol. **193**, 1069-1098 (2015)

- G. Goracci, A. Arbe, A. Alegría, V. García Sakai, S. Rudić, G. S. Schneider, W. Lohstroh, F. Juranyi, J. Colmenero  
*Influence of solvent on poly (2-(dimethylamino) ethyl methacrylate) dynamics in polymer-concentrated mixtures: A combined neutron scattering, dielectric spectroscopy, and calorimetric study*  
Macromolecules **48**, 6724-6735 (2015)
- G. Goracci, A. Arbe, A. Alegría, W. Lohstroh, Y. Su, J. Colmenero  
*Dynamics of tetrahydrofuran as minority component in a mixture with poly (2-(dimethylamino) ethyl methacrylate): A neutron scattering and dielectric spectroscopy investigation*  
J. Chem. Phys. **143**, 094505 (2015)
- S. Guo, B. Cao, W. Wang, J.- F. Moulin, P. Müller-Buschbaum  
*Effect of alcohol treatment on the performance of PTB7:PC<sub>71</sub>BM bulk heterojunction solar cells*  
ACS Appl. Mater. Interfaces **7**, 4641-4649 (2015)
- S. Guo, J. Ning, V. Körstgens, Y. Yao, E. M. Herzig, S. V. Roth, P. Müller-Buschbaum  
*The effect of fluorination in manipulating the nanomorphology in PTB7:PC<sub>71</sub>BM bulk heterojunction system*  
Adv. Energy Mater **5**, 1401315 (2015)
- G. Gupta, C. R. Singh, R. H. Lohwasser, M. Himmerlich, S. Krischok, P. Müller-Buschbaum, M. Thelakkat, H. Hoppe, T. Thurn-Albrecht  
*Morphology, crystal structure and charge transport in donor-acceptor block copolymer thin films*  
ACS Appl. Mater. Interface **7**, 12309-12318 (2015)
- A. Hexemer P. Müller-Buschbaum  
*Advanced grazing incidence techniques for modern soft matter materials analysis (feature article)*  
IUCrJ **2**, 106-125 (2015)
- T. K. Huber, H. Breitzkreutz, W. Petry, C. Reiter, S. Elgeti, D. E. Burkes, J. Casella, A. M. Casella, F. N. Smith, D.M. Wachs  
*The thermal properties of fresh and spent U-MO fuels: an overview*  
European Research Reactor Conference (RRFM 2015)
- Z. Huesges, M. M. Koza, J. P. Embs, T. Fennell, G. G. Simeoni, C. Geibel, C. Krellner, O. Stockert  
*Ferromagnetic fluctuations in YbNi<sub>4</sub>P<sub>2</sub> measured by inelastic neutron scattering*  
Journal of Physics: Conference Series **592**, 012083 (2015)
- D. Jehnichen, D. Pospiech, P. Friedel, G. He, J. Zhang, A. Sepe, C.M. Papadakis, R. Taurino, J. Perlich  
*Thin film morphologies of block copolymers with nanoparticles*  
Powder Diffraction **30 (S1)**, S16-S24 (2015)

- W. K. Kipnusu, M. M. Elmahdy, E. U. Mapesa, J. Zhang, W. Böhlmann, D.-M. Smilgies, C. M. Papadakis, F. Kremer  
*Structure and dynamics of asymmetric poly(styrene-*b*-1,4-isoprene) diblock copolymer under 1D and 2D nanoconfinement*  
ACS Appl. Mater. Interfaces **7**, 12328-12338 (2015)
- V. Körstgens, S. Pröller, T. Buchmann, D. Moseguí González, L. Song, Y. Yao, W. Wang, J. Werhahn, G. Santoro, S. V. Roth, H. Iglev, R. Kienberger, P. Müller-Buschbaum  
*Laser-ablated titania nanoparticles for aqueous processed hybrid solar cells*  
Nanoscale **7**, 2900-2904 (2015)
- P. Lellig, M. Meister, J. W. Ochsmann, M. A. Niedermeier, M. Rawolle, F. Laquai, P. Müller-Buschbaum, J. S. Gutmann  
*Application of hybrid blocking layers in solid-state dye-sensitized solar cells*  
SpringerPlus **4**, 502 1-8 (2015)
- W. Lohstroh, Z. Evenson  
*TOFTOF: Cold neutron time-of-flight spectrometer*  
Journal of large-scale research facilities **1**, 15 (2015)
- D. Magerl, M. Philipp, E. Metwalli, P. Gutfreund, X.-P. Qiu, F. M. Winnik, P. Müller-Buschbaum  
*Influence of confinement on the chain conformation of cyclic poly(*N*-Isopropylacrylamide)*  
ACS Macro Lett. **4**, 1362-1365 (2015)
- D. Magerl, M. Philipp, X.-P. Qiu, F. M. Winnik, P. Müller-Buschbaum  
*Swelling and thermo-responsive behavior of linear versus cyclic poly(*N*-isopropylacrylamide) thin films*  
Macromolecules **48**, 3104-3111 (2015)
- E. Metwalli, M. Rasool, S. Brunner, P. Müller-Buschbaum  
*Lithium-salt-containing high-molecular-weight polystyrene-block-polyethylene oxide block copolymer films*  
ChemPhysChem **16**, 2881-2889 (2015)
- D. Moseguí González, V. Körstgens, Y. Yao, L. Song, G. Santoro, S. V. Roth, P. Müller-Buschbaum  
*Improved power conversion efficiency of P3HT:PCBM organic solar cells by strong spin-orbit-coupling-induced delayed fluorescence*  
Adv. Energy Mater. **5**, 1401770 (2015)
- C. M. Palumbiny, F. Liu, T. P. Russell, A. Hexemer, C. Wang, P. Müller-Buschbaum  
*The crystallization of PEDOT:PSS polymeric electrodes probed in-situ during printing*  
Adv. Mater. **27**, 3391-3397 (2015)
- N. Paul, J. Brumbarov, A. Paul, Y. Chen, J.-F. Moulin, P. Müller-Buschbaum, J. Kunze-Liebhäuser, R. Gilles  
*GISAXS and TOF-GISANS studies on surface and depth morphology of self-organized TiO<sub>2</sub> nanotube arrays: model anode material in Li-ion batteries*  
J. Appl. Cryst. **48**, 444-454 (2015)

- N. Paul, E. Metwalli, Y. Yao, M. Schwartzkopf, S. Yu, S. V. Roth, P. Müller-Buschbaum, A. Paul  
*Templating growth of gold nanostructures with a CdSe quantum dot array*  
*Nanoscale* **7**, 9703-9714 (2015)
- V. K. Peterson, C. M. Papadakis  
*Functional materials analysis using in operando X-ray and neutron scattering*  
*IUCrJ* **2**, 292-304 (2015)
- W. Petry  
*Neutrons for industry*  
*EPJ Web of Conferences* **104**, 01001 (2015)
- M. Philipp, V. Körstgens, D. Magerl, C. Heller, Y. Yao, W. Wang, G. Santoro, S. V. Roth, P. Müller-Buschbaum  
*Sorption of water and initial stages of swelling of thin PNIPAM films using in-situ GISAXS microfluidics*  
*Langmuir* **31**, 9619-9627 (2015)
- T. Pietsch, P. Müller-Buschbaum, B. Mahltig, A. Fah  
*Nanoporous thin films and binary nanoparticle superlattices created by directed self-assembly of block-copolymer hybrid materials*  
*ACS Appl. Mater. Interfaces* **7**, 12440-12449 (2015)
- D. Pinkowicz, H. I. Southerland, C. Avendano, A. Prosvirin, C. Sanders, W. Wernsdorfer, K. S. Pedersen, J. Dreiser, R. Clérac, J. Nehr Korn, G. G. Simeoni, A. Schnegg, K. Holldack, K. R. Dunbar  
*Cyanide single-molecule magnets exhibiting solvent dependent reversible "on" and "off" exchange bias behavior*  
*J. Am. Chem. Soc.* **137**, 14406-14422 (2015)
- K. Pluhackova, H. Morhenn, L. V. Lautner, W. Lohstroh, K. Nemkovskiy, T. Unruh, R. A. Böckmann  
*Extension of the LOPLS-AA Force Field for Alcohols, Esters and Monoolein Bilayers and Its Validation by Neutron Scattering Experiments*  
*J. Phys. Chem. B* **119**, 15287-15299 (2015)
- K. N. Raftopoulos, S. Koutsoumpis, M. Jancia, J. P. Lewicki, K. Kyriakos, H. E. Mason, S. J. Harley, E. Hebda, C. M. Papadakis, K. Pielichowski, P. Pissis  
*Reduced phase separation and slowing of dynamics in polyurethanes with three-dimensional POSS-based cross-linking moieties*  
*Macromolecules* **48**, 1429-1441 (2015)
- M. H. Rosnes, M. Opitz, M. Frontzek, W. Lohstroh, J. P. Embs, P. A. Georgiev, P. D. C. Dietzel  
*Intriguing differences in hydrogen adsorption in CPO-27 materials induced by metal substitution*  
*J. Mater. Chem. A* **3**, 4827-4839 (2015)
- S. V. Roth, R. Döhrmann, R. Gehrke, R. Röhlberger, K. Schlage, E. Metwalli, V. Körstgens, M. Burghammer, C. Riekel, C. David, P. Müller-Buschbaum  
*Mapping the morphological changes of deposited gold nanoparticles across an imprinted groove*  
*J. Appl. Cryst.* **48**, 1827-1833 (2015)

- S. V. Roth, G. Santoro, J. F. H. Risch, S. Yu, M. Schwartzkopf, T. Boese, R. Döhrmann, P. Zhang, B. Besner, P. Bremen, D. Rukser, M. A. Rübhausen, N. J. Terrill, P. A. Staniec, Y. Yao, E. Metwalli, P. Müller-Buschbaum  
*Patterned diblock co-polymer thin films as templates for advanced anisotropic metal nanostructures*  
ACS Appl. Mater. Interfaces **7**, 12470-12477 (2015)
- P. Saal, L. Meter, X. H. Li, M. Hofmann, M. Hoelzel, J. N. Wagner W. Volk  
*In situ study of the influence of nickel on the phase transformation kinetics in austempered ductile iron*  
Metallurgical and Materials Transactions A **47a**, 661-671 (2015)
- K. Sarkar, E. V. Braden, S. A. Bonke, U. Bach, P. Müller-Buschbaum  
*Screen-printing of ZnO nanostructures from sol-gel solutions for their application in dye-sensitized solar cells*  
ChemSusChem **8**, 2696-2704 (2015)
- C. J. Schaffer, J. Schlipf, E. Dwi Indari, B. Su, S. Bernstorff, P. Müller-Buschbaum  
*Effect of blend composition and additives on the morphology of PCPDTBT:PC<sub>71</sub>BM thin films for organic photovoltaics*  
ACS Appl. Mater. Interfaces **7**, 21347-21355 (2015)
- M. Schindler, M. Koller, P. Müller-Buschbaum  
*Pressure sensitive adhesives under the influence of relative humidity: inner structure and failure mechanisms*  
ACS Appl. Mater. Interfaces **7**, 12319-12327 (2015)
- M. Schindler, J.-F. Moulin, P. Müller-Buschbaum  
*Adhesive-adherent interfaces probed with grazing incidence small angle neutron scattering;*  
J. Appl. Cryst. **48**, 1047-1054 (2015)
- J. Schlipf, P. Docampo, C. J. Schaffer, V. Körstgens, L. Bießmann, F. Hanusch, N. Giesbrecht, S. Bernstorff, T. Bein, P. Müller-Buschbaum  
*A closer look into 2-step perovskite conversion with x-ray scattering*  
J. Phys. Chem. Lett. **6**, 1265-1269 (2015)
- M. Schwartzkopf, G. Santoro, C. J. Brett, A. Rothkirch, O. Polonskyi, A. Hinz, E. Metwalli, Y. Yao, T. Strunskus, F. Faupel, P. Müller-Buschbaum, S. V. Roth  
*Real-time monitoring of morphology and optical properties during sputter deposition for tailoring metal-polymer-interfaces*  
ACS Appl. Mater. Interface **7**, 13547-13556 (2015)
- H. M. Specht, T. Neff, W. Reuschel, F. M. Wagner, S. Kampfer, J. J. Wilkens, W. Petry, S. E. Combs  
*Paving the road for modern particle therapy – What can we learn from the experience gained with fast neutron therapy in Munich?*  
Frontiers in Oncology **5** (2015)
- R. Tietze, H. Unterweger, S. Dürr, S. Lyer, L. Canella, P. Kudejova, F. M. Wagner, W. Petry, N. Taccardic, C. Alexiou  
*Boron containing magnetic nanoparticles for neutron capture therapy – an innovative approach for specifically targeting tumors*  
Applied Radiation and Isotopes **106**, 151-155 (2015)

- J. C. G. Tedesco, A. M. G. Carvalho, N. B. Christensen, W. Kockelmann, M. T. F. Telling, F. Yokaichiya, D. M. Töbrens, G. G. Simeoni, L. P. Cardoso, A. A. Coelho, H. Bordallo  
*Analysis of the crystallographic and magnetic structures of the  $Tb_{0.1}Pr_{0.9}Al_2$  and  $Tb_{0.25}Pr_{0.75}Al_2$  magnetocaloric compounds by means of neutron scattering*  
Journal of Materials Science **50**, 2884-2892 (2015)
- X. Wang, J.-Q. Meng, M. Wang, Y. Xiao, R. Liu, Y. Xia, Y. Yao, E. Metwalli, Q. Zhang, B. Qiu, Z. Liu, J. Pan, L.-D. Sun, C.-H. Yan, P. Müller-Buschbaum, Y.-J. Cheng  
*Facile scalable synthesis of  $TiO_2$ /carbon nanohybrids with ultrasmall  $TiO_2$  nanoparticles homogeneously embedded in carbon matrix;*  
ACS Appl. Mater. Interfaces **7**, 24247-24255 (2015)
- W. Wang, S. Pröllner, M. A. Niedermeier, V. Körstgens, M. Philipp, B. Su, S. Yu, S. V. Roth, P. Müller-Buschbaum  
*Development of the morphology during functional stack build-up of P3HT:PCBM bulk heterojunction solar cells with inverted geometry*  
ACS Appl. Mater. Interfaces **7**, 602-610 (2015)
- W. Wang, M. A. Ruderer, E. Metwalli, S. Guo, E. M. Herzig, J. Perlich, P. Müller-Buschbaum  
*Effect of methanol addition on resistance and morphology of PEDOT:PSS layers on top of carbon nanotubes for use as flexible electrodes*  
ACS Appl. Mater. Interfaces **7**, 8789-8797 (2015)
- W. Wang, C. J. Schaffer, L. Song, V. Körstgens, S. Pröllner, E. Dwi Indari, T. Wang, A. Abdelsamie, S. Bernstorff, P. Müller-Buschbaum  
*In-operando morphology investigation of inverted bulk heterojunction organic solar cells by GISAXS*  
J. Mater. Chem. A **3**, 8324-8331 (2015)
- J.-A. Weber, A. Bauer, P. Böni, H. Ceeh, S. B. Dugdale, D. Ernsting, W. Kreuzpaintner, M. Leitner, Ch. Pfeleiderer, Ch. Hugenschmidt  
*Spin-resolved fermi surface of the localized ferromagnetic Heusler compound  $Cu_2MnAl$  measured with spin-polarized positron annihilation*  
Phys. Rev. Lett. **115**, 206404 (2015)
- Y. Xiao, X. Wang, T. Wagner, J. Thiel, Y. Yao, Y. Lin, E. Metwalli, R. Liu, H. J. Butt, P. Müller-Buschbaum, J.-Q. Meng, L. Chen, L.-D. Sun, C.-H. Yan, Y.-J. Cheng  
*Solvothermal synthesis of hierarchical  $Eu_2O_3$  nanostructures templated by amphiphilic diblock copolymer PS-*b*-PMAA: Morphology control via simple variation of water content*  
J. Mater. Chem. A **3**, 5789-5793 (2015)
- Y. Yao, E. Metwalli, B. Su, V. Körstgens, D. Moseguí González, A. Miasnikova, A. Laschewsky, M. Opel, G. Santoro, S. V. Roth, P. Müller-Buschbaum  
*Arrangement of maghemite nanoparticles via wet chemical self-assembly in PS-*b*-PNIPAM diblock copolymer films*  
ACS Appl. Mater. Interfaces **7**, 13080-13091 (2015)
- S. Yu, G. Santoro, Y. Yao, D. Babonneau, M. Schwartzkopf, P. Zhang, S. Koyiloth Vayalil, P. Wessels, R. Döhrmann, M. Drescher, P. Müller-Buschbaum, S. V. Roth  
*Following the island growth in real time: Ag nanocluster layer on  $Alq_3$  thin film*  
J. Phys. Chem. C **119**, 4406-4413 (2015)

- Q. Zhong, E. Metwalli, M. Rawolle, G. Kaune, A. M. Bivigou-Koumba, A. Laschewsky, C. M. Papadakis, R. Cubitt, P. Müller-Buschbaum  
*Rehydration of thermo-responsive poly(monomethoxy-diethylenglycol acrylate) films probed in-situ by real-time neutron reflectivity*  
*Macromolecules* **48**, 3604-3612 (2015)
- Q. Zhong, Y. Y. Chen, S. L. Guan, Q. S. Fang, T. Chen, P. Müller-Buschbaum, J. P. Wang  
*Smart cleaning cotton fabrics cross-linked with thermo-responsive and flexible poly(2-(2-methoxyethoxy) ethoxyethyl methacrylate-co-ethylene glycol methacrylate)*  
*RSC Advances* **5**, 38382-38390 (2015)

## 8.2 Talks

- A. V. Berezkin, I. I. Potemkin, C. M. Papadakis  
*Simulations of solvent vapor annealing of cylinder-forming block-copolymer thin films*  
DPG Frühjahrstagung, Berlin, 15 – 20 Mar 2015
- A. Campanella, Z. Di, M.S. Appavou, A. Luchini, L. Paduano, A. Klapper, O. Petravic, P. Müller-Buschbaum, H. Frielinghaus, D. Richter  
*Nanocomposites composed of HEUR polymer and magnetite iron oxide nanoparticles*  
DPG-Frühjahrstagung, Berlin, 15 – 20 Mar 2015
- A. Campanella, A. Bràs, K. N. Raftopoulos, M. S. Appavou, P. Müller-Buschbaum, H. Frielinghaus, D. Richter  
*Nanocomposites composed of HEUR polymer and magnetite iron oxide nanoparticles*  
SoftComp Annual Meeting 2015, 9 – 11 Jun 2015, Ancona, Italy
- K.-L. Claude  
*Differential scanning calorimetry and dielectric relaxation spectroscopy measurements on PNIP-MAM*  
National Technical University of Athens, Greece, 24 Nov 2015
- M. A. Dyakonova, M.-T. Popescu, K. Kyriakos, S. Jaksch, C. Tsitsilianis, C. M. Papadakis  
*Stimuli-responsive polyampholyte hydrogels - influence of charge asymmetry and ionic strength*  
DPG-Frühjahrstagung, Berlin, 15 – 20 Mar 2015
- M. A. Dyakonova, N. Stavrouli, M. T. Popescu, A. V. Berezkin, K. Kyriakos, C. Tsitsilianis, C. M. Papadakis  
*Physical hydrogels via charge-driven self-organization of a triblock polyampholyte system in dependence on charge asymmetry and ionic strength*  
Discussion Workshop on (bio)Macromolecular Ionic Systems, Český Krumlov, Czech Republic, 10 – 14 May 2015
- M. A. Dyakonova, K. Kyriakos, A. V. Berezkin, M. T. Popescu, N. Stavrouli, I. Grillo, M. Philipp, S. Jaksch, Z. Di, C. Tsitsilianis, C. M. Papadakis  
*Stimuli-responsive reversible hydrogels from triblock polyampholytes and terpolymers*  
2nd Internal Biennial Science Meeting of the MLZ, Grainau, 15 – 18 Jun 2015
- M. A. Dyakonova, K. Kyriakos, S. Gkempoura, M. T. Popescu, S. Filippov, P. Štěpánek, Z. Di, C. Tsitsilianis, C. M. Papadakis  
*Stimuli-responsive polyampholyte hydrogels - influence of charge asymmetry and ionic strength*  
Workshop 'Crosslinking Science: Hydrogel Microsystems', Meissen, 14 – 15 Oct 2015
- H. Gerstenberg, C. Hesse, Chr. Müller, W. Petry  
*Mo-99 production at FRM II, status and perspectives*  
Physik Journal/DPG 2015, 19 Feb 2015
- W. K. Kipnusu, M. M. Elmahdy, E. U. Mapesa, J. Zhang, D.-M. Smilgies, C. M. Papadakis, F. Kremer  
*Structure and dynamics of asymmetric poly(styrene-*b*-1,4-isoprene) diblock copolymer under 1D and 2D nanoconfinement*  
DPG-Frühjahrstagung, Berlin, 15 – 20 Mar 2015

- V. Körstgens, S. Pröller, C. Mayr, G. Santoro, S. V. Roth, H. Iglev, R. Kienberger, P. Müller-Buschbaum  
*Laser-ablated titania nanoparticles for aqueous processed hybrid solar cells*  
DPG-Frühjahrstagung, Berlin, 15 – 20 Mar 2015
- V. Körstgens, S. V. Roth, P. Müller-Buschbaum  
*The investigation of structure and function of fiber coatings: Studies on human hair*  
IWRC 13, International Wool Research Conference, Hangzhou, China, 10 – 14 Jun 2015
- V. Körstgens, C. J. Schaffer, J. Schlipf, L. Biessmann, S. Bernstorff, P. Müller-Buschbaum  
*Hierarchically structured surfaces via metal decoration of colloidal films*  
ICCE-23, International Conference on Composites or Nano Engineering, Chengdu, China, 12 – 18 Jul 2015
- K. Kyriakos, M. Philipp, J. Adelsberger, S. Jaksch, A.V. Berezkin, D.M. Lugo, W. Richtering, I. Grillo, A. Miasnikova, A. Laschewsky, P. Müller-Buschbaum, C. M. Papadakis  
*Cononsolvency in P(S-b-NIPAM) diblock copolymers - a time-resolved SANS study of the aggregation process*  
DPG-Frühjahrstagung, Berlin, 15 – 20 Mar 2015
- K. Kyriakos, A. V. Berezkin, M. Philipp, P. Müller-Buschbaum, A. Miasnikova, A. Laschewsky, I. Grillo, C.M. Papadakis  
*Cononsolvency of water/methanol mixtures for PNIPAM and PS-b-PNIPAM: pathway of aggregate formation investigated using time-resolved SANS*  
15th Conference of the International Association of Colloid and Interface Scientists, Mainz, 24 – 29 May 2015
- K. Kyriakos, M. Philipp, A. V. Berezkin, I. Grillo, A. Miasnikova, A. Laschewsky, P. Müller-Buschbaum, C. M. Papadakis  
*Cononsolvency of water/methanol mixtures for PNIPAM and PS-b-PNIPAM: pathway of aggregate formation investigated using time-resolved SANS*  
European Polymer Federation Congress 2015, Dresden, 21 – 26 Jun 2015
- K. Kyriakos, A. V. Berezkin, M. Philipp, A. Zacccone, I. Grillo, A. Miasnikova, A. Laschewsky, P. Müller-Buschbaum, C. M. Papadakis  
*Cononsolvency in thermoresponsive micellar solutions: pathway of aggregate formation investigated using time-resolved SANS*  
VI European Conference on Neutron Scattering, Zaragoza, Spain, 30 Aug - 4 Sep 2015
- K. Kyriakos, A. V. Berezkin, M. Philipp, P. Müller-Buschbaum, A. Miasnikova, A. Laschewsky, I. Grillo, C. M. Papadakis  
*Cononsolvency of water/methanol mixtures for PNIPAM and PS-b-PNIPAM: pathway of aggregate formation investigated using time-resolved SANS*  
16th International Conference on Small-Angle Scattering, Berlin, 13 – 18 Sep 2015
- A. Laschewsky, V. Hildebrand, P. Müller-Buschbaum, C. M. Papadakis, N. Vishhnevetskaya  
*'Schizophrenic' micellar self-organization of twofold switchable zwitterionic block copolymers*  
Geesthachter Polymertage 2015, Geesthacht, 10 – 11 Nov 2015
- M. Leitner  
*Spatio-temporal dynamics of the cholera epidemic of 1831/1832 in Austria*  
DPG-Frühjahrstagung, Berlin, 15 – 20 Mar 2015

- M. Leitner  
*Thermodynamics of point defects and diffusion mechanisms in B2-ordered compounds*  
DPG-Frühjahrstagung, Berlin, 15 – 20 Mar 2015
- M. Leitner  
*Dispersal in plants and animals: modelling*  
Diffusion Fundamentals VI, Dresden, 15 – 19 Sep 2015
- M. Leitner, P. Neibecker, W. Petry  
*Magnetism of disordered Heusler alloys*  
20<sup>th</sup> International Conference on Magnetism, Barcelona, 5 – 10 Jul 2015
- X. Li, P. Saal, L. Meier, M. Hölzel, W. Gan, M. Hofmann  
*In-situ synchrotron and neutron diffraction studies on phase transformation in austempered ductile iron (ADI)*  
2nd Internal Biennial Science Meeting of the MLZ, Grainau, 15 – 18 Jun 2015
- W. Lohstroh  
*Cold chopper spectrometer CSPEC*  
IKON 9 - The Ninth In-Kind Contributions Meeting for Neutron Science for ESS, Lund, Sweden, 21 – 22 Sep 2015
- E. Metwalli  
*Morphological characterization of solar cell materials using neutron scattering*  
EMN-PV, Orlando, FL, USA, 12 – 15 Jan 2015
- E. Metwalli, V. Körstgens, Y. Yao, M. Schwartzkopf, S. Yu, G. Santoro, S. V. Roth, P. Müller-Buschbaum  
*In-operando GISAXS study of metal nanoparticles growth on polymer templates*  
DESY Photon Science Users' Meeting, Satellite Meeting, Hamburg, 29 Jan 2015
- E. Metwalli, V. Körstgens, Y. Yao, M. Schwartzkopf, S. Yu, S. V. Roth, P. Müller-Buschbaum  
*Metal nanopatterning using block copolymers: Differences between ionic and atomic metal selectivity*  
DPG-Frühjahrstagung, Berlin, 15 – 20 Mar 2015
- E. Metwalli  
*Introduction to soft matter*  
2nd Internal Biennial Science Meeting of the MLZ, Grainau, 15 – 18 Jun 2015
- E. Metwalli  
*Introduction to GISAXS/GISANS*  
2nd Internal Biennial Science Meeting of the MLZ, Grainau, 15 – 18 Jun 2015
- E. Metwalli  
*In-operando GISAXS study of metal nanoparticles growth on polymer films*  
GISAS, Nice, France, 8 – 11 Sep 2015
- E. Metwalli  
*Self-assembly of soft hybrid materials*  
Greek–German Workshop 2015 'Structural investigation and molecular dynamics of nano-structured polymeric materials, Athens, 28 Sep – 1 Oct 2015

- E. Metwalli, M. Rasool, S. Brunner, P. Müller-Buschbaum  
*Block copolymer based membranes for lithium ion microbatteries*  
Soft Matter and Neutrons Go Energy, Feldafing, 8 – 9 Oct 2015
- D. Moseguí González, V. Körstgens, Y. Yao, L. Song, G. Santoro, S. V. Roth, C. J. Schaffer, S. Pröller, J. Schlipf, S. Bernstorff, P. Müller-Buschbaum  
*Nanomorphology and crystallinity of P3HT:PCBM solar cells doped with iron oxide nanoparticles*  
Synchrotron Radiation in Polymer Science 2015, Madrid, 7 – 10 Sep 2015
- P. Müller-Buschbaum  
*Tailoring titania nanostructures for solar cell applications*  
Workshop „Energy Materials Nanotechnology EMN Photovoltaics Meeting 2015“ in Orlando, USA, 12 – 15 Jan 2015
- P. Müller-Buschbaum  
*Tailoring zinc oxide nanostructures for solar cell applications*  
SAXS/WAXS satellite workshop of DESY User Meeting, 29 – 30 Jan 2015
- P. Müller-Buschbaum  
*Report of the Users Committee (DPS-UC) - report 2014*  
DESY User Meeting, Hamburg, 29 – 30 Jan 2015
- P. Müller-Buschbaum, S. Guo, B. Cao, W. Wang, J.-F. Moulin  
*Effect of alcohol treatment on the morphology and performance of PTB7:PC<sub>71</sub>BM bulk heterojunction solar cell*  
DPG Frühjahrstagung, Berlin, 15 – 20 Mar 2015
- P. Müller-Buschbaum, K. Sarkar, E. V. Braden, L. Song, M. Rawolle, S. V. Roth  
*Tailoring zinc oxide nanostructures for solar cell applications*  
249th American Chemical Society National Meeting in Denver, USA, 22 - 26 Mar 2015
- P. Müller-Buschbaum  
*Inorganic-organic hybrid photovoltaic solar cells using novel hybrid materials*  
Initiation meeting of International Research Training Groups 2022 of Munich International Graduate School for Environmentally Responsible Functional Hybrid Materials (ATUMS), Munich, 10 Apr 2015
- P. Müller-Buschbaum  
*Magnetic nanoparticles enhance performance of organic solar cells*  
„Scientists Meet Scientists – Wednesday Coffee Talk“, Institute of Advanced Study, München, 15 Apr 2015
- P. Müller-Buschbaum  
*Probing nanostructures generated by block copolymer self-assembly using advanced scattering techniques*  
E-MRS, Lille, France, 11 – 15 May 2015
- P. Müller-Buschbaum  
*In-operando study of polymer based organic solar cells*  
European Polymer Federation Congress 2015, Dresden, 21 – 26 Jun 2015

- P. Müller-Buschbaum  
*Switching kinetics of thin thermo-responsive hydrogel films*  
Lecture at Zhejiang Sci-Tech University in Hangzhou, China, 9 Jun 2015
- P. Müller-Buschbaum  
*Structure and function of thin thermo-responsive hydrogel films*  
13th International Wool Research Conference (IWRC-13) and AATCC Sustainability Symposium (AATCC-SS), Hangzhou, China, 10 – 14 Jun 2015
- P. Müller-Buschbaum  
*Tailoring zinc oxide nanostructures for solar cell applications*  
International Conference on Composites/Nano Engineering (ICCE-23) Chengdu, China, 12 – 18 Jul 2015
- P. Müller-Buschbaum  
*Polymer and hybrid nanostructures for applications in organic electronics*  
JCNS-1 and ICS-1 Seminar, Jülich, 27 Aug 2015
- P. Müller-Buschbaum  
*Nanostructured polymer films for energy harvesting applications*  
JCNS Workshop 2015 "Neutron Scattering on Nanostructured Soft Matter", Tutzing, 5 – 8 Oct 2015
- P. Müller-Buschbaum  
*Tailoring titania nanostructures for solar cell applications*  
Workshop „Soft Matter and Neutrons GO Energy”, Feldafing, 8 – 9 Oct 2015
- P. Müller-Buschbaum  
*Novel devices based on polymer-inorganic hybrid materials*  
ATUMS Kick-off meeting, Edmonton, Canada, 30 Oct – 2 Nov 2015
- P. Müller-Buschbaum  
*Advanced morphology characterization based on grazing incidence small angle neutron scattering*  
GISANS workshop@KTH, Stockholm, Sweden, 26 – 27 Nov 2015
- P. Müller-Buschbaum  
*Polymer and hybrid nanostructures for applications in organic solar cells investigated with advanced scattering techniques*  
PC-Kolloquium der Universität Hamburg, Hamburg, 1 – 2 Dec 2015
- P. Neibecker, M. Leitner, G. Benka, W. Petry  
*Ordering kinetics in Ni-Mn based ferromagnetic shape memory alloys*  
DPG-Frühjahrstagung, Berlin, 15 – 20 Mar 2015
- P. Neibecker, M. Leitner, G. Benka, W. Petry  
*Increasing the achievable state of order in Ni-Mn-based Heusler alloys*  
20th International Conference on Magnetism, Barcelona, 5 – 10 Jul 2015
- P. Neibecker, J. Neuhaus, M. Leitner, K. Hradil, W. Petry, A. Glensk, B. Grabowski, T. Hickel, J. Neugebauer  
*Temperature dependence and linewidths of Al phonon dispersions*  
35<sup>th</sup> Symposium on Dynamical Properties of Solids, Freising, 13 – 17 Sep 2015

- C. M. Papadakis  
*Phase behavior of thermoresponsive polymers*  
Greek–German Workshop 2015 "Structural Investigation and Molecular Dynamics of Nanostructured Polymeric Material", Athens, Greece, 28 Sep – 1 Oct, 2015
- W. Petry  
*The Heinz Maier-Leibnitz Zentrum at TUM - an open access endeavour for research with neutrons*  
Forum on access to existing EU nuclear fission research infrastructure, Brussels 29 Jan 2015
- W. Petry  
*The Heinz Maier-Leibnitz Zentrum - where we are*  
MLZ User Meeting 2015, Ismaning, 23 – 24 Feb 2015
- W. Petry  
*Neutron and X-ray studies of advanced materials VIII: diffraction limit and beyond organic and functional materials*  
TMS 2015, Orlando, Florida, USA 15 – 19 Mar 2015
- W. Petry  
*Neutrons for research, industry and science*  
Visit of the Global Partnership Working Group (GPWG), Garching, 23 Apr 2015
- W. Petry, A. Kastenmüller, K. Seebach  
*Forschungs-Neutronenquelle Heinz Maier-Leibnitz (FRM II) – Status und Perspektiven*  
Visit of the City Council of Garching 2015, Garching, 27 Apr 2015
- W. Petry  
*The Neutron Source Heinz Maier-Leibnitz (FRM II) at TUM – neutrons for research, industry and medicine*  
Visit of The National Academies of Science – Nuclear and Radiation Studies Board (NRSB), Garching, 7 May 2015
- W. Petry  
*Neutronen für Wissenschaft, Industrie und Medizin*  
Ringvorlesung, Physics Department TUM, Garching, 2 Jun 2015
- W. Petry  
*Auf der Suche nach dem Wissen von morgen – mit Neutronen die Welt entdecken*  
Managing Board of TUM, Munich, 9 Jun 2015
- W. Petry  
*Batteries – Uncovering the inside*  
International Symposium on Current Challenges in Structural Physics – on the occasion of the retirement of Prof. Dr. Andreas Magerl, Friedrich-Alexander-Universität Erlangen-Nürnberg, 7 Jul 2015
- W. Petry  
*Testing the physical basis for advanced high density UMo fuel at TUM*  
Argonne National Laboratory, Illinois, USA, 13 Jul 2015

- W. Petry  
*Non-destructive, in-situ, in-operando material testing*  
IAEA General Assembly – Scientific Forum, Vienna, Austria, 16 Sep 2015
- W. Petry  
*Mit Neutronen die Welt entdecken: auf der Suche nach Wissen von morgen*  
Volkshochschule Garching – IAS, TUM Garching, 20 Sep 2015
- W. Petry  
*Mit Neutronen die Welt erforschen: auf der Suche nach dem Wissen von morgen*  
ARD-Campus, München, 21 Oct 2015
- W. Petry  
*Physics at NaWi Graz*  
Scientific Advisory Board Meeting NaWi Graz, Graz, Austria, 19 Nov 2015
- W. Petry  
*Neutrons for research, industry and science*  
Visit of the Non-Proliferation Directors Group (NPDG) upon Invitation of the Foreign Federal Office in the Framework of the G7 Presidency of the Federal Republic of Germany, Garching, 24 Nov 2015
- W. Petry  
*Neutronen – wozu?*  
TUM - Dies academicus, 3 Dec 2015
- W. Petry  
*Heavy ions, high intensity, high energy for materials science*  
MLL workshop on Future Science 2019 and beyond, TUM Garching, 16 Dec 2015
- M. Philipp  
*Transitions de phases et phénomènes interfaciaux de la matière condensée molle*  
Habilitation à diriger des recherches, Université de Lorraine, Nancy, France, 30 Jan 2015
- M. Philipp  
*Phase transitions in soft condensed matter*  
Workshop Temperature modulated refractometry, Hannover, 4 – 6 Mar 2015
- M. Philipp, R. Aleksandrova, U. Müller, J. K. Krüger, P. Müller-Buschbaum  
*Molecular versus macroscopic perspective on the phase separation mechanisms of thermo-responsive solutions*  
DPG-Frühjahrstagung, Berlin, 15 – 20 Mar 2015
- M. Philipp  
*Nonlinear and kinetic processes at demixing transitions of polymer solutions*  
Seminar of the Laboratoire de Science et Ingénierie de la Matière Molle (SIMM), Ecole Supérieure de Physique et de Chimie Industrielles de la Ville de Paris, ESPCI ParisTech, Paris, France, 9 Apr 2015
- M. Philipp  
*Demixing phase transitions in stimuli-responsive solutions: the role of nonlinearities and molecular kinetics*  
Festkörperkolloquium, TUM, 30 Apr 2015

- M. Philipp, P. Müller-Buschbaum  
*Structure and properties of magnetic hydrogels*  
Workshop 'Progress in hydrogel-based microsystems', Baltic Sea, 15 – 18 Jun 2015
- M. Philipp, J. K. Krüger  
*Introduction into the glass transition*  
Workshop: Relaxation processes in condensed matter, Romanèche-Thorins, France, 4 – 9 Sep 2015
- M. Philipp, K. Kyriakos, U. Müller, W. Lohstroh, W. Petry, C. M. Papadakis, J. K. Krüger, P. Müller-Buschbaum  
*Immense elastic softening and the responsible molecular mechanisms near the demixing phase transition of thermo-responsive polymer solutions*  
35th Symposium on Dynamic Properties of Solids (DyProSo 2015), Freising, 14 – 17 Sep 2015
- M. Philipp, K. Kyriakos, U. Müller, W. Lohstroh, W. Petry, C. M. Papadakis, J. K. Krüger, P. Müller-Buschbaum  
*Studying the volume phase transition by quasi-elastic scattering techniques*  
Greek–German Workshop 2015 'Structural investigation and molecular dynamics of nano-structured polymeric materials', Athens, Greece, 28 Sep – 1 Oct 2015
- M. Philipp, V. Körstgens, D. Magerl, C. Heller, Y. Yao, W. Wang, G. Santoro, S. V. Roth, P. Müller-Buschbaum  
*Sorption of water and initial stages of swelling of thin hydrophilic polymer films*  
Soft Matter and Neutrons GO Energy, Feldafing, 8 – 9 Oct 2015
- K. N. Raftopoulos, S. Koutsoumpis, M. Jancia, K. Kyriakos, E. Hebda, C. M. Papadakis, K. Pielichowski, P. Pissis  
*Organic inorganic hybrid PU-POSS networks: A multi-length-scale investigation of morphology and a multi-time-scale investigation of dynamics*  
DPG Frühjahrstagung, Berlin, 15 – 20 Mar 2015
- K. N. Raftopoulos  
*Small angle neutron scattering. Tutorial talk.*  
2nd internal biennial science meeting of the MLZ, Grainau, 15 – 18 Jun 2015
- K. N. Raftopoulos, S. Koutsoumpis, M. Jancia, K. Kyriakos, E. Hebda, P. Pissis, K. Pielichowski, C. M. Papadakis  
*Microphase separation & molecular dynamics in organic-inorganic hybrid polyurethanes with POSS chemical crosslinks. Little surprises in mechanical properties*  
European Polymer Federation Congress 2015, Dresden, 21 – 26 Jun 2015
- K. N. Raftopoulos  
*Small angle scattering. Tutorial Talk.*  
Greek–German Workshop 2015 'Structural investigation and molecular dynamics of nano-structured polymeric materials', Athens, Greece, 28 Sep – 1 Oct 2015
- N. Saxena, A. Greppmair, F. Baumer, T. Nilges, M. S. Brandt, P. Müller-Buschbaum  
*Hybrid thermoelectrics based on conducting polymers*  
MSE Colloquium, Garching, Germany, 9 Jul 2015

- C. J. Schaffer, J. Schlipf, B. Su, E. D. Indari, S. Bernstorff, P. Müller-Buschbaum  
*The influence of octanedithiol on the nanomorphology and stability of PCPDTBT : PC<sub>71</sub>BM thin films for organic photovoltaics*  
4<sup>th</sup> International SolTech Workshop, Kloster Banz (Germany), Mar 2015
- C. J. Schaffer, C. M. Palumbiny, M. A. Niedermeier, C. Jendrzewski, G. Santoro, S. V. Roth, P. Müller-Buschbaum  
*Watching morphological degradation in polymer-based solar cells*  
International Conference on Composites/Nano Engineering (ICCE-23) Chengdu, China, 12 – 18 Jul 2015
- L. Song, W. Wang, V. Körstgens, D. Moseguí González, Y. Yao, N. K. Minar, J. M. Feckl, T. Bein, D. Fattakhova-Rohlfing, G. Santoro, S. V. Roth, P. Müller-Buschbaum  
*Spray deposition of titania films with incorporated crystalline nanoparticles for solid-state dye-sensitized solar cells*  
DPG-Frühjahrstagung, Berlin, 15 – 20 Mar 2015
- L. Song, M. Philipp, N. Saxena, C. M. Palumbiny, M. Haese-Seiller, J.-F. Moulin, N. Hüsing, N. K. Minar, D. Fattakhova-Rohlfing, P. Müller-Buschbaum  
*Films with hierarchical porosity assembled from ultra-small titania nanoparticles*  
JCNS-Workshop “Neutron Scattering on Nano-Structured Soft Matter: Synthetic and Bio-Materials“, Tutzing, 5 – 8 Oct 2015
- N. Vishnevetskaya, V. Hildebrand, M. Philipp, A. Laschewsky, P. Müller-Buschbaum, C. M. Papadakis  
*Aggregation behavior of doubly thermo-responsive poly(sulfobetaine-b-(N-isopropylmethacrylamide) diblock copolymers*  
DPG-Frühjahrstagung, Berlin, 15 – 20 Mar 2015
- N. Vishnevetskaya, V. Hildebrand, M. Philipp, A. Laschewsky, P. Müller-Buschbaum, C. M. Papadakis  
*Aggregation behavior of doubly thermo-responsive poly(sulfobetaine-b-(N-isopropylmethacrylamide) diblock copolymers*  
2nd internal biennial science meeting of the MLZ, Grainau, 15 — 18 Jun 2015
- N. Vishnevetskaya, V. Hildebrand, M. Philipp, A. Laschewsky, I. Grillo, P. Müller-Buschbaum, C. M. Papadakis  
*Aggregation behavior of doubly thermo-responsive poly(sulfobetaine-b-(N-isopropylmethacrylamide) diblock copolymers*  
Greek–German Workshop 2015 ‘Structural investigation and molecular dynamics of nanostructured polymeric materials’, Athens, 28 Sep – 1 Oct 2015
- R. Wang, Z. Di, H. Frielinghaus, P. Müller-Buschbaum, D. Richter  
*Conjugated diblock copolymer/fullerene bulk heterojunction system in organic photovoltaic application*  
DPG-Frühjahrstagung, Berlin, 15 – 20 Mar 2015
- J. Zhang, D. Posselt, D.-M. Smilgies, J. Perlich, I. I. Potemkin, C. M. Papadakis  
*Time-resolved GISAXS investigations during solvent vapor treatment of block copolymer thin films*  
6th International Conference on Synchrotron Radiation in Polymer Science, Madrid, Spain, 7 – 10 Sep 2015

### 8.3 Posters

- E. Barabino, W. Wang, P. Müller-Buschbaum  
*Characterization of PTB7-Th:PC<sub>71</sub>BM bulk heterojunction solar cells*  
DPG-Frühjahrstagung, Berlin, 15 – 20 Mar 2015
- E. Barabino, W. Wang, P. Müller-Buschbaum  
*Characterization of PTB7-Th:PC<sub>71</sub>BM bulk heterojunction solar cells: influence of blend ratio*  
2nd internal biennial science meeting of the MLZ, Grainau, 15 – 18 Jun 2015
- E. Barabino, W. Wang, P. Müller-Buschbaum  
*Characterization of PTB7-Th:PC<sub>71</sub>BM bulk heterojunction solar cells: influence of blend ratio*  
5th Colloquium of the Munich School of Engineering, Garching, 9 Jul 2015
- L. Bießmann, C. J. Schaffer, J. Schlipf, V. Körstgens, S. Bernstorff, P. Müller-Buschbaum  
*Investigations on ZnO scattering layers for OLED applications*  
DPG-Frühjahrstagung, Berlin, 15 – 20 Mar 2015
- L. Bießmann, C. J. Schaffer, J. Schlipf, V. Körstgens, S. Bernstorff, P. Müller-Buschbaum  
*Investigations on ZnO scattering layers for OLED applications*  
2nd Internal Biennial Science Meeting of the MLZ, Grainau, 1 – 18 Jun 2015
- L. Bießmann, P. Müller-Buschbaum  
*Investigations on ZnO scattering layers for OLED applications*  
5th Colloquium of the Munich School of Engineering, Garching, 9 Jul 2015
- A. Campanella, Z. Di, A. Bràs K. N. Raftopoulos, M.S. Appavou, P. Müller-Buschbaum, H. Frielinghaus, L. Paduano, D. Richter  
*Nanocomposites composed of HEUR polymer and magnetite nanoparticles: structure and dynamics*  
SUPOLEN Summer School 2015, Capri, 6 – 10 Jul 2015
- K.-L. Claude, S. Pinzek, K. Kyriakos, A. Schulte, A. Miasnikova, A. Laschewsky, P. Müller-Buschbaum, C.M. Papadakis  
*Phase transition of thermoresponsive polymers in dependence on temperature and pressure*  
Greek-German Workshop 2015 'Structural investigation and molecular dynamics of nanostructured polymeric materials', Athens, Greece, 28 Sep — 1 Oct 2015
- M. Coriç, N. Saxena, J. Wernecke, S. Langner, P. Müller-Buschbaum, M. Krumrey, E. M. Herzig  
*Resonant grazing incidence small angle X-ray scattering of conducting polymers*  
GISAS Conference 2015, Nizza, France, 8 – 11 Sep 2015
- M. Coriç, N. Saxena, J. Wernecke, S. Langner, P. Müller-Buschbaum, M. Krumrey, E. M. Herzig  
*Resonant grazing incidence small angle X-ray scattering of conducting polymers*  
MatHero Summerschool, Freudenstadt, 23 – 27 Aug 2015
- M. Coriç, N. Saxena, J. Wernecke, S. Langner, P. Müller-Buschbaum, M. Krumrey, E. M. Herzig  
*Resonant grazing incidence small angle X-ray scattering of conducting polymers*  
5th Colloquium of the Munich School of Engineering, Garching, 9 Jul 2015

- M. Coriç, N. Saxena, J. Wernecke, S. Langner, P. Müller-Buschbaum, M. Krumrey, E. M. Herzig  
*Resonant GISAXS of conducting polymers*  
DPG-Frühjahrstagung, Berlin, 15 – 20 Mar 2015
- M. Dodenhöft, C. Steyer, R. Jungwirth, H. Breitzkreutz, W. Petry  
*Metallographic preparation of Uranium-Molybdenum*  
RERTR 2015, Seoul, Korea 11 – 14 Oct 2015
- F. Englbrecht, S. Pröller, E. M. Herzig, P. Müller-Buschbaum  
*Influence of drying dynamics on performance of printed organic solar cells*  
5th Colloquium of the Munich School of Engineering, Garching, 9 Jul 2015
- M. H. Futscher, M. Philipp, P. Müller-Buschbaum, A. Schulte  
*Demixing transition and molecular interactions in Poly(N-isopropyl acrylamide) solutions compared to its monomer*  
DPG-Frühjahrstagung, Berlin, 15 – 20 Mar 2015
- M. H. Futscher, M. V. Nardi, J. Niederhausen, P. Müller-Buschbaum, N. Koch  
*Energy-level alignment at the hybrid interface between ZnO and the organic semiconductor  $\alpha$ -NPD doped with F<sub>6</sub>TCNNQ*  
2nd Internal Biennial Science Meeting of the MLZ, Grainau, 15 – 18 Jun 2015
- M. Gouveia, C. Crucho, J. P. S. Farinha, C.M. Papadakis  
*Collapse behavior of a thermo- and pH-responsive block copolymer in water*  
2nd Internal Biennial Science Meeting of the MLZ, Grainau, 15 – 18 Jun 2015
- X. Li, P. Saal, W. Gan, M. Hölzel, M. Hofmann  
*Strain induced martensitic Transformation in Austempered Ductile Iron (ADI)*  
ICM12, Karlsruhe, 10 – 14 May 2015
- F.C. Löhner, S. Guo, P. Müller-Buschbaum  
*Characterization and comparison of the optical properties of high-efficiency polymers PBDTT-FTTE and PBT7*  
DPG-Frühjahrstagung, Berlin, 15 – 20 Mar 2015
- F. C. Löhner, V. Körstgens, P. Müller-Buschbaum  
*Characterization of the optical and morphological properties of high-efficiency polymers*  
2nd Internal Biennial Science Meeting of the MLZ, Grainau, 15 – 18 Jun 2015
- F. C. Löhner, V. Körstgens, P. Müller-Buschbaum  
*Characterization of the optical and morphological properties of high-efficiency polymers*  
Tag der Physikerinnen/Day of Female Physicists, Garching, 23 Jun 2015
- F. C. Löhner, V. Körstgens, P. Müller-Buschbaum  
*Low band gap polymers – the future in organic photovoltaics?*  
5th Colloquium of the Munich School of Engineering, Garching, 9 Jul 2015
- E. Metwalli, Y. Yao, V. Körstgens, W. Weijia, S. Yu, G. Santoro, M. Schwartzkopf, S. V. Roth, P. Müller-Buschbaum  
*Metal-polymer nanocomposite films: Structure and properties*  
DESY Photon Science Users' Meeting, Hamburg, 28 – 30 Jan 2015

- E. Metwalli, M. A. Ruderer, M. Rawolle, J.-F. Moulin, P. Müller-Buschbaum  
*Morphological investigations of nanostructured polymer thin films at buried interfaces*  
MLZ User Meeting, Ismaning, 23 – 24 Feb 2015
- E. Metwalli, M. Rasool, S. Brunner, P. Müller-Buschbaum  
*Block copolymer based membranes for lithium-ion microbatteries*  
5th Colloquium of the Munich School of Engineering, Garching, 9 Jul 2015
- E. Metwalli, Y. Yao, J.-F. Moulin, M. Opel, P. Müller-Buschbaum  
*Structural investigation of metal oxide-block copolymer hybrid thin films*  
JCSN Workshop, Tutzing, 5 – 8 Oct 2015
- D. Moseguí González, V. Körstgens, Y. Yao, L. Song, G. Santoro, S. V. Roth, P. Müller-Buschbaum  
*Performance of P3HT:PCBM solar cells modified with iron oxide nanoparticles*  
NIM Summer Retreat, Lenggries, 27 – 29 Jul 2015
- D. Moseguí González, V. Körstgens, Y. Yao, L. Song, G. Santoro, S. V. Roth, P. Müller-Buschbaum  
*Performance of P3HT:PCBM solar cells modified with iron oxide nanoparticles*  
5th Colloquium of the Munich School of Engineering, Garching, 9 Jul 2015
- D. Moseguí González, V. Körstgens, Y. Yao, L. Song, G. Santoro, S. V. Roth, P. Müller-Buschbaum  
*Performance of P3HT:PCBM solar cells modified with iron oxide nanoparticles*  
DPG-Frühjahrstagung, Berlin, 15 – 20 Mar 2015
- D. Moseguí González, V. Körstgens, Y. Yao, L. Song, G. Santoro, S. V. Roth, P. Müller-Buschbaum  
*Performance of P3HT:PCBM solar cells modified with iron oxide nanoparticles*  
4th International Solar Technologies Go Hybrid-Workshop, Kloster Banz, 12 – 14 Mar 2015
- B. J. Niebuur, N. Vishnevetskaya, E. Lomkova, P. Chytil, S. K. Filippov, C. M. Papadakis  
*Drug carriers based on HPMA nanoparticles: influence of molar mass*  
DPG-Frühjahrstagung, Berlin, 15 – 20 Mar 2015
- B. J. Niebuur, N. Vishnevetskaya, E. Lomkova, P. Chytil, S. K. Filippov, C. M. Papadakis  
*HPMA-based micelles as drug-carriers: influence of chain-architecture and molar mass*  
2nd Internal Biennial Science Meeting of the MLZ, Grainau, 15 – 18 Jun 2015
- B. J. Niebuur, N. Vishnevetskaya, E. Lomkova, P. Chytil, S. K. Filippov, C. M. Papadakis  
*HPMA-based micelles as drug-carriers: influence of chain-architecture and molar mass*  
FCS in Polymer Science Workshop, Aachen, 24 – 25 Sep 2015
- B. J. Niebuur, N. Vishnevetskaya, E. Lomkova, P. Chytil, S. K. Filippov, C. M. Papadakis  
*HPMA-based micelles as drug-carriers: influence of chain-architecture and molar mass*  
Greek-German Workshop 2015 'Structural investigation and molecular dynamics of nanostructured polymeric materials', Athens, Greece, 28 Sep – 1 Oct 2015
- M. Philipp, K. Kyriakos, L. Silvi, W. Lohstroh, W. Petry, J. K. Krüger, C. M. Papadakis, P. Müller-Buschbaum  
*From molecular dehydration to volume expansion of phase-separating PNIPAM solutions*  
MLZ User Meeting 2015, Ismaning, 23 – 24 Feb 2015

- M. Philipp, K. Kyriakos, L. Silvi, W. Lohstroh, W. Petry, J. K. Krüger, C. M. Papadakis, P. Müller-Buschbaum  
*From molecular dehydration to volume expansion of phase-separating PNIPAM solutions*  
JCNS Workshop 2015, Tutzing, 5 – 8 Oct 2015
- S. Pröller, F. Liu, C. Zhu, C. Wang, T. P. Russell, A. Hexemer, P. Müller-Buschbaum, E. M. Herzig  
*Following the evolution of nanostructures in active layers of printed solar cells*  
5th Colloquium of the Munich School of Engineering, Garching, 9 Jul 2015
- S. Pröller, F. Liu, C. Zhu, C. Wang, T. P. Russell, A. Hexemer, P. Müller-Buschbaum, E. M. Herzig  
*Following the evolution of nanostructures in active layers of printed solar cells*  
RACIRI summer school, Rügen, 22 – 29 Aug 2015
- S. Pröller, F. Liu, C. Zhu, C. Wang, T. P. Russell, A. Hexemer, P. Müller-Buschbaum, E. M. Herzig  
*Following the evolution of nanostructures in active layers of printed solar cells*  
Printed Electronics Workshop, Würzburg, 9 Oct 2015
- K. N. Raftopoulos, M. Rasool, E. Metwalli, P. Müller-Buschbaum, C. M. Papadakis  
*Morphology of nanocomposite copolymer electrolytes for Li<sup>+</sup>/polymer batteries*  
DPG Frühjahrstagung, Berlin, 15-20 March 2015
- N. Saxena, A. Greppmair, M. S. Brandt, P. Müller-Buschbaum  
*Novel thermoelectric films based on a polymer-nanoparticle composite*  
DPG-Frühjahrstagung, Berlin, 15 – 20 Mar 2015
- N. Saxena, A. Greppmair, M. S. Brandt, P. Müller-Buschbaum  
*Novel thermoelectric films based on a polymer-nanoparticle composite*  
2nd Internal Biennial Science Meeting of the MLZ, Grainau, 15 – 18 Jun 2015
- N. Saxena, A. Greppmair, M. S. Brandt, P. Müller-Buschbaum  
*Novel thermoelectric films based on a polymer-nanoparticle composite*  
Congress of European Polymer Federation, Dresden, Germany, 21 – 26 Jun 2015
- N. Saxena, M. Coriç, J. Wernecke, S. Langner, M. Krumrey, E. M. Herzig, P. Müller-Buschbaum  
*Hybrid thermoelectrics based on a polymer/nanoparticle composite*  
SAS 2015, Berlin, 13 – 18 Sep 2015
- N. Saxena, M. Philipp, L. Song, C. M. Palumbiny, M. Haese-Seiller, J.-F. Moulin, P. Müller-Buschbaum  
*Hybrid thermoelectrics based on a polymer/nanoparticle composite*  
Jülich Center for Neutron Science Workshop, Tutzing, 5 – 8 Oct 2015
- C. J. Schaffer, C. M. Palumbiny, M. A. Niedermeier, C. Jendrzejewski, G. Santoro, S. V. Roth, P. Müller-Buschbaum  
*Degradation in polymer based solar cells - A live broadcast -*  
E-MRS, Lille, France, 11 – 15 May 2015

- C. J. Schaffer, J. Schlipf, B. Su, E. D. Indari, S. Bernstorff, P. Müller-Buschbaum  
*Morphology of PCPDTBT:PC<sub>71</sub>BM Thin films for organic photovoltaics*  
DPG-Frühjahrstagung, Berlin, 15 – 20 Mar 2015
- C. J. Schaffer, J. Schlipf, B. Su, E. D. Indari, S. Bernstorff, P. Müller-Buschbaum  
*Degradation in organic solar cells: Why structure matters*  
5th Colloquium of the Munich School of Engineering, Garching, 9 Jul 2015
- S. Schaper, E. Metwalli, M. Rasool, S. Brunner, P. Müller-Buschbaum  
*Lithium ion containing block copolymer membrane for lithium ion microbatteries*  
2nd Biennial Science Meeting of the MLZ, Grainau, 15 – 18 Jun 2015
- L. Song, W. Wang, V. Körstgens, D. Moseguí González, Y. Yao, N. K. Minar, J. M. Feckl, T. Bein, D. Fattakhova-Rohlfing, G. Santoro, S. V. Roth, P. Müller-Buschbaum  
*Spray deposition of titania films with introduction of crystalline nanoparticles for solid-state dye-sensitized solar cells*  
4th International Solar Technologies Go Hybrid-Workshop, Kloster Banz, 12 – 14 Mar 2015
- L. Song, W. Wang, V. Körstgens, D. Moseguí González, Y. Yao, N. K. Minar, J. M. Feckl, T. Bein, D. Fattakhova-Rohlfing, S. V. Roth, P. Müller-Buschbaum  
*Spray deposition of titania films with incorporated crystalline nanoparticles for solid-state dye-sensitized solar cells*  
5th Colloquium of the Munich School of Engineering, Garching, 9 Jul 2015
- J. R. Stockhausen, C. J. Schaffer, P. Müller-Buschbaum  
*Degradation of printed polymer:fullerene thin films for organic photovoltaics*  
DPG-Frühjahrstagung, Berlin, 15 – 20 Mar 2015
- J. R. Stockhausen, C. J. Schaffer, P. Müller-Buschbaum  
*Degradation of printed polymer:fullerene thin films for organic photovoltaics*  
2nd Internal biennial science meeting of the MLZ, Grainau, 15 – 18 Jun 2015
- J. R. Stockhausen, C. J. Schaffer, P. Müller-Buschbaum  
*Degradation of printed polymer:fullerene thin films for organic photovoltaics*  
5th Colloquium of the Munich School of Engineering, Garching, 9 Jul 2015
- B. Su, Y. C. Rui, V. Körstgens, S. Bernstorff, P. Müller-Buschbaum  
*Light harvesting structured titania films prepared by PDMS molds*  
DPG-Frühjahrstagung, Berlin, 15 – 20 Mar 2015
- B. Su, H. A. Caller-Guzman, V. Körstgens, C. J. Schaffer, Y. Yao, S. V. Roth, P. Müller-Buschbaum  
*Foam-like structure of spray coated titania films for photovoltaic application*  
5th Colloquium of the Munich School of Engineering, Garching, 9 Jul 2015
- N. Vishnevetskaya, V. Hildebrand, M. Philipp, A. Laschewsky, P. Müller-Buschbaum, C. M. Papadakis  
*Aggregation behavior of doubly thermo-responsive poly(sulfobetaine-*b*-(*N*-isopropyl methacrylamide) diblock copolymers*  
15th Conference of the International Association of Colloid and Interface Scientists, Mainz, 24 – 29 May 2015

- R. Wang, P. Müller-Buschbaum, H. Frielinghaus  
*Conjugated diblock copolymer/fullerene bulk heterojunction system in organic photovoltaic application*  
Hybrid and Organic Photovoltaics Conference 2015, Rome, 10 – 13 May 2015
- W. Wang, S. Pröller, M. A. Niedermeier, V. Körstgens, M. Philipp, B. Su, S. Yu, S. V. Roth, P. Müller-Buschbaum  
*Evolution of the morphology during functional stacks build-up of P3HT:PCBM inverted solar cells*  
DPG-Frühjahrstagung, Berlin, 15 – 20 Mar 2015
- W. Wang, S. Pröller, V. Körstgens, M. Philipp, B. Su, S. Yu, S. V. Roth, P. Müller-Buschbaum  
*Evolution of the structure during functional stacks build-up of inverted organic solar cells*  
5th Colloquium of the Munich School of Engineering, Garching, 9 Jul 2015
- S. Xia, E. Metwalli, Y. Yao, M. Schwartzkopf, D. Chekrygina, B. Beyersdorff, S. V. Roth, P. Müller-Buschbaum  
*In-situ GISAXS investigation of aluminum deposition on PS-b-P3HT diblock copolymer thin film*  
DPG-Frühjahrstagung, Berlin, 15 – 20 Mar 2015
- Y. Yao, E. Metwalli, J. -F. Moulin, B. Su, M. Opel, and P. Müller-Buschbaum  
*Morphology investigation of self-assembly of metal oxide-diblock copolymer nanocomposite films*  
DPG-Frühjahrstagung, Berlin, 15 – 20 Mar 2015
- Y. Yao, E. Metwalli, J. -F. Moulin, B. Su, M. Opel, and P. Müller-Buschbaum  
*Maghemite nanoparticles embedded in thin block copolymer films*  
2nd internal biennial science meeting of the MLZ, Grainau, 15 – 18 June 2015
- X. Zhang, K. Kyriakos, E. N. Kitiri, E. N. Kitiri, C. Patrickios, C. M. Papadakis  
*Single and double networks from amphiphilic star block copolymers*  
DPG-Frühjahrstagung, Berlin, 15 – 20 Mar 2015
- X. Zhang, B. J. Niebuur, E. Lomkova, P. Chytil, S. K. Filippov, C. M. Papadakis  
*A fluorescence life-time study of the drug delivery system based on HPMA copolymers*  
2nd Internal Biennial Science Meeting of the MLZ, Grainau, 15 – 18 Jun 2015
- X. Zhang, K. Kyriakos, E. N. Kitiri, M. Rikkou-Kalourkoti, C. Patrickios, C. M. Papadakis  
*Single and double networks from amphiphilic star block copolymers*  
16th International Conference on Small-Angle Scattering, Berlin, 13 – 18 Sep 2015

## 8.4 Invited Talks at LS Funktionelle Materialien

- Helena vom Stein, ETH Zürich  
*Direct and inverse opal photonic balls for structural coloration*  
4 Feb 2015
- Angelika Beinert, Fraunhofer Institut für Solare Energiesysteme ISE  
*The influence of the additive composition on the mechanical degradation behavior of ethylene-vinyl acetate in photovoltaics*  
31 Mar 2015
- Dr. Neelima Paul, FRM II  
*An insight into Li-ion battery research using X-ray and neutron scattering techniques*  
21 Apr 2015
- Georg Bothmann  
*Thermoelectric studies on transition element substituted GeSbTe-phases*  
19 May 2015
- Stephan Saller, TUM  
*Design and fabrication of lateral THz emitting nonlinear quantum cascade lasers*  
21 May 2015
- Jakob Lenz, Ludwig-Maximilians-Universität München  
*Control of chemical reactions at the nanoscale due to plasmonic heating of gold nanoparticles*  
22 May 2015
- Moritz Futscher, Humboldt Universität Berlin  
*Energy-level alignment at hybrid interfaces between ZnO and organic semiconductors*  
2 Jun 2015
- Florian Siebel, German Patent and Trademark Office  
*The German Patent and Trademark Office and its e-services patent searches with DEPATISnet*  
30 Jun 2015
- Dr. Ian D. Sharp, Joint Center for Artificial Photosynthesis (JCAP), Lawrence Berkeley National Laboratory, Physical Biosciences Division, Berkeley, USA  
*Functional materials and interfaces for photocatalytic conversion of solar energy to fuel*  
6 Jul 2015
- Dr. Bernhard Ferse, TU Dresden, Institut für Halbleiter- und Mikrosystemtechnik  
*Hydrogels in microfluidics*  
14 Jul 2015
- Sophia Ramirez Bernini, TUM  
*DNA nanorods as probes for diffusion in hydrogels*  
21 Jul 2015
- Dr. Ricky Dunbar, CSIRO PV Performance Laboratory Energy Flagship, Mayfield West, Australia  
*Achieving high accuracy performance measurements of perovskite solar cells at standard test conditions*  
31 Aug 2015

- Prof. Apostolos Kyritsis, Dept. of Physics, National Technical University of Athens, Greece  
*Thermal and dielectric studies on interfacial water in hydrated biomolecules*  
18 Nov 2015
- Dr. Paul A. Staniec, Diamond Light Source Ltd, UK  
*Upgrade to the I22 SAXS beamline to perform GI-SAXS experiments*  
30 Nov 2015
- Prof. Koen Vandewal, TU Dresden  
*Charge-transfer states for organic solar cells and NIR photo-detectors*  
11 Dec 2015
- Prof. Tiberio A. Ezquerra, IEM-CSIC, Madrid, Spain  
*Improving information density in ferroelectric polymer films by using nanostructured surfaces*  
16 Dec 2015

## 8.5 Funding

### Deutsche Forschungsgemeinschaft:

- *Zweifach und orthogonal schaltbare Blockcopolymerer aus zwitterionischen und thermoresponsiven Blöcken: Synthese und Strukturen in Lösung und im dünnen Film*  
Grant Number: MU 1487/17-1  
Project Leader: Prof. Dr. Peter Müller-Buschbaum
- *In-situ Untersuchungen zu Kondensation, Nukleation und Wachstum von Metallfilmen und Nanostrukturen auf organischen Oberflächen während Sputterbeschichtung*  
Grant Number: MU 1487/18-1  
Project Leader: Prof. Dr. Peter Müller-Buschbaum
- 1. Teilprojekt *Inorganic-organic hybrid photovoltaic solar cells using novel hybrid materials* im GRK 2022: University of Alberta / Technische Universität München Internationale Graduiertenschule für Funktionelle Hybridmaterialien (ATUMS) der DFG IRTG-2022  
Project Leader: Prof. Dr. Peter Müller-Buschbaum
- *In-situ-Messung deformationsinduzierter Martensitbildung in ausferritischem Gusseisen (ADI)*  
Grant Number: PE 580/14-1  
Project Leader: Prof. Dr. Winfried Petry
- Within DFG Collaborative Research Centre SFB TRR 80/2:  
*Elektronische Struktur und martensitische Phasenumwandlungen*  
Teilprojekt: G04  
Project Leader: Prof. Dr. Winfried Petry
- Im Rahmen des Memorandums of Understanding on Cooperation between DFG and RFBR:  
*Mischungen aus Lösungsmitteln und Mischungen aus Blockcopolymeren für die kontrollierte Präparation strukturierter dünner Blockcopolymerfilme*  
Grant Number: PA 771/10-2  
Project Leader: Prof. Dr. Christine Papadakis
- *Zweifach und orthogonal schaltbare Blockcopolymerer aus zwitterionischen und thermoresponsiven Blöcken: Synthese und Strukturen in Lösung und im dünnen Film*  
Grant Number: PA 771/14-1  
Project Leader: Prof. Dr. Christine Papadakis
- Im Rahmen des Memorandums of Understanding on Scientific Cooperation between DFG and GACR:  
*Kugelförmiges Pferd im Vakuum oder anwendbare Mizellen?*  
Grant Number: PA 771/17-1  
Project Leader: Prof. Dr. Christine Papadakis

**Bayerisches Staatsministerium für Bildung und Kultus, Wissenschaft und Kunst:**

- Im Rahmen der Munich School of Engineering (MSE):  
*Solar Technologies Go Hybrid (SolTech) - Forschungsnetzwerk TUM.solar*  
Project Leader: Prof. Dr. Peter Müller-Buschbaum
- Im Rahmen der Munich School of Engineering (MSE): Netzwerk Regenerative Energien  
*Aufbau eines interdisziplinären Netzwerks aus Lehrstühlen der Technischen Universität München und anderen Forschungseinrichtungen zur Förderung der Forschungsaktivitäten im Bereich der regenerativen Energien*  
Project Leader: Prof. Dr. Peter Müller-Buschbaum
- Seedfunding im Rahmen des Energy Valley Bavaria (Munich School of Engineering, MSE)  
*Novel Nanostructured Thermoelectric Hybrid Materials (NovelNTHM)*  
Project Leader: Prof. Dr. Peter Müller-Buschbaum
- Nachwuchsgruppe im Rahmen des Energy Valley Bavaria (Munich School of Engineering, MSE)  
*Organische Photovoltaik*  
Project Leader: Dr. Eva M. Herzig

**Technische Universität München:**

- Im Rahmen der International Graduate School of Science and Engineering (IGSSE)  
*Interface Science for Photovoltaics - a EuroTech GreenTech Initiative*  
Project Leader: Prof. Dr. Peter Müller-Buschbaum
- Im Rahmen der TUM University Foundation  
*Fellowship to support postdoctoral researchers and to foster their scientific careers*  
Project Leader: Prof. Dr. Christine Papadakis

**Others:**

- Im Rahmen des Exzellenzclusters Nanosystems Initiative Munich (NIM)  
*Nanosystems for Energy Conversion*  
Principal Investigator: Prof. Dr. Peter Müller-Buschbaum
- Im Rahmen der Leonhard-Lorenz-Stiftung  
*Untersuchung der magnetischen Domänenstruktur in ferromagnetischen Formgedächtnislegierungen*  
Project Leader: Prof. Dr. Winfried Petry
- Im Rahmen von Bund der Freunde der TUM  
*Autark durch gedruckte Energieversorgung*  
Project Leader: Dr. Eva M. Herzig; Collaboration Partner: Prof. Dr. Peter Müller-Buschbaum
- Im Rahmen des Programms Hochschulpartnerschaften mit Griechenland (Deutscher Akademischer Austausch Dienst, DAAD)  
*Thermoresponsive polymers of complex architecture (ResComp)*  
Project Leader: Prof. Dr. Christine Papadakis; Co-Project Leader: Prof. Dr. Apostolos Kyritsis (National Technical University of Athens, NTUA).

## 9 The chair



### 9.1 Staff

**Chair:** Prof. Dr. Winfried Petry

**Head:** Prof. Dr. Peter Müller-Buschbaum

**Professor:**

Prof. Dr. Christine Papadakis

**Fellows:**

Dr. Anatoly Berezkin  
Dr. Eva Maria Herzig  
Dr. Volker Körstgens  
Dr. Michael Leitner  
Dr. Wiebke Lohstroh

Dr. Ezzeldin Metwalli Ali  
Dr. Jürgen Neuhaus  
Dr. Martine Philipp  
Dr. Konstantinos Raftopoulos

**PhD students:**

Bruno Baumeister	Claudia M. Palumbiny
Lorenz Bießmann	Stephan Pröller
Antonella Campanella	Christian Reiter
Tobias Chemnitz	Nitin Saxena
Mihael Coriç	Christop Schaffer
Stefan Döge	Rupert Schauer
Margarita Dyakonova	Robert Schenk
Shuai Guo	Johannes Schlipf
Nuri Hohn	Luca Silvi
Tobias Hollmer	Lin Song
Tanja Huber	Florian Soutschek
Lukas Karge	Christian Steyer
Bettina Kracke	Bo Su
Konstaninos Kyriakos	Natalya Vishnevetskaya
Jenny Lebert	Kun Wang
Jakob Lenz	Rui Wang
Xiaohan Li	Weijia Wang
Franziska Löhner	Stephan Wlokka
David Magerl	Senlin Xia
Daniel Moseguí González	Yuan Yao
Kai Müller	Dan Yang
Pascal Neibecker	Xiaohan Zhang

**Master students:**

Edoardo Barabino	Marvin Koch
Michael Bahr	Sumit Maity
Herbert A. Caller-Guzman	Juan Felipe Martinez Grisales
Florian Dreher	Anjani Kumar Maurya
Oliver Filonik	Martin Finkel
Christoph Mayr	Moritz Futscher
Bart-Jan Niebuur	Micael Gouveia
Lukas Oesinghaus	Sebastian Günther
Ali Özkü	Arnulf Grimm
Shambhavi Pratap	Sixin He
Anna Sanina	Ali Hassan
Erwin Heldmann	Stefanie Seidl
Nuri Hohn	Christoph Senfter
Chih-Chun Huang	Bernhard Springer
Stefan Huber	Richard Stockhausen
Florian Jung	Rosa Maria Torrademé
Maximilian Kaepfel	Markus Trunk
Thomas Kaps	Tobias Widmann
Chiahsin Ko	Simon Schaper

**Bachelor students:**

Alexander Bauer  
Oliver Bienek  
Fabian Englbrecht  
Julian Fischer  
Simon Hiller  
Regina Kluge  
Marinus Kundinger

Justus Oberhausen  
Christian Oberleitner  
Simon Pinzek  
Philipp Riederer  
Florian Ristow  
Matthias Vogt  
Stefan Weber

**Students assistants:**

Kora-Lee Claude  
Florian Jung

Matthias Steinmaßl  
Hong Xu

**Technical/administrative staff:**

Susanna Fink  
Reinhold Funer  
Josef Huber  
Josef Kaplonski

Matthias Maier  
Dieter Müller  
Nick Schröder  
Marion Waletzki

## 9.2 Graduations

### • External habilitation

Martine Philipp

*'Transformations de phases et phénomènes interfaciaux de la matière condensée molle', Habilitation à diriger des recherches, Université de Lorraine, France.*

### • Accomplished PhD Theses

Konstantinos Kyriakos

*Cononsolvency of PNIPAM in water/alcohol mixtures – A neutron scattering study*

Tobias Hollmer

*Development of a PVD-based manufacturing process of monolithic LEU irradiation targets for  $^{99}\text{Mo}$  production*

Claudia Maria Palumbiny

*Polymeric PEDOT:PSS electrodes for organic electronics: Understanding the conductivity-structure relation*

### • Accomplished Master Theses

Michael Bahr

*Hybrid magnetic thin films*

Sebastian Max Günther

*Implementing an OPV slot die coating device and determining the ramifications on morphology and solar cell performance*

Herbert A. Guzman Caller

*In-situ growth of titania films by spray coating*

Ali Hassan

*Nanoparticle based active layers for organic photovoltaics*

Erwin Heldmann

*Evaluation of prompt gamma spectra using different models*

Nuri Hohn

*Structure and performance of water soluble solar cells functionalized with high-k nanoparticles*

Chih-Chun Huang

*Laser-ablated nanoparticles for hybrid solar cells*

Stefan Otto Huber

*Structure of polydimethylsiloxane melts, networks and nanocomposites with silica*

Sumit Maity

*Temperature dependent oxygen disorder in  $\text{Pr}(2-x)\text{Sr}(x)\text{NiO}(4+\delta)$  investigated by high resolution single crystal neutron diffraction on HEiDi @ FRM II*

Juan Felipe Martínez Grisales

*Effects of a selective solvent additive on P3HT:PCBM based solar cells*

Christoph Mayr

*Hybrid solar cells based on aqueous processed titania nanoparticles*

Bart-Jan Niebuur

*Characterization of polymeric nanoparticles for drug delivery with fluorescence and scattering methods*

Stefanie Seidl

*Characterization of a velocity selector for UCN*

Rosa Maria Torrademé

*Ternary organic solar cells based on PTB7:PC<sub>70</sub>BM*

Tobias Widmann

*Fabrication and characterization of active layers for flexible hybrid solar cells*

• **Accomplished Bachelor Theses**

Alexander Bauer

*Metal decorated colloidal films for application in organic photovoltaics*

Oliver Bienek

*Block copolymer membranes for lithium ion microbatteries*

Fabian Englbrecht

*Influence of drying dynamics on performance of printed organic solar cells*

Julian Benedikt Fischer

*In-situ degradation of thin films for organic photovoltaics*

Simon Hiller

*Aufbau einer Apparatur zur Lichtstreuung unter Hochdruck*

Regina Michaela Kluge

*Thermoelectric thin films based on conducting polymers*

Marinus Kundinger

*Role of molecular interactions for stimuli-responsive polymers of potential use in soft robotics*

Justus Oberhausen

*Nanostructured block copolymer thin films – computer simulations*

Christian Oberleitner

*Metal-polymer nanocomposites for sensor applications*

Simon Pinzek

*Phase behavior of responsive polymers under high pressure*

Philipp Riederer

*Layer-optimization for high efficiency perovskite solar cells*

Florian Ristow

*Nanoparticles via laser ablation for hybrid solar cells*

Matthias Vogt

*Characterization of a velocity selector for UCN*

Stefan Weber

*Design and implementation of an impedance spectroscopy cell for thick polymer films for battery applications*

### 9.3 Guests

- Irati Barandiaran, University of the Basque Country, Spain  
*2 Feb – 30 Apr 2015*
- Micael Gouveia, University of Lisbon, Portugal  
*5 Apr – 31 Sep 2015*
- Prof. Dr. Alfons Schulte, University of Central Florida, USA  
*16 – 20 Apr, 6 May – 25 Jun, 14 – 18 Oct 2015*
- Michael Ford, University of California at Santa Barbara, USA  
*1 Jun – 12 Jun 2015*
- Prof. Dr. Jan Kristian Krüger and Nicolas Merlinge, University of Luxembourg  
*26 – 29 Jun 2015*
- Prof. Dr. Jochen Gutmann, Universität Duisburg-Essen  
*29 Jun 2015*
- Dr. Ian D. Sharp, Joint Center for Artificial Photosynthesis (JCAP), Lawrence Berkeley National Laboratory, Berkeley, USA  
*29 Jun – 14 Jul 2015*
- Razan Al-Esseili, University of Jordan  
*6 Jul – 2 Aug 2015*
- Robin Tyburski, University of Uppsala  
*6 Jul – 28 Aug 2015*
- Dr. Bernhard Ferse, Technische Universität Dresden  
*14 Jul 2015*
- Dr. Ricky Dunbar, CSIRO PV Performance Laboratory Energy Flagship, Mayfield West, Australia  
*31 Aug 2015*
- Alvaro Rodriguez, Soft and Polymer Matter Group, CSIC, Madrid, Spain  
*22 Sep – 22 Dec 2015*
- Stefanos Koutsoumpis, National Technical University of Athens, Greece  
*19 Oct – 28 Nov 2015*
- Dr. Qi Zhong, Zhejiang Sci-Tech University, PR China  
*4 – 15 Nov 2015*
- Prof. Apostolos Kyritsis, National Technical University of Athens, Greece  
*16 – 20 Nov 2015*
- Dimosthenis Georgopoulos, National Technical University of Athens, Greece  
*16 – 21 Nov 2015*
- Prof. Dr. Koen Vandewal, TU Dresden  
*11 Dec 2015*
- Prof. Dr. Tiberio A. Ezquerro, CSIC Madrid, Spain  
*15 – 16 Dec 2015*